UNIVERSITAT POLITÈCNICA DE CATALUNYA

DEPARTAMENT DE ÒPTICA I OPTOMETRIA

Thorough characterization and analysis of a multispectral imaging system developed for colour measurement

Thesis

Student: Marta De Lasarte Rigueiro

SUMMARY

Nowadays, imaging systems based on CCD cameras are widely used in several fields, and particularly in the field of scientific image, due to its high resolution, high quantum efficiency, wide spectral response, acceptable signal-to-noise ratio, linearity, geometric fidelity, fast response, small size and durability.

In spite of this, if a CCD camera is wanted to be used as a measuring instrument, one must bear in mind that CCD cameras are not perfect detectors, but there are various noise sources inherent to their performance that alter the digital levels corresponding to each pixel, distort the real image acquired in an unknown manner, and diminish the radiometric accuracy, the image quality and the resolution.

Two of the relatively recent applications of the imaging systems based on CCD cameras are colour measurement and spectral reconstruction. The first one basically consists of estimating the XYZ tristimulus values associated to a colour sample from the system's response digital levels, whereas the second one consists of estimating the reflectance spectrum of a colour sample from its corresponding system's response digital levels.

Nevertheless, performing colour measurements and/or spectral reconstructions using this kind of devices requires a previous characterization or calibration of the imaging system aimed to determine the transformation that defines the correspondence between system's digital responses and either a colour space independent of the device, such as the XYZ or the CIELAB, or the reflectance spectra space. This is due to the fact that system's digital responses, even the RGB output signals for a trichromatic imaging system, do not correspond with the device independent tristimulus values based on the CIE standard colorimetric observer.

Methods for colorimetric characterization can be divided in two general categories: methods based on spectral sensitivities and methods based on a colour sample chart. Some of the methods based on spectral sensitivities are usually only applied to colorimetric configurations of imaging systems, i.e. with three acquisition channels, due to its growing complexity when the number of acquisition channels is increased. These methods require the previous knowledge of the system's spectral sensitivities for each acquisition channel, which can be determined through the spectral characterization of the imaging system.

Regarding the methods for spectral reconstruction, their main objective is to recover the reflectance, transmittance or radiance spectra of a colour sample from the corresponding digital responses of the imaging system. These methods are usually applied to multispectral configurations since linear models of reflectance spectrum used require at least four acquisition channels to be able to estimate real reflectance spectra.

In order an imaging system based on a CCD camera can be used as a measuring instrument with high spatial resolution, so that the whole system's detection area is useful for measuring, it is mandatory to correct the spatial non-uniformity of the system's response. Basically two kinds of techniques are used with this purpose. Firstly, the scene-based techniques are based on applying an algorithm to the original or raw image (image to be corrected) in order to obtain a considerable improvement in image quality at the expense of radiometric accuracy. Secondly, the flat-field correction or spatial non-uniformity correction techniques are based on calibrating the detector by means of two images: a dark image and a uniform field or flat-field image, which are linearly combined with the original or raw image. This second type of techniques allows one to use a CCD camera to perform accurate radiometric measurements. Several

variants of these flat-field correction or spatial non-uniformity correction techniques can be found in literature. The most general of these variants allows the correction of the spatial non-uniformity of the system's response independently of the spatial non-uniformity of the scene illumination, which is quite useful in several measurement imaging conditions, such as in case of images corresponding to self-radiating objects. Using an imaging system based on a CCD camera for high spatial resolution colour measurement and/or spectral reconstruction requires applying one of the second type of techniques for the spatial non-uniformity correction.

The fact that the spectral sensitivities of most of the commercial colour CCD cameras (3 acquisition channels) do not verify the Luther condition, i.e., are not linear transformations of the CIE colour matching functions, limits seriously the colorimetric applications of the imaging systems based on colour CCD cameras, giving rise to estimated tristimulus values dependent on the illuminant. This property of spectral sensitivities leads to use multispectral imaging systems, since the only way to assure a colour matching for all observers and under changes in illumination is achieving a spectral matching. The most direct method to obtain spectral information from the measured samples is to increase the sampling over the three traditional acquisition channels by means of narrowband filters, which is known as a multispectral imaging system. The application fields of the multispectral imaging systems have increased enormously in last years, fundamentally due to the possibility that offer of estimating accurately the reflectance spectrum at each pixel and, from it, the XYZ tristimulus values avoiding metamerism.

The main aim of this work is to develop a multispectral imaging system for colour measurement and spectral reconstruction. The design and development of a prototype of multispectral imaging system in the visible range of the spectrum and its thorough characterization and analysis are presented in this PhD thesis. For this purpose, an imaging system based on a CCD camera is used. Therefore, in order to be able to perform accurate colour measurements and/or spectral reconstructions with high spatial resolution it will be necessary to carry out, firstly, the noise correction of system's response, particularly the correction of the spatial non-uniformity. Secondly, the previously mentioned characterization or calibration of the imaging system should be applied to obtain the XYZ tristimulus values and/or the reflectance spectra, respectively, from system's digital responses.

Two imaging systems based on a CCD camera are used in this work: one based on a colour 10-bits CCD camera, and another based on a monochrome 12-bits cooled CCD camera. Two configurations of this last imaging system are considered: a colorimetric configuration with 3 acquisition channels, and a multispectral configuration with 7 acquisition channels. The spectral characterization is carried out only for the colorimetric configuration of the previously mentioned imaging systems, in order to be able to apply a method for colorimetric characterization based on the spectral sensitivities of the imaging system.

The multispectral imaging system designed and developed in this work comprises a monochrome 12-bits cooled CCD camera, a motorized filter wheel controlled via software with a set of narrowband filters, and an objective lens of variable focal length. Results obtained in the NIR region of the spectrum in previous works have been extrapolated to the visible range, and a set of seven narrowband interference filters covering the whole visible range of the spectrum, with equal FWHM and equidistant central wavelengths, have been used. Each filter constitutes an acquisition channel of the multispectral imaging system, which corresponds to the multispectral configuration of the imaging system mentioned previously.

Different methods for colour measurement and spectral reconstruction are applied to the two configurations of the imaging system based on a monochrome 12-bits cooled CCD camera, and compared using all possible combinations of the GretagMacbeth ColorChecker Color Rendition chart (CCCR) and the GretagMacbeth ColorChecker DC chart (CCDC) as training and test sets. The aim is to determine the most suitable methods for each configuration, i.e., the methods that allow one to achieve the best accuracy of both colour measurement and spectral reconstruction for each configuration. At the same time, the performance of the two configurations is also compared in terms of accuracy of both colour measurement and spectral reconstruction.

The first stage to be followed before an imaging system based on a CCD camera can be used as a measuring instrument with high spatial resolution is to carry out the correction of the different noise sources inherent to the CCD's performance and, especially, the correction of the spatial non-uniformity of the sensor's response. With this purpose, the experimental methodology to correct these noise sources has been developed and a linear algorithm for the spatial non-uniformity correction of the system's response has been optimized.

Several analyses have also been carried out in order to improve the accuracy of colour measurement and spectral reconstruction performed using imaging systems based on CCD cameras. These analyses are described below.

Firstly, considering the basic concepts applied in high dynamic range imaging (HDRI) to obtain a device independent representation of the visual content of a real scene, a luminance adaptation model (LAM) is developed to increase the dynamic range of the imaging system by taking images at different exposure times in order to obtain useful digital levels for all pixels. The application of this LAM allows one to measure colour at each pixel of the image, increasing the dynamic range of the imaging system by this way.

Secondly, the influence of the number of samples of the training set on accuracy of colour measurement and spectral reconstruction is analyzed in order to determine whether there exists a relationship between accuracy of colour measurement and spectral reconstruction, and the size of the training set used. Accuracy of system's performance improves by increasing the size of the training set up to 110 colour samples approximately, and becomes independent of the training set used for training sets having a number of colour samples greater or equal to 110.

Next, colour measurement and spectral reconstruction performed using both the colorimetric and the multispectral configurations of the imaging system are analyzed depending on colour ranges measured, i.e. sets of colour samples grouped by their hue property, with the aim of determining whether these configurations are especially sensitive to some hues and/or some other colour properties or not. Firstly, general tendencies are analyzed using the CCDC chart as training and test sets, and secondly, the 1269 colour patches of the Munsell Book of Color – Matte Collection, classified in 10 Munsell hues and each one of these in 4 sub-hues, are used to analyze the influence of homogeneity in hue of the training set on system's performance.

Homogeneity in hue of the training set is proved to allow improving meaningfully the accuracy of system's performance in terms of both colour measurement and spectral reconstruction. On the other hand, three combinations of training and test sets of Munsell's colour patches are used in order to vary the degree of homogeneity in hue of the training set. Best results are obtained using the training sets most homogeneous in hue.

Furthermore, results obtained are also analyzed depending on colour characteristics of samples measured such as the CIELAB coordinates, and the Munsell

hue, value and chroma coordinates. No correlation is observed between accuracy of system's performance and CIELAB coordinates, whereas accuracy of system's performance tends to get worse for samples having Munsell Values V > 7 – 8.

The influence of the illuminant used is also analyzed by comparing results obtained using two illuminants: an incandescent lamp illuminant, which is the one used in the analyses mentioned before, and a D65 simulator illuminant. The best combination of system's configuration and illuminant resulted to be the multispectral configuration and the D65 simulator illuminant.

Then, accuracy of colour measurement and spectral reconstruction is analyzed depending on the reflectance spectra of colour samples measured, in order to determine whether there exists any kind of correlation between them or not. This study is performed using the best proved combination of system's configuration and illuminant, and the CCDC chart and the Munsell's colour patches as training and test sets. Accuracy of colour measurement and spectral reconstruction is analyzed depending on, on one hand, the Area Under the Curve (AUC) of the reflectance spectra and, on the other hand, on the smoothness of the reflectance spectra by means of their Discrete Fourier Transform (DFT), which is frequently used in spectral analysis. Considering the AUC analysis, accuracy of colour measurement tends to improve for colour samples with higher AUCs of their reflectance spectra, whereas this tendency is not observed in terms of the accuracy of spectral reconstruction. However, any direct relationship cannot be established either between the accuracy of colour measurement and the AUC of the reflectance spectra of colour samples. Considering the DFT analysis, accuracy of colour measurement seems to be independent of the shape and/or the smoothness of reflectance spectra, whereas the best accuracy of spectral reconstruction is frequently associated to a smooth reflectance spectrum, although any general correlation cannot be established between them either.

Once the multispectral imaging system developed is thoroughly analyzed, and its limitations in terms of accuracy of colour measurement and spectral reconstruction are established, the next stage is determining whether any other number and/or combination of commercially available interference filters would allow one to improve, at least theoretically, the accuracy of the multispectral imaging system in terms of colour measurement and spectral reconstruction. For this purpose, a simulation study of an optimum multispectral imaging system for colour measurement and spectral reconstruction is presented. This study is performed considering the spectral response of the monochrome 12-bits cooled CCD camera used and a database of commercially available interference filters selected among the databases of Edmund Optics, OptoSigma and CVI. Accuracy of system's performance is improved in terms of accuracy of both colour measurement and spectral reconstruction with an increasing number of interference filters. Nevertheless, this improvement is limited and tends to be insignificant for more than 8 filters. Optimum filters tend to make up for the spectral response of the CCD camera over the whole visible range, but considering the drawback the unknown real spectral transmittances of filters supposes (simulations depend greatly on the real spectral transmittances of filters, which not always can be easily simulated from the specifications provided by suppliers), selecting a set of interference filters having equidistant peak positions covering the whole visible range, equal FWHMs that allow a slight overlapping between them, and the higher transmittance possible, as it was done in this work, constitutes an acceptable option to obtain a worthy multispectral imaging system.

Finally, the applicability of the multispectral imaging system developed is tested not only using standardized colour charts, such as the CCCR, CCDC, and the Munsell's

colour patches used so far, but also using real samples, such as a set of 56 textile samples grouped in 28 pairs, which were made specifically to test the applicability of colour difference formulas, and the D65 simulator illuminant. Different combinations of training and test sets are analyzed. Best results are obtained, in average, using training sets homogeneous in hue and carrying out a previous hue classification of the textile samples used as test set. Moreover, the multispectral imaging system developed is proved to be able to detect slight differences both in colour and in reflectance spectra between real samples, making it useful for applications that require discrimination, although a quite low accuracy of system's performance is obtained in detecting both colour differences and spectral differences between pairs of textile samples.

CONTENTS

Agradecimientos / *Ackowledgements*

Los agradecimientos son, probablemente, una de las partes más difíciles de redactar, sintetizar y detallar de forma exhaustiva de todo el proceso de elaboración y escritura de la tesis doctoral, así como, al menos desde mi punto de vista, una de las fundamentales ya que ¿quién hubiera sido capaz de llevarlo a cabo sin todas aquellas personas que, de un modo u otro, nos han ayudado, escuchado, animado y apoyado? Por este motivo incluyo los agradecimientos en dos lenguas, el inglés, que es la lengua en la que he redactado este trabajo doctoral, y el español, mi lengua materna, con la que me expreso con mayor soltura.

Durante los cuatro años y medio que ha durado este proceso para mí, son numerosas las personas a las que me gustaría dar las gracias por todo lo positivo que me han aportado durante este periodo. Intentaré ser lo más exhaustiva posible, aunque pido disculpas de antemano por si cometo alguna omisión.

A mis directores de tesis, los doctores D. Jaume Pujol Ramo y Dña. Montserrat Arjona Carbonell, debo agradecerles su apoyo y ayuda durante estos cuatro años y medio, permitiéndome desarrollar libremente mi proyecto de tesis doctoral, y haciendo posible mi asistencia a numerosos congresos, tanto nacionales como internacionales, lo que me ha permitido a su vez adentrarme fácilmente en el mundo de la investigación en los campos del color y la imagen multiespectral. Debo agradecer también a la doctora Dña. Meritxell Vilaseca Ricart su accesibilidad, disponibilidad y disposición a ofrecer su ayuda en todo momento en que la he necesitado.

A los doctores de la Universidad de Alicante D. Francisco Miguel Martínez Verdú (Verdú) y Dña. Maria Dolores de Fez Saiz (Dolo) les agradezco su ayuda y dedicación así como también, junto con el doctor D. Vicent Camps Sanchis (Vincent), su amable acogida durante mi estancia en su laboratorio en septiembre-octubre de 2004.

Gracias también al doctor D. Joaquín Campos Acosta por financiar las estancias de estudiantes de doctorado en laboratorios a través de las redes temáticas de ciencia y tecnología del color. A estas ayudas debo mi estancia en el Laboratorio de Imágenes Multiespectrales del Departamento de Óptica de la Universidad de Granada en enero de 2005, a cuyos miembros agradezco su atención, hospitalidad y ayuda durante mi estancia. En concreto, agradezco muy especialmente su atención, hospitalidad y dedicación a los doctores D. Javier Hernández Andrés (Javi) y D. Rafael Huertas Roa (Rafa), quienes redujeron al mínimo mis momentos de soledad durante los días de mi estancia y me mostraron algunos de los lugares más bonitos de la maravillosa ciudad de Granada.

Agradezco a todo el personal del CD6 su accesibilidad, disponibilidad y disposición a ofrecer su ayuda en todo momento en que la he necesitado, especialmente a nuestros técnicos, Xavier Murcia Navarro en el taller mecánico y Fermín Alarcón Escobar en el taller electrónico, quienes han estado siempre ahí para resolver cualquier inconveniente, por pequeño que fuese.

Agradezco a la AGAUR ("Agència de Gestió d'Ajuts Universitaris i de Recerca") de la "Generalitat de Catalunya" la beca FI que me fue concedida y que disfruté entre los meses de enero y abril de 2004, permitiéndome iniciar mis estudios de doctorado, y al Ministerio de

Educación y Ciencia de España la beca FPU que me fue concedida a partir de abril de 2004 y que me ha permitido completarlos y finalizarlos, así como complementarlos realizando una estancia de tres meses en el Departamento de Ciencia del Color de la Universidad de Leeds (Leeds, Reino Unido). En relación a esta estancia quiero agradecer a los doctores D. Ronnier Luo, D. Changjun Li y D. Wei Ji su hospitalidad, amabilidad y gran ayuda durante mi estancia en su departamento, así como a la doctora Dña. Seo Young Choi su generosidad, compañía y disposición en todo momento que hicieron mis primeros días en Leeds mucho más fáciles y mi estancia allí mucho más agradable.

Gracias al doctor D. Josep Valldeperas y al Sr. Joan Antoni Navarro del INTEXTER por su amable colaboración.

A los amigos que he ido conociendo a lo largo de esta etapa, Albert, Alberto, David, Fer, y muy espacialmente Cristina y Jordi, les agradezco el haber compartido buenos y malos momentos, el haber sabido escuchar y los buenos momentos que hemos pasado juntos. A Inma, que es como una segunda madre para mí, le agradezco sinceramente su apoyo, interés, confianza, alegría y todos los ánimos y consejos que me ha dado en mis malos momentos durante este periodo de tiempo, que me han ayudado enormemente a sobrellevar el día a día.

Finalmente, mis agradecimientos más profundos son para mis padres, Alberto y Asunción, mi hermana Sirvi, mi gran amiga, y Miguel Ángel, mi gran amor. A mis padres y a mi hermana les agradezco de todo corazón el haber estado siempre a mi lado, el haberme apoyado y ayudado de forma incondicional siempre, el haber creído y confiado en mí incluso en aquellos momentos en los que yo no lo hacía, el haberme escuchado en todo momento, aún siendo repetitiva hasta la saciedad, y haber intentado comprenderme y ayudarme, el haberme enseñado el valor de las cosas y de las personas y a luchar y defender mis intereses. Gracias a ellos acabé la Licenciatura de Física y gracias a ellos decidí finalizar los estudios de doctorado en un momento en el que estaba dispuesta a abandonarlo todo.

A Miguel Ángel le agradezco el haber sido valiente, a pesar del paso del tiempo y los factores adversos, haber luchado por lo que quería y haber hecho posible que ahora estemos compartiendo nuestro día a día. Gracias por haber cambiado mi vida completamente desde hace un año y pocos meses, por interesarse por mi trabajo y haberme devuelto la ilusión por él y por acabar mi tesis, por apoyarme cada día, sobre todo los días malos que no han sido pocos, por aguantar mis bajones e intentar ayudarme a superarlos, y por su ayuda en la fase final de mi trabajo doctoral y en el proceso de escritura, compartiendo conmigo todos sus conocimientos sin ningún tipo de recelo profesional.

Acknowledgements are probably one of the most difficult sections to write, synthesise and detail exhaustively of the whole development and writing process of a PhD thesis, just as, at least from my point of view, a fundamental one since who would have been able to carry it out without any of those people who, in one way or another, have helped, listened, encouraged and supported us? This is the reason why I enclose acknowledgements written in two languages, English, which is the language this doctoral work is written in, and Spanish, my mother tongue, with which I express myself more fluently.

I would like to thank numerous persons for all positive things they gave me during the four years and a half length of this process to me. Though I will try to be the most exhaustive possible, and please forgive any omission in advance.

I must thank my thesis directors, Doctors Mr Jaume Pujol Ramo and Mrs Montserrat Arjona Carbonell, for their support and help during these four years and a half, allowing me to develop freely my PhD project, and making my attendance to numerous conference, both national and international, possible, which allowed me, at the same time, to go into the research world in the fields of colour and multispectral imaging. I must also thank Doctor

Mrs Meritxell Vilaseca Ricart for her accessibility, availability and disposition to offer her help at any moment I needed it.

I am also very grateful to Doctors of the University of Alicante, Mr Francisco Miguel Martínez Verdú (Verdú) and Ms Maria Dolores de Fez Saiz (Dolo) for their help and dedication, just as, together with Doctor Mr Vicent Camps Sanchis (Vincent), for their kind welcome during my stay at their laboratory in September-October 2004.

I thank Doctor Mr Joaquín Campos Acosta for funding the PhD student's stays at laboratories through the thematic networks of science and colour technology. I owe these funding my stay at the Multispectral Imaging Laboratory of the Department of Optics of the University of Granada during January 2005, whose members I thank for their attention, hospitality and help during my stay. I especially want to express my deep gratitude to Doctors Mr Javier Hernández Andrés (Javi) and Mr Rafael Huertas Roa (Rafa), who reduced to a minimum my moments of solitude during the days of my stay, and showed me some of the most beautiful places of the wonderful city of Granada.

I am grateful to all the staff of the CD6 for their accessibility, availability and disposition to offer their help at any moment I needed it, especially to our technicians, Xavier Murcia Navarro in the mechanical workshop and Fermín Alarcón Escobar in the electronic workshop, who were always there to solve any problem, no matter the slight it was.

I am also very grateful to the 'AGAUR' ("Agència de Gestió d'Ajuts Universitaris i de Recerca") of the "Generalitat de Catalunya" (Government of Catalonia) for the FI grant I was awarded and I enjoyed from January to April 2004, allowing me to start my PhD studies, and to the 'Ministerio de Educación y Ciencia de España' (Ministry of Education and Science of Spain) for the FPU grant I was awarded from April 2004, and which allowed me to complete and to finish, just as complement them carrying out a stay of three months length at the Department of Colour Science of the University of Leeds (Leeds, UK). Regarding this stay I owe my special thanks to Doctors Mr Ronnier Luo, Mr Changjun Li, and Mr Wei Ji for their hospitality, kindness and great help during my stay at their department, just as to Doctor Ms Seo Young Choi for her generosity, company and disposition at any moment that made my first days in Leeds much easier and my stay there much more pleasant.

Thanks to Doctor Mr Josep Valldeperas and Mr Joan Antoni Navarro from the INTEXTER, for their kind collaboration.

I thank the friends I met during this period, Albert, Alberto, David, Fer, and very especially Cristina and Jordi, for having shared good and bad moments with me, having listened, and all good moments we spent together. I also want to express my deeply thanks to Inma, who is like a second mum for me, for all her support, interest, confidence, joy and all the encouragements and pieces of advice she gave me in my low moments during this period of time, which helped me enormously to bear the day by day.

Finally, my deepest gratitude is due to my parents, Alberto and Asunción, my sister Sirvi, my great friend, and Miguel Ángel, my great love. I express my sincere thanks to my parents and my sister for having supported and helped me always in a wholehearted way, for having believed in and trusted me even in those moments I did not, for having listened me at every moment, even being repetitive over and over again, and having tried to understand me and help me, for having taught me the worth of things and persons and to fight and protect my interests. Thanks to them I finished my degree in Physics, and thanks to them I fought to finish my PhD studies when I was determined to drop out everything.

I sincerely thank Miguel Ángel for having been courageous, in spite of the passage of time and adverse factors, and having fight to reach what he wanted and having made possible that today we were sharing our day by day. Thanks for having completely changed my life since one year and a few months ago, for having interested in my work and returned me my hope on it and on finishing my PhD thesis, for having supported me every day and mainly on

bad days, for having bore my low moments and tried to help me to overcome, and for his help in the final stage of my doctoral work and in the writing process, sharing with me all his knowledge without any kind of professional mistrust.

1 Introduction and Objectives

Nowadays, imaging systems based on CCD cameras are widely used in several fields, and particularly in the field of scientific image, due to its high resolution, high quantum efficiency, wide spectral response, acceptable signal-to-noise ratio, linearity, geometric fidelity, fast response, small size and durability [Holst, 1996; Holst, 2001; Janesick, 2001]. In spite of this, if a CCD camera is wanted to be used as a measuring instrument, one must bear in mind that CCD cameras are not perfect detectors, but there are various noise sources inherent to their performance that alter the digital levels corresponding to each pixel, distort the real image acquired in an unknown manner, and diminish the radiometric accuracy, the image quality and the resolution [Janesick, 2001].

Two of the relatively recent applications of the imaging systems based on CCD cameras are colour measurement and spectral reconstruction. Colour measurement basically consists of estimating the XYZ tristimulus values associated to a colour sample from system's response digital levels, whereas spectral reconstruction consists of estimating the reflectance spectrum of a colour sample from its corresponding system's response digital levels. Nevertheless, performing colour measurement and/or spectral reconstruction using this kind of devices requires a previous characterization or calibration of the imaging system. On one hand, colour measurement requires to determine the transformation that defines the correspondence between system's digital responses and a colour space independent of the device, such as the XYZ or the CIELAB, since system's digital responses, even the RGB output signals for a trichromatic imaging system, do not correspond with the device independent tristimulus values based on the CIE standard colorimetric observer [Hong et al., 2001]. On the other hand, spectral reconstruction requires to determine the transformation that defines the correspondence between system's digital responses and the reflectance spectra space. Methods for colorimetric characterization can be divided in two general categories: methods based on spectral sensitivities, some of which are usually only applied to colorimetric configurations of imaging systems, i.e. with three acquisition channels, due to its growing complexity when the number of acquisition channels is increased, and methods based on a colour sample chart. Methods based on spectral sensitivities require the previous knowledge of system's spectral sensitivities for each acquisition channel, which can be determined through the spectral characterization of the imaging system.

Regarding the methods for spectral reconstruction, their main objective is to reconstruct the reflectance, transmittance or radiance spectra of a colour sample from the corresponding digital responses of the imaging system. These methods are usually applied to multispectral configurations since linear models of reflectance spectrum used require at least four acquisition channels to be able to estimate real reflectance spectra [Shi et al., 2002].

In order an imaging system based on a CCD camera can be used as a measuring instrument with high spatial resolution, so that the whole system's detection area is useful for measuring, it is mandatory to correct the spatial non-uniformity of the system's response. Basically two kinds of techniques are used with this purpose. Firstly, the scene-based techniques are based on applying an algorithm to the original or raw image (image to be

corrected) in order to obtain a considerable improvement in image quality at the expense of radiometric accuracy. Secondly, the flat-field correction or spatial non-uniformity correction techniques are based on calibrating the detector by means of two images: a dark image and a uniform field or flat-field image, which are linearly combined with the original or raw image. This second type of techniques allows one to use a CCD camera to perform accurate radiometric measurements. Several variants of these flat-field correction or spatial non-uniformity correction techniques can be found in literature. The most general of these variants allows the correction of the spatial non-uniformity of the system's response independently of the spatial non-uniformity of the scene illumination, which is quite useful in several measurement imaging conditions, such as in case of images corresponding to self-radiating objects.

Using an imaging system based on a CCD camera for high spatial resolution colour measurement and/or spectral reconstruction requires applying one of the second type techniques for the spatial non-uniformity correction. In this work, the experimental methodology developed to correct the inherent noise sources of an imaging system based on a CCD camera, and the optimization of a spatial non-uniformity correction algorithm to obtain the best spatial non-uniformity correction possible are presented.

The main aim of this work is to develop a multispectral imaging system for colour measurement and spectral reconstruction. The design and development of a prototype of multispectral imaging system in the visible range of the spectrum and its thorough characterization and analysis are presented in this work. For this purpose, an imaging system based on a CCD camera is used. Therefore, in order to be able to perform accurate colour measurements and/or spectral reconstructions with high spatial resolution it will be necessary to carry out, firstly, the noise correction of system's response, particularly the correction of the spatial non-uniformity. Secondly, the previously mentioned characterization or calibration of the imaging system should be applied to obtain the XYZ tristimulus values and/or the reflectance spectra, respectively, from system's digital responses.

Two imaging systems based on a CCD camera are used in this work: one based on a colour 10-bits CCD camera, and another based on a monochrome 12-bits cooled CCD camera. Two configurations of this last imaging system are considered: a colorimetric configuration with 3 acquisition channels, and a multispectral configuration with 7 acquisition channels. The spectral characterization is carried out only for the colorimetric configuration of the previously mentioned imaging systems, in order to be able to apply a method for colorimetric characterization based on the spectral sensitivities of the imaging system. Different methods for colour measurement and spectral reconstruction are applied to the two configurations of the imaging system based on a monochrome 12-bits cooled CCD camera, and compared using all possible combinations of the GretagMacbeth ColorChecker Color Rendition chart (CCCR) and the GretagMacbeth ColorChecker DC chart (CCDC) as training and test sets, in order to determine the most suitable methods for each configuration, i.e., the methods that allow one to achieve the best accuracy of both colour measurement and spectral reconstruction for each configuration. At the same time, the performance of the two configurations is also compared in terms of both accuracy of colour measurement and accuracy of spectral reconstruction. The fact that the spectral sensitivities of most of the commercial colour CCD cameras (3 acquisition channels) do not verify the Luther condition [Wyszecki et al., 1982], i.e., are not linear transformations of the CIE colour matching functions, limits seriously the colorimetric applications of the imaging systems based on colour CCD cameras, giving rise to estimated tristimulus values dependent on the illuminant. This property of spectral sensitivities motivates the use of multispectral imaging systems, since the only way to assure a colour matching for all observers and under changes in illumination is achieving a spectral matching. The most direct method to obtain spectral

information of the measured samples is to increase the sampling over the three traditional acquisition channels by means of narrowband filters, which is known as a multispectral imaging system. The application fields of the multispectral imaging systems have increased enormously in last years, fundamentally due to the possibility that offer of estimating accurately the reflectance spectrum at each pixel and, from it, the XYZ tristimulus values avoiding metamerism.

The multispectral imaging system designed and developed in this work comprises a monochrome 12-bits cooled CCD camera, a motorized filter wheel controlled via software with a set of narrowband filters, and an objective lens of variable focal length. A set of seven narrowband interference filters covering the whole visible range of the spectrum, with equal FWHM and equidistant central wavelengths, are used following the results obtained in previous works [Vilaseca, 2005] in the NIR region of the spectrum, and extrapolating them to the visible range. Each filter constitutes an acquisition channel of the multispectral imaging system, which corresponds to the multispectral configuration of the imaging system mentioned previously.

Another fundamental objective of this work is to improve the accuracy of colour measurement and spectral reconstruction performed using imaging systems based on CCD cameras. For this purpose, several analyses are carried out throughout this work.

Firstly, considering the basic concepts applied in high dynamic range imaging (HDRI) to obtain a device independent representation of the visual content of a real scene, a luminance adaptation model (LAM) is proposed to increase the dynamic range of the imaging system by taking images at different exposure times in order to obtain useful digital levels for all pixels.

Secondly, the influence of the number of samples of the training set on accuracy of colour measurement and spectral reconstruction is analyzed in order to determine whether there exists a relationship between accuracy of colour measurement and spectral reconstruction, and the size of the training set. This analysis is considered to be the first step in the process of studying the accuracy of colour measurement and spectral reconstruction depending on the training set used.

After that, colour measurement and spectral reconstruction performed using both the colorimetric and the multispectral configurations of the imaging system are analyzed depending on the colour ranges measured, i.e. sets of colour samples grouped by their hue property, with the aim of determining whether these configurations are especially sensitive to some hues and/or some other colour properties or not. Firstly, general tendencies are analyzed using the CCDC chart as training and test sets. Secondly, the 1269 colour patches of the Munsell Book of Color – Matte Collection, classified in 10 Munsell hues and each one of these in 4 sub-hues, are used to analyze the influence of homogeneity in hue of the training set on system's performance. Three combinations of training and test sets of Munsell's colour patches are used in order to vary the degree of homogeneity in hue of the training set. Furthermore, results obtained are also analyzed depending on the colour characteristics of samples measured such as the CIELAB coordinates, and the Munsell hue, value and chroma coordinates. The influence of the illuminant used is also analyzed by comparing results obtained using two illuminants: an incandescent lamp illuminant, which is the one used in the analyses mentioned before, and a D65 simulator illuminant.

Next, the accuracy of colour measurement and spectral reconstruction is analyzed depending on the reflectance spectra of colour samples measured, in order to determine whether there exists any kind of correlation between them or not. This study is performed using the best proved combination of system's configuration and illuminant, which is multispectral configuration and D65 simulator illuminant, and the GretagMacbeth ColorChecker DC chart (CCDC) and the 1269 colour patches of the Munsell Book of Color –

Matte Collection, as training and test sets. Accuracy of colour measurement and spectral reconstruction is analyzed depending on the Area Under the Curve (AUC) and on the Discrete Fourier Transform (DFT) of the reflectance spectra.

Once the multispectral imaging system developed is thoroughly analyzed, and its limitations in terms of accuracy of colour measurement and spectral reconstruction are established, the next stage is determining whether any other number and/or combination of commercially available interference filters would allow one to improve, at least theoretically, the accuracy of the multispectral imaging system in terms of colour measurement and spectral reconstruction. For this purpose, a simulation study of an optimum multispectral imaging system for colour measurement and spectral reconstruction is presented. This study is performed considering the spectral response of the monochrome 12-bits cooled CCD camera used and a database of commercially available interference filters.

Finally, the applicability of the multispectral imaging system developed is tested not only using standardized colour charts, such as the CCCR, CCDC, and the Munsell Book of Color – Matte Collection used so far, but also using real samples, such as a set of textile samples and the D65 simulator illuminant.

This work was part of the research project 'Development of a new spectrophotometric instrumentation for colour measurement based on optoelectronic image sensors', belonging to the '*Programa Nacional de Tecnologías avanzadas de la Producción*' and funded by the '*Ministerio de Ciencia y Tecnología*' of Spain (DPI2002-00118) until 2005. From 2006 on, this work is part of the new research project 'Development of new techniques and advanced instrumentation in visual optics and colour based on image capture devices', also belonging to the '*Programa Nacional de Tecnologías avanzadas de la Producción*' and funded by the '*Ministerio de Ciencia y Tecnología*' of Spain (DPI2005-08999-C02-01). This work has been carried out at the Centre for Sensors, Instruments and Systems Development (CD6) of the Optics and Optometry Department (DOO) of the Technical University of Catalonia (UPC), through a FPU grant ('*Formación de Personal Universitario*') awarded by the '*Ministerio de Educación y Ciencia*' (MEC) of Spain.

This work is structured in 15 chapters. In chapter 1, the main objectives of the work and the work carried out are introduced. In chapter 2, the state of the art on fields directly related with this work are presented, such as the multispectral imaging systems, the charge coupled devices (CCDs), the spectral characterization of imaging systems based on CCD cameras, the use of an imaging system based on a CCD camera as an instrument for colour measurement and spectral reconstruction, and the increase of the dynamic range of an imaging system. In chapter 3 the material and method used and applied throughout this work are detailed. In chapter 4, the experimental methodology developed for the noise correction of an imaging system based on a CCD camera and the optimization of an algorithm for the spatial non-uniformity correction of system's response are presented. In chapter 5, the colorimetric configurations of two imaging systems based on CCD cameras (a colour 10-bits CCD camera and a monochrome 12-bits cooled CCD camera) are spectrally characterized, and their colorimetric characterization based on the previously determined spectral sensitivities is subsequently carried out. In chapter 6, different methods for colour measurement and spectral reconstruction are applied and compared for the two configurations (colorimetric and multispectral) of the imaging system based on a monochrome 12-bits cooled CCD camera. In chapter 7, the dynamic range of the imaging system is increased through the proposed luminance adaptation model of proven validity. In chapter 8, the influence of the number of colour samples of the training set on accuracy of colour measurement and spectral reconstruction is analyzed for the two configurations (colorimetric and multispectral) of the

imaging system based on a monochrome 12-bits cooled CCD camera. In chapter 9, the influence of colour ranges on accuracy of colour measurement and spectral reconstruction is analyzed for the two configurations (colorimetric and multispectral) of the imaging system based on a monochrome 12-bits cooled CCD camera. The influence of the illuminant on system's performance is also analyzed using an incandescent lamp illuminant and a D65 simulator illuminant. In chapter 10, the influence of reflectance spectra on accuracy of colour measurement and spectral reconstruction is analyzed using the best proved combination of system's configuration and illuminant, which is multispectral configuration and D65 simulator illuminant. In chapter 11, a simulation study of an optimum and commercially available multispectral imaging system for colour measurement and spectral reconstruction is carried out. In chapter 12, the multispectral imaging system's applicability is tested by performing colour measurement and spectral reconstruction of a set of textile samples. In chapter 13, the conclusions of this work and some ideas for future work are presented. In chapter 14, the references used throughout this work are detailed. Finally, some appendixes containing datasheets and specifications of the instruments and material used in this work, and detailed tables and graphics to which some of the previously mentioned chapters are referred can be found.

2 State of the Art

2.1 Multispectral imaging systems

A multispectral imaging system is, by definition, an imaging system able to provide complete spectral information instantaneously at each pixel of the captured image of a scene [Hardeberg, 1999]. Therefore, a multispectral image not only presents a high spatial resolution, but also provides the radiance spectrum of the illuminant, the reflectance spectrum of the object, or the combined colour signal, at each pixel. Knowing the spectral information of the scene, the complete colorimetric information of the image is also known, since the tristimulus values in any colour system can be calculated from the spectral information [Wyszecki et al., 1982]. Spectral information at each pixel of the image is also useful to obtain printings or reproductions of a scene with high colour accuracy, and even avoiding the metamerism due to changes in illuminant. Since the multispectral imaging systems appearance, spectral measurements were carried out exclusively using spectroradiometers or spectrophotometers, which are quite slow and only provide one spectral measurement each time.

The main component of a multispectral imaging system is a CCD or CMOS camera, whose response must be linear versus the received radiance and the exposure time. This property is named the reciprocity law by some authors [Ferrero et al., 2006 – 1]. Digital image acquisition systems are commonly classified in literature depending on the number of acquisition channels [Imai et al., 1999; Imai et al., 2003]: monochromatic with 1 acquisition channel, RGB or trichromatic with 3 acquisition channels, multispectral with 4 – 9 acquisition channels, hyperespectral with 10 – 100 acquisition channels, and ultraspectral with more than 100 acquisition channels.

The CCD sensor is a monochrome imaging device, i.e. photo-electrons induced by light of different wavelengths are indistinguishable. To create a colour image the incoming light needs to be selected before it hits the CCD. In the RGB or trichromatic image acquisition systems, also called colorimetric imaging systems, the three acquisition channels, usually red (R), green (G), and blue (B), can be obtained through several methods [Sharma, 2003]:

- *Colour filter arrays (CFAs)*. Most digital cameras use a single image sensor overlaid with a mosaic pattern of colours, known as colour filter array or CFA. Because the green region of the spectrum is perceptually more significant, these CFAs have green, red and blue recording pixels in the ratio 2:1:1 or 3:1:1. Each photodetector is sensitive to only one colour spectral band, and, as a result, de-mosaicing must be used to produce a full-colour image. There are a variety of colour filter patterns, being the most common one the Bayer CFA and de-mosaicing algorithms. The mostly used filter pattern is the Bayer CFA [Lukac et al., 2005], which is a mosaic of tiny RGB colour filters placed over the pixel sensors allowing to obtain information about the intensity of light in red, green, and blue wavelength regions.
- *Colour sequential*. In this method, the colour image is produced by taking successive exposures while switching in optical filters having the desired RGB transmission characteristics. The resulting colour image is formed by combining the three colour separation

images. The filters may be dichroic or absorptive RGB filters mounted in a colour wheel or a tunable LCD filter.
- *Multi-sensor colour*. This method uses a beam splitter, which is typically a dichroic prism, to separate the light into red, green and blue components. These are focused onto three separate monochrome image sensors.
- *Three layer direct image sensor (Foveon X3)*. A three layer direct image senor has three layers of pixels embedded in silicon to take advantage of the fact that red, green, and blue light penetrate silicon to different depths – forming the first and only image sensor that captures full colour at every point in the captured image.

The main aim of the multispectral imaging systems is to obtain spectral information of the measured samples. The most common configuration of a multispectral imaging system comprises a monochrome CCD camera and a set of narrowband filters covering the whole visible range of the spectrum [Imai et al., 2000 – 2; Imai et al., 2002], although configurations that comprise a colour CCD camera and one or several absorption filters are also used [Imai, 1998; Imai et al., 1998; Imai et al., 1999; Imai et al., 2000 – 1; Imai et al., 2000 – 2; Imai et al., 2002].

The spectral sensitivities of most of the commercial colour CCD cameras (colorimetric configuration) do not verify the Luther's condition [Wyszecki et al., 1982], i.e., are not linear transformation of the CIE colour matching functions. Therefore, two surfaces spectrally different under a same illuminant can give identical camera's RGB responses and, consequently, identical XYZ tristimulus values applying the colorimetric characterization of the camera, although surfaces were visually different. This is known as device metamerism and limits considerably the colorimetric applications of the imaging systems based on colour CCD cameras. Moreover, the obtained tristimulus values depend on the illuminant.

The unique way to assure the colour matching for all observers and under changes in illuminant is achieving a spectral matching. The most direct method to obtain spectral information of the measured samples is to increase the sampling above the three traditional acquisition channels, which is known as a multispectral imaging system. Taken to the limit, this would be equivalent to use a spectrophotometer at each pixel, so that, applying and appropriate calibration, the imaging system would become a spectrophotometer with spatial resolution.

Errors in estimate of tristimulus values are considered negligible using wavelength increases and bandwidths of 5nm, corresponding to 81 channels for the visible spectrum [Imai et al., 1999]. Due to the fact that the spectral properties of the most of surfaces are relatively smooth functions of the wavelength, it is possible to reduce the number of acquisition channels without a significant loss of spectral information. Several studies demonstrated that spectral reflectance functions can be accurately fitted by linear models of low dimensionality [Maloney, 1986; Vrhel et al., 1994 – 2; Shimano 2005], although a minimum of four degrees of freedom are required to fit real reflectance spectra [Shi et al., 2002]. The minimum number of acquisition channels required for an accurate spectral reconstruction of reflectance spectra of surfaces depends on the application but, considering spectral analyses of colour stimulus performed using linear models, a number of acquisition channels less than 10 is usually required [Maloney, 1986; Jaaskelainen et al., 1990; Vrhel et al., 1994 - 2].

Multispectral imaging systems allow both, estimating the reflectance spectrum at each pixel by means of a previous spectral analysis carried out with direct measurements and images of colour samples to establish a relationship between the digital levels of the system's response and the reflectance spectra [Imai et al., 1999], and improving the accuracy of the colorimetric characterization [Tominaga, 1999] and subsequently improving the accuracy of the XYZ tristimulus values estimate.

2.1.1 Different configurations of multispectral imaging systems

The acquisition channels of a multispectral imaging system can be classified into wideband and narrowband regarding their spectral profile. The wideband acquisition channels usually correspond to absorption plastic colour filters (with wide spectral profile) that are combined with a colour CCD camera to constitute the multispectral imaging system. The narrowband acquisition channels usually correspond to interference filters whose transmittance spectra is a Gaussian centred in a certain wavelength, combined with a monochrome CCD camera to constitute the multispectral imaging system.

Three different configurations of multispectral imaging systems can be distinguished depending if the acquisition channels are wideband, narrowband, or a combination of both.

2.1.1.1 Multispectral imaging systems based on colour CCD cameras

The simplest multispectral imaging system, or the lowest cost one, consists of a colour CCD camera (with 3 acquisition channels) combined with different wideband absorption plastic colour filters, which are added successively to capture successive images. This multispectral imaging system configuration has been widely used [Imai et al., 1999; Day, 2003; Nieves et al., 2005]. Each image captured using a new filter provides three acquisition channels to the global system. The number and shape of the wideband filters depend on the spectral sensitivities of the camera's RGB channels, the inherent noise and the shape of the reflectance spectra that want to be reconstructed [Day, 2003].

Other possible configuration of a multispectral imaging system based on a colour CCD camera consists of using different light sources as illuminant [Heikkinen et al., 2008]. In this case, each image captured using a different light source as illuminant provides three acquisition channels to the global system.

Finally, in order to use these multispectral imaging systems to perform colour measurements and/or spectral reconstructions, it is essential to carry out a previous training of the system that allows one to relate the digital responses of the multispectral imaging system to the spectra and/or the XYZ tristimulus values that originates them, respectively, by using a training set of samples with known spectra. The methods for colour measurement and spectral reconstruction used in this work are described further on in this section.

2.1.1.2 Multispectral imaging systems based on monochrome CCD cameras and narrowband filters

Interference filters and tunable filters, such as solid state liquid crystal tunable filters (LCTF), are narrowband and usually present a Gaussian transmittance spectrum, which allow one to use them in two different ways to perform spectral measurements, but always combined with monochrome CCD cameras.

The first way consists of a small number of filters and an algorithm for spectral reconstruction. The most common configuration for this kind of narrowband multispectral imaging systems comprises a monochrome CCD camera and a set of interference filters. Interference filters present several drawbacks such as having a transmittance depending on the incidence angle or having not exactly coplanar surfaces, which gives rise to spatial shifts and distortions on captured image. Moreover, there exist internal reflections due to reflections between the filters and the original image, and between the filters and the camera's lens, which also contribute to the experimental error associated to these multispectral imaging

systems. Alternatively to interference filters, the solid state liquid crystal tunable filters (LCTF) can also be used. These filters are easily controlled via software and are free of non-uniformities introduced by the angular sensitivity as it happens with interference filters. This kind of narrowband multispectral imaging systems requires a previous training of the system.

The second way assumes that the narrowband filter is completely monochromatic and, therefore, only provides information at the maximum transmittance wavelength. If the monochrome camera used is radiometrically calibrated [Healey et al., 1994; Ferrero et al. 2006 – 2], and the filter's transmittance is known, the radiance incident over the system can be directly sampled at each wavelength. If a greater spectral accuracy than that provided by the filter's maximum transmittance wavelength is required, interpolation techniques [Vilaseca, 2005] or a greater number of filters, being then an hyperespectral imaging system, can be used. The narrowband multispectral or hyperespectral imaging systems based on sampling require neither the use of spectral reconstruction algorithms nor a previous training, but a previous radiometric calibration of the system.

2.1.2 Designing an optimized multispectral imaging system

Numerous methods and studies on the design and optimum selection of filters in a multispectral imaging system exist, just as on the optimum number of filters both from a colorimetric point of view, i.e., regarding the colour estimate performed using the multispectral imaging system [Vrhel et al., 1992; Vrhel et al., 1994 – 1; Vrhel et al., 1995; Hosoi et al., 1999], and from a spectral point of view, completing the colorimetric selection of filters regarding the spectral reconstruction performed using the multispectral imaging system [Imai et al., 2001; Imai et al., 2002: Day, 2003], hence obtaining a set of filters that allows performing highly accurate colour measurement, and another set that allows performing highly accurate spectral reconstructions.

There also exist studies whose aim is to determine theoretically the minimum number of filters necessary in a multispectral imaging system in order to achieve a minimum error in reconstructing spectra. This is carried out by means of simulating the design of optimized filters for the reconstruction of a concrete set of reflectance spectra and having a maximum resistance to noise, for a simulated multispectral imaging system [Connah et al., 2006]. The basic disadvantage of these filters is that are not real filters and depend on the set of reflectance spectra considered in their design, the noise and the validity of the noise model applied.

Two different configurations of multispectral imaging systems have been previously described: one comprising a colour CCD camera and wideband absorption filters, and the other one comprising a monochrome CCD camera and a set of narrowband (interference or tunable) filters. The third way of constructing a multispectral imaging system, which combines wideband and narrowband filters, consists of designing a set of optimum sensors that allow one to reconstruct spectra with the best accuracy possible. Several authors [Sharma et al., 1998; Hardeberg, 1999; Connah et al., 2002; López-Álvarez et al., 2005; Shimano, 2006; López-Álvarez et al., 2007 – 1] studied the optimum design of sensors, based on the possibility of manufacturing almost any spectral response using semiconductors properly doped [Lerch et al., 2001], or even using manufacturing or implementation methods of the optimum sensors with semiconductor devices having a spectral profile electronically tunable due to NiPiN structures [Park et al., 2002; Yotter et al., 2003].

2.1.3 Applications of multispectral imaging systems

Due to the possibility offered by the multispectral imaging systems of estimating accurately the reflectance spectrum at each pixel and the corresponding XYZ tristimulus values from it, avoiding metamerism, the application fields of multispectral imaging systems have increased considerably in last years.

Some of the applications of the multispectral imaging systems are, for instance, the acquisition of high dynamic range images [Haneishi, 2005], the estimate of natural illuminants [López-Álvarez et al., 2005], the classification of fluorescents used as illuminants [Tominaga et al., 2005], the rejuvenating of artworks [Berns, 2005], the restoration and conservation of paintings [Schmitt et al., 2005; Bonifazzi et al., 2007], the characterization of products in food science [Sáenz Gamasa et al., 2006], the estimation of the reflectance spectrum of the human skin [Doi et al., 2006; Martinkauppi et al., 2008] and the visualization of its moisturizing capacity [Iwasaki et al., 2006], the infrared thermography [Cerón-Correa, 2006], the satellite images [Alecu et al., 2006], the natural vision systems [Yamaguchi et al., 2006] with applications, for example, in medical images, electronic commerce (e-commerce), digital files and electronic museums, colour reproduction [Ueda et al., 2006] and research on historical materials [Miyata et al., 2006], agriculture [Kane et al., 2007; Lu et al., 2007], research on chemistry [Chourpa et al., 2008], etc.

2.2 Charge Coupled Devices: CCDs

Charge-coupled devices (CCDs) were invented by Boyle and Smith in 1970. Since then, considerable literature has been written on CCD physics, fabrication, and operation. However, the array does not create an image by itself. It requires and optical system to image the scene onto the array's photosensitive area. The array requires a bias and clock signals, and its output is a series of analog pulses that represents the scene intensity at a series of discrete locations [Holst et al., 2007].

In this section, a brief description of what CCDs are and how they work, the noise sources inherent to a CCD camera performance and their correction, and the applications of the CCD cameras are presented. Finally, the charge-coupled devices (CCDs) are compared to the Complementary Metal Oxide Semiconductor (CMOS) in an attempt to clarify one of the most discussed questions in digital imaging: CCD or CMOS?

2.2.1 What they are and how they work

The heart of the solid state cameras is a two-dimensional matrix of charge coupled devices or CCDs that convert the light intensity in measurable voltage signals [Holst, 1998; Holst et al., 2007]. In a CCD camera, detectors are placed in a layer of semiconductor material, in this case silicon, located in the focal plane of an optical system that allows capturing an image. Each individual detector in the matrix is named pixel (abbreviation of 'picture element'). Its size can vary between few to several tens of microns, and the smaller the pixels size is, the greater the resolution of the captured image will be. The total number of pixels in a CCD matrix varies from thousands to millions of pixels, and the greater the number of pixels in the array is, the greater the field of view of the CCD will be. Each individual pixel collects photons and holds the electrons produced through the electron-hole pair generation process [Sze, 1981]. These electrons are read from the CCD matrix and used to produce a digital image of the variable light intensities detected by the CCD, allowing the

digital storage, the reproduction and the processing of the information represented in the image [Colleen Gino, 2004].

Technically, a CCD must carry out four primary operations in the generation of an image. These operations are: charge generation, charge collection, charge transfer, and charge measurement [Janesick, 2001]. Charge is generated at each pixel proportionally to the present incident light level, so the joint effect of all pixels is to produce a spatially sampled representation of a continuous scene [Holst, 1998; Holst et al., 2007].

The charge generation is the ability of each sensor (pixel) to intercept incoming photons and generate signal electrons through the electron-hole pair generation. Charge generation takes place at each pixel in the silicon body of the CCD, so each pixel behaves like an electron well and accumulates a number of electrons proportional to the number of incident photons [Colleen Gino, 2004]. The charge generation efficiency is described by means the quantum efficiency function (QE), which is the fraction of incident photons that produce useful charge in the silicon chip. An ideal CCD would have 100% QE at all wavelengths, but QE strongly depends on wavelength, dropping at near-infrared (NIR) and blue wavelengths. A CCD's response can potentially cover an enormous wavelength range, from 10nm to 1000nm, including the NIR (700nm – 1100nm), the visible, the ultraviolet (UV), the extreme ultraviolet (EUV), and soft x-ray regions (below 0.2nm) [Janesick, 2001]. Charge generation in the visible range (380nm – 780nm) presents a typical peak near 650nm, falling to a small percentage at 400nm due to the photon absorption by the gate structure of the CCDs covering the silicon.

The second operation is the charge collection, which is the ability of the sensor to accurately reproduce an image after electrons are generated. The digital image produced consists of the pattern of electric charge present at each pixel of the array that holds the produced electrons during the integration period. This process depends, basically, on four parameters: the area or number of pixels on the chip or CCD matrix, the number of signal electrons a pixel can hold, i.e., the charge capacity of a pixel (also known as full well capacity) that mainly depends on the pixel's physical size, the variation in sensitivity from pixel to pixel, and the ability of a pixel to efficiently collect electrons without loss to its neighbours when are generated. This last parameter, the charge collection efficiency (CCE), is a critical one because it defines the spatial resolution of the detector, which is directly related to the pixel size and the charge diffusion characteristics. For most of scientific applications the number of pixel on the matrix must be the greater possible [Janesick, 2001].

At the end of the integration period, when no more light is allowed to reach the CCD's detector, the charge held at each pixel is transferred, pixel by pixel, to an amplifier. For quantitative scientific measurements, such as those carried out in astronomy, it is important to have the less charge losses possible during the charge transfer process [Janesick, 2001].

Finally, in the readout process of the matrix the charge must move from the detection region to a zone where the quantity of charge can be measured. Several diagrams exist to carry out this process [Colleen Gino, 2004]. The detection and measurement of the charge collected at each pixel is achieved by spilling the charge in a small capacitor connected to an output amplifier that generates a voltage for each pixel proportional to the charge signal transferred [Janesick, 2001]. This voltage signal is digitized sequentially by means of an analog-to-digital converter (ADC), measured and kept at this converter.

There exists a great quantity of literature about the physics, manufacture, and operation of CCDs [Holst, 1998; Janesick, 2001; Holst et al., 2007]. Due to the fact that the aim of this work is not the study of these devices by themselves but its use, a brief introduction of some of the most fundamental characteristics and properties of these devices will only be made.

2.2.2 Noise sources in a CCD camera: fundamental characteristics

Noise sources inherent to the performance of a CCD camera alter the digital levels corresponding to each pixel, distort the real image captured in an unknown way and degrade the radiometric precision, the image quality and its resolution. Numerous studies on noise sources in a CCD device [Healey et al., 1994; Holst, 1998; Janesick, 2001; Holst et al., 2007] exist. In this work, the most relevant noise sources, which can influence on captured images using a CCD camera in a significant way, and their fundamental characteristics, are briefly described.

Noise sources in a CCD can be classified into temporal and spatial. Temporal noise can be reduced by frame averaging, while spatial noise cannot. However, some spatial noise can be removed by frame subtraction or gain/offset correction techniques. Temporal noise sources include shot noise, reset noise, output amplifier noise, and dark current shot noise. Spatial noise sources include photo response non-uniformity (PRNU) and dark current non-uniformity, which gives rise to the fixed pattern noise (FPN) [Kodak Appl. Note, 2006]. Although different noise sources have different origins, all of them are demonstrated as variations in image intensity.

Photon Shot Noise

The photon shot noise is associated to the random arrival of photons at any detector, and it is nature's fundamental limit on noise performance in light detection systems.

The time between photon arrivals is governed by Poisson statistics, so the photon shot noise is equal to the square root of the signal, both expressed in electrons.

Quantization Noise

The analog-to-digital converter (ADC) produces discrete output digital levels, so that a certain range of similar input voltages can produce the same output. It is a zero mean random noise independent of the signal (exposure time).

Read Noise

The read noise is an electronic noise that is added to the final signal above the device readout. It is independent of the exposure time and is produced during the conversion of the analog signal to a digital level.

The read noise can be isolated and removed by subtracting the 'bias' image. A 'bias' image is an image captured with a zero exposure time reading the CCD without having been exposed to light, isolating the read noise effect, since the thermal noise produced by the heat generated by the device electronics and light contributions to the exposure are minimum [Colleen Gino, 2004].

Dark Current Noise: Dark Current Non-Uniformity (FPN) and Dark Current Shot Noise

Dark current is the result of imperfections or impurities in the depleted bulk silicon or at the silicon-silicon dioxide interface. These sites introduce electronic states in the forbidden gap which act as steps between the valence and conduction bands, providing a path for valence electrons to sneak into the conduction band, adding to the signal measured in the pixel. The efficiency of a generation centre depends on its energy level, with states near mid-band generating most of the dark current. The generation of dark current is a thermal process wherein electrons use thermal energy to hop to an intermediate state, from which they are emitted into the conduction band. For this reason, the most effective way to reduce dark current is to cool the CCD, robbing electrons of the thermal energy required to reach an intermediate state.

Dark current noise is multiplicative. Its level is proportional to the exposure time and generates two types of noise: dark current non-uniformity (fixed pattern noise, FPN) and dark current shot noise.

Dark current non-uniformity or fixed pattern noise results from the fact that each pixel generates a slightly different amount of dark current due to slight differences in detector size, in the doping density and in the strange matter that can be trapped during the manufacture. This noise can be eliminated by subtracting a dark reference frame from each image, both taken at the same temperature and with the same integration time.

Regarding the dark current shot noise, it is a type 'shot' noise, so that it will be equal to the square root of the dark signal both expressed in electrons. The dark noise in an image resulting from the subtraction of a raw image and a dark frame is more than this by a factor of $\sqrt{2}$.

Photo Response Non-Uniformity (PRNU)

PRNU is consequence of differences in sensitivity to light existing between pixels due to variations in their manufacture process. The result at the pixel-to-pixel level is a faint checkerboard pattern in a flat-field image. Usually this variation is on the order of a percent or two of the average signal, and is linear with average signal.

PRNU depends on the signal and can be removed by 'flat-fielding,' a process by which a previously captured uniform flat-field (uniform field) image is used to calibrate out the differences between pixels. Although this process removes the photo response non-uniformity, the subtraction of images introduces an $\sqrt{2}$ increase in shot noise.

It is common to specify all noise sources in output equivalent electron units. Noise magnitude is given in terms of the root mean squared error (rmse(*)) of the random process that caused noise. Due to the fact that the noise sources are non-correlated, the total noise is given by the sum of the quadratic power of the different noise types.

2.2.3 Noise correction in CCD cameras

Due to their origin and fundamental characteristics, image averaging removes all noise sources except the FPN and the PRNU. These two types of noise give rise together to the spatial non-uniformity of the CCD camera's response, which must be corrected if the imaging system based on the CCD camera is wanted to be used as a measuring instrument with high spatial resolution.

Two types of techniques are usually used to carry out the spatial non-uniformity correction. The first type of techniques is based on calibrating the detector by means of two images: a dark image and a uniform field or flat-field image. The spatially corrected image results from the linear combination of these two images with the image to correct. The main objective of this first type of techniques is using a CCD camera to perform accurate radiometric measurements. These techniques are known as flat-field correction or spatial non-uniformity correction.

The second type of techniques, usually known as scene based techniques, are based on the application of an algorithm to the original or raw image in order to obtain a considerable

(*) $rmse = \sqrt{\frac{1}{n}\sum_{i=1}^{n}\left(y_i - \hat{y}_i\right)^2}$ where y_i represents the individual value of the measurement *i*, and $\hat{y}_i$ the expected value of this measurement *i*.

improvement in image quality at the expense of radiometric accuracy. There is a great variety of this type of techniques depending on the algorithm applied: statistic algorithms [Hayat et al., 1999], movement algorithms [Hardie et al., 2000], algebraic algorithms [Ratliff et al., 2002], and the method of the shape of the inverse covariance [Torres et al., 2003]. A correction technique that combines the calibration with an algebraic algorithm also has been developed, allowing a scene based correction with radiometric accuracy [Ratliff et al., 2003 – 1; Ratliff et al., 2003 – 2]. New vectorial filtering techniques have been recently applied to remove the noise in colour images [Lukac et al., 2005]. One of the fields where these techniques are higher applied is the astronomy due to the fact that high quality images are required and it is not possible to obtain the necessary images to perform the sensor's calibration [Oppenheim et al., 1968; Heijmans, 1994; Young et al., 1998].

The spatial non-uniformity correction or flat-field correction techniques allow an imaging system based on a CCD camera to be used as a measuring instrument with high spatial resolution and radiometric accuracy. Basically there exist two variants of the spatial non-uniformity correction or flat-field correction techniques, and both require two images: a dark image captured at the same temperature and with the same exposure time that the image to be corrected, and with the objective lens covered, and a uniform field image.

In the first variant of spatial non-uniformity correction or flat-field correction techniques [Tyson, 1986; Berns, 2001; Janesick, 2001; Colleen Gino, 2004], the uniform field image corresponds to the image of a uniform grey surface or an illuminated screen, placed exactly where images to be corrected will be subsequently taken, so that it is captured at the same illumination and exposure conditions. Assuming that the image of the grey surface (illuminated screen) is completely uniform, this will be used to numerically compensate for the spatial non-uniformity [Thomson et al., 2001] on each one of the images captured using the imaging system. This is carried out by capturing a uniform field image to which dark image captured with the same exposure time is subtracted. The uniform field image corrected by the dark image will be used as the uniform field image in the calibration. In case of capturing several images by using filters, a uniform field image is obtained for each filter. In this case, the spatial non-uniformity of both the scene illumination and the device's response contribute to the spatial non-uniformity of the image. Unfortunately, every change in illumination conditions requires capturing a new grey surface image. In addition, the approach does not allow the correction of the spatial non-uniformity of the device response independently. The basic process of calibration is described mathematically by the equation (2.1).

$$I_c = \frac{I - I_{dark}}{I_{uf}} \tag{2.1}$$

where I_c represents the corrected image, I represents the original or raw non-corrected image, I_{dark} represents the dark image, and I_{uf} represents the uniform field image (corrected by the dark image).

In case of applications with low level of illumination, the 'bias' image correction must also be applied, since read noise could be non negligible in front of the measured signal, unlike what happens with medium or high illumination levels, where the 'bias' image is considered to be included in the dark image due to its little importance in front of the image to be corrected. When the 'bias' image correction is applied, the uniform field image used in the calibration is obtained by subtracting the 'bias' image and the corresponding dark image to the non-corrected uniform field image. In this case, the calibration process is described by the equation (2.2) [Colleen Gino, 2004].

$$I_c = \frac{I - I_{bias} - I_{dark}}{I_{uf}} \tag{2.2}$$

where I_c represents the corrected image, I represents the original or raw non-corrected image, I_{bias} represents the 'bias' image, I_{dark} represents the dark image, and I_{uf} represents the uniform field image (corrected by the 'bias' image and the dark image).

In the second variant of spatial non-uniformity correction or flat-field correction techniques, the uniform field image corresponds to the image of a uniform radiance field and hereinafter will be called base correction image. The base correction image usually used is the known as brilliant image [Aikens et al., 1989; Bellia et al., 2003], which is defined as the image with the highest mean digital level without having any saturated pixel. The dark image and the base correction image are combined with the image to be corrected by means of two linear algorithms [van Vliet et al., 1998; Roper Scientific, 2004; Arneson]. In the first algorithm, images are directly combined according to the equation (2.3).

$$DL_c(i,j) = k\,\frac{DL(i,j) - DL_0(i,j)}{DL_B(i,j) - DL_0(i,j)} \tag{2.3}$$

where $DL_c(i,j)$, $DL(i,j)$, $DL_0(i,j)$ y $DL_B(i,j)$ are the digital levels at the (i,j) pixel of the corrected image, the original or raw non-corrected image, the dark image, and the base correction image, respectively, and k is a calibration constant that is estimated by the mean digital level of the image resulting from the difference between the base correction image and the dark image.

The second algorithm is based on the calculation of the gain and offset matrixes [Aikens et al., 1989; Bellia et al., 2003; de Lasarte et al., 2007 – 1] given by the equations (2.4).

$$\begin{aligned} DL_c(i,j) &= O(i,j) + G(i,j)DL(i,j) \\ G(i,j) &= \frac{DL_B - DL_0}{DL_B(i,j) - DL_0(i,j)} \\ O(i,j) &= DL_0 - G(i,j)DL_0(i,j) \end{aligned} \tag{2.4}$$

where $O(i,j)$ (i = 1,…, m and j = 1,…, n) represents the (i,j) element of the correction offset matrix **O**, $G(i,j)$ represents the (i,j) element of the correction gain matrix **G**, and DL_0 and DL_B are the called reference digital levels of the dark image and the base correction image, respectively. The mean digital level for all of the image's pixels is generally used as the reference digital level [Aikens et al., 1989; Bellia et al., 2003].

The size of these matrixes (mxn) depends on the number of pixels available on the CCD sensor used (m corresponds to the number of pixels present in a row of the CCD sensor and n to the number of pixels in any column).

Differences between the elements of the correction offset matrix **O** and gain matrix **G** are due to slight fluctuations in the responses of the individual pixels. These fluctuations cause the fixed pattern noise that is inherent to the camera's response, which is intended to be corrected by applying the above-mentioned linear correction algorithm.

As stated previously, the reference digital level and the base correction image usually used are the mean digital level and the brilliant image, respectively. Although using these values provided acceptable results, the non-uniformity correction could be significantly improved by applying the linear algorithm using other values. The influence of the dark image, which can have a zero or non-zero value, the base correction image, which can be

different to the brilliant one used so far, and the reference digital level, which can be different to the mean commonly used, have been studied in order to optimize the spatial non-uniformity correction [de Lasarte et al., 2007 - 1]. This study on the influence of these algorithm variables on the correction and their optimum values is presented in this work, together with the experimental methodology developed as a result.

Both of the linear algorithms described allow the independent spatial non-uniformity correction of the device's response and do not require the flat field image to be captured anew if the illumination conditions change. This may be useful in several measurement imaging conditions, such as in case of images corresponding to self-radiating objects.

2.2.4 Applications of CCD cameras

Modern image sensors are based on solid state technology. Five great fields of application of the imaging systems based on CCD sensors exist: TV transmission, commercial camcorders, artificial vision, military applications and scientific applications [Holst, 1998].

In the field of scientific applications, the CCD cameras are the most outstanding image devices due to their high resolution, high quantum efficiency, wide spectral response, low noise level (reduced dark current and read noise), large dynamic range, linearity, geometric fidelity, small size and durability [Holst, 1998; Janesick, 2001].

A great variety of scientific applications in which CCD cameras are used as image sensors exists. In particular, CCD cameras are widely used in computer vision systems and have progressively replaced the photographic films and plates as a mean of detecting images, in fields such as, for example, the transmission electron microscopy (TEM) and the professional astronomic image, where they have meant an authentic revolution due to their characteristics and performances. This is due to the great number of advantages of the CCD cameras opposite to the traditional photographic films and plates: images are available almost instantaneously in digital format, the response is practically linear over a wide dynamic range and their sensitivity is greater than many photographic emulsions allowing the detection of individual photons [Meyer et al., 2000].

On the other hand, a great number of scientific applications in which CCD cameras conveniently calibrated are used as measuring instruments also have been developed. The photometers based on CCD cameras, which allow collecting a great quantity of information of extensive surfaces in a much shorter time and with greater resolution that traditional luminancimeters [Bellia et al., 2003], are an example. This gives rise to a simpler and faster measuring procedure that the knowledge of luminance at some individual points, when the luminance distribution must be evaluated over an extensive surface. Possible applications of this kind of measurements are the illumination control and the illumination design in internal and external environments.

Another example of using a CCD camera as a measuring instrument, in which this work is focused, is the colour measurement using a CCD camera. In this case, the measuring device comprises a CCD camera and a set of filters that allow increasing the number of acquisition or measurement channels, improving the accuracy of colour calibration in principle. Conventional colorimeters do not provide spatial information of colour, whereas a CCD camera, conveniently corrected and calibrated, allows one to estimate with high spatial resolution, both the XYZ tristimulus values [Wu et al., 2000] at a certain pre-selected illumination conditions, and the reflectance spectra [Berns et al., 2005] associated to each pixel of the image, from the corresponding digital levels. Colour measurement using CCD cameras is applied in very different fields, such as the medical image to quantify the colour characteristics of tissue injuries [Balas, 1997], the characterization of colour of teeth in

odontology [Wu et al., 2000], the characterization of colour of human iris [Melgosa et al., 2000; Imai, 2000; Vilaseca et al., 2006 – 1; Vilaseca et al., 2008], the characterization of colour and changes in colour of skin [Storring et al., 2004; Mitsui et al. 2005; Iwasaki et al., 2006], etc.. Imaging systems based on CCD cameras are also used to obtain spectral images of artworks in museums, constructing databases in which files of master digital images of high quality of paintings figure to be used, for instance, in their own preservation [Saunders et al., 1993; Berns et al., 2002; Liang et al., 2004], in the illumination design by representing the image under different illumination conditions [Berns et al., 2005], in estimating the size and concentration of particles in the atmosphere [Olmo et al., 2008], etcetera.

2.2.5 Comparison with other photo-electronic image devices: Charge Coupled Device (CCD) versus Complementary Metal Oxide Semiconductor (CMOS)

A charge coupled device (CCD) is a detector chip, which was originally conceived in the Bell Laboratories in the USA as a new type of storage device for use in computers. At the beginning of the 1970s, the opto-electrical properties of the chip (interaction with light and charge transfer) proved to be predestined for other industrial applications. In the following years a component, which had many diverse uses in image acquisition and signal processing, was developed from the newly-constructed storage chip.

Nearly at the same time the first CMOS sensors became available. Complementary Metal-Oxide Semiconductors consist of photodiodes and oppositely connected transistors that have to digitize the analog signals received from single pixels. The image quality obtained from CMOS sensors at the time was inferior as compared to the quality of CCD images. Also, the lithographic process technologies of the semiconductor industry were not sufficiently mature for the manufacture of the necessary circuits. Both technologies, CCD and CMOS, are based on the same physical principle, namely, the internal electron-hole pair generation process, where the incidence of photons in semiconductors causes the generation of electrical charges. In recent years CMOS sensors have developed into strong competitors to CCD technology – in particular in machine vision and in industrial image processing.

Both the CCD and the CMOS devices are image sensors constituted by an array of metal-oxide semiconductors that accumulate charge proportional to the local light intensity at each pixel, giving rise to a representation of the light intensity distribution with spatial resolution [Janesick, 2001, Janesick, 2002]. Once the exposure is completed, a CCD transfers the charge at each pixel sequentially to the common output structure that converts the charge in voltage, accumulates it and sends it out of the chip. In a CMOS, on the contrary, the charge-voltage conversion takes place at each pixel. This difference in the readout technique has significant implications in sensor's architecture, its capacities and its limitations [Litwiller, 2001].

The comparison of the CCD and CMOS image sensors is usually carried out based on the analysis of the attributes that characterize the performance of an image sensor. Firstly, considering the responsivity, the CMOS sensors are in general slightly superior to the CCDs due to the fact that the gain elements are easier to be placed in a CMOS sensor. Their complimentary transistors allow low power and high gain amplifiers, whereas amplification in a CCD usually requires a significant power.

Regarding the dynamic range, CCDs are superior to CMOSs in approximately a factor 2 in comparable circumstances, and present significant advantages in front of CMOSs regarding the noise due, for instance, to a smaller on-chip circuitery and to the fact that common output amplifiers can be easily adapted to reach the minimum noise. Noise levels are usually higher in CMOS sensors because pixels are active and present a smaller collection

area. Nevertheless, these differences become less evident as anti-overflowing techniques are applied in CCD cameras, and designs of CMOS cameras are improved.

Considering the uniformity of the response between pixels, it can be distinguished between uniformity under illumination conditions and uniformity under dark conditions. The CMOS sensors are traditionally quite worse than the CCD sensors under both conditions since the gain and offset at each pixel can vary considerably between pixels, worsening the uniformity with regard to the CCD sensors, both under illumination conditions and under dark conditions. Certain amplifier structures allow reaching a greater uniformity in gain between pixels under illumination conditions, becoming the uniformity of the illuminated CMOS sensors similar to the CCD's one. The offset variations, highlighted as non-uniformities under dark conditions, make the CMOS sensors to be still worse in non-uniformity terms than CCD sensors under dark conditions. This is a quite relevant factor in applications where the signal levels are limited and non-uniformities under dark conditions contribute significantly to the global degradation of image [Litwiller, 2001]. Other characteristic properties of CMOS sensors are their high integration capacity and low power consumption [Litwiller, 2005].

An ability that has been unique of CMOS technology until recently is the possibility of referencing and reading out individual pixels or regions of interest (roi) of the image sensor, allowing very high readout speeds of images or lines for small regions of interest. This feature is based on the "active pixel sensor" (APS) technology, where every pixel consists of an optically active area and the respective readout electronics. It performs many steps of the (pre) processing of the signal at chip level with a very low current consumption and hence with moderate heat generation. This capacity has also been recently developed for CCD sensors, allowing the CCD windowing, i.e., the selection of the portion of the chip actually read out [Monacos et al., 2003; NASA, 2004; Metcalfe, 2007].

Another typical and unique characteristic of the CMOS sensors is the absence of blooming when an overexposure occurs. However, in CCD sensors the application of specific engineering is necessary to remove the blooming and, in general, it is not possible to remove it totally in CCD sensors developed for scientific applications [Litwiller, 2001].

Regarding their performance, both sensors are equally reliable in most of industrial and consumer applications. In extremely adverse environmental conditions, the CMOS sensors have the advantage that all functions of the circuit can be located in only one chip of integrated circuit, minimizing the presence of cables and soldered joints, which are the most common origin of failures. The CMOS sensors also have the capacity of being much more easily integrable than CCD devices, so that a CMOS camera can be significantly smaller than a comparable CCD camera [Litwiller, 2001].

Nowadays, the CMOS sensors dominate, for example, the low cost image market, although there does not exist a significant difference in production costs between both technologies at similar levels and of small size image devices, whereas CCD sensors are oriented to satisfy the highest level image necessities. Both technologies can be considered complementary, since each one presents own advantages in concrete areas and it is expected that in the course of time the CMOS image sensors could be used in applications of every higher level [Litwiller, 2001; Janesick, 2002].

2.3 Spectral characterization of imaging systems based on CCD cameras

The spectral characterization of a CCD camera consists of determining its relative spectral sensitivities for each acquisition channel. Following the ISO/WD 17321-1 [ISO/WD

17321-1] regulation, the methods for spectral characterization of a CCD camera can be classified into two groups.

Firstly, there are the methods based on direct spectral measurements [Poletto et al., 1999; Mermelstein et al., 2000; Martínez-Verdú, 2001; MacDonald et al., 2002; Martínez-Verdú et al., 2002; Vilaseca et al., 2002] of monochromatic images obtained by means of a monochromator, or a tunable laser, sampling the visible spectrum with constant wavelength increases, and using the optoelectronic spectral conversion functions (OESCFs) obtained following the ISO 15424/DIS [Hunt, 2004] regulation. A relative radiance is associated to each monochromatic image and, together with the OESCFs and the sets of monochromatic images, allows one to obtain the camera's relative spectral sensitivities. This first type of methods for spectral characterization are agreed to be the most accurate, but they also are tedious and by no means error-free, since an image needs to be taken at each wavelength and results depend on the accuracy of the image capture and the data processing.

Secondly, there are methods that estimate the spectral sensitivity from the camera's responses to a set of standard samples with known reflectance or transmittance [Pratt et al., 1976; Sharma et al., 1993; Hubel et al., 1994; Trussell et al., 1994; Vora et al. 1997; Harderberg et al., 1998; Harderberg, 1999; Herzog et al., 1999; Hong et al., 2001; Cheung et al., 2004 – 1; Alsam et al., 2007]. The camera's response to the standard samples is related to the sample's reflectance spectra by the equation (2.5).

$$\mathbf{X_P} = \mathbf{P} \cdot \mathbf{S}_\lambda \tag{2.5}$$

where $\mathbf{X_P}$ is a *nx1* column vector whose components are the camera's responses to the *n* standard samples, $\mathbf{S}_\lambda$ is a *mx1* column vector that represents the camera's spectral sensitivity, and $\mathbf{P}$ is a *nxm* matrix where each column corresponds to the energy reflected by each standard sample at *m* wavelengths, including the spectral power distribution of the illuminant, the reflectance spectrum of the standard sample, and the transmittance of the optical path between the sample and the camera. Some of the techniques used to solve the equation (2.5) and estimate the $\mathbf{S}_\lambda$ vector are the Moore-Penrose pseudoinverse, the Wiener estimation and the principal component analysis (PCA).

Some of the drawbacks of these methods are, on one hand, that the use of spectral data of commercially available calibration charts is an ill-conditioned problem that has an infinite number of solutions and, on the other hand, the acquisition noise inherent to a CCD camera's performance is not considered in sensor estimation, which is in part based on fairly arbitrary assumptions being made that may or may not hold for the sensor considered. Some recent studies introduced a method to estimate the sensor's spectral sensitivity functions based on metamers [Alsam et al., 2007], and considered the acquisition noise inherent to a CCD camera's performance in sensor estimation, assuming that noise is known and bounded, and do not make any a priori statement about the shape of the spectral sensitivity curves, finding sets of possible spectral sensitivities and the uncertainty in the spectral recovery performed [Alsam et al., 2008].

The spectral characterization method applied in this work [Martínez-Verdú et al., 2002], although being a variant of the standard technique for the measurement of the spectral sensitivity of a digital image capture device, in this case a CCD camera [Cohen, 1988; Trussell, 1991; Sharma et al., 1998; ISO/TC42, 1999], belongs to the first type of methods described before, and it is the method traditionally used for spectral characterization in the CD6's colour research group.

The first step in the applied method for spectral characterization consists of determining the OESCFs that relate the normalized digital levels (NDLs) of the camera's

spectral response for different exposure levels, with the spectral exposure H_λ, for each acquisition channel.

The spectral exposure received by the CCD sensor can be calculated from the incident spectral radiance by the equation (2.6).

$$H_\lambda = \frac{\pi}{4} \cdot \frac{A_{sensor}}{\left(1 + m_{obj}\right)^2} \cdot \frac{L_{e\lambda}}{N^2} \tau_{obj} T_{atm} t \tag{2.6}$$

where A_{sensor} is the radiated CCD sensor's area, $L_{e\lambda}$ is the incident spectral radiance, τ_{obj} is the spectral transmittance of the objective lens, T_{atm} is the atmosphere's spectral transmittance, t is the integration time, m_{obj} is the lateral magnification of the objective lens, and N is the aperture f-number [Martínez-Verdú et al., 2003].

The camera's spectral response for different exposure levels is obtained by capturing monochromatic images of variable radiance obtained using a monochromator and varying systematically its entrance/exit slits.

The OESCFs (NDL_λ vs H_λ) obtained for each acquisition channel k, and at each wavelength λ, are fitted mathematically by a 4-parameter sigmoidal function given by equation (2.7).

$$NDL_{\lambda k} = a_{\lambda k} + \frac{b_{\lambda k}}{1 + \exp\left(-\frac{H_\lambda - c_{\lambda k}}{d_{\lambda k}}\right)} \tag{2.7}$$

The spectral responsivities $r_R(\lambda,H)$, $r_G(\lambda,H)$, $r_B(\lambda,H)$, and the action spectra $a_R(\lambda,NDL)$, $a_G(\lambda,NDL)$, $a_B(\lambda,NDL)$, are calculated from the experimental data and the previous modelization by equations (2.8) and (2.9).

Both the responsivity and the action spectrum, for each wavelength – channel (λk) combination, present a sudden increase that is associated to the H or NDL for which the background noise is exceeded, and a sudden stop in the increase associated to the device's saturation.

$$r_k(\lambda, H) = \frac{a_{\lambda k} + \frac{b_{\lambda k}}{1 + \exp\left(-\frac{H - c_{\lambda k}}{d_{\lambda k}}\right)}}{H} \tag{2.8}$$

$$a_k(\lambda, NDL) = \frac{NDL}{c_{\lambda k} - d_{\lambda k} \ln\left(\frac{b_{\lambda k}}{NDL - a_{\lambda k}} - 1\right)} \tag{2.9}$$

The $r_k(\lambda,H)$ vs H and $a_k(\lambda,NDL)$ vs NDL graphs are the two-dimensional profiles of the corresponding three-dimensional functions, being the wavelength axis λ the third dimension.

The absolute spectral sensitivities are obtained for a concrete H or NDL value, selecting the spectral profiles ($r_k(\lambda,H)$ $\forall\lambda$ or $a_k(\lambda,NDL)$ $\forall\lambda$, respectively) corresponding to these H or, equivalently, NDL constant values.

The absolute spectral sensitivities normalized to 1, for a sampling of H or NDL values, avoiding the extreme values corresponding to the background noise and the saturation, are

superimposed giving rise to a unique spectral profile common to both the spectral responsivity ($r_k(\lambda)$ vs λ) and the action spectrum ($a_k(\lambda)$ vs λ), which is known as relative spectral sensitivity. The relative spectral sensitivity value for each wavelength λ is obtained averaging the absolute spectral sensitivities normalized to 1 at this λ [Martínez-Verdú et al., 2002].

2.4 Using an imaging system based on a CCD camera as an instrument for colour measurement and spectral reconstruction

CCD cameras recently began to be used to perform colour measurements and as sensors in multispectral imaging systems, whose application in very diverse fields, such as the artwork maintenance, the internet commerce and the telemedicine, have increased considerably in last years. Nevertheless, many of these applications are still in an experimental stage.

Colour measurement and spectral reconstruction using imaging systems based on CCD cameras basically consists of estimating the XYZ tristimulus values and the reflectance spectrum, respectively, associated to a colour sample, from the digital levels of the CCD camera's response for all acquisition channels used.

2.4.1 Colorimetric characterization of CCD cameras: methods for colour measurement

The digital responses of a CCD camera, firstly, depend on the device and, secondly, in case of having three RGB acquisition channels, are not colorimetric, i.e., the RGB output digital signals do not correspond directly with the device independent tristimulus values based on the CIE standard colorimetric observer [Hong et al., 2001]. This is due to the fact that the spectral sensitivities of the colour sensors used in colour digital cameras, which are characteristic of each device and vary notably between different devices, do not satisfy the Luther condition [Wyszecki et al., 1982], i.e., cannot be expressed as a linear combination of the CIE colour matching functions [CIE 15.2, 1986]. Consequently, the transformation that defines the correspondence between the camera's digital responses and a colour space independent of the device, either the XYZ or the CIELAB, is essential to achieve a high fidelity reproduction of colour. The process of deriving this transformation is usually known as the colorimetric characterization of a CCD camera. Methods for colorimetric characterization can be divided into two general categories: methods based on spectral sensitivities, and methods based on a colour sample chart [Hong et al., 2001].

Methods based on spectral sensitivities require the previous measurement of system's spectral sensitivities (spectral characterization of the imaging system). The relationship between the camera's spectral sensitivities and the CIE colour matching functions must be found in order to use it subsequently to transform the system's digital responses into the XYZ values.

Regarding methods based on colour sample charts, the fundamental idea is using a reference colour chart containing a number of colour samples as a training set for the imaging system. These colour samples are measured using both the imaging system based on the CCD camera and a tele-spectracolorimeter to obtain the system's digital responses and the XYZ values. Different methods can be applied to obtain the transformation matrix between the system's digital responses and the XYZ values for the colour samples of the training set, for

instance, interpolation methods, estimation methods based on least squares fitting, on polynomial modelizations [Hong et al., 2001; Cheung et al, 2004 – 1], etc..

Methods for colour measurement applied in this work are detailed next.

2.4.1.1 Colorimetric characterization based on the spectral sensitivities of the imaging system

The algorithm for the colorimetric characterization of digital cameras applied in this work, which allows one to use them as tele-colorimeters with colour CIE XYX output in cd/m^2, was proposed by Martínez-Verdú et al. [Martínez-Verdú et al., 2002; Martínez-Verdú et al., 2003]. This method for colorimetric characterization is usually only applied to colorimetric configurations of imaging systems, i.e. with three acquisition channels, due to its growing complexity when the number of acquisition channels is increased.

Firstly, the pseudo-colour matching functions of the imaging system are obtained starting from the relative spectral sensitivities obtained by the spectral characterization of the camera, and considering the relative joint scaling and the equal-energy white balance of the relative spectral sensitivities for all acquisition channels.

Relative joint scaling of the relative spectral sensitivities of the imaging system

First, the wavelength at which the absolute spectral sensitivity is the maximum is determined for each acquisition channel ($a_{\lambda_{\max} k}$ in terms of action spectra and totally equivalent in terms of spectral responsivities), λ_{maxk}, and the channel with the greatest maximum of absolute spectral sensitivity is chosen as the reference channel (*kref*). Considering the radiometric formalism used in the spectral characterization of the imaging system (equation (2.7)), digital levels corresponding to an equal-energy stimulus **E**, with a range of exposure values H_E so that the digital levels obtained were placed within the background noise level and the saturation level, are calculated for each acquisition channel ($DL_{\lambda_{\max k},k}$). The slope of the linear fitting by least squares of the digital levels ($DL_{\lambda_{\max k},k}$) of the acquisition channels different from the reference one ($k \neq kref$), plotted versus the digital levels of the reference acquisition channel ($DL_{\lambda_{\max kref},kref}$) gave the joint normalization of the relative spectral sensitivities of the imaging system $p_R : p_G : p_B$, being $p_{kref} = 1$. Once the parameters of the relative joint scaling p_R, p_G and p_B are obtained, the joint scaled relative spectral sensitivities are defined by equation (2.10).

$$a'_k(\lambda) = p_k \cdot a_k(\lambda) \tag{2.10}$$

Equal-energy white balance of the joint scaled relative spectral sensitivities of the imaging system

The equal-energy white balance consists of performing a new scaling on the joint scaled relative spectral sensitivities depending on the chromatic response to an equal-energy stimulus **E**, independently of the absolute radiance level.

Considering the radiometric formalism used in the spectral characterization, the pseudo-tristimulus values for each acquisition channel are given by equations (2.11) and (2.12) [Martínez-Verdú et al., 2002].

$$DL_k = \left(2^{bits} - 1\right) \sum_{380nm}^{780nm} NDL_{\lambda k} \Delta\lambda = \left(2^{bits} - 1\right) \sum_{380nm}^{780nm} H_\lambda \cdot r_k(\lambda, H) \Delta\lambda \tag{2.11}$$

$$DL_k = \left(2^{bits} - 1\right) \sum_{380nm}^{780nm} \left[a_{\lambda k} + \frac{b_{\lambda k}}{1 + \exp\left(- \frac{\left(H_E - c_{\lambda k}\right)}{d_{\lambda k}} \right)} \right] \Delta\lambda \tag{2.12}$$

Due to the fact that digital image devices are not strictly linear over their whole dynamic range, the equal-energy white balance must be checked for each absolute exposure level. Therefore, the pseudo-tristimulus values DL_k are calculated for each acquisition channel k using the previous equations, considering an equal-energy stimulus **E** ($H_\lambda = H_E \; \forall \; \lambda$) and the spectraradiometric data ($a_{\lambda k}$, $b_{\lambda k}$, $c_{\lambda k}$, and $d_{\lambda k}$ parameters) previously obtained from the OESCFs. Plotting the calculated pseudo-tristimulus values DL_k versus the exposure levels H_E considered for the equal-energy stimulus allows one to determine the most sensitive acquisition channel, since it is the first in reaching saturation. The most sensitive acquisition channel is chosen to be the reference acquisition channel in this equal-energy white balance (*kref-E*).

The calculated pseudo-tristimulus values DL_k for the three acquisition channels are related linearly between channels within the background noise level and the saturation level. The slope of the linear fitting by least squares of the normalized digital levels of the acquisition channels NDL_k different from the reference one, plotted versus the normalized digital levels of the reference acquisition channel, gave the parameters of the real white balance of the device $bal_R : bal_G : bal_B$, being $bal_{kref-E} = 1$.

The relative spectral sensitivities are turned into the pseudo-colour matching functions of the imaging system $\mathbf{T_{RGB}} = \left[\bar{\mathbf{r}} \quad \bar{\mathbf{g}} \quad \bar{\mathbf{b}}\right]$ by applying the equal-energy white balance to the joint scaled relative spectral sensitivities in the way described by equations (2.13), (2.14), and (2.15).

$$\bar{\mathbf{r}}_{\boldsymbol{\lambda}} = bal_R \cdot \left(\frac{\sum_{380nm}^{780nm} a'_{kref-E}}{\sum_{380nm}^{780nm} a'_R(\lambda)} \right) \cdot \mathbf{a_R}(\lambda) \tag{2.13}$$

$$\bar{\mathbf{g}}_{\boldsymbol{\lambda}} = bal_G \cdot \left(\frac{\sum_{380nm}^{780nm} a'_{kref-E}}{\sum_{380nm}^{780nm} a'_G(\lambda)} \right) \cdot \mathbf{a_G}(\lambda) \tag{2.14}$$

$$\bar{\mathbf{b}}_{\boldsymbol{\lambda}} = bal_B \cdot \left(\frac{\sum_{380nm}^{780nm} a'_{kref-E}}{\sum_{380nm}^{780nm} a'_B(\lambda)} \right) \cdot \mathbf{a_B}(\lambda) \tag{2.15}$$

Once the pseudo-colour matching functions are determined, it is necessary to set the real scaling factor, i.e. relative to the absolute scaling of the colour matching functions $\mathbf{T_{XYZ}}$, for each acquisition channel, since the parameters of the real white balance of the device

($bal_R : bal_G : bal_B$) are relative to the reference channel *kref-E*, for which $bal_{kref-E} = 1$. With this aim, the basic colorimetric profile $\mathbf{M}$ of the imaging system [Brainard, 1995] is determined. The basic colorimetric profile $\mathbf{M}$ is a *3x3* matrix that associates the relative RGB colorimetric values ($\mathbf{t'_{RGB}}$) to the relative tristimulus values ($\mathbf{t'_{XYZ}}$), both normalized to an equal-energy stimulus by equations (2.16) and (2.17) [Martínez-Verdú et al., 2003].

$$\hat{\mathbf{t}}'_{\mathbf{XYZ}} = \mathbf{M} \cdot \mathbf{t}'_{\mathbf{RGB}} \qquad (2.16) \qquad \text{with} \qquad \mathbf{T_{XYZ}}^{\mathbf{t}} = \mathbf{M} \cdot \mathbf{T_{RGB}}^{\mathbf{t}} \qquad (2.17)$$

The relative colorimetric values $\mathbf{t'_{RGB}}$ normalized to an equal-energy stimulus are obtained by applying a grey balance to the measured RGB digital levels resulting from the noise correction of the image (DL_{ck}) and the subtraction of the dark image (DL_{0k}: mean digital level of dark image), by equation (2.18).

$$\mathbf{t}'_{\mathbf{RGB}} = \begin{bmatrix} R \\ G \\ B \end{bmatrix} = \begin{bmatrix} (DL_{cR} - DL_{oR}) / (bal_R \cdot ((2^{bits} - 1) - DL_{0R})) \\ (DL_{cG} - DL_{oG}) / (bal_G \cdot ((2^{bits} - 1) - DL_{0G})) \\ (DL_{cB} - DL_{oB}) / (bal_B \cdot ((2^{bits} - 1) - DL_{0B})) \end{bmatrix} \qquad (2.18)$$

In order to carry out an absolute estimation (in cd/m^2) of the XYZ tristimulus values, the RGB data obtained from the device must be related with a set of luminance values associated to the equal-energy stimulus **E**. This relation corresponds to the optoelectronic conversion function (OECF) for each channel, which is described by equation (2.19).

$$\mathbf{t}'_{\mathbf{RGB}} = \begin{bmatrix} R \\ G \\ B \end{bmatrix} = \begin{bmatrix} OECF_R(L) \\ OECF_G(L) \\ OECF_B(L) \end{bmatrix} \Rightarrow \hat{\mathbf{t}}'_{\mathbf{XYZ}} = \frac{1}{L_E} \mathbf{M} \cdot \begin{bmatrix} OECF_R^{-1}(R) \\ OECF_G^{-1}(G) \\ OECF_B^{-1}(B) \end{bmatrix} \qquad (2.19)$$

where L is the luminance value of the object (in cd/m^2) and L_E is the luminance value of the equal-energy stimulus.

Among the different ways of obtaining the basic colorimetric profile $\mathbf{M}$ of the imaging system, two categories can be distinguished depending on the optimization method: least squares or regression methods [Finlayson et al., 1997], and principal components methods [Vhrel et al., 1992].

In this work, the basic colorimetric profile $\mathbf{M}$ of the imaging system is determined by applying a method of maximum ignorance, i.e., only the spectral sensitivities of the colour device are required to be known, using a least squares regression as optimization method. The colorimetric profile is obtained from the CIE standard observer colour matching functions $\mathbf{T_{XYZ}}$, and the pseudo-colour matching functions of the imaging system $\mathbf{T_{RGB}}$, by equation (2.20).

$$\mathbf{M} = \mathbf{T_{XYZ}}^{\mathbf{t}} \cdot \mathbf{T_{RGB}} \cdot \left(\mathbf{T_{RGB}}^{\mathbf{t}} \cdot \mathbf{T_{RGB}}\right)^{-1} \qquad (2.20)$$

Comparison between the estimated colour matching functions $\hat{\mathbf{T}}_{\mathbf{XYZ}} = \mathbf{T_{RGB}} \cdot \mathbf{M}^{\mathbf{t}}$, and the real ones $\mathbf{T_{XYZ}}$, clearly highlights that the combined spectral functions $\mathbf{T_{RGB}}$ are not strictly colour matching functions, which is the reason why they are called pseudo-colour matching functions.

Once the basic colorimetric profile $\mathbf{M}$ of the imaging system is calculated, the absolute estimated tristimulus values $\hat{\mathbf{t}}_{\mathbf{XYZ}}$ can be expressed as:

$$\hat{\mathbf{t}}_{\mathbf{XYZ}} = \begin{bmatrix} \hat{X} \\ \hat{Y} \\ \hat{Z} \end{bmatrix} = M \cdot \left\{ \begin{bmatrix} m_R(N,t) & 0 & 0 \\ 0 & m_G(N,t) & 0 \\ 0 & 0 & m_B(N,t) \end{bmatrix} \cdot \begin{bmatrix} R \\ G \\ B \end{bmatrix} + \begin{bmatrix} h_R(N,t) \\ h_G(N,t) \\ h_B(N,t) \end{bmatrix} \right\} \left(cd/m^2 \right) \quad (2.21)$$

where the *m* and *h* parameters correspond to the linear fitting parameters of the inverse OECFs within the background noise level and the saturation level, plotted versus the colorimetric values $\mathbf{t'}_{\mathbf{RGB}}$, at exposure conditions fixed by the aperture f-number *N* of the objective lens, and the exposure time *t* considered. When varying the exposure conditions, the linear fitting parameters *m* and *h* will also vary, so are considered to be functions of *N* and *t*. Determining this dependence allows one to adapt the dynamic range of the imaging system, which is limited by the OESCFs, to the real dynamic range of luminance values of any image, and it is known as luminance adaptation model [Martínez-Verdú et al., 2003].

The comparison between the tristimulus values estimated from the model associated to the imaging system $\hat{\mathbf{t}}_{\mathbf{XYZ}}$, and those measured $\mathbf{t}_{\mathbf{XYZ}}$ using a tele-spectracolorimeter, for the colour samples of a chart placed in a special light booth, shows that colour compensation is needed to improve the colorimetric estimation provided by the model so far. A linear colour compensation model [Martínez-Verdú et al., 2003] derived from the linear fitting by least squares of the measured tristimulus values versus the estimated ones is applied to the estimated tristimulus values (equation (2.22)).

$$\mathbf{t}_{\mathbf{XYZ}} = \begin{bmatrix} X \\ Y \\ Z \end{bmatrix} = \mathbf{A}_{\mathbf{C}} + \mathbf{B}_{\mathbf{C}} \cdot \hat{\mathbf{t}}_{\mathbf{XYZ}} = \begin{bmatrix} a_X \\ a_Y \\ a_Z \end{bmatrix} + \begin{bmatrix} b_X & 0 & 0 \\ 0 & b_Y & 0 \\ 0 & 0 & b_Z \end{bmatrix} \cdot \begin{bmatrix} \hat{X} \\ \hat{Y} \\ \hat{Z} \end{bmatrix} \quad (2.22)$$

where $\mathbf{A}_{\mathbf{C}}$ is the offset tristimulus vector, and $\mathbf{B}_{\mathbf{C}}$ is a diagonal scaling matrix that allows one to obtain the definitive scaling of the pseudo-colour matching functions of the imaging system by $\mathbf{T}_{\mathbf{RGB}} \cdot \mathbf{B}_{\mathbf{C}}$, and the raw colorimetric profile of the imaging system $\mathbf{B}_{\mathbf{C}} \cdot \mathbf{M}$ by adding the luminance adaptation model. The $\mathbf{A}_{\mathbf{C}}$ vector describes the systematic colour deviations of the device, i.e., the error associated to the difference between the real and the estimated values that is due, basically, to the fact that spectral sensitivities of most of digital cameras are not linear transformations of the spectral sensitivities of the average human visual system.

2.4.1.2 Colorimetric characterization based on measuring a training set

Methods for colorimetric characterization of a CCD camera based on measuring a training set applied in this work can be classified as direct transformation methods. In these methods, the XYZ tristimulus values associated to each colour sample of the training set are related to the corresponding digital responses of the imaging system trhough a transformation matrix.

Two methods based on measuring a training set are applied in this work: the pseudoinverse method for XYZ (PSE_{XYZ}), and the second order non-linear method for XYZ ($NLIN(2)_{XYZ}$). For these two methods the transformation matrixes that relate the digital

responses of the imaging system with the XYZ tristimulus values for the colour samples of the training set are determined by applying the Moore-Penrose pseudoinverse technique. A detailed description of the Moore-Penrose pseudoinverse and these two methods can be found next.

2.4.1.2.1 The Moore-Penrose pseudoinverse

The Moore-Penrose pseudo-inverse is a general way to find the solution to the following system of linear equations:

$$\vec{b} = \mathbf{A}\vec{y} \qquad \vec{b} \in \Re^m,\ \vec{y} \in \Re^n,\ \mathbf{A} \in \Re^{mxn} \tag{2.23}$$

E. H. Moore in 1920 and R. Penrose in 1955 showed independently that there is a general solution to these equations (which will be named the Moore-Penrose solution) of the form $\vec{y} = \mathbf{A}^{\dagger}\vec{b}$, being the matrix $\mathbf{A}^{\dagger}$ the Moore-Penrose 'pseudoinverse'. This is the unique matrix that satisfies the following properties:

$$(1)\quad \mathbf{A}\cdot\mathbf{A}^{\dagger}\cdot\mathbf{A} = \mathbf{A} \tag{2.24}$$

$$(2)\quad \mathbf{A}^{\dagger}\cdot\mathbf{A}\cdot\mathbf{A}^{\dagger} = \mathbf{A}^{\dagger} \tag{2.25}$$

$$(3)\quad (\mathbf{A}\cdot\mathbf{A}^{\dagger})^{\mathrm{T}} = \mathbf{A}\cdot\mathbf{A}^{\dagger} \tag{2.26}$$

$$(4)\quad (\mathbf{A}^{\dagger}\cdot\mathbf{A})^{\mathrm{T}} = \mathbf{A}^{\dagger}\cdot\mathbf{A} \tag{2.27}$$

The Moore-Penrose pseudoinverse has the following properties. When:

(a) $m = n$, if **A** is full rank: $\mathbf{A}^{\dagger} = \mathbf{A}^{-1}$ (2.28)

(b) $m > n$, the solution is the one that minimizes the quantity $\|\vec{b} - \mathbf{A}\vec{y}\|$. In this case there are more constraining equations than there are free variables $\vec{y}$. Hence, it is not generally possible to find a solution to these equations. The pseudoinverse gives the solution $\vec{y}$ such that $\mathbf{A}\vec{y}$ is 'closest' (in a least-squares sense) to the desired solution vector $\vec{b}$.

(c) $m < n$, then the Moore-Penrose solution minimizes the 2-norm of $\vec{y}: \|\vec{y}\|$. In this case, there are generally an infinite number of solutions, and the Moore-Penrose solution is the particular solution whose vector 2-norm is minimal.

(d) When **A** is full rank, the Moore-Penrose pseudoinverse can be directly calculated as follows:

case 1: if $m < n$ $\quad \mathbf{A}^{\dagger} = \mathbf{A}^{\mathrm{T}}\cdot(\mathbf{A}\cdot\mathbf{A}^{\mathrm{T}})^{-1}$ (2.29)

case 2: if $m > n$ $\quad \mathbf{A}^{\dagger} = (\mathbf{A}^{\mathrm{T}}\cdot\mathbf{A})^{-1}\cdot\mathbf{A}^{\mathrm{T}}$ (2.30)

However, when **A** is not full rank, then these formulas can not be used.

2.4.1.2.2 Pseudoinverse method for XYZ

In the pseudoinverse method for XYZ (PSE_{XYZ}) [Vhrel et al., 1994; Harderberg et al., 1999], the XYZ tristimulus values associated to each colour sample are related to the corresponding digital responses of the *k* acquisition channels of the imaging system by means of a transformation matrix. Using a training set of *N* colour samples with known XYZ tristimulus values, the transformation matrix is determined by applying the Moore-Penrose pseudoinverse (case 1, equation (2.29)):

$$XYZ_{(3xN)} = D_{PSEXYZ(3xk)} \cdot P(k)_{(kxN)} \tag{2.31}$$

$$D_{PSEXYZ} = XYZ \cdot P(k)^T \cdot \left(P(k) \cdot P(k)^T\right)^{-1} \tag{2.32}$$

where XYZ is the *3xN* matrix of the XYZ tristimulus values of the *N* colour samples of the training set, and *P(k)* is the *kxN* matrix of the digital responses of the *k* acquisition channels of the imaging system for the *N* colour samples of the training set:

$$XYZ = \begin{pmatrix} X^{(1)} & X^{(2)} & \dots & X^{(N)} \\ Y^{(1)} & Y^{(2)} & \dots & Y^{(N)} \\ Z^{(1)} & Z^{(2)} & \dots & Z^{(N)} \end{pmatrix} \tag{2.33}$$

$$P(k) = \begin{pmatrix} DL_1^{(1)} & DL_1^{(2)} & \dots & DL_1^{(N)} \\ DL_2^{(1)} & DL_2^{(2)} & \dots & DL_2^{(N)} \\ \dots & \dots & \dots & \dots \\ DL_k^{(1)} & DL_k^{(2)} & \dots & DL_k^{(N)} \end{pmatrix} \tag{2.34}$$

Once the D_{PSEXYZ} transformation matrix is obtained, the XYZ tristimulus values of any colour sample can be directly estimated from its corresponding digital levels by the equation (2.31), always assuming that the training set used constitutes a good representation of the subsequently measured colour samples.

2.4.1.2.3 Second order non-linear method for XYZ

In the second order non-linear method for XYZ ($NLIN(2)_{XYZ}$) [Herzog et al., 1999; Hong et al., 2001; Cheung et al., 2004 – 1], the transformation matrix relates the XYZ tristimulus values associated to each colour sample with a second order polynomial of the digital responses of the imaging system. Using a training set of *N* colour samples with known XYZ tristimulus values, the transformation matrix is determined by applying the Moore-Penrose pseudoinverse:

$$XYZ_{(3xN)} = D_{NLIN(2)_{XYZ}(3xp)} \cdot P(k,2)_{(pxN)} \tag{2.35}$$

$$D_{NLIN(2)_{XYZ}} = XYZ \cdot P(k,2)^T \cdot \left(P(k,2) \cdot P(k,2)^T\right)^{-1} \tag{2.36}$$

where XYZ is the *3xN* matrix of the XYZ tristimulus values of the *N* colour samples of the training set, and *P(k,2)* is the *pxN* matrix of the second order polynomials of the digital responses of the *k* acquisition channels of the imaging system for the *N* colour samples of the training set:

$$P(k,2)_{(pxN)} = \begin{pmatrix} 1 & 1 & \dots & 1 \\ DL_1^{(1)} & DL_1^{(2)} & \dots & DL_1^{(N)} \\ DL_2^{(1)} & DL_2^{(2)} & \dots & DL_2^{(N)} \\ \dots & \dots & \dots & \dots \\ \left(DL_1^{(1)}\right)^2 & \left(DL_1^{(2)}\right)^2 & \dots & \left(DL_1^{(N)}\right)^2 \\ \left(DL_2^{(1)}\right)^2 & \left(DL_2^{(2)}\right)^2 & \dots & \left(DL_2^{(N)}\right)^2 \\ \dots & \dots & \dots & \dots \\ DL_1^{(1)} \cdot DL_2^{(1)} & DL_1^{(2)} \cdot DL_2^{(2)} & \dots & DL_1^{(N)} \cdot DL_2^{(N)} \\ DL_1^{(1)} \cdot DL_3^{(1)} & DL_1^{(2)} \cdot DL_3^{(2)} & \dots & DL_1^{(N)} \cdot DL_3^{(N)} \\ \dots & \dots & \dots & \dots \end{pmatrix} \quad (2.37)$$

and $p = \left(1 + 2k + \binom{k}{2} = 1 + 2k + \frac{k!}{(k-2)!\cdot 2!}\right)$ is the number of components of the second order polynomial of the k digital responses associated to each colour sample.

Once the $D_{NLIN(2)_{XYZ}}$ transformation matrix is obtained, the XYZ tristimulus values of any colour sample can be directly estimated from its corresponding digital levels by the equation (2.35), always assuming that the training set used constitutes a good representation of the subsequently measured colour samples.

2.4.2 Methods for spectral reconstruction

The main objective of methods for spectral reconstruction is to reconstruct the reflectance, transmittance or radiance spectra of a colour sample from the corresponding digital responses of the imaging system. Methods for spectral reconstruction are usually applied to multispectral configurations since the linear models of reflectance spectrum used require at least four acquisition channels to be able to estimate real reflectance spectra [Shi et al., 2002].

Several mathematical methods for spectral reconstruction of radiance, reflectance or transmittance from measurements performed by a digital imaging system exist. These methods are based on measuring the reflected/transmitted energy by the colour sample through different acquisition channels, which are obtained by means of filters with different spectral characteristics, so that each channel allows one to capture images with characteristic spectral information from which the radiance, reflectance or transmittance can be recovered. The mathematical methods for spectral reconstruction can be classified into interpolation methods, such as the Lagrange polynomial interpolation, the cubic Spline interpolation, the cubic interpolation, the discrete Fourier transform (DFT) or the modified discrete sine transformation (MDST), and estimation methods, such as the pseudoinverse method, the pseudoinverse with smoothing, the Wiener estimation (also known as Wiener's pseudoinverse or direct pseudoinverse), the non-linear methods, the principal component analysis (PCA), the independent component analysis (ICA), or the non-negative matrix factorization (NMF). Estimation methods are usually based on a previous knowledge of the type of spectrum to be recovered through a set of measurements performed previously, which is the so-called training set.

The particular application of some of these mathematical methods for spectral reconstruction mentioned carried out by some authors, gave rise to various particular methods

for spectral reconstruction as, for instance, the Maloney-Wandell [Maloney et al., 1986] method, the Imai-Berns [Imai et al., 1999] method, the Li-Luo [Li et al., 2001] method, and the Shi-Healey [Shi et al., 2002] method, which are based on different applications of the PCA. These four methods present different performances with regard to the spectral reconstruction and the subsequent colour measurement, and depending on the dimensionality of the linear model of reflectance considered [Cheung et al., 2005; López-Álvarez et al., 2007 - 1]. In case of trichromatic cameras, the best method in terms of colour accuracy is the Li-Luo method, which uses a linear model of high dimensionality in which the degrees of freedom (dimension - 3) are optimized to determine the smoother reflectance consistent with a set of camera's response three-values, and spectral reconstruction is evaluated in colorimetric terms.

Three methods for spectral reconstruction are applied in this work, all of them based on measuring a training set, using both a tele-spectracolorimeter and the imaging system, and the determination of the transformation matrix that allows one to relate the system's digital responses with the reflectance spectra of the colour samples measured. A detailed description of these methods is presented next.

2.4.2.1 Pseudoinverse method

In the pseudoinverse method (PSE), the reflectance spectra of the colour samples are considered to be related to the corresponding digital responses of the imaging system through a transformation matrix (equation (2.38)). Using a training set of N colour samples with known reflectance spectra, the transformation matrix is determined by applying the Moore-Penrose pseudoinverse (sub-section 2.4.1.2.1, equation (2.29)):

$$R_{(LxN)} = D_{PSE(Lxk)} \cdot P(k)_{(kxN)} \tag{2.38}$$

$$D_{PSE} = R \cdot P(k)^T \cdot \left(P(k) \cdot P(k)^T\right)^{-1} \tag{2.39}$$

where R is the LxN matrix of reflectance spectra of the N colour samples of the training set, sampled in L wavelengths (in this work the reflectance spectrum is sampled from 380nm to 780nm in intervals of 10nm, so $L = 41$), $P(k)$ is the kxN matrix of the digital responses of the k acquisition channels of the imaging system for the N colour samples of the training set, and D_{PSE} is the Lxk transformation matrix that relates them.

2.4.2.2 Second order non-linear method

In the second order non-linear method (NLIN(2)), the reflectance spectra of the colour samples are considered to be related to a second order polynomial of the corresponding digital responses of the imaging system through a transformation matrix (equation (2.40)). Using a training set of N colour samples with known reflectance spectra, the transformation matrix is determined by applying the Moore-Penrose pseudoinverse (sub-section 2.4.1.2.1, equation (2.29)):

$$R_{(LxN)} = D_{NLIN(2)_{(Lxp)}} \cdot P(k,2)_{(pxN)} \tag{2.40}$$

$$D_{NLIN(2)} = R \cdot P(k,2)^T \cdot \left(P(k,2) \cdot P(k,2)^T\right)^{-1} \tag{2.41}$$

where *R* is the *LxN* matrix of reflectance spectra of the *N* colour samples of the training set, sampled in *L* wavelengths (in this work the reflectance spectrum is sampled from 380nm to 780nm in intervals of 10nm, so *L* = 41), *P(k,2)* is the *pxN* matrix of the second order polynomials of the digital responses of the *k* acquisition channels of the imaging system for the *N* colour samples of the training set (2.37)., and $D_{NLIN(2)}$ is the *Lxp* transformation matrix that relates them

2.4.2.3 Principal Component Analysis

The objective of the principal component analysis (PCA) method [Harderberg, 1999; Imai et al., 2000 – 1; Harderberg et al., 2002] is to determine a smaller set of variables, with less redundancy, which provides the best representation possible of the original set, from a set of statistical variables measured, where each one is considered to be a random vector **r**. In the PCA method, redundancy is measured through the correlation between elements, so it is necessary that these elements are mutually correlated and some kind of redundancy exists between them, making the compression possible. The PCA method is not applicable when elements are independent.

The starting point is an original *LxN* data matrix **R**, with N columns corresponding to the *N* training vectors of the system having *L* components, which is associated to a vector space. In this work, these vectors correspond to the measured reflectance spectra of the *N* colour samples of the training set, sampling the visible spectrum from 380nm to 780nm with wavelength increases of 10nm, being *L* = 41.

The eigenvectors of the variance-covariance matrix **Cov** of the original data matrix **R** are proved to provide the best reconstruction of the vector subspace with a number of vectors generally lower than the dimension of the vector space. The variance-covariance matrix **Cov** of the original data matrix **R** can be calculated as follows:

$$\mathbf{Cov} = \left(\frac{1}{p}\right) \cdot \mathbf{R} \cdot \mathbf{R}^{T} \tag{2.42}$$

The eigenvectors of this matrix, also called principal components, correspond to the maximum variance direction and are obtained by diagonalizing the variance-covariance matrix **Cov**:

$$\mathbf{V}^{-1} \cdot \mathbf{Cov} \cdot \mathbf{V} = \mathbf{T} \tag{2.43}$$

where **V** is the matrix of eigenvectors of the **Cov** matrix, and **T** is the diagonal matrix of the corresponding eigenvalues ordered in decreasing order.

The original *Lx1* column vector **r**, the reflectance spectrum associated to each colour sample in this work, can be obtained by a linear combination of the principal components:

$$\mathbf{r} = \mathbf{V} \cdot \mathbf{C} = \mathbf{v_1} \cdot c_1 + \mathbf{v_2} \cdot c_2 + \mathbf{v_3} \cdot c_3 + \mathbf{...} + \mathbf{v_p} \cdot c_p \tag{2.44}$$

where **V** is here the *Lxp* matrix whose columns are the *p* principal components considered that constitute the PCA basis, and **C** is a *px1* column vector whose components are the scalar coefficients of the vector **r** in the PCA basis.

A small set of principal components is proved to allow reproducing a high percentage of variability of the original vectors, and others similar, due to the fact that the eigenvalues of the variance-covariance matrix are strongly decreasing.

In the particular case of the spectral reconstruction using an imaging system, the number of principal components considered is usually the same that the number of acquisition channels. The scalar coefficients of the reflectance spectra of *N* colour samples of a training set on the PCA basis are considered to be related to the digital responses of the imaging system through a transformation matrix that is determined by applying the Moore-Penrose pseudoinverse:

$$C_{(pxN)} = D_{PCA(pxk)} \cdot P(k)_{(kxN)} \tag{2.45}$$

$$D_{PCA} = C \cdot P(k)^T \cdot \left(P(k) \cdot P(k)^T\right)^{-1} \tag{2.46}$$

where *P(k)* is the *kxN* matrix of the digital responses of the *k* acquisition channels of the imaging system for the *N* colour samples of the training set, *C* is the *pxN* matrix of the scalar coefficients of the reflectance spectra of the *N* colour samples of the training set on the PCA basis, and D_{PCA} is the *pxk* transformation matrix that relates them.

This transformation matrix allows one to calculate the coefficients of the reflectance spectra of any colour sample on the PCA basis, from its digital responses of the imaging system. The linear combination of the vectors of the PCA basis with the calculated coefficients provides an estimation of the reflectance spectrum of the colour sample.

Finally, it is outstanding to notice that methods for spectral reconstruction have a fundamental advantage with regard to methods for colour measurement, since allow one to recover the reflectance spectra of the colour samples measured, which is the most accurate representation of the colour of an object and totally independent of the imaging system and the illuminant used in the image acquisition. Knowing the reflectance spectra at all pixels in an image allow one to reproduce this image under any illuminant and, therefore, to accurately represent the colour considering the colour appearance characteristics of the human visual system under any illumination condition.

2.4.3 Training and test sets for an imaging system

In some methods for colorimetric characterization of imaging systems, just like in spectral reconstruction, sets of colour samples are used to characterize the imaging system, i.e., to establish a relationship between the digital levels of the response of the imaging system and the corresponding tristimulus values or reflectance spectra. As it was previously mentioned, different methods that allow one to determine this relationship by applying different techniques exist. Nevertheless, all these methods require a set of colour samples to train the imaging system, the so-called training set, from which the imaging system is characterized, and another set of colour samples to test the system's characterization and evaluate the accuracy of the estimation performed applying the system's characterization, the so-called test set.

Both the training and the test set can be made up by physical colour charts or sets of colour samples especially selected or manufactured. Universal training and test sets to characterize an imaging system do not exist, although there are sets of colour samples widely used (as it is the case of the GretagMacbeth colour charts), but in many cases the training and test sets are selected depending on the application of the imaging system. In order to be able to determine a transformation that allows one to obtain accurate estimations, it is advisable the training set of the imaging system to be made up by a set of colour samples sufficiently representative of the colour samples that will be subsequently measured, and the test set to be

made up by colour samples typical in the measurements that will be carried out with the imaging system.

The training and test sets usually used are, for instance, the GretagMacbeth ColorChecker DC chart (CCDC) [Imai et al., 2001; Imai et al., 2002; Cheung et al., 2005; Smoyer et al., 2005] and the GretagMacbeth ColorChecker Color Rendition chart (CCCR) [Burns et al., 1996; Imai, 2000; Imai et al., 2002], the IT8 chart [Hong et al., 2001; Smoyer et al., 2005], the colour samples of the Munsell Book of Color [Wu et al., 2000], the colour samples of the NCS [Cheung et al., 2004 – 2; Cheung et al., 2005], colour samples made with pigments used in painting for restoration and preservation applications [Imai et al., 2000 – 2; Imai et al., 2001; Imai et al., 2002; Imai et al., 2003], colour samples from natural objects [Wu et al., 2000; Imai et al., 2001; Imai et al., 2002; Cheung et al., 2004 – 2], etc.

There exist various methods and criteria to select the colour samples that constitute the training and test sets in order to generate a set of colour samples the most diverse among them possible, with a minimum number of colour samples and allowing to characterize the greater number of systems. Some of these methods and criteria consist of, for example, selecting an initial number of colour samples equal to some of the yet existing colour charts (CCDC, CCCR) [Cheung et al., 2004 – 2] with the aim of comparing them from the point of view of their utility in system's characterization, so that the reflectance spectra of the selected colour samples are as different as possible among them [Harderberg, 1999], a random selection of colour samples so that the sum of the colour difference among selected samples is maximum or that the minimum colour difference among selected samples is maximum [Cheung et al., 2004 – 2]. Comparison of results obtained using a trichromatic camera and both sets of colour samples specially made and the standard colour charts (CCDC and CCCR) show that colour samples of these last charts are rather properly selected and are appropriate to be used in the characterization of image acquisition systems [Cheung et al., 2004 – 2].

Other methods used to select the training set in case of multispectral imaging systems are, for instance, the hue analysis method (HAM), the camera output analysis method (COAM), and the linear distance maximization method (LDMM) [Pellegri et al., 2004]. The HAM consists of selecting colour samples the most separated possible in the C_{ab}*h_{ab} plane and covering the entire plane, i.e., the whole hue range. In the COAM, the PCA is applied to the initial set of colour samples and for each principal component the nearest non-selected colour sample is selected. Proximity is measured in terms of the cosine of the angle between the vector associate to the colour sample and the principal component, maximizing the orthogonality of the selected colour samples, or in terms of the maximum absolute coordinate of the vector associate to the colour sample on the principal component, maximizing the relative linear distance between selected vectors in case that vectors associated to colour samples are very close among them, or selecting the colour samples with maximum and minimum absolute coordinate for each principal component (doubling the number of samples) until completing the desired number of training colour samples. In the LDMM colour samples are selected iteratively depending directly on the linear distance (standard Euclidean distance) between them and the yet selected ones. The colour sample, whose associate vector has a maximum norm among all possible colour samples, i.e., the brightest one for certain acquisition conditions, is selected as the first colour sample. Training sets selected by these methods present a relatively reduced number of colour samples (lower or equal to 62 colour samples) and a wide applicability range, being these methods comparable to the one introduced by Hardeberg [Harderberg et al., 1998], and being the LDMM the best to be applied in a general context [Pellegri et al., 2004]. The maximization of the CSCM (Colorimetric and Spectral Combiner Metric) is also used as a criterion to select spectra [López-Álvarez et al., 2008].

Regarding the influence of the number of colour samples of the training set on accuracy of the estimation performed by the imaging system, for a trichromatic camera the accuracy of the colorimetric estimation (XYZ tristimulus values) directly from the camera's response digital levels increases by increasing the number of colour samples of the training set until approximately 60, from which on there is not a noticeable improvement. Hence, a kind of 'limit' in the improvement of the accuracy by increasing the number of colour samples of the training set is established [Hong et al., 2001; Cheung et al., 2004 – 1; de Lasarte et al., 2007 – 2; López-Álvarez et al., 2007 – 2; de Lasarte et al., 2008 – 1]. Estimate with a reasonable accuracy requires a training set having between 40 and 60 colour samples [Hong et al., 2001; de Lasarte et al., 2007 – 2; López-Álvarez et al., 2007 – 2; de Lasarte et al., 2008 – 1]. For training sets having more than 40 colour samples the mean error in colour measurement performed from spectral reconstruction is practically independent of the size of the training set of the imaging system [Cheung et al., 2005; de Lasarte et al., 2007 – 2; López-Álvarez et al., 2007 - 2; de Lasarte et al., 2008 – 1].

2.5 Increasing the dynamic range of an imaging system: High Dynamic Range Imaging (HDRI)

Scenes from the real world can exhibit a broad range of light variations. This is particularly true for scenes containing both areas of low and high illumination. It is clear that in such scenes, the dynamic range, i.e., the ratio of the highest and lowest recorded level of light, can be very high. Therefore it is impossible to obtain an adequate representation of a scene having a wide dynamic range by using a film or a digital still camera (DSC) as a recording system. Some information will be lost due to the limited dynamic range of the used device. In the case of a DSC, the dynamic range is usually described in terms of the ratio between the maximum charge that the sensor can collect (full well capacity) and the minimum charge that just overcomes sensor noise (noise floor) [Healey et al., 1994]. The light values captured by a CCD or CMOS sensor are usually finally quantized (linearly or not) in a range between 0 and $(2^{bits} - 1)$ to cover the input signal. This yields a coarse resolution interpretation of the physically continuously varying values present in the real world. Information loss is observed in highly illuminated areas, where all light variations are mapped to the same value, and thus become saturated, and in dimly illuminated areas, where information is overridden by sensor-noise [Battiato et al., 2003].

The main benefit of high dynamic range images is not only high accuracy that matches or exceeds the processing of the human eye, but also the concept of a scene-referred representation of data, which, unlike commonly used output-referred representations, contains enough information to achieve the desired appearance of the scene on a variety of output devices. High dynamic range imaging promises truly device independent representation of visual content. The need for such a device independent format has become even more important recently, as exchange of digital images, either by Internet or by mobile phones, has become ubiquitous. Preserving appearance across the variety of displays is almost impossible, but still, all these displays can show an acceptable image that would preserve the most important image features if they are provided with sufficient information on the image content, encoded, for instance, in an HDR image. Display devices are no longer intended to display the content as it is, but they also apply complex image processing to enhance the resulting image. However, to fully utilize capabilities of the display and its display algorithms, the input content must be device-independent and of possible high quality, exceeding the standards of traditional imaging. High dynamic range image representation

meets both of these requirements and therefore offers a good alternative to the traditional image representation [Mantiuk et al., 2007].

High dynamic range images can be captured using a sequence of pictures of the same scene taken with different exposure times, using the so called multi-exposure technique. This technique allows one to increase the dynamic range and to reduce the noise in an image. The values of luminance recovered using multi-exposure techniques are not meant to be exact measurements, since they can be severely distorted by camera optics. The accuracy of reconstructed luminance values depends on a scene, with better accuracy for scenes containing a fewer number of bright pixels. The goal of the method is to vary the exposure in order to control the light levels to be captured [Mantiuk et al., 2007]. If multiple pictures of the same scene are acquired using different exposure settings, each of them will reveal different details, covering a wider dynamic range than the one that would have been captured with a single shot: pictures taken with short exposure times provide highlight information and vice versa. Multiple shots are acquired with the aim of merging them into a single image of increased dynamic range. By using differently exposed images, the measured brightness values change with the exposure, while radiance values remain constant. Because of this, once the imaging system transfer function is known, it is possible to use its inverse to estimate the underlying (properly scaled) radiance values, and build an accurate estimation of the original scene values, the so-called radiance map [Battiato et al., 2003]. Different techniques have been developed for this purpose. Firstly, the high dynamic range image recovering using exposure times [Debevec et al., 1997] uses a sequence of digitized pictures, representing the same scene acquired at different known exposure times to estimate the camera response function, using the constraint of sensor reciprocity, and then to reconstruct the high dynamic range radiance map. The high dynamic range image recovery using automatically estimated exposure ratios [Mitsunaga et al., 1999] have nearly the same basic concepts than the previous algorithm but, in this case, instead of using images with known exposure times, exposure ratios between them are known. The high dynamic range image recovery using a parametric response curve [Mann et al., 1995; Mann, 2000] propose approximating the camera response function, which defines the relation between pixels values and the intensity of light that reaches camera's CCD sensor, by using a simple parametric function that relates pixel values to the received light, called photo-quantity. Another approach to the high dynamic range image recovery considers the notion of spatially varying pixel sensitivities for high dynamic range imaging [Nayar et al., 2000] by implementing a pattern over the detector array that leads adjacent pixels to have different exposures. The brightness level associated with each pixel represents its sensitivity, such that, the brighter pixels have greater exposure to image irradiance and the darker ones have lower exposure. The spatial dimensions and the exposure dimensions of image irradiance are simultaneously sampled: when a pixel is saturated in the acquired image, it is likely to have a neighbour that is not, and when a pixel produces zero brightness, it is likely to have a neighbour that produces non-zero brightness. This spatial-exposure sampling is exploited to compute a high dynamic range image of the scene [Nayar et al., 2000].

Previously mentioned methods are suited only to static scenes, i.e., the imaging system, the scene objects, and their radiances must remain constant during the sequential capture of images under different exposure times. Regarding real time images, beam splitters can be used to expose a few sensors of a different sensitivity simultaneously, generating multiple copies of the optical image of the scene. Each copy is detected by an image detector whose exposure is preset by using an optical attenuator or by changing the exposure time of the detector. This approach has the advantage of producing high dynamic range images in real time. Hence, the scene objects and the imaging system are free to move during the capture process. The disadvantage, of course, is that this approach is expensive as it requires multiple

image detectors, precision optics for the alignment of all acquired images and additional hardware for the capture and processing of multiple images [Nayar et al., 2000].

3 Material and Method

Two imaging systems based on a CCD camera are used in this work: one based on a colour 10-bits CCD camera, and another based on a monochrome 12-bits cooled CCD camera. Two configuration of this last imaging system are considered: a colorimetric configuration with 3 acquisition channels, and a multispectral configuration with 7 acquisition channels.

In order to be able to perform accurate colour measurements and/or spectral reconstructions with high spatial resolution using these imaging systems, it is necessary to carry out, firstly, the noise correction of the system's response, particularly the correction of the spatial non-uniformity, and secondly, the characterization or calibration of the imaging system to be able to obtain the XYZ tristimulus values and/or the reflectance spectra, respectively, from the system's digital responses.

The material and experimental setup used to correct the inherent noise sources of an imaging system based on a CCD camera are presented in section 3.1.

The spectral characterization is carried out only for the colorimetric configuration of the previously mentioned two imaging systems, in order to be able to apply a method for colorimetric characterization based on the spectral sensitivities of the imaging system. The material and experimental setup used just as the experimental procedure followed are presented in section 3.2.

The different methods for colour measurement and spectral reconstruction applied through out this work to the two configurations of the imaging system based on a monochrome 12-bits cooled CCD camera, are listed and briefly described in section 3.3.

Finally, the colorimetric and the multispectral configurations of the imaging system based on a monochrome 12-bits cooled CCD camera are presented and each one of their components detailed in section 3.4.

3.1 Noise correction and spatial characterization

Noise sources inherent to the performance of a CCD camera can be classified into two types: temporal and spatial. The contribution of temporal noise sources can be reduced by frame averaging, while spatial noise cannot and a spatial non-uniformity correction is required. Among the existing methods for the spatial non-uniformity correction (sub-section 2.2.3), the one applied in this work is based on the calibration of the detector by means of two images: a dark image, and a uniform field image. The original linear correction algorithm that is subsequently optimized is given by equations (2.4) (sub-section 2.2.3), and it is based on the calculation of the gain and offset matrixes from these dark and uniform field images.

In order to obtain a uniform radiance field, an integrator cube was made by the colour research group at the CD6, whose sides were 50cm long, and which had an 18cm x 18cm window of a white translucent diffuser material on one of its sides. A light source (Philips 150W halogen lamp) connected to a power supply (Hewlett Packard 6642A DC) for stable illumination was placed at the centre of the cube. The sides of the integrator cube were painted white to increase light diffusion, and a white baffle that did not let the direct light of

the lamp reach the window was also used. This baffle was placed parallel to the window at the centre of the cube, and the light source was fixed at the centre of the baffle on the side opposite to the cube window. Consequently, the window of the cube acted as a uniform radiance field and had a spatial variation percentage of 0.50% over the 10cm x 8cm centred region that constituted the camera's viewing field. This spatial variation percentage was determined by measuring the radiance over the camera's viewing field region using a Photo Research PR-650 SpectraScan Colorimeter with the MS-75 objective lens, with an aperture of 1º (Appendix 1, Figure 3.1).

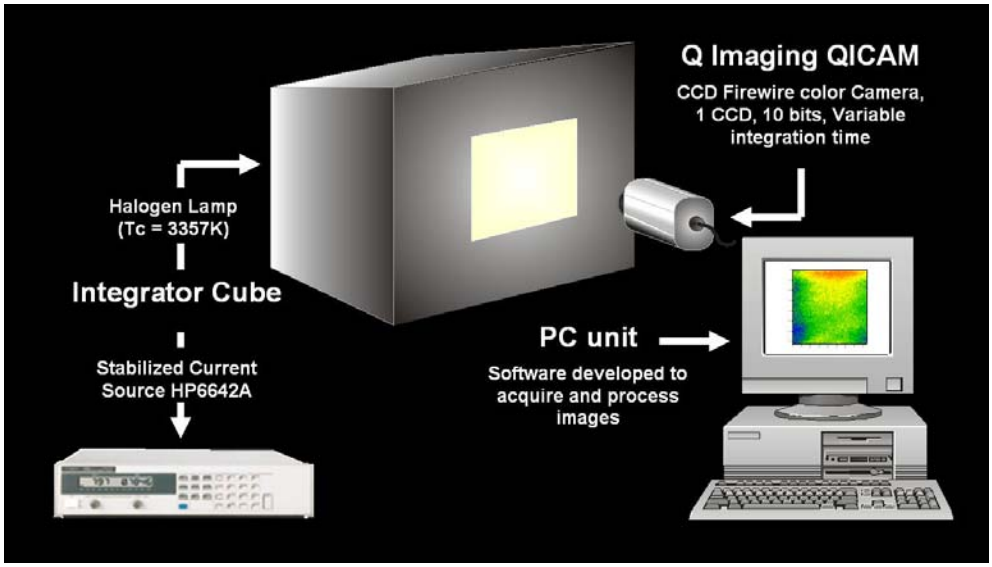

Figure 3.1 *Experimental setup used in the spatial characterization and noise correction of the response of an imaging system based on a CCD camera.*

The imaging system used in the development of the experimental methodology to correct the noise sources inherent to the performance of a CCD camera (presented in section 4.1), comprises a colour CCD camera QImaging QICAM of 10-bit digitalization depth, and an objective lens Cosmicar Television 16mm, 1:14 (Appendix 1, Figure 3.2). The CCD sensor used has a spatial resolution of 1024x1360 pixels and an RGB Bayer color filter array (CFA). The CFA image captured is demosaiced obtaining one image is for the R and B acquisition channels, and two images for the G acquisition channel, which are averaged to obtain one final image. Spatial interpolation is not performed in this case and, as a result, the spatial resolution of the final images for the R, G and B acquisition channels is 518×680 effective pixels.

Figure 3.2 *Colour CCD camera QImaging QICAM of 10-bit digitalization depth, and an objective lens Cosmicar Television 16mm, 1:14.*

The spatial non-uniformity correction of the imaging system is carried out using dark images and images captured from the uniform radiance field, and using different exposure

levels that are modified by varying the exposure time of the CCD sensor, since the radiance level of the integrator cube is fixed.

The quality of the spatial non-uniformity correction performance is evaluated in terms of the spatial non-uniformity of the digital levels associated to the pixels of an image of the uniform radiance field, which can be quantified in different ways [Holst, 1996]. In this work it is quantified by means of the spatial non-uniformity percentage (SNUP), given by the equation (3.1):

$$SNUP = 100 \cdot \frac{\sigma(Mean)}{Mean} \tag{3.1}$$

where *Mean* represents the average digital level over all pixels in the image, and $\sigma(Mean)$ is its associated standard deviation.

The experimental methodology developed for noise correction and the linear correction algorithm optimized (section 4.1) are subsequently applied to correct the response of the two configurations of the imaging system based on a monochrome CCD camera QImaging QICAM Fast 1394 12-bits cooled (Appendix 1): a colorimetric configuration with three acquisition channels and a multispectral configuration with seven acquisition channels, which will be used throughout this work. A detailed description of these two configurations can be found in section 3.4.

3.2 Spectral characterization

The first stage of the spectral characterization method applied (section 2.3) consists of determining the opto-electronic spectral conversion functions (OESCFs), which relate the normalized digital levels (NDLs) of the CCD camera's spectral response for different exposure levels, with the spectral exposure H_λ, for each acquisition channel.

The experimental setup used comprises a halogen lamp and a monochromator CVI Laser DIGIKRŌM 240 with constant spectral resolution (Appendix 1), which provide a uniform radiance field on a light diffuser, and whose radiance is varied by means of the monochromator's entrance/exit slits (Figure 3.3), a tele-spectracolorimeter Photo Research PR-650, and the CCD camera to be spectrally characterized.

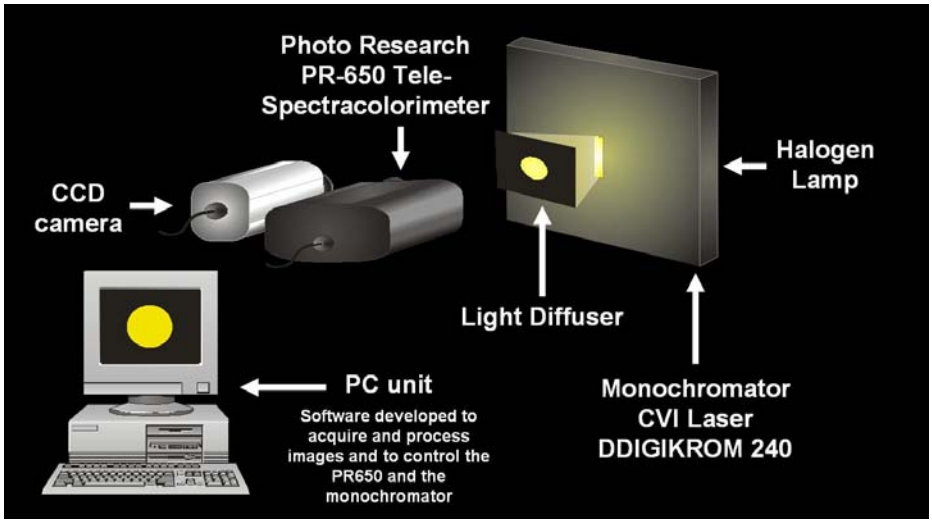

Figure 3.3 *Experimental setup used in the spectral characterization of an imaging system based on a CCD camera.*

The spectral exposure received by the CCD sensor depends on the incident spectral radiance (section 2.3, equation (2.6)), which is measured by the tele-spectracolorimeter.

The spectral response of the CCD camera for different exposure levels is obtained by capturing monochromatic images (images of the light diffuser placed in front of the monochromator exit) of variable radiance obtained using the monochromator and varying its entrance/exit slits in a systematic way. The CCD camera's digital responses for each acquisition channel and the corresponding spectral radiances are measured between 380nm and 780nm, with increments in wavelength of $\Delta\lambda = 4$nm.

The OESCFs are obtained by relating the NDLs of the CCD camera's spectral response for different exposure levels, with the spectral exposure H_λ, for each acquisition channel. The OESCFs (NDL_λ vs H_λ) are obtained for each wavelength λ, and for each acquisition channel k, and are fitted mathematically to a 4-parameter logistic (sigmoidal) function given by equation (2.7) (section 2.3).

Next, the spectral responsivities ($r_k(\lambda,H)$) and the action spectra ($a_k(\lambda,NDL)$) given by equations (2.8) and (2.9) (section 2.3), respectively, are obtained for each acquisition channel k from the experimental data and the previously modelled data.

For each wavelength – acquisition channel combination (λk), both the spectral responsivity and the action spectrum present a sharp increase associated to H or NDL when the background noise is exceeded, and a sharp decrease when the device reaches the saturation.

The $r_k(\lambda,H)$ vs H and $a_k(\lambda,NDL)$ vs NDL plots are the two dimensional profiles of the corresponding three dimensional functions, being the wavelength axis λ the third dimension. The absolute spectral sensitivities associated to a value of H or NDL are obtained by selecting the spectral profiles corresponding to these constant values of H or, equivalently, of NDL.

The absolute spectral sensitivities normalized to 1, for a sweep of H or NDL values, avoiding the extreme values corresponding to background noise and saturation, are superimposed giving rise to a unique and common spectral profile for both the spectral responsivity ($r_k(\lambda)$ vs λ) and the action spectrum ($a_k(\lambda)$ vs λ), which is known as relative spectral sensitivity. The relative spectral sensitivity value for each wavelength λ is obtained by averaging the absolute spectra sensitivities normalized to 1 at this λ [Martínez-Verdú et al., 2002].

3.3 Colour measurement and spectral reconstruction

The experimental setup used for the colour measurement and spectral reconstruction performed throughout this work comprises an imaging system based on a CCD camera, a tele-spectracolorimeter PhotoResearch PR650 with the MS-75 objective lens (Appendix 1), and a special light booth (63cm x 64cm x 52cm) with two kinds of lamps, which provided a uniform illumination field over the colour samples placed at the bottom of the light booth (Figure 3.4).

A big window (35cm x 24cm) on the opposite side of the light booth allowed the measurement of the patches with both the CCD camera, that provides the digital signals, and a tele-spectracolorimeter that provides the XYZ tristimulus values and the radiance spectra. Two kinds of lamps are used in this work in order to study the influence of the illuminant on the accuracy of colour measurement and spectral reconstruction: a set of six incandescent lamps MAZDA 22c 40W 230V Softone, and two D65 simulator illuminant fluorescent lamps 600mm VeriVide Artificial Daylight D65.

(a)

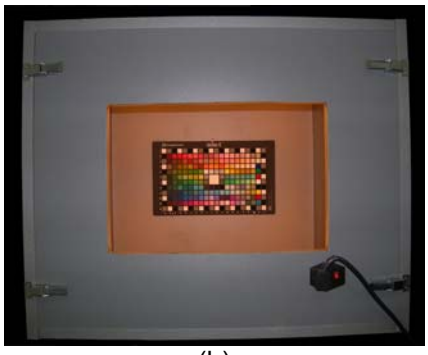

(b)

(c)

Figure 3.4 *Light booth used in the colour measurement and spectral reconstruction performed by an imaging system based on a CCD camera. (a) A set of six incandescent lamps MAZDA 22c 40W 230V Softone, just as the two D65 simulator illuminant fluorescent lamps, provide a uniform illumination field over the colour samples placed at the bottom of the light booth. (b) A big window on the opposite side of the light booth allowed the measurement of the colour samples with both the CCD camera and (c) a tele-spectracolorimeter Photo Research PR-650.*

Regarding the colour samples, the GretagMacbeth ColorChecker DC (CCDC) chart, the GretagMacbeth ColorChecker Color Rendition (CCCR) chart, the Munsell Book of Color – Matte Collection, and some combinations of them are used as training and test sets in the analysis of the accuracy of colour measurement and spectral reconstruction performed by an imaging system based on a CCD camera carried out throughout this work (Figure 3.5). A set of textile samples (Appendix 9) is also used to test the applicability of an imaging system based on a CCD camera not only using standardized colour charts, but also using real samples (chapter 13).

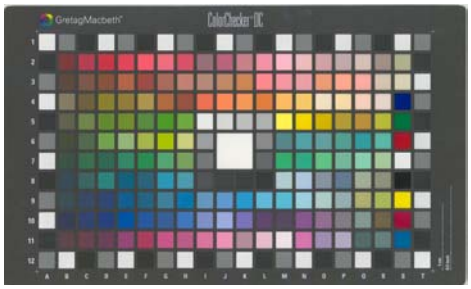

(a)

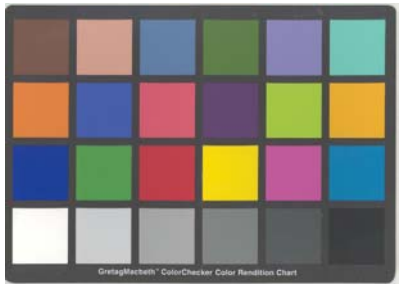

(b)

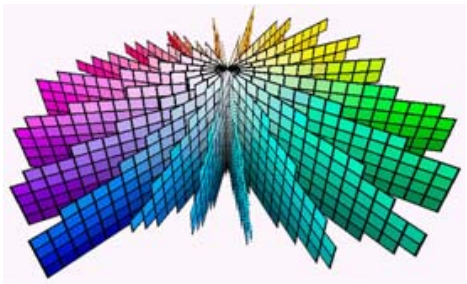

(c)

Figure 3.5 *Standardized colour charts used: (a) GretagMacbeth ColorChecker DC (CCDC) chart, (b) GretagMacbeth ColorChecker Color Rendition (CCCR) chart, (c) Munsell Book of Color – Matte Collection (source: http://www.codeproject.com/directx/d3dmunsell.asp).*

3.3.1 Methods for colour measurement

Methods for colour measurement, usually known as methods for colorimetric characterization, allow one to determine the transformation that defines the correspondence between the digital responses of the imaging system for all acquisition channels used, and a colour space independent of the device, such as the CIE 1931 XYZ colour space. Three methods for colour measurement are used in this work. The first one is based on the spectral sensitivities of the imaging system. The other two methods are based on measuring a training set using both a tele-spectracolorimeter and the imaging system. These are: the pseudoinverse method for XYZ (PSE_{XYZ}) and the second order non-linear method for XYZ ($NLIN(2)_{XYZ}$).

3.3.1.1 Method based on the spectral sensitivities of the imaging system

The method based on the spectral sensitivities of the imaging system proposed by Martínez-Verdú et al. [Martínez-Verdú et al., 2002; Martínez-Verdú et al., 2003] is the one applied in this work. Usually, this method is only applied to colorimetric configurations of imaging systems, i.e. with three acquisition channels, due to its growing complexity when the number of acquisition channels is increased.

Firstly, a relative joint scaling is performed to the relative spectral sensitivities of the imaging system. Then, the pseudo-colour matching functions of the imaging system $\mathbf{T_{XYZ}}$ are obtained by applying an equal-energy white balance to the spectral sensitivities resulting from the relative joint scaling for all acquisition channels. A detailed description and the formulas used in the relative joint scaling and the equal-energy white balance can be found in sub-section 2.4.1.1.

Once the pseudo-colour matching functions of the imaging system $\mathbf{T_{XYZ}}$ are obtained, it is necessary to determine the real scaling factor for each acquisition channel, i.e. relative to the absolute scaling of the pseudo-colour matching functions of the imaging system $\mathbf{T_{XYZ}}$, since the parameters of the equal-energy white balance of the device ($bal_R : bal_G : bal_B$) are relative to the reference channel *kref-E*, for which $bal_{kref-E} = 1$. With this aim, the basic colorimetric profile $\mathbf{M}$ of the imaging system, which is a *3x3* matrix that relates the relative colorimetric values RGB ($\mathbf{t'_{RGB}}$) with the relative tristimulus values normalized to an equal-energy stimulus ($\mathbf{t'_{XYZ}}$), is determined. A detailed description and the formulas used in the process followed to determine the basic colorimetric profile $\mathbf{M}$ of the imaging system can be found in sub-section 2.4.1.1.

Finally, once the basic colorimetric profile $\mathbf{M}$ of the imaging system is determined, the XYZ tristimulus values of a set of colour samples can be estimated from the model associated to the imaging system. The comparison between the estimated and the measured XYZ tristimulus values using a tele-spectracolorimeter highlights that a colour correction is necessary to improve the colorimetric estimation. With this aim, a linear colour compensation model is subsequently applied determining an offset tristimulus vector $\mathbf{A_C}$, which describes the systematic colour deviations of the device, and a diagonal scaling matrix $\mathbf{B_C}$ that allows to obtain the definitive scaling of the pseudo-colour matching functions of the imaging system and the raw colorimetric profile of the imaging system adding the luminance adaptation balance. A detailed description of this compensation process can be found in sub-section 2.4.1.1.

3.3.1.2 Pseudoinverse method for XYZ

In the pseudoinverse method for XYZ (PSE_{XYZ}), the XYZ tristimulus values associated to each colour sample are related to the corresponding digital responses of the *k* acquisition channels of the imaging system by means of a transformation matrix. Using a training set of *N* colour samples with known XYZ tristimulus values, the transformation matrix is determined by applying the Moore-Penrose pseudoinverse:

$$XYZ_{(3xN)} = D_{PSEXYZ(3xk)} \cdot P(k)_{(kxN)} \tag{3.1}$$

$$D_{PSEXYZ} = XYZ \cdot P(k)^t \cdot \left(P(k) \cdot P(k)^t\right)^{-1} \tag{3.2}$$

where XYZ is the *3xN* matrix of the XYZ tristimulus values of the *N* colour samples of the training set, and *P(k)* is the *kxN* matrix of the digital responses of the *k* acquisition channels of the imaging system for the *N* colour samples of the training set:

$$XYZ = \begin{pmatrix} X^{(1)} & X^{(2)} & \dots & X^{(N)} \\ Y^{(1)} & Y^{(2)} & \dots & Y^{(N)} \\ Z^{(1)} & Z^{(2)} & \dots & Z^{(N)} \end{pmatrix} \tag{3.3}$$

$$P(k) = \begin{pmatrix} DL_1^{(1)} & DL_1^{(2)} & \dots & DL_1^{(N)} \\ DL_2^{(1)} & DL_2^{(2)} & \dots & DL_2^{(N)} \\ \dots & \dots & \dots & \dots \\ DL_k^{(1)} & DL_k^{(2)} & \dots & DL_k^{(N)} \end{pmatrix} \tag{3.4}$$

A detailed description of the Moore-Penrose pseudoinverse and its properties can be found in sub-section 2.4.1.2.1.

Once the D_{PSEXYZ} transformation matrix is obtained, the XYZ tristimulus values of any colour sample can be directly estimated from its corresponding digital levels by the equation (3.1).

3.3.1.3 Second order non-linear method for XYZ

In the second order non-linear method for XYZ ($NLIN(2)_{XYZ}$), the transformation matrix relates the XYZ tristimulus values associated to each colour sample with a second order polynomial of the digital responses of the imaging system. Using a training set of *N* colour samples with known XYZ tristimulus values, the transformation matrix is determined by applying the Moore-Penrose pseudoinverse:

$$XYZ_{(3xN)} = D_{NLIN(2)_{XYZ}(3xp)} \cdot P(k,2)_{(pxN)} \tag{3.5}$$

$$D_{NLIN(2)_{XYZ}} = XYZ \cdot P(k,2)^t \cdot \left(P(k,2) \cdot P(k,2)^t\right)^{-1} \tag{3.6}$$

where XYZ is the *3xN* matrix of the XYZ tristimulus values of the *N* colour samples of the training set, and *P(k,2)* is the *pxN* matrix of the second order polynomials of the digital responses of the *k* acquisition channels of the imaging system for the *N* colour samples of the training set:

$$P(k,2)_{(pxN)} = \begin{pmatrix} 1 & 1 & \dots & 1 \\ DL_1^{(1)} & DL_1^{(2)} & \dots & DL_1^{(N)} \\ DL_2^{(1)} & DL_2^{(2)} & \dots & DL_2^{(N)} \\ \dots & \dots & \dots & \dots \\ \left(DL_1^{(1)}\right)^2 & \left(DL_1^{(2)}\right)^2 & \dots & \left(DL_1^{(N)}\right)^2 \\ \left(DL_2^{(1)}\right)^2 & \left(DL_2^{(2)}\right)^2 & \dots & \left(DL_2^{(N)}\right)^2 \\ \dots & \dots & \dots & \dots \\ DL_1^{(1)} \cdot DL_2^{(1)} & DL_1^{(2)} \cdot DL_2^{(2)} & \dots & DL_1^{(N)} \cdot DL_2^{(N)} \\ DL_1^{(1)} \cdot DL_3^{(1)} & DL_1^{(2)} \cdot DL_3^{(2)} & \dots & DL_1^{(N)} \cdot DL_3^{(N)} \\ \dots & \dots & \dots & \dots \end{pmatrix} \tag{3.7}$$

and $p = \left(1 + 2k + \binom{k}{2} = 1 + 2k + \frac{k!}{(k-2)!\cdot 2!}\right)$ is the number of components of the second order polynomial of the *k* digital responses associated to each colour simple.

A detailed description of the Moore-Penrose pseudoinverse and its properties can be found in sub-section 2.4.1.2.1.

3.3.2 Methods for spectral reconstruction

The main objective of methods for spectral reconstruction is to reconstruct the reflectance or radiance spectra of a colour sample from the corresponding digital responses of the imaging system. In this case also three methods are used, all of them based on measuring a training set, using both a tele-spectracolorimeter and the imaging system.

3.3.2.1 Pseudoinverse method

In the pseudoinverse method (PSE), the transformation matrix relates the reflectance spectra of the colour samples with the corresponding digital responses of the imaging system. Using a training set of *N* colour samples with known reflectance spectra, the transformation matrix is determined by applying the Moore-Penrose pseudoinverse:

$$R_{(41xN)} = D_{PSE\,(41xk)} \cdot P(k)_{(kxN)} \tag{3.8}$$

$$D_{PSE} = R \cdot P(k)^t \cdot \left(P(k) \cdot P(k)^t\right)^{-1} \tag{3.9}$$

where *R* is the *41xN* matrix of reflectance spectra of the *N* colour samples of the training set, sampling the reflectance spectrum from 380nm to 780nm in intervals of 10nm, and *P(k)* is the *kxN* matrix of the digital responses of the *k* acquisition channels of the imaging system for the *N* colour samples of the training set.

A detailed description of the Moore-Penrose pseudoinverse and its properties can be found in sub-section 2.4.1.2.1.

3.3.2.2 Second order non-linear method

In the second order non-linear method (NLIN(2)), the transformation matrix relates the reflectance spectra of the colour samples with a second order polynomial of the corresponding digital responses of the imaging system. Using a training set of *N* colour samples with known reflectance spectra, the transformation matrix is determined by applying the Moore-Penrose pseudoinverse:

$$R_{(41xN)} = D_{NLIN(2)(41xp)} \cdot P(k,2)_{(pxN)} \tag{3.10}$$

$$D_{NLIN(2)} = R \cdot P(k,2)^t \cdot \left(P(k,2) \cdot P(k,2)^t\right)^{-1} \tag{3.11}$$

where *R* is the *41xN* matrix of reflectance spectra of the *N* colour samples of the training set, sampling the reflectance spectrum from 380nm to 780nm in intervals of 10nm, and *P(k,2)* is the *pxN* matrix of the second order polynomials of the digital responses of the *k* acquisition channels of the imaging system for the *N* colour samples of the training set (3.7).

A detailed description of the Moore-Penrose pseudoinverse and its properties can be found in sub-section 2.4.1.2.1.

3.3.2.3 Principal Component Analysis

The third method applied is the Principal Component Analysis (PCA). In this method, a principal component analysis is applied on the matrix of reflectance spectra of the colour samples of the training set, obtaining the PCA basis and the coefficients of the reflectance spectra in this PCA basis:

$$R_{(41xN)} = V_{(41xp)} \cdot C_{(pxN)} \tag{3.12}$$

where *R* is the *41xN* matrix of reflectance spectra of the *N* colour samples of the training set, sampling the reflectance spectrum from 380nm to 780nm in intervals of 10nm, *V* is the *41xp* matrix of the *p* first vectors of the PCA basis, and *C* is the *pxN* matrix of scalar coefficients of the reflectance spectra of the *N* colour samples of the training set on the PCA basis *V*.

The scalar coefficients of the reflectance spectra of the *N* colour samples of the training set on the PCA basis are related to the digital responses of the imaging system by means of a transformation matrix that is determined by applying the Moore-Penrose pseudoinverse:

$$C_{(pxN)} = D_{PCA(pxk)} \cdot P(k)_{(kxN)} \tag{3.13}$$

$$D_{PCA} = C \cdot P(k)^t \cdot \left(P(k) \cdot P(k)^t\right)^{-1} \tag{3.14}$$

where *P(k)* is the *kxN* matrix of the digital responses of the *k* acquisition channels of the imaging system for the *N* colour samples of the training set.

This transformation matrix allow to calculate the coefficients of any colour sample on the PCA basis from its digital responses of the imaging system, and the linear combination of the vectors of the PCA basis with the coefficients calculated provides an estimation of the reflectance spectrum of the colour sample.

A detailed description of the PCA method and the Moore-Penrose pseudoinverse can be found in sub-sections 2.4.2.3 and 2.4.1.2.1, respectively.

3.4 Colorimetric configuration and multispectral configuration of the imaging system based on a monochrome CCD camera QImaging QICAM Fast 1394 12-bits cooled

Two configurations of the imaging system based on a monochrome CCD camera QImaging QICAM Fast 1394 12-bits cooled and an objective lens Nikon AF Nikkor 28 – 105 mm, are used throughout this work.

The colorimetric configuration (Figure 3.6), with three acquisition channels, is obtained by inserting an RGB tunable filter QImaging RGB-HM-NS, which is controlled through the camera via software, between the CCD camera and the objective lens.

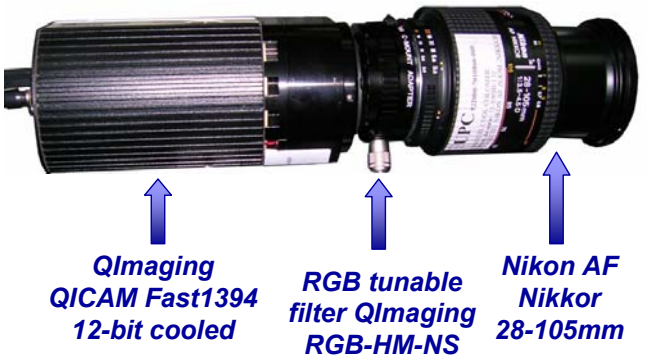

Figure 3.6 *Colorimetric Configuration (3 acquisition channels) of the imaging system based on a monochrome CCD camera QImaging QICAM Fast 1394 12-bits cooled.*

The multispectral configuration (Figure 3.7), with seven acquisition channels, is obtained by inserting a motorized filter wheel with seven CVI Laser interference filters covering the whole visible range of the spectrum (Figure 3.8) controlled via software, between the CCD camera and the objective lens.

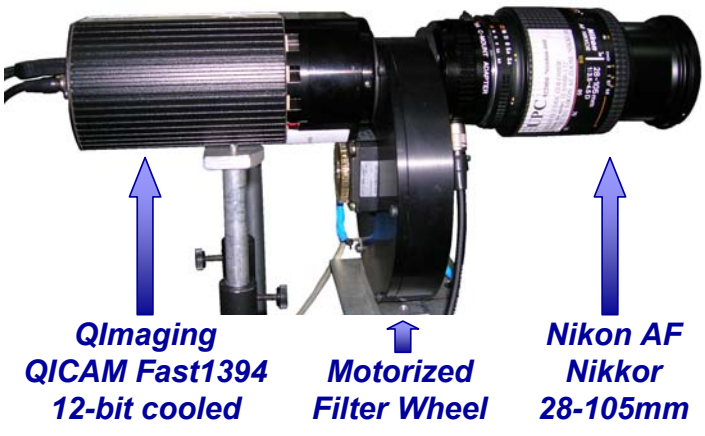

Figure 3.7 *Multispectral Configuration (7 acquisition channels) of the imaging system based on a monochrome CCD camera QImaging QICAM Fast 1394 12-bits cooled.*

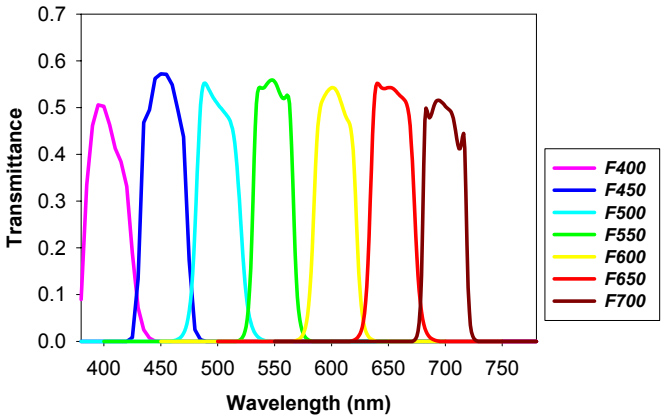

Figure 3.8 *Transmittance spectra of the interference filters used in the multispectral configuration of the imaging system. Interference filters are named by their central wavelength.*

The supplier specifications for the interference filters, which are usually considered to be approximately gaussian, are: peak positions or central wavelengths (CWLs) at 400nm, 450nm, 500nm, 550nm, 600nm, 650nm, and 700nm, full widths at half maximum (FWHMs) of 40nm for all of them, and peak transmittances of 35%, 45%, and 50% depending on the CWL (Appendix 8). The selection of the interference filters used was based on results about the theoretical optimum filters obtained previously by our research group on multispectral systems for reflectance reconstruction in the near-infrared region [Vilaseca, 2005]. The extrapolation of these results to the visible region of the spectrum led to select a set of gaussian interference filters having equidistant peak positions covering the whole visible range, equal FWHMs that allow a slight overlapping between them, and the higher transmittance possible. Among the commercially available interference filters, the seven CVI Laser interference filters selected fulfilled all these requirements.

4 Noise Correction of an Imaging System Based on a CCD Camera

In this chapter the experimental methodology developed to correct the noise sources inherent to the performance of a CCD camera and the optimization of a linear algorithm for the spatial non-uniformity correction of the system's response are presented.

It is necessary to correct the several existing noise sources inherent to the performance of a CCD camera if an imaging system based on it is wanted to be used as a measuring instrument with high spatial resolution. Particularly, it is essential to correct the spatial non-uniformity of the system's response so that the whole detection area of the camera be useful for measuring and, consequently, the system had a high spatial resolution. Among the existing methods for the spatial non-uniformity correction (sub-section 2.2.3), the most general one is considered. It is based on the calibration of the detector by means of two images: a dark image, and a uniform field image, allowing the performance of accurate radiometric measurements using a CCD sensor. Moreover, this method allows one to correct the spatial non-uniformity of the system's response independently of the non-uniformity of the scene illumination.

The original linear correction algorithm is given by equations (2.4) (sub-section 2.2.3), is based on the calculation of the gain and offset matrixes, and its variables are the dark image, the base correction image (an image of a uniform radiance field) and the reference digital level. The optimization of this algorithm is carried out assessing the influence of its variables on the quality of the spatial non-uniformity correction, and determining their optimal values and the application range of the correction achieved by this algorithm [de Lasarte et al., 2007 – 1].

4.1 Experimental methodology developed to correct the noise sources inherent to the performance of a CCD camera

The imaging system used in the development of the experimental methodology to correct the noise sources inherent to the performance of a CCD camera comprises a colour CCD camera QImaging QICAM 10-bit (Appendix 1) and an objective lens Cosmicar Television 16mm, 1:14 (section 3.1).

This experimental methodology can be applied to any imaging system based on a CCD camera, and is next applied to the two configurations of the imaging system based on a monochrome CCD camera QImaging QICAM Fast 1394 12-bits cooled (Appendix 1) and an objective lens Nikon AF Nikkor 28 – 105 mm (section 3.4).

4.1.1 Selection of the camera's gain and offset parameters

For the CCD camera used, just as for most of the commercial CCD cameras, the exposure time, the electronic gain of the output amplifier and the zero electronic offset of the

A/D converser, are variable parameters so the user can select the gain and offset values to optimize the final correction of the spatial non-uniformity. The criterion applied in the selection of these gain and offset parameters is the RGB acquisition channels' response be a linear function of the exposure over a certain range of exposure. Under this requirement, the gain and offset values that allowed having a zero and non-zero dark image are determined in order to establish the influence of the dark image on the correction.

The R and G channel of the used camera are more sensitive than the B channel, which needs much more exposure to saturate, and presents a linear response over a certain exposure range for all possible values of the gain and offset parameters (Figure 4.1 (a)).

On the other hand, the B channel's response presents two linear zones of different slope before the saturation for certain values of the gain and offset parameters (Figure 4.1 (b)), which must be avoided if the imaging system is wanted to be used as a measuring instrument.

It is proved that the offset values must be higher than 1100 to obtain a non-zero dark image, and the gain value must be lower than 1200 (Figure 4.1 (b)) to generate a linear response of the B acquisition channel having a unique slope. Taking these results into account, the gain and offset values are selected to be 1000 and 850, respectively, to have a zero dark image, and to be 1000 and 1400, respectively, to have a non-zero dark image. These last values of gain and offset allow one to obtain a dark image with a mean digital level of 35, which is approximately 4% of the maximum useful (linear response zone) digital level of the 10-bit camera. The linear response zone of a CCD camera is typically placed between the 3% - 5% and the 85% - 90% of the maximum digital level ($2^{bits} - 1$) of the camera. As it is shown further on this section, these gain and offset parameter values produce the best spatial non-uniformity correction of images.

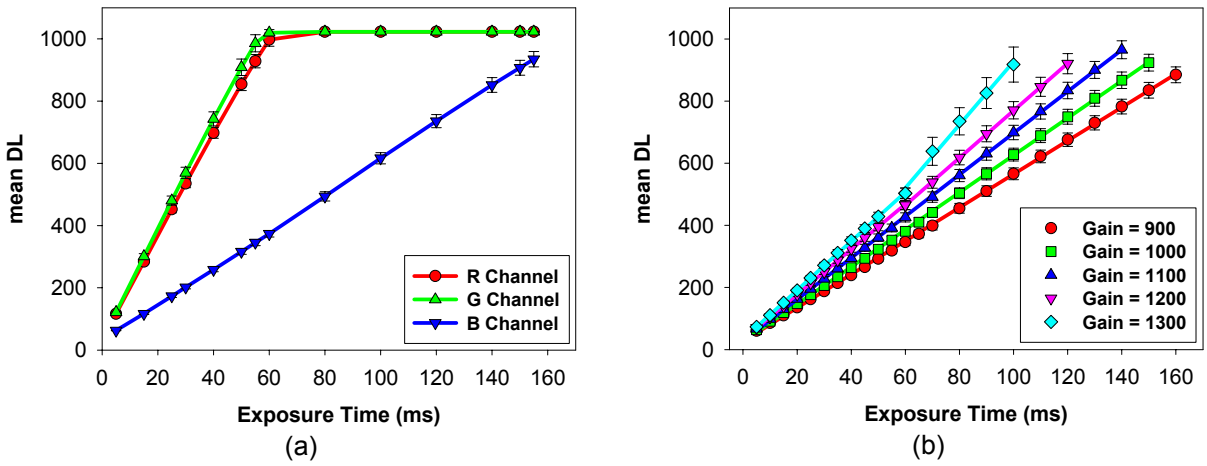

Figure 4.1 *Mean digital level (DL) of the image plotted versus the exposure time for (a) the R, G and B acquisition channels of the imaging system based on a colour CCD camera QImaging QICAM 10-bits (gain = 1000, offset = 1400), and (b) the B acquisition channel for different gain values and a fixed offset value of 1400.*

4.1.2 Number of images

The contribution of different zero-mean noise components to the digitized image of the radiance uniform field must be reduced as much as possible before carrying out the spatial non-uniformity correction. With this aim, the variation in the quality of the correction is

analyzed depending on the number of averaged images, and the minimum number of images that needed to be averaged to obtain the best correction possible is determined.

A simplified noise model for a CCD camera is assumed [Holst, 1996], which considered the total noise associated with the system can be expressed as the sum of the contributions of the shot noise (photon shot noise and dark current), the pattern noise (fixed pattern noise (FPN) and photo-response non-uniformity (PRNU)) and the floor noise (reset noise, amplifier noise and quantization noise) (sub-section 2.2.2). Bearing in mind the statistics associated with these noise sources, image averaging reduces the contribution of all random noise sources to image noise in a factor inversely proportional to the number of averaged images.

In order to determine the number of images to be averaged, the variation of the SNUP of the resulting image is analyzed depending on the number of averaged images (Figure 4.2 and Table 4.1). Several images are captured with a fixed exposure time of 40 ms for all channels of the CCD camera's imaging system, which provided a mean digital level of 683 for the R channel, 737 for the G channel and 257 for the B channel. The camera's gain and offset parameters are selected to be 1000 and 1400, respectively.

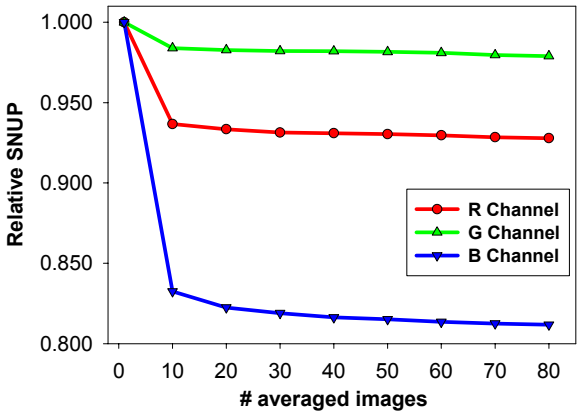

Figure 4.2 *Relative SNUP plotted versus the number of images averaged for the R, G, and B acquisition channels of the imaging system.*

Table 4.1 *SNUP values and percentage of reduction of the SNUP (% reduc.) values for the image resulting from averaging, for the different number of images averaged (# av. im.), for the R, G, and B channels of the imaging system.*

	R Channel		G Channel		B Channel	
# av. im.	**SNUP**	**% reduc.**	**SNUP**	**% reduc.**	**SNUP**	**% reduc.**
1	2.664	-	3.135	-	3.082	-
10	2.496	6.306	3.085	1.604	2.565	16.748
20	2.487	0.361	3.081	0.120	2.535	1.204
30	2.482	0.201	3.079	0.065	2.524	0.422
40	2.480	0.081	3.079	0.010	2.516	0.325
50	2.479	0.040	3.078	0.045	2.512	0.139
60	2.477	0.081	3.076	0.058	2.507	0.207
70	2.475	0.081	3.071	0.143	2.504	0.124
80	2.473	0.081	3.070	0.062	2.502	0.092

Although progressively increasing the number of averaged images improved the spatial uniformity of the averaged image, using more than 20 images does not lead to an

outstanding improvement. This result would be expected on the basis of the fact that the standard deviation associated with the resulting image, which constitutes an approximation to the total noise of the image, varies in a manner that is approximately inversely proportional to the square root of the number of averaged images, although not exactly since image averaging reduces all random noise sources except those that generate spatial non-uniformity (pattern noise), which, if they are not corrected, still contribute to image noise.

Hereinafter, and unless otherwise indicated, any image referred to will be the image resulting from averaging 20 individual images successively captured.

Next, the spatial non-uniformity correction is carried out by means of the application of the linear correction algorithm given by the equations (2.4) (sub-section 2.2.3). The quality of the correction is optimized considering different dark images, different base correction images and different reference digital levels.

4.1.3 Influence of dark image, base correction image, and reference digital level on the quality of the spatial non-uniformity correction

Firstly, the linear spatial non-uniformity correction algorithm given by equations (2.4) (sub-section 2.2.3) is applied to images captured with two different camera gain and offset values, which allowed to have zero (gain value of 1000 and offset value of 850) and non-zero (gain value of 1000 and offset value of 1400) dark images, respectively. The image with a mean digital level placed in the middle of the useful linear response range of the camera is used as the base correction image, and the mean digital level of the image as the reference digital level.

Table 4.2 *Mean values of the SNUP of images on the useful linear response range of the CCD camera, selecting the gain and offset values corresponding to zero dark image (ZDI) and non-zero dark image (NZDI), for the R, G, and B acquisition channels.*

	R Channel	G Channel	B Channel
ZDI	0.516	0.509	1.843
NZDI	0.406	0.359	0.628

In order to analyze the influence of having a zero or non-zero dark image, the spatial non-uniformity correction quality of several corrected images is compared by means of the SNUP (Table 4.2). The use of a non-zero dark image improved the spatial non-uniformity correction from 21% up to 66%, depending on the acquisition channel, with regard to corrected images obtained with a zero dark image. Consequently, in order to obtain images with high spatial non-uniformity correction, it is essential to work with gain and offset values that produce non-zero dark images.

Regarding the influence of the base correction image on the quality of the spatial non-uniformity correction, several images are selected as base correction image: the brilliant image (BI), which is the one usually found in literature and has the highest mean digital level without having any saturated pixels; the central image (CI), which is the image with a mean digital level placed in the middle of the useful linear response range of the CCD camera's imaging system; and the extreme image (EI), whose mean digital level is placed at the end of the useful linear response range of the camera and is the closest one to the brilliant image, but in the camera's linear response range. In this case, as in the analysis of the influence of the dark image, the mean digital level of the image is taken as reference digital level.

As can be seen from Table 4.3, using both the central and extreme images as base correction images leads to a clear improvement in the quality of the spatial non-uniformity correction for the R and G channels. The best correction is commonly achieved using the central image, for which an improvement of the spatial non-uniformity correction of 41% is obtained for the R channel, and an improvement of 29% for the G channel. For the B channel, results obtained using the different selected images as base correction images are quite similar. This is probably due to the fact that the B channel's response shows two linear zones. Although the gain and offset values are selected in order to obtain a unique slope, this linear behaviour is observed when the average of the entire image is considered. However, the linearity of the individual response of each pixel is not guaranteed, and this may affect results obtained.

Table 4.3 *Exposure time (t_{exp}) corresponding to each base correction image and mean SNUP values of the corrected images on the useful linear response range of the system, for the R, G, and B acquisition channels, and using the brilliant image (BI), the central image (CI), and the extreme image (EI) as base correction images.*

	R Channel		G Channel		B Channel	
	t_{exp} (ms)	mean SNUP	t_{exp} (ms)	mean SNUP	t_{exp} (ms)	mean SNUP
BI	60	0.691	55	0.508	155	0.582
CI	30	0.406	30	0.359	80	0.628
EI	55	0.431	50	0.367	150	0.613

Although one might think that taking the brilliant image as base correction image would enable the full response range of the camera to become involved, this image is placed at the beginning of the saturation zone of the camera response and this might be why the brilliant image leads to worse results than the central and extreme images, which are both within the linear response range. Hereinafter, the base correction image is taken to be the central image.

Finally, as in the case of the base correction image, several values are taken as reference digital level in order to determine its influence on the quality of the spatial non-uniformity correction: the mean digital level, which is the one that is usually used in literature; the mode of all digital levels of the pixels in the image; and the digital level corresponding to the central pixel of the image. The central images for each R, G, and B acquisition channels are taken as base correction images.

Table 4.4 *Mean SNUP values for the R, G, and B acquisition channels of the imaging system corresponding to corrected images using the mean digital level (Mean DL) of the image, the mode of all digital levels of the pixels in the image (Mode DL), and the digital level corresponding to the central pixel of the image (Central DL)*

	R Channel	G Channel	B Channel
Mean DL	0.406	0.359	0.628
Mode DL	0.406	0.359	0.629
Central DL	0.407	0.361	0.632

Results obtained in terms of the spatial non-uniformity correction quality are very similar for all reference digital levels considered (Table 4.4). Results corresponding to the mean and mode digital levels are practically identical and slightly better than those obtained for the central digital level. This could be due to the statistical nature of these two reference

digital levels, since they are related to the digital level value distribution of an image. Consequently, from this point on, the mean digital level is taken as the reference digital level in the linear spatial non-uniformity correction algorithm, since it is usually used as the reference digital level in literature.

Once the spatial non-uniformity linear correction algorithm of an imaging system based on a CCD camera is optimized, its range of application is determined by analyzing its performance on different exposure time ranges.

4.1.4 Range of application of the optimized spatial non-uniformity linear correction algorithm

Up to this point, the illumination conditions are fixed and, as a result, the range of exposure time in which the camera's linear response is useful is also fixed, depending on the gain and offset settings. However, the range of exposure time can change depending on the image captured.

The optimized algorithm for spatial non-uniformity correction (equations (2.4), sub-section 2.2.3) depends fundamentally on the correction gain matrix, since the correction offset matrix is calculated from the correction gain matrix and the dark image captured under the same conditions as the image to be corrected. For this reason, assessing the application of the optimized algorithm for spatial non-uniformity correction involves determining if a correction gain matrix calculated for certain fixed illumination conditions, and thus, a fixed range of exposure time, leads to high quality spatial non-uniformity correction when it is used to correct an image captured in any other range of exposure time, beyond the useful linear response range of the camera.

In order to check the application of the optimized algorithm for spatial non-uniformity correction, several groups of images of a uniform radiance field are captured for several radiance levels by varying the current intensity applied to the halogen lamp of the integration cube. A correction gain matrix ($\mathbf{G}^{(i)}$ (i = 1, 2, 3, 4, 5, 6 radiance levels)) is calculated for each radiance level (range of exposure time). Each one of these correction gain matrixes is used to correct the groups of images corresponding either to its own radiance level or to the rest of the radiance levels considered. The radiance levels are selected on the basis of the ranges of exposure time corresponding to the useful linear response range of the imaging system associated with them for each acquisition channel (Table 4.5). From this point on, by radiance level it will be referring to the corresponding range of exposure time of the R, G, and B acquisition channels responses, rather than the numerical radiance level itself.

Table 4.5 *Radiance values and ranges of exposure time corresponding to the useful linear response range of the imaging system associated with them for each acquisition channel (R, G, and B), for the six radiance levels considered.*

		Range of Exposure Time (ms)		
Radiance Levels	**Radiance (W/sr·m^2)**	**R Channel**	**G Channel**	**B Channel**
1	5.263	5 – 60	5 – 50	10 – 160
2	3.846	10 – 80	10 – 80	10 – 225
3	2.662	10 – 100	10 – 100	50 – 400
4	1.758	25 – 175	25 – 175	50 – 700
5	1.092	25 – 300	25 – 300	100 – 1300
6	0.630	50 – 500	100 – 700	200 – 2500

The mean SNUP obtained for each radiance level (from 1 to 6) depending on the radiance level of each correction gain matrix used is shown for the different radiance levels in Figure 4.3, for the R, G, and B acquisition channels. The mean SNUP of the original non-corrected images for the different radiance levels is also shown.

The best results are obtained when images corresponding to a radiance level are corrected using the correction gain matrix calculated for the same radiance level or for the radiance levels closest to it. High radiance levels, corresponding to low exposure time ranges, lead to better results than lower ones, probably due to the growing contribution of dark current noise on the camera's response, as a result of using longer exposure times.

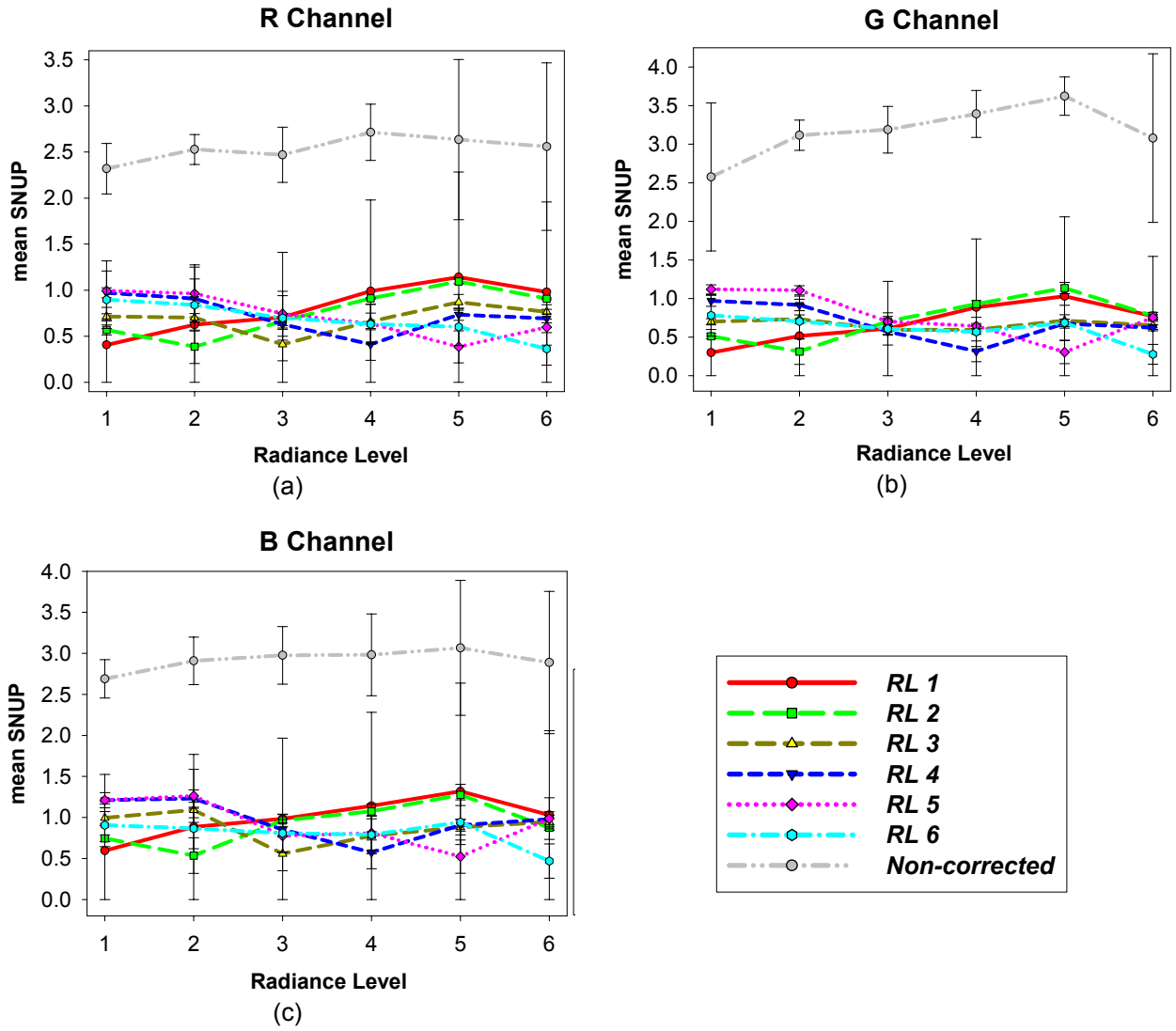

Figure 4.3 *Mean SNUP values and standard deviation associated to the mean (error bars) for each radiance level (RL, from 1 to 6), plotted as a function of the radiance levels of each one of the gain correction matrices used in the optimized spatial non-uniformity correction algorithm applied, for the (a) R, (b) G, and (c) B acquisition channels of the imaging system.*

In spite of this, comparing the mean SNUP of the corrected images of different radiance levels using the gain correction matrixes calculated for all radiance levels, with the mean SNUP of the non-corrected images for the same radiance levels, it can be seen that the calculation of a correction gain matrix at a certain radiance level (preferably a high radiance level) and, thus, at a certain range of exposure time of the R, G, and B acquisition channels

(preferably a low exposure time range), would be sufficient to achieve a high quality spatial non-uniformity correction of images corresponding to any radiance level, when the optimized linear spatial non-uniformity correction algorithm is applied to them using this gain matrix.

Obtaining different radiance levels by varying the current intensity applied to the halogen lamp of the integration cube modified considerably the radiance spectrum of the incident light in the CCD camera's imaging system (Figure 4.4). Therefore, the fact that high quality spatial non-uniformity correction of images is achieved for different ranges of exposure time proves that the correction performed by this optimized algorithm is independent of changes in the radiance spectrum of the incident light, and that the algorithm may be successfully applied in a wide range of exposure conditions

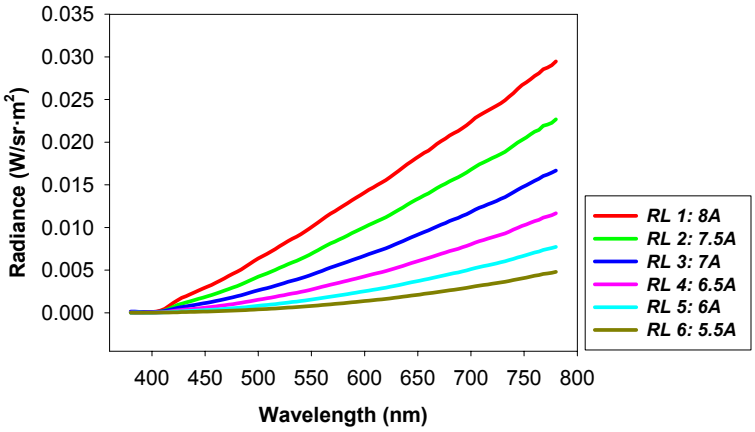

Figure 4.4 *Radiance spectrum of the incident light in the CCD camera's imaging system. Different radiance levels are obtained by varying the current intensity applied to the halogen lamp of the integration cube.*

Both the experimental methodology developed to correct the noise sources inherent to the performance of a CCD sensor and the optimized linear algorithm for the spatial non-uniformity correction can be applied to any imaging system based on a CCD camera, allowing to minimize the contributions of the CCD's inherent noise sources to the system's performance and making the whole CCD sensor's area useful.

The experimental methodology developed and the optimized linear correction algorithm are subsequently applied to correct the response of the two configurations of the imaging system based on a monochrome CCD camera QImaging QICAM Fast 1394 12-bits cooled: a colorimetric configuration with three acquisition channels, and a multispectral configuration with seven acquisition channels. A detailed description of these two configurations of the imaging system, which will be used throughout this work, can be found in section 3.4.

4.2 Application of the experimental methodology developed to correct the noise sources inherent to the performance of a CCD camera

Next, the experimental methodology developed to correct the noise sources inherent to the performance of a CCD camera is applied to the two configurations of the imaging system based on the monochrome CCD camera QImaging QICAM Fast 1394 12-bits cooled.

4.2.1 Selection of the camera's gain and offset parameters

Using a monochrome CCD camera, the system's response is always linear, in a certain exposure range, for all acquisition channels and for any value of the gain and offset parameters. This is the reason why the gain parameter is initially fixed in a value of 8, which is an intermediate value within the range of possible values for this parameter (it ranges from 0.6 to 15). Using this gain value and an exposure time of 100ms, due to the fact that the fluctuation of the mean digital level of the dark image depending on the exposure time was proved to be negligible since it is a cooled camera, the offset value is determined so that the mean digital level of the dark image is approximately the 4% of the maximum digital level of the useful response range of the camera (3700 aprox.). The final selected values for these parameters are a gain value of 8 and an offset value of 2200, for both configurations of the imaging system.

4.2.2 Number of images

Averaging images reduces the contribution of all random noise sources to image noise, but not the pattern noise (fixed pattern noise (FPN) and photo-response non-uniformity (PRNU)). All these noise sources affect the dark image and the uniform field image in the same way, so the number of images to be averaged is determined from averaging dark images, using an exposure time of 100ms. Since the imaging system is based on a monochrome CCD camera, the result obtained was proved to be common to both configurations and to all acquisition channels for each configuration (Table 4.6).

As it could be expected considering noise statistics, the greater reduction of the SNUP values is observed averaging 10 images (Table 4.6). Similarly to the colour CCD camera of 10-bits analyzed previously, and outstanding improvement in the spatial uniformity of the image is not observed averaging more than 20 images. For images resulting of averaging more than 20 images, the reduction in the SNUP is lower than the 1% of the SNUP corresponding to the average of 20 images.

Table 4.6 *SNUP values and percentage of reduction of the SNUP (% reduc.) values for the image resulting from averaging, for the different number of images averaged (# av. im.), for the R, G, and B channels of the colorimetric configuration of the imaging system.*

	R Channel		G Channel		B Channel	
# av. im.	**SNUP**	**% reduc.**	**SNUP**	**% reduc.**	**SNUP**	**% reduc.**
1	19.731	-	19.686	-	19.669	-
10	6.459	13.271	6.456	13.230	6.438	13.230
20	4.765	1.694	4.697	1.759	4.694	1.744
30	3.984	0.781	3.973	0.724	3.967	0.728
40	3.480	0.504	3.475	0.498	3.479	0.488
50	3.156	0.324	3.150	0.325	3.142	0.337
60	2.901	0.255	2.896	0.254	2.899	0.242
70	2.789	0.112	2.779	0.117	2.807	0.092
80	2.626	0.163	2.618	0.161	2.616	0.191

Hereinafter, any image referred to will be the image resulting from averaging 20 individual images successively captured, for both configurations of the imaging system.

4.2.3 Spatial non-uniformity correction

The optimized linear algorithm for the spatial non-uniformity correction is applied to all acquisition channels of both configurations of the imaging system. Results obtained in terms of the SNUP of both the non-corrected and the corrected images, and the reduction in the SNUP achieved by applying the correction algorithm, are presented next.

4.2.3.1 Colorimetric Configuration

In a cooled CCD camera the contribution of the dark current, both of the shot noise and of the fixed pattern noise, to the total noise of the image is considerably reduced since it is a noise source of thermal origin. This explains the low SNUP obtained for the non-corrected images (Table 4.7). In spite of this, the application of the optimized algorithm allows one to obtain a considerable reduction of the SNUP for the three acquisition channels, as can be seen from Table 4.7.

Table 4.7 *Colorimetric Configuration: mean SNUP of non-corrected and corrected images on the linear response range of the imaging system, and percentage of reduction of the SNUP (% reduc. SNUP) resulting of applying the spatial non-uniformity correction to the three acquisition channels.*

	mean SNUP non-corrected images	mean SNUP corrected images	% reduc. SNUP
R Channel	1.569	1.008	38.536
G Channel	1.262	0.984	26.364
B Channel	1.251	0.995	26.127

4.2.3.2 Multispectral Configuration

Results obtained for the seven acquisition channels of the multispectral configuration when applying the optimized algorithm for the spatial non-uniformity correction are presented in Table 4.8. Quite similar results are obtained for all acquisition channels and, despite of the fact that the SNUP of the non-corrected images is quite low, applying the optimized linear algorithm for the spatial non-uniformity correction allows obtaining a considerable improvement of the spatial uniformity of images.

Table 4.8 *Multispectral Configuration: mean SNUP of non-corrected and corrected images on the linear response range of the imaging system, and percentage of reduction of the SNUP (% reduc. SNUP) resulting of applying the spatial non-uniformity correction to the seven acquisition channels. The acquisition channels are named using their central wavelength.*

	mean SNUP non-corrected images	mean SNUP corrected images	% reduc. SNUP
Channel 1 – F400	1.141	1.072	6.073
Channel 2 – F450	1.313	1.101	16.130
Channel 3 – F500	1.430	1.100	23.112
Channel 4 – F550	1.301	1.026	21.113
Channel 5 – F600	1.493	1.227	17.798
Channel 6 – F650	1.409	1.190	15.528
Channel 7 – F700	1.469	1.168	20.502

Considering results obtained for both configurations of the imaging system, from here on any image referred to will be the image resulting from averaging 20 individual images successively captured and the subsequent application of the optimized linear algorithm for spatial non-uniformity correction. By this way, images used in all analyses of system's performance carried out are assured to have the minimum contribution possible of noise sources inherent to CCD sensors' performance.

5 Colorimetric Characterization Based on the Spectral Sensitivities of the Imaging System

The colorimetric characterization of an imaging system is the process of deriving the transformation that defines the correspondence between the camera's digital responses and a colour space independent of the device, either the XYZ or the CIELAB, which is essential to achieve a high fidelity reproduction of colour.

Methods for colorimetric characterization based on spectral sensitivities require the previous knowledge of the system's spectral sensitivities, which can be determined through the spectral characterization of the imaging system. The relationship between the camera's spectral sensitivities and the CIE colour matching functions must be found in order to use it subsequently to transform the system's digital responses into the XYZ tristimulus values. These methods are usually only applied to colorimetric configurations of imaging systems, i.e. with three acquisition channels, due to its growing complexity when the number of acquisition channels is increased.

In this work, the spectral characterization of the imaging system is performed as the previous stage to the colorimetric characterization based on the spectral sensitivities. These spectral and colorimetric characterization are applied to the imaging system based on a colour CCD camera QImaging QICAM of 10-bits digitalization depth (Q10) and an objective lens Cosmicar Television 16mm (section 3.1), and to the colorimetric configuration (3 acquisition channels) of the imaging system based on a monochrome CCD camera QImaging QICAM Fast 1394 12-bits cooled (Q12) and an objective lens Nikon AF Nikkor 28 – 105 mm (section 3.4).

5.1 Spectral Characterization of an Imaging System Based on a CCD Camera

The spectral characterization of a CCD camera allows to determine the camera's absolute and relative spectral sensitivities for each acquisition channel (section 2.3), which are necessary to be known if a colorimetric characterization based on the spectral sensitivities of the imaging system is wanted to be applied, or if system's response is wanted to be simulated.

In this work, the method for colorimetric characterization proposed by Martínez-Verdú et al. [Martínez-Verdú et al., 2002; Martínez-Verdú et al., 2003] (section 2.3), which is based on the relative spectral sensitivities of the imaging system's acquisition channels, is applied. Due to the complexity of this method it is only applied to colorimetric configurations (3 acquisition channels) of imaging systems. Therefore, the spectral characterization of the imaging system based on the Q10 camera and an objective lens Cosmicar Television 16mm (section 3.1), and of the colorimetric configuration (3 acquisition channels) of the imaging system based on the Q12 camera and an objective lens Nikon AF Nikkor 28 – 105 mm (section 3.4) are only carried out.

The spectral characterization method applied is fully described in section 2.3, and is based in direct spectral measurements and obtaining of the opto-electronic spectral conversion

functions (OESCFs) to the subsequent determination of the absolute and relative spectral sensitivities of each acquisition channel. The experimental setup used is detailed in section 3.2.

Once the CCD camera's digital responses for each acquisition channel and the corresponding spectral radiances are measured between 380nm and 780nm, with increments in wavelength of $\Delta\lambda = 4$nm, the OESCFs are obtained by relating the normalized digital levels (NDLs) of the CCD camera's spectral response to different exposure levels, with the spectral exposure H_λ, for each acquisition channel (Figure 5.1). The OESCFs (NDL_λ vs H_λ) obtained for each wavelength λ, and for each acquisition channel k are fitted mathematically to a 4-parameter sigmoidal function (Figure 5.1, Table 5.1) given by equation (2.7) (section 2.3).

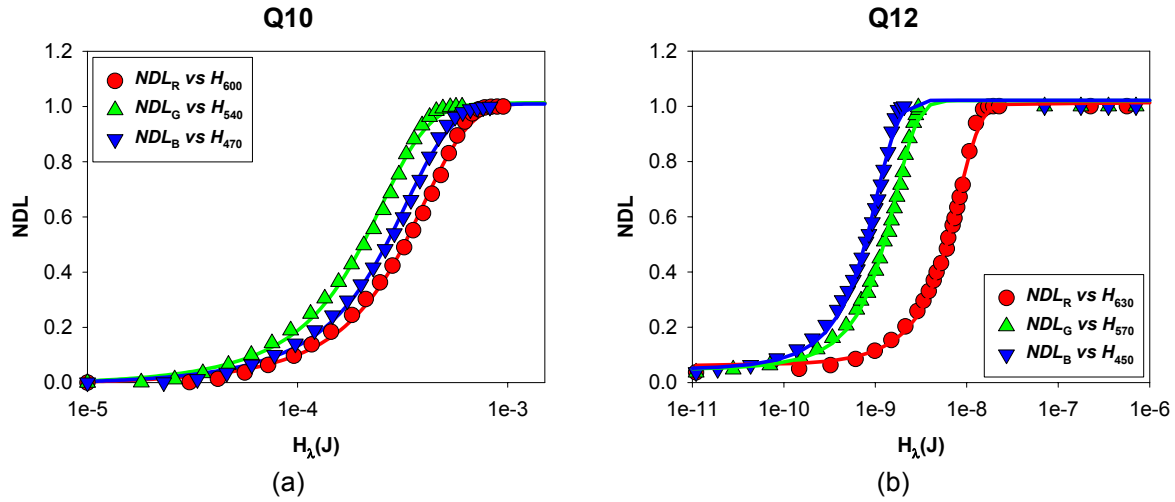

Figure 5.1 *OESCs: normalized digital level (NDL) of the R, G, and B acquisition channels plotted versus the spectral exposure at a wavelength λ (H_λ) for (a) the imaging system based on the Q10 camera, and (b) the colorimetric configuration of the imaging system based on the Q12 camera. The OESCFs are fitted to a 4-parameter sigmoidal function.*

Table 5.1 *Parameters of the 4-parameter sigmoidal function fitting of the OESCFs in Figure 5.1., for the imaging system based on the Q10 camera, and the colorimetric configuration of the imaging system based on the Q12 camera.*

	k	λ (nm)	$a_{\lambda k}$	$b_{\lambda k}$	$c_{\lambda k}$	$d_{\lambda k}$
Q10	R	600	-1.924E-01	1.200	4.102E-10	3.039E-10
	G	540	-2.155E-01	1.219	2.621E-10	2.039E-10
	B	470	-2.666E-01	1.275	2.871E-10	2.602E-10
Q12	R	630	-1.283E-01	1.141	1.677E-09	1.043E-09
	G	570	-1.424E-01	1.163	1.097E-09	6.712E-10
	B	450	-1.401E-01	1.162	6.844E-10	4.164E-10

The absolute spectral sensitivities associated to an H or NDL value are obtained by selecting the spectral profiles of the spectral responsivities ($r_k(\lambda,H)$) or the action spectra ($a_k(\lambda,NDL)$) corresponding to the constant values of H or NDL, respectively. In this case, the absolute spectral sensitivities associated to different values of NDL (from 0.1 to 0.9 in 0.1 steps) for the R, G, and B acquisition channels of the two imaging systems considered (Q10 and Q12) can be observed in Figures 5.2 and 5.3.

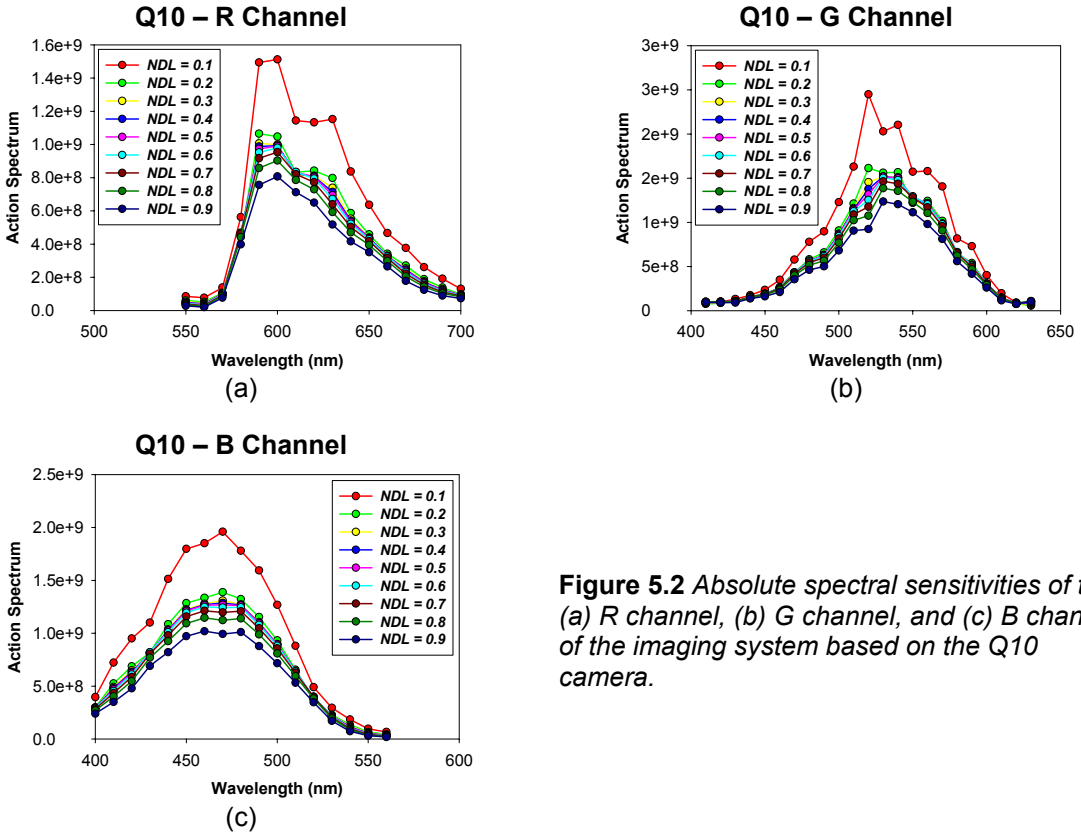

Figure 5.2 *Absolute spectral sensitivities of the (a) R channel, (b) G channel, and (c) B channel of the imaging system based on the Q10 camera.*

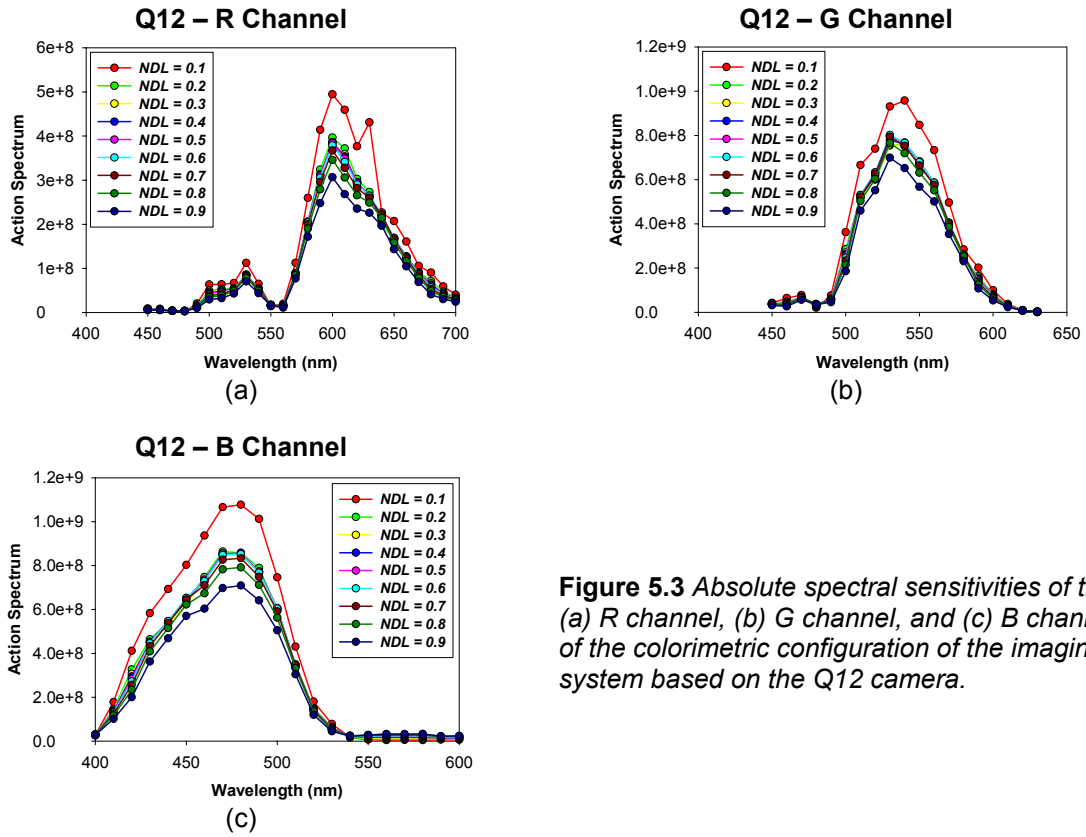

Figure 5.3 *Absolute spectral sensitivities of the (a) R channel, (b) G channel, and (c) B channel of the colorimetric configuration of the imaging system based on the Q12 camera.*

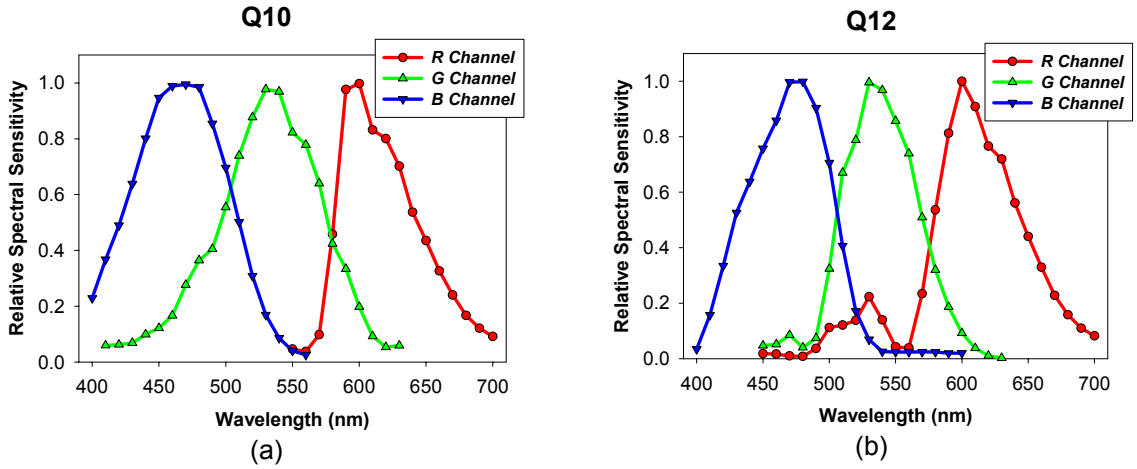

Figure 5.4 *Relative spectral sensitivities of (a) the imaging system based on the Q10 camera, and (b) the colorimetric configuration of the imaging system based on the Q12 camera.*

Finally, the absolute spectral sensitivities normalized to 1, for a sweep, in this case of *NDL* values avoiding the extreme values corresponding to background noise and saturation, are superimposed giving rise to a unique and common spectral profile, which is known as relative spectral sensitivity. The relative spectral sensitivities obtained for the imaging system based on the Q10 camera, and of the colorimetric configuration of the imaging system based on the Q12 camera are presented in Figure 5.4.

5.2 Colorimetric characterization based on the spectral sensitivities of the imaging system

Once the relative spectral sensitivities of the imaging system are obtained through its previous spectral characterization, the pseudo-colour matching functions are calculated starting from the relative spectral sensitivities, and considering the relative joint scaling and the equal-energy white balance of the relative spectral sensitivities, for all acquisition channels.

5.2.1 Relative joint scaling of the relative spectral sensitivities of the imaging system

The wavelength corresponding to the maximum absolute spectral sensitivity is determined for each acquisition channel. The channel with the greatest maximum of absolute spectral sensitivity is chosen as the reference channel. Considering the radiometric formalism used in the spectral characterization of the imaging system (equation (2.7)), the digital levels corresponding to an equal-energy stimulus **E**, with a range of exposure values H_E so that the digital levels obtained are placed within the background noise level and the saturation level, are calculated for each acquisition channel.

The slopes of the linear fittings by least squares of the digital levels of the acquisition channels different from the reference one, plotted versus the digital levels of the reference acquisition channel give the joint normalization of the relative spectral sensitivities of the imaging system. Finally, the joint scaled relative spectral sensitivities are obtained scaling the initial relative spectral sensitivities by means of the previously determined parameters of the relative joint scaling.

Results obtained for the imaging system based on the Q10 camera, and the colorimetric configuration (3 acquisition channels) of the imaging system based on the Q12 camera are presented in Table 5.2 and in Figures 5.5 and 5.6.

Table 5.2 *Wavelength of maximum absolute spectral sensitivity in terms of the action spectra (λ_{max}), maximum absolute spectral sensitivity ($a_{\lambda max}$), and parameters of the linear fitting by least squares ($y = p \cdot x + b$) of the digital levels of the acquisition channels different from the reference one, plotted versus the digital levels of the reference acquisition channel, for the imaging system based on the Q10 camera, and the colorimetric configuration (3 acquisition channels) of the imaging system based on the Q12 camera).*

		λ_{max} (nm)	$a_{\lambda max}$	*p*	*b*	r^2
Q10	***R Channel***	600	1.512E+09	0.7786	1.8135	0.9985
	G Channel	520	1.959E+09	0.9732	10.985	0.9987
	B Channel	470	2.449E+09	1	0	1

		λ_{max} (nm)	$a_{\lambda max}$	*p*	*b*	r^2
Q12	***R Channel***	600	4.946E+08	0.4186	8.4013	0.9994
	G Channel	540	9.574E+08	0.9044	2.1386	0.9995
	B Channel	480	1.077E+09	1	0	1

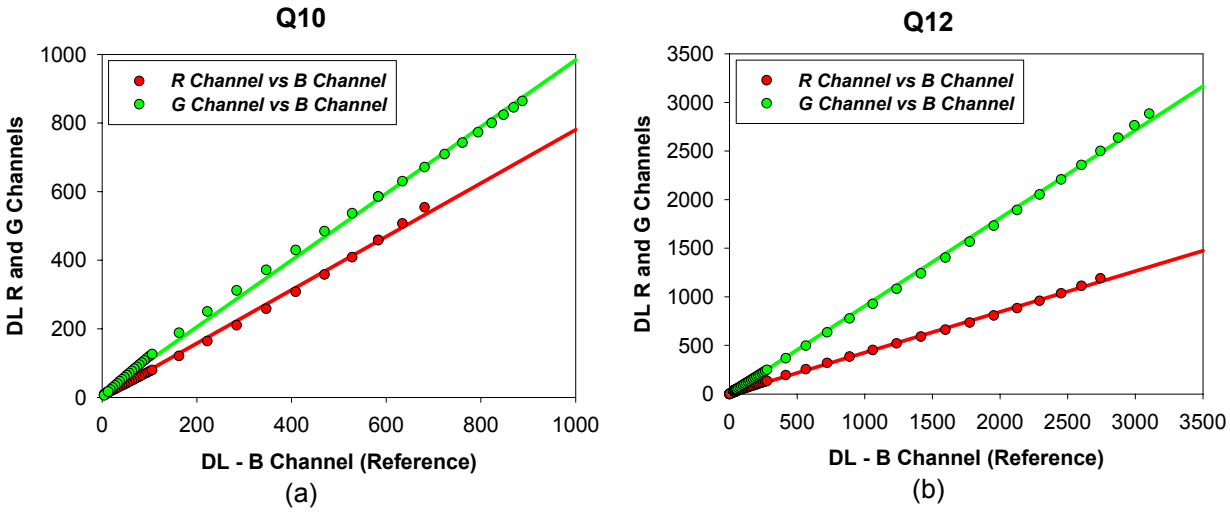

Figure 5.5. *Linear fitting by least squares ($y = p \cdot x + b$) of the digital levels (DL) of the acquisition channels different from the reference one plotted versus the digital levels of the reference acquisition channel, for (a) the imaging system based on the Q10 camera, and (b) the colorimetric configuration (3 acquisition channels) of the imaging system based on the Q12 camera.*

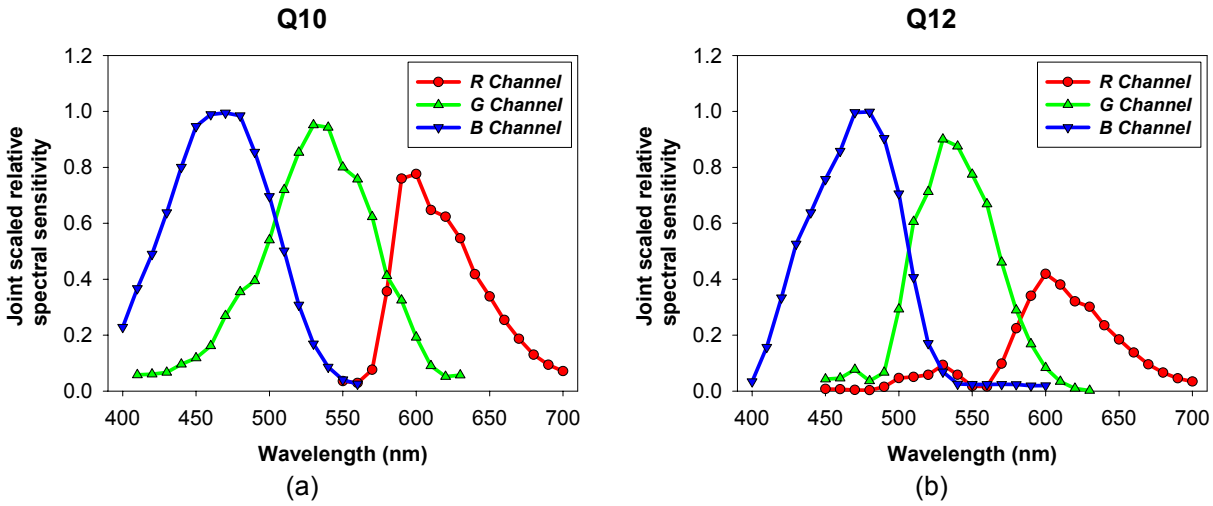

Figure 5.6 *Joint scaled relative spectral sensitivities for (a) the imaging system based on the Q10 camera, and (b) the colorimetric configuration (3 acquisition channels) of the imaging system based on the Q12 camera.*

5.2.2 Equal-energy white balance of the joint scaled relative spectral sensitivities of the imaging system

The equal-energy white balance consists of performing a new scaling on the joint scaled relative spectral sensitivities depending on the chromatic response to an equal-energy stimulus **E**, independently of the absolute radiance level.

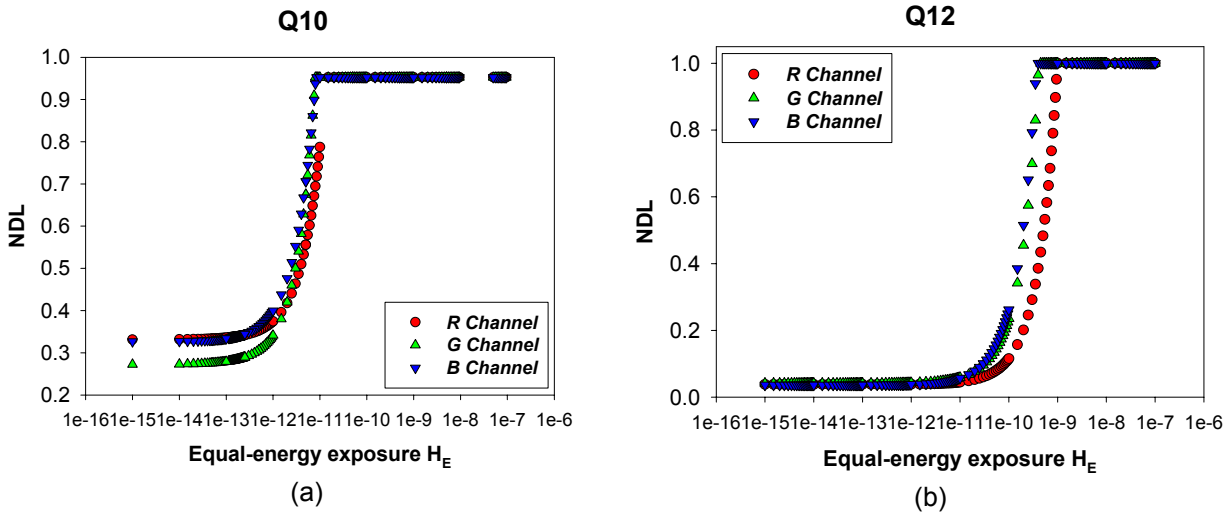

Figure 5.7 *Calculated pseudo-tristimulus values (normalized digital levels, NDL) plotted versus the equal-energy exposure levels H_E considered for (a) the imaging system based on the Q10 camera, and (b) the colorimetric configuration (3 acquisition channels) of the imaging system based on the Q12 camera.*

The pseudo-tristimulus values (normalized digital levels, NDL) are calculated for each acquisition channel considering an exposure corresponding to an equal-energy stimulus **E** ($H_\lambda = H_E \ \forall \ \lambda$), the radiometric formalism used in the spectral characterization (equations (2.11) and (2.12)), and the spectraradiometric data ($a_{\lambda k}$, $b_{\lambda k}$, $c_{\lambda k}$, and $d_{\lambda k}$ parameters) previously

obtained from the OESCFs. Plotting the calculated pseudo-tristimulus values versus the exposure levels H_E considered for the equal-energy stimulus allows one to determine the most sensitive acquisition channel, since it is the first in reaching saturation (Figure 5.7). The most sensitive acquisition channel is chosen to be the reference acquisition channel in this equal-energy white balance.

The calculated pseudo-tristimulus values for the three acquisition channels are related linearly between channels within the background noise level and the saturation level (Figure 5.8). The slopes of the linear fittings by least squares of the normalized digital levels of the acquisition channels different from the reference one, plotted versus the normalized digital levels of the reference acquisition channel, give the parameters of the real white balance of the device $bal_R : bal_G : bal_B$, being $bal_{kref-E} = 1$ (Table 5.3).

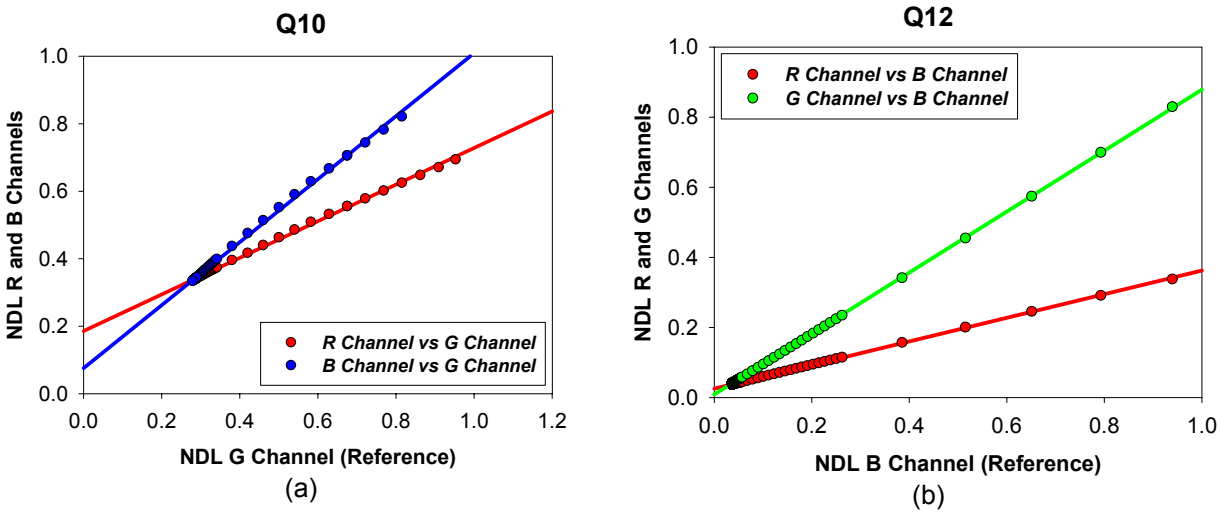

Figure 5.8 *Linear fitting by least squares (y = bal·x + b) of the normalized digital levels of the acquisition channels different from the reference one, plotted versus the normalized digital levels of the reference acquisition channel for (a) the imaging system based on the Q10 camera, and (b) the colorimetric configuration (3 acquisition channels) of the imaging system based on the Q12 camera.*

Table 5.3 *Parameters of the linear fitting by least squares (y = bal·x + b) of the normalized digital levels of the acquisition channels different from the reference one, plotted versus the normalized digital levels of the reference acquisition channel for (a) the imaging system based on the Q10 camera, and (b) the colorimetric configuration (3 acquisition channels) of the imaging system based on the Q12 camera.*

	Q10				Q12		
	R	***G***	***B***		***R***	***G***	***B***
bal	0.5427	1	0.9337	***bal***	0.3293	0.8809	1
b	0.1856	0	0.0757	***b***	0.0259	0.0092	0
$\mathbf{r^2}$	0.9991	1	0.9989	$\mathbf{r^2}$	0.9998	1.0000	1

In order to obtain the pseudo-colour matching functions of the imaging system from the relative spectral sensitivities, the equal-energy white balance is applied to the joint scaled relative spectral sensitivities in the way described by equations (2.13), (2.14), and (2.15).

Once the pseudo-colour matching functions (Figure 5.9) are determined, it is necessary to determine the real scaling factor, i.e. relative to the absolute scaling of the colour

matching functions, for each acquisition channel. With this aim, firstly, the basic colorimetric profile of the imaging system **M** is determined. Following the procedure described in sub-section 2.4.1.1, the basic colorimetric profiles of the imaging system based on the Q10 camera, and the colorimetric configuration (3 acquisition channels) of the imaging system based on the Q12 camera are determined. The tristimulus values of the colour samples of the GretagMacbeth ColorChecker DC (CCDC) chart placed in a light booth (section 3.3), and using incandescent lamps as illuminant, are estimated from the basic colorimetric profile of the imaging system (equation (2.21)).

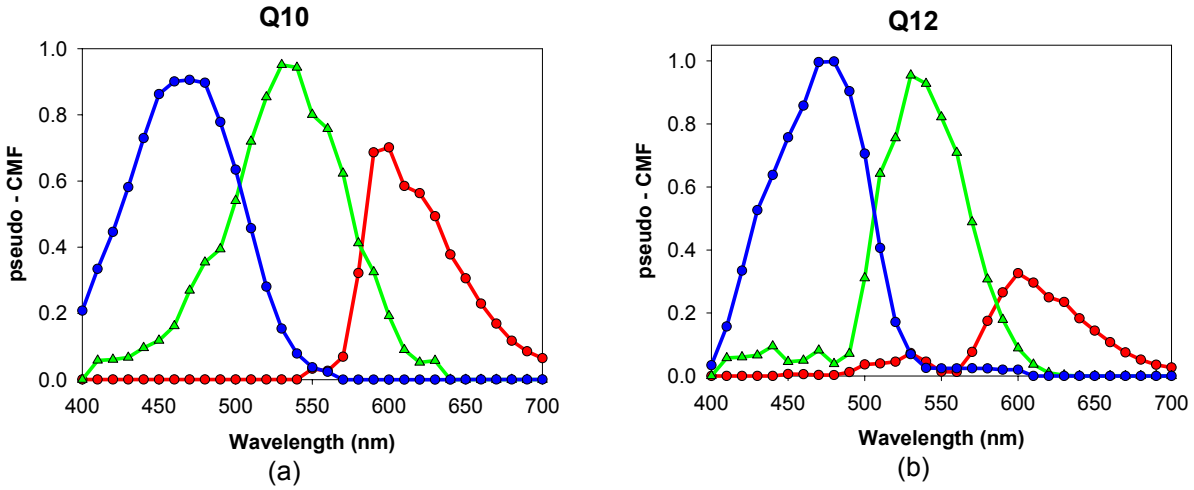

Figure 5.9 *Pseudo-colour matching functions (CMFs) of (a) the imaging system based on the Q10 camera, and (b) the colorimetric configuration (3 acquisition channels) of the imaging system based on the Q12 camera.*

The comparison between the estimated tristimulus values and the measured ones using a tele-spectracolorimeter, shows that a colour compensation is needed to improve the colorimetric estimation provided by the model so far. A linear colour compensation model derived from the linear fitting by least squares of the measured tristimulus values versus the estimated ones (Figure 5.10) is applied to the estimated tristimulus values (equation (2.22)).

The linear colour compensation model allows one to determine an offset tristimulus vector $\mathbf{A}_C$, which describes the systematic colour deviations of the device, and a diagonal scaling matrix $\mathbf{B}_C$ that allows to obtain the definitive scaling of the pseudo-colour matching functions of the imaging system and the raw colorimetric profile.

After applying the linear colour compensation model, the accuracy of the estimation of the XYZ tristimulus values is analyzed in terms of the mean, minimum, maximum and standard deviation values of the CIELAB colour differences for the colour samples of the CCDC chart. As can be observed from Table 5.4, very large CIELAB colour difference values are obtained for most of the colour samples of the CCDC chart for the two imaging systems considered, leading to notably large mean, minimum, maximum and standard deviation values. These large results are probably due to the fact that, despite of all the steps on this method resulted to be very clear conceptually, their application involve several fittings of experimental data and simulations using parameters obtained from these fittings, which make it possible a considerably amount of errors to be easily accumulated on the estimations of the XYZ tristimulus values.

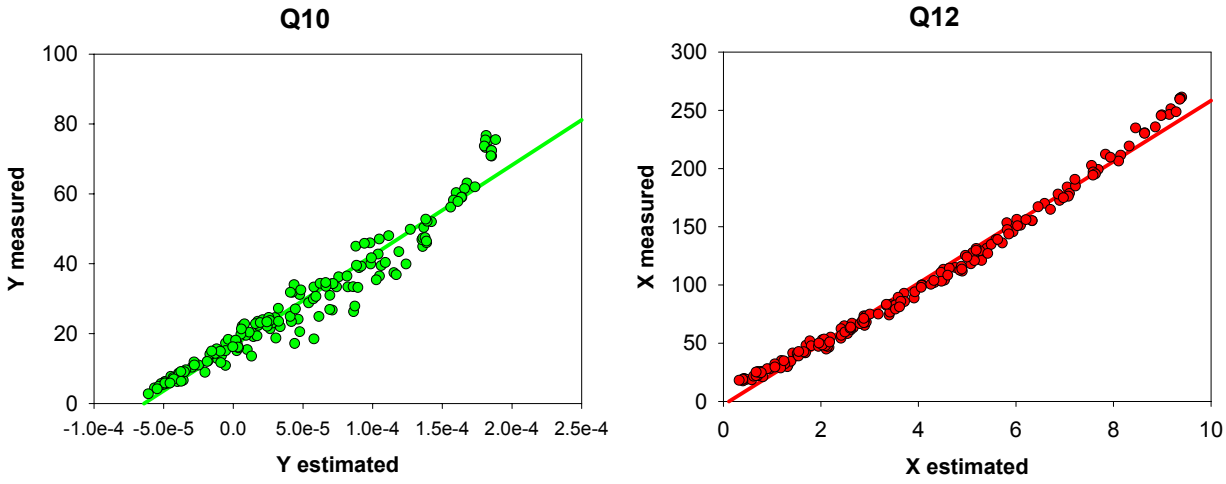

	a	*b*	r^2
X	2.036E+05	23.61	0.9607
Y	2.583E+05	16.56	0.9466
Z	3.563E+05	22.83	0.9290

(a)

	a	*b*	r^2
X	26.14	-2.966	0.9885
Y	25.43	-2.878	0.9828
Z	56.89	2.325	0.9700

(b)

Figure 5.10 *Parameters of the linear fitting by least squares (y = ax + b) of the measured vs estimated XYZ tristimulus values of the colour samples of the CCDC chart, and plots of (a) Y tristimulus values for the imaging system based on the Q10 camera, and (b) X tristimulus values for the colorimetric configuration (3 acquisition channels) of the imaging system based on the Q12 camera.*

Table 5.4 *Mean, minimum, maximum, and standard deviation values of the CIELAB colour differences for the colour samples of the CCDC chart using the imaging systems based on the Q10 and Q12 cameras.*

	Q10	**Q12**
mean ΔE^*_{ab}	10.92	10.17
minimum ΔE^*_{ab}	1.456	0.2810
maximum ΔE^*_{ab}	47.77	38.41
std. dev. ΔE^*_{ab}	8.167	8.408

Finally, as it was expected, slightly better results are achieved using the colorimetric configuration of the imaging system based on the 12-bits CCD camera than using the imaging system based on the 10-bits CCD camera.

6 Comparison of Methods for Colour Measurement and Spectral Reconstruction

In this section, some of the most commonly used methods for colour measurement and spectral reconstruction are compared in order to determine the most suitable one for each of the two configurations of the imaging system based on the QImaging QICAM Fast 1394 12 bits cooled monochrome CCD camera: the colorimetric configuration, with three acquisition channels, and the multispectral configuration, with seven acquisition channels.

Methods for colour measurement are usually known as methods for colorimetric characterization. The colorimetric characterization of an imaging system based on a CCD camera is the process by means of which the transformation that defines the correspondence between the digital responses of the imaging system for all acquisition channels used, and a colour space independent of the device, such as the CIE 1931 XYZ colour space, is derived allowing to perform colour measurements through an imaging system based on a CCD camera. Three methods for colour measurement are compared in this section: the first one is based on the spectral sensitivities (SSs) of the imaging system and it is thoroughly described in sub-section 2.4.1.1. The other two methods for colour measurement compared are based on measuring a training set using both a tele-spectracolorimeter (PhotoResearch PR650) and the imaging system. In these methods, the XYZ tristimulus values associated to each colour sample of the training set are related to the corresponding digital responses of the imaging system by means of a transformation matrix. In the first of these methods, that will be called the pseudoinverse method for XYZ (PSE_{XYZ}), the transformation matrix relates the XYZ tristimulus values with the digital responses of the imaging system, and is determined by applying the Moore-Penrose pseudoinverse. In the second of these methods, that will be called the second order non-linear method for XYZ ($NLIN(2)_{XYZ}$), the transformation matrix relates the XYZ tristimulus values with a second order polynomial of the digital responses of the imaging system, and is determined also by applying the Moore-Penrose pseudoinverse. The Moore-Penrose pseudoinverse, and the PSE_{XYZ} and the $NLIN(2)_{XYZ}$ methods are also thoroughly described in sub-sections 2.4.1.2.1, 2.4.1.2.2 and 2.4.1.2.3, respectively.

Regarding the methods for spectral reconstruction, their main objective is to reconstruct the reflectance or radiance spectrum of a colour sample from the corresponding digital responses of the imaging system. In this case also three methods are compared, all of them based on the measurement of a training set using both a tele-spectracolorimeter (PhotoResearch PR650) and the imaging system. In the first method, that will be called the pseudoinverse method (PSE), the transformation matrix relates the reflectance spectra of the colour samples with the corresponding digital responses of the imaging system, and is determined by applying the Moore-Penrose pseudoinverse. In the second method, that will be called the second order non-linear method (NLIN(2)), the transformation matrix relates the reflectance spectra of the colour samples with a second order polynomial of the corresponding digital responses of the imaging system, and is determined also by applying the Moore-Penrose pseudoinverse. The third method compared is the Principal Component Analysis (PCA). In this method, a principal component analysis is performed on the matrix of reflectance spectra of the colour samples of the training set, obtaining the PCA basis and the

coefficients of the reflectance spectra on this PCA basis. These coefficients are related to the digital responses of the imaging system by means of a transformation matrix that is determined by applying the Moore-Penrose pseudoinverse. Therefore, this transformation matrix allow to calculate the coefficients of any colour sample on the PCA basis from its digital responses of the imaging system, and the linear combination of the vectors of the PCA basis with the coefficients calculated provides an estimation of the reflectance spectrum of the colour sample. The PCA method is further described in sub-section 2.4.2.3.

Considering the methods for colour measurement, the method based on the spectral sensitivities (SS) of the imaging system is only applied to the colorimetric configuration of the imaging system due to the high complexity in calculations that involves and the low accuracy achieved, and only the PSE_{XYZ} and the $NLIN(2)_{XYZ}$ methods for colour measurement are applied to the multispectral configuration. The system's performance resulting for each method applied is evaluated in terms of the accuracy of colour measurement by means of the mean, minimum, maximum and standard deviation of the CIELAB colour difference values obtained for the test set.

Regarding the methods for spectral reconstruction, the three methods mentioned ire applied to both configurations. In this case, the system's performance resulting for each method applied is evaluated in terms of the accuracy of both colour measurement and spectral reconstruction, by means of the mean, minimum, maximum and standard deviation of the CIELAB colour difference values and of the RMSE values obtained for the test set, respectively.

All possible combinations of the GretagMacbeth ColorChecker Color Rendition chart (CCCR) and the GretagMacbeth ColorChecker DC chart (CCDC) are used as training and test sets of the imaging system.

Next, results obtained applying the methods for colour measurement and for spectral reconstruction mentioned are presented for the two configurations of the imaging system.

6.1 Colorimetric Configuration

6.1.1 Methods for colour measurement

Results obtained for the colorimetric configuration, applying the method based on the spectral sensitivities (SS) of the imaging system, the pseudoinverse method for XYZ (PSE_{XYZ}), and the second order non-linear method for XYZ ($NLIN(2)_{XYZ}$) for colour measurement, are presented in Table 6.1 and Figure 6.1.

As can be straight observed from Figure 6.1, the best results are obtained using the $NLIN(2)_{XYZ}$ method, followed by the PSE_{XYZ} method, and the method based on SS. Using this last method, very large CIELAB colour difference values are obtained for most of the colour samples of the charts used as test sets, for all possible combinations of the GretagMacbeth ColorChecker (CC) charts, leading to notably large mean, minimum, maximum and standard deviation values (Table 6.1). As it was previously said in chapter 6, these large results are probably due to the fact that, despite of all the steps on this method resulted to be very clear conceptually, their application involved several fittings of experimental data and simulations using parameters obtained from these fittings, which make it possible a considerably amount of errors to be easily accumulated on the estimations of the XYZ tristimulus values.

In case of the PSE_{XYZ} method, a least squares fitting between the matrix of digital responses associated to the colour samples of the training set (a 3xN matrix, being 3 the number of acquisition channels of the colorimetric configuration and N the number of

samples of the training set) and the matrix of the XYZ tristimulus values of the colour samples of the training set (a 3x*N* matrix, being 3 the XYZ tristimulus values of the colour samples and *N* the number of colour samples of the training set) is performed applying the Moore-Penrose pseudoinverse, obtaining the *3x3* transformation matrix that relates both sets of data. As it was expected, best results are obtained when the same set is used as training and test than using different sets as training and test sets (Table 6.1). Specifically, the best results are obtained using the CCDC chart as training and test set.

Table 6.1 *Colorimetric Configuration: mean, minimum, maximum and standard deviation of the CIELAB colour difference values obtained using all possible combinations of the CC charts as training and test sets, and applying the method based on the spectral sensitivities (SS), the pseudo-inverse method for XYZ (PSE_{XYZ}), and the second order non-linear method for XYZ ($NLIN(2)_{XYZ}$).*

	Training	**CCDC**	**CCDC**	**CCCR**	**CCCR**
	Test	**CCDC**	**CCCR**	**CCCR**	**CCDC**
SS	**mean ΔE^*_{ab}**	12.112	48.989	27.007	27.218
	min ΔE^*_{ab}	1.365	5.026	2.698	3.769
	max ΔE^*_{ab}	71.814	180.463	57.554	141.053
	std. dev.	13.344	48.427	15.203	22.237

	Training	**CCDC**	**CCDC**	**CCCR**	**CCCR**
	Test	**CCDC**	**CCCR**	**CCCR**	**CCDC**
PSE_{XYZ}	**mean ΔE^*_{ab}**	4.264	6.573	4.999	5.106
	min ΔE^*_{ab}	0.492	2.395	0.796	1.076
	max ΔE^*_{ab}	12.380	12.435	12.015	12.243
	std. dev.	2.717	3.065	3.370	2.284

	Training	**CCDC**	**CCDC**	**CCCR**	**CCCR**
	Test	**CCDC**	**CCCR**	**CCCR**	**CCDC**
$NLIN(2)_{XYZ}$	**mean ΔE^*_{ab}**	2.734	5.196	3.188	5.123
	min ΔE^*_{ab}	0.374	2.163	0.457	0.702
	max ΔE^*_{ab}	9.085	10.335	9.334	17.861
	std. dev.	1.984	2.053	2.366	2.685

Regarding the $NLIN(2)_{XYZ}$ method, a least squares fitting between the matrix of the second order polynomials of the digital responses associated to the colour samples of the training set (a 10x*N* matrix, being 10 the number of components of the second order polynomial having 3 acquisition channels and *N* the number of samples of the training set) and the matrix of the XYZ tristimulus values of the colour samples of the training set is performed applying the Moore-Penrose pseudoinverse, obtaining the 3x10 transformation matrix that relates both sets of data. In this case, results obtained using the same chart as training and test set are outstandingly better than those obtained using different charts as training and test sets (Table 6.1). Just as for the PSE_{XYZ} method, the best results are obtained using the CCDC chart as training and test sets. On the other hand, quite similar results are obtained in average (mean ± std. dev.) using different charts as training and test sets. Comparing results obtained using the PSE_{XYZ} and the $NLIN(2)_{XYZ}$ methods, similar results are obtained applying both methods when different charts are used as training and test sets,

although best results are obtained applying the $NLIN(2)_{XYZ}$ method when the same chart is used as training and test set (Table 6.1, Figure 6.1).

Taking all these results into account it can be concluded that the most advisable methods for colour measurement for the colorimetric configuration would be the $NLIN(2)_{XYZ}$ and the PSE_{XYZ} methods. Both of them are recommended due to the fact that both lead to similar results when different sets of colour samples are used as training and test sets, which will be the more common situation for an imaging system that is going to be used as an instrument for colour measurement: colour samples to be measured, although being the same kind, could be different from the specific colour samples used to train the imaging system.

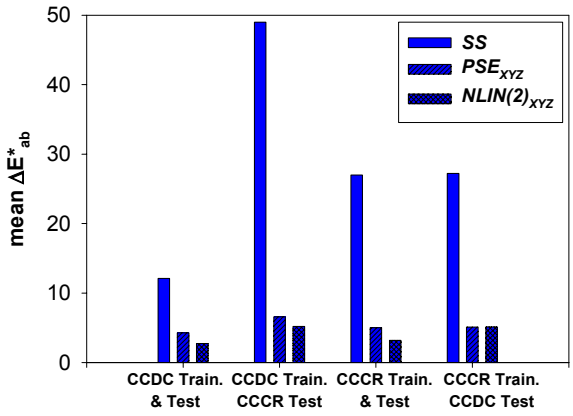

Figure 6.1 *Colorimetric Configuration: Bar plot of the mean CIELAB colour difference values obtained using all possible combinations of the CC charts as training and test sets, and applying the methods for colour measurement: the method based on the spectral sensitivities (SS), the pseudo-inverse method for XYZ (PSE_{XYZ}), and the second order non-linear method for XYZ ($NLIN(2)_{XYZ}$).*

6.1.2 Methods for spectral reconstruction

Results obtained for the colorimetric configuration, applying the pseudoinverse method (PSE), the second order non-linear method (NLIN(2)), and the principal component analysis method (PCA) for spectral reconstruction, are presented in Tables 6.2 and 6.3, and in Figure 6.2. These results are analyzed both in terms of accuracy of colour measurement (CIELAB colour difference values, Table 6.2 and Figure 6.2 (a)) and in terms of accuracy of spectral reconstruction (RMSE values, Table 6.3 and Figure 6.2 (b)).

In case of the PSE method, a least squares fitting between the matrix of digital responses associated to the colour samples of the training set (a 3x*N* matrix, being 3 the number of acquisition channels of the colorimetric configuration and *N* the number of samples of the training set) and the matrix of the reflectance spectra of the colour samples of the training set (a 41x*N* matrix, being 41 the number of wavelengths between 380nm and 780nm in steps of 10nm, and *N* the number of colour samples of the training set) is performed applying the Moore-Penrose pseudoinverse, obtaining the *41x3* transformation matrix that relates both sets of data.

Regarding the NLIN(2) method, a least squares fitting between the matrix of the second order polynomials of the digital responses associated to the colour samples of the training set (a 10x*N* matrix, being 10 the number of components of the second order polynomial having 3 acquisition channels and *N* the number of samples of the training set) and the matrix of the reflectance spectra of the colour samples of the training set (a 41x*N* matrix) is performed applying the Moore-Penrose pseudoinverse, obtaining the *41x10* transformation matrix that relates both sets of data.

In the PCA method, a principal component analysis is firstly performed on the matrix of reflectance spectra of the colour samples of the training set, obtaining the PCA basis and

the coefficients of the reflectance spectrum of each colour sample of the training set on this PCA basis. The number of vectors of the PCA basis, usually called principal vectors, considered as a basis of reflectance spectra is traditionally chosen in literature to be equal to the number of acquisition channels. Then, a least squares fitting between the matrix of digital responses associated to the colour samples of the training set (a *3xN* matrix) and the matrix of coefficients of the reflectance spectra of the colour samples of the training set on the PCA basis (a 3x*N* matrix, being 3 the number of acquisition channel and the number of vectors on the PCA basis, and *N* the number of colour samples of the training set) is performed applying the Moore-Penrose pseudoinverse, obtaining the *3x3* transformation matrix that relates both sets of data.

Considering the accuracy of colour measurement, the best results are obtained using the NLIN(2) method, followed by the PSE method, and the PCA method (Table 6.2, Figure 6.2 (a)). For the NLIN(2) method, the best results are obtained using the same CC chart as training and test set, specifically using the CCDC, and similar results are obtained for the other two combinations of different CC charts used as training and test set. For the PSE and the PCA methods, the best results are obtained using the CCDC chart as training and test set, and similar results are obtained for the rest of combinations of the CC charts used as training and test sets. Slightly better results are obtained using the PSE method than using the PCA method.

Table 6.2 *Colorimetric Configuration: mean, minimum, maximum and standard deviation of the CIELAB colour difference values obtained using all possible combinations of the CC charts as training and test sets, and applying the pseudo-inverse method (PSE), the second order non-linear method (NLIN(2)), and the principal component analysis method (PCA).*

	Training	**CCDC**	**CCDC**	**CCCR**	**CCCR**
	Test	**CCDC**	**CCCR**	**CCCR**	**CCDC**
PSE	**mean ΔE^*_{ab}**	5.020	7.275	6.051	5.193
	min ΔE^*_{ab}	0.545	0.907	0.548	0.647
	max ΔE^*_{ab}	17.142	19.117	17.224	14.899
	std. dev.	3.554	5.232	4.755	3.008
	Training	**CCDC**	**CCDC**	**CCCR**	**CCCR**
	Test	**CCDC**	**CCCR**	**CCCR**	**CCDC**
NLIN(2)	**mean ΔE^*_{ab}**	2.027	2.909	2.416	3.507
	min ΔE^*_{ab}	0.194	0.969	0.181	0.661
	max ΔE^*_{ab}	10.687	8.905	9.979	14.831
	std. dev.	1.630	1.817	2.190	2.284
	Training	**CCDC**	**CCDC**	**CCCR**	**CCCR**
	Test	**CCDC**	**CCCR**	**CCCR**	**CCDC**
PCA	**mean ΔE^*_{ab}**	5.609	8.068	7.457	6.241
	min ΔE^*_{ab}	0.513	0.765	0.427	0.907
	max ΔE^*_{ab}	17.470	20.519	18.975	18.659
	std. dev.	3.854	5.302	5.106	3.655

Considering the accuracy of spectral reconstruction, the best results are also obtained using the NLIN(2) method, followed by the PSE method, and the PCA method (Table 6.3,

Figure 6.2 (b)). The best results are obtained using the same chart as training and test set, specifically the CCDC chart, for the three methods. Just as in terms of accuracy of colour measurement, similar results are obtained for the rest of combinations of the CC charts used as training and test sets for the PSE and the PCA methods, and quite similar results are obtained using these two methods.

Table 6.3 *Colorimetric Configuration: mean, minimum, maximum and standard deviation of the RMSE values obtained using all possible combinations of the CC charts as training and test sets, and applying the pseudo-inverse method (PSE), the second order non-linear method (NLIN(2)), and the principal component analysis method (PCA).*

	Training	**CCDC**	**CCDC**	**CCCR**	**CCCR**
	Test	**CCDC**	**CCCR**	**CCCR**	**CCDC**
PSE	**mean RMSE**	4.576E-02	5.801E-02	5.296E-02	5.353E-02
	min RMSE	1.388E-02	3.158E-02	2.350E-02	1.685E-02
	max RMSE	17.16E-02	17.17E-02	16.24E-02	16.29E-02
	std. dev.	2.229E-02	2.891E-02	2.699E-02	2.376E-02

	Training	**CCDC**	**CCDC**	**CCCR**	**CCCR**
	Test	**CCDC**	**CCCR**	**CCCR**	**CCDC**
NLIN(2)	**mean RMSE**	1.492E-02	5.304E-02	4.564E-02	2.563E-02
	min RMSE	0.234E-02	2.244E-02	1.425E-02	0.445E-02
	max RMSE	8.153E-02	21.18E-02	16.93E-02	8.461E-02
	std. dev.	1.003E-02	3.793E-02	2.979E-02	1.464E-02

	Training	**CCDC**	**CCDC**	**CCCR**	**CCCR**
	Test	**CCDC**	**CCCR**	**CCCR**	**CCDC**
PCA	**mean RMSE**	4.682E-02	5.797E-02	5.453E-02	5.658E-02
	min RMSE	1.580E-02	3.557E-02	2.910E-02	1.893E-02
	max RMSE	17.00E-02	16.99E-02	16.00E-02	16.09E-02
	std. dev.	2.155E-02	2.770E-02	2.660E-02	2.498E-02

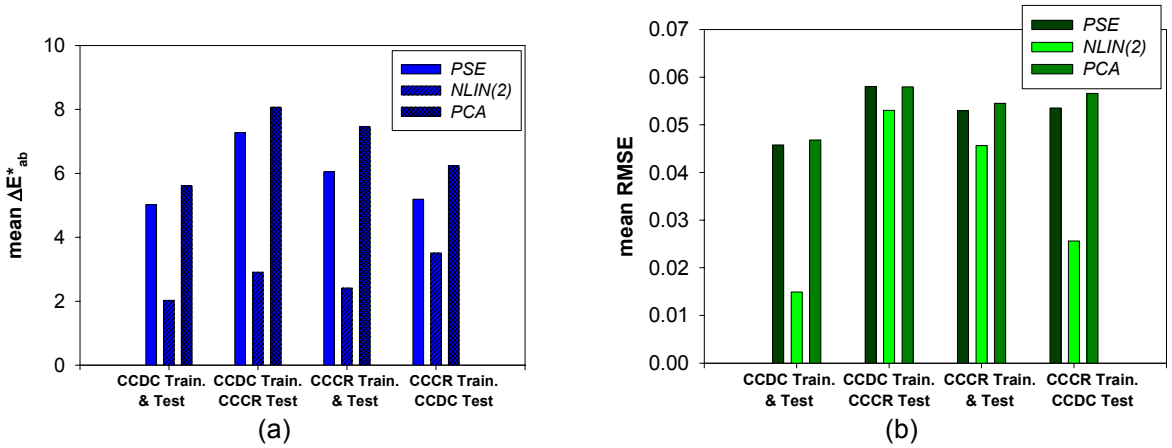

Figure 6.2 *Colorimetric Configuration: Bar plots of the mean (a) CIELAB colour difference values and (b) RMSE values obtained using all possible combinations of the CC charts as training and test sets, and applying the methods for spectral reconstruction: the pseudo-inverse method (PSE), the second order non-linear method (NLIN(2)), and the principal component analysis method (PCA).*

Taking all these results into account it can be concluded that the most advisable method for spectral reconstruction for the colorimetric configuration, both in terms of accuracy of colour measurement and spectral reconstruction, would be the NLIN(2), followed by the PSE and the PCA methods, which lead to similar results.

6.2 Multispectral Configuration

6.2.1 Methods for colour measurement

Results obtained for the multispectral configuration applying the pseudoinverse method for XYZ (PSE_{XYZ}) and the second order non-linear method for XYZ ($NLIN(2)_{XYZ}$) for colour measurement, are presented in Table 6.4 and Figure 6.3. The method based on the spectral sensitivity (SS) of the imaging system is not applied to the multispectral configuration of the imaging system due to the high complexity in calculations that involves and the low accuracy achieved.

In case of the PSE_{XYZ} method, the matrix of digital responses (a 7x*N* matrix, being 7 the number of acquisition channels, and *N* the number of colour samples of the training set) and the matrix of tristimulus values (a 3x*N* matrix) are related by the transformation matrix (a *3x7* matrix) obtained applying the Moore-Penrose pseudoinverse. Applying this method, the best results are obtained using the same CC chart as training and test set, specifically the CCDC chart (Table 6.4). Similar results are obtained for the two other combinations using different CC charts as training and test sets.

Table 6.4 *Multispectral Configuration: mean, minimum, maximum and standard deviation of the CIELAB colour difference values obtained using all possible combinations of the CC charts as training and test sets, and applying the pseudo-inverse method for XYZ (PSE_{XYZ}), and the second order non-linear method for XYZ ($NLIN(2)_{XYZ}$).*

	Training / ***Test***	**CCDC / CCDC**	**CCDC / CCCR**	**CCCR / CCCR**	**CCCR / CCDC**
PSE_{XYZ}	**mean ΔE^*_{ab}**	3.228	5.757	3.558	4.232
	min ΔE^*_{ab}	0.521	1.970	0.203	0.843
	max ΔE^*_{ab}	11.18	22.31	11.91	9.929
	std. dev.	2.286	4.212	3.169	1.870

	Training / ***Test***	**CCDC / CCDC**	**CCDC / CCCR**	**CCCR / CCCR**	**CCCR / CCDC**
$NLIN(2)_{XYZ}$	**mean ΔE^*_{ab}**	1.472	4.363	Non Applicable	Non Applicable
	min ΔE^*_{ab}	0.185	1.559		
	max ΔE^*_{ab}	6.188	14.429		
	std. dev.	1.088	2.768		

Regarding the $NLIN(2)_{XYZ}$ method, the matrix of digital responses (a 36x*N* matrix, being 36 the number components of the second order polynomial having 7 acquisition channels, and *N* the number of colour samples of the training set) and the matrix of tristimulus values (a 3x*N* matrix) are related by a transformation matrix (a *3x36* matrix) obtained applying the Moore-Penrose pseudoinverse. The Moore-Penrose pseudoinverse is not applicable when the column rank of the matrix to be pseudoinverted is lower than its row

rank. In case of the matrix of digital responses, the column rank is *N*, and the row rank is 36 for 7 acquisition channels. Consequently, the $NLIN(2)_{XYZ}$ method is not applicable when the number of colour samples of the training set is lower than the number of coefficients of the second order polynomial of the digital responses. This is the particular case of the CCCR, which has 24 colour samples, when it is used as training set. Using the CCDC chart (166 useful colour patches) as training set, the best results are also obtained using the same chart as test set, and these are outstandingly better than those obtained applying the PSE_{XYZ} method (Table 6.4, Figure 6.3). Results obtained using different CC charts as training and test sets are similar for both the PSE_{XYZ} method and the $NLIN(2)_{XYZ}$ method, when applicable.

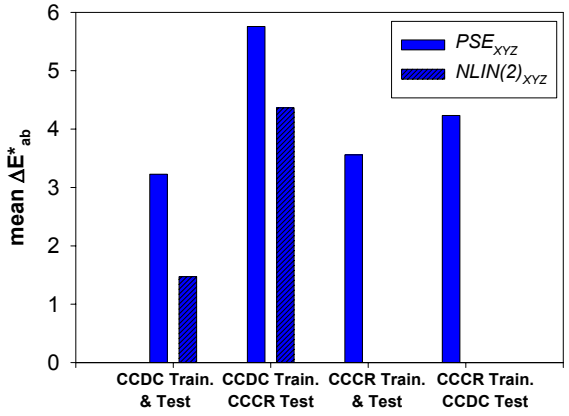

Figure 6.3 *Multispectral Configuration: Bar plot of the mean CIELAB colour difference values obtained using all possible combinations of the CC charts as training and test sets, and applying the methods for colour measurement: the pseudo-inverse method for XYZ (PSE_{XYZ}), and the second order non-linear method for XYZ ($NLIN(2)_{XYZ}$).*

In spite of the fact that the $NLIN(2)_{XYZ}$ method leads to better results when applicable (Table 6.4), having restrictions on the minimum number of colour samples of the training set depending on the number of acquisition channels of the imaging system seriously limits its applicability. This is the case, for instance, of analyzing the influence of the number of samples of the training set on system's performance (chapter 8), or the influence of colour ranges on system's performance (chapter 9), which require to work with a variable and sometimes low number of samples. Consequently, it can be concluded that the most advisable method for colour measurement for the multispectral configuration would be the PSE_{XYZ} method.

Comparing both configurations of the imaging system, better results are obtained using the same PSE_{XYZ} and $NLIN(2)_{XYZ}$ methods for the multispectral configuration than for the colorimetric configuration (Tables 6.1 and 6.4).

6.2.2 Methods for spectral reconstruction

The same methods for spectral reconstruction applied to the colorimetric configuration are also applied to the multispectral configuration: the pseudoinverse method (PSE), the second order non-linear method (NLIN(2)), and the principal component analysis method (PCA). Results obtained for the multispectral configuration applying these methods are presented in Tables 6.5 and 6.6, and in Figure 6.4. These results are analyzed both in terms of accuracy of colour measurement (CIELAB colour difference values, Table 6.5 and Figure 6.4 (a)) and in terms of accuracy of spectral reconstruction (RMSE values, Table 6.6 and Figure 6.4 (b)).

In case of the PSE method, the matrix of digital responses (a *7xN* matrix) and the matrix of the reflectance spectra of the colour samples of the training set (a *41xN* matrix) are

related by a transformation matrix (a *41x7* matrix) obtained applying the Moore-Penrose pseudoinverse.

Regarding the NLIN(2) method, the matrix of the second order polynomial of digital responses (a *36xN* matrix) and the matrix of the reflectance spectra of the colour samples of the training set (a *41xN* matrix) are related by a transformation matrix (a *41x36* matrix) obtained applying the Moore-Penrose pseudoinverse. Just as for the $NLIN(2)_{XYZ}$ method, the NLIN(2) method is not applicable when the CCCR chart is used as training set.

In the PCA method, after performing the principal component analysis on the matrix of reflectance spectra of the colour samples on the training set, the matrix of digital responses associated to the colour samples of the training set (a *7xN* matrix) and the matrix of coefficients on the PCA basis of the colour samples of the training set (a *7xN* matrix, being 7 the number of acquisition channel and the number of principal vectors on the PCA basis, and *N* the number of colour samples of the training set) are related by a transformation matrix (a *7x7* matrix) obtained applying the Moore-Penrose pseudoinverse.

Considering the accuracy of colour measurement, the best results are obtained using the NLIN(2) method, when applicable, followed by the PSE and the PCA methods (Table 6.5, Figure 6.4 (a)). The best results are obtained using the same CC chart as training and test set, specifically using the CCDC, for the three methods. Quite similar results are obtained for the PSE and the PCA methods for all combinations of the CC charts considered.

Table 6.5 *Multispectral Configuration: mean, minimum, maximum and standard deviation of the CIELAB colour difference values obtained using all possible combinations of the CC charts as training and test sets, and applying the pseudo-inverse method (PSE), the second order non-linear method (NLIN(2)), and the principal component analysis method (PCA).*

	Training	**CCDC**	**CCDC**	**CCCR**	**CCCR**
	Test	**CCDC**	**CCCR**	**CCCR**	**CCDC**
PSE	**mean ΔE^*_{ab}**	3.266	5.407	3.680	3.645
	min ΔE^*_{ab}	0.234	0.946	0.242	0.528
	max ΔE^*_{ab}	11.49	20.12	12.44	10.61
	std. dev.	2.556	4.271	3.046	2.157
	Training	**CCDC**	**CCDC**	**CCCR**	**CCCR**
	Test	**CCDC**	**CCCR**	**CCCR**	**CCDC**
NLIN(2)	**mean ΔE^*_{ab}**	0.772	1.810	Non Applicable	Non Applicable
	min ΔE^*_{ab}	0.101	1.054		
	max ΔE^*_{ab}	2.741	2.619		
	std. dev.	0.442	0.486		
	Training	**CCDC**	**CCDC**	**CCCR**	**CCCR**
	Test	**CCDC**	**CCCR**	**CCCR**	**CCDC**
PCA	**mean ΔE^*_{ab}**	3.349	5.463	3.831	3.759
	min ΔE^*_{ab}	0.103	1.088	0.492	0.477
	max ΔE^*_{ab}	12.12	21.65	12.45	10.41
	std. dev.	2.558	4.500	3.201	2.185

Just as for the methods for colour measurement, comparing both configurations of the imaging system, better results in terms of accuracy of colour measurement are obtained using

the same PSE method and NLIN(2) method, when applicable, for the multispectral configuration than for the colorimetric configuration (Tables 6.2 and 6.5).

Considering the accuracy of spectral reconstruction, the best results are also obtained using the NLIN(2) method, when applicable, followed by the PSE and the PCA methods (Table 6.6, Figure 6.4 (b)). The best results are also obtained using the same chart as training and test set, specifically the CCDC chart, for the three methods. Just as in terms of accuracy of colour measurement, similar results are obtained for the rest of combinations of the CC charts as training and test sets for the PSE and the PCA methods. Quite similar results are also obtained for these two methods for all combinations of the CC charts considered.

Taking these results into account, it can be concluded that the most advisable methods for spectral reconstruction for the multispectral configuration, in terms of both the accuracy of colour measurement and the accuracy of spectral reconstruction, would be the PSE and the PCA methods. Just as for the methods for colour measurement, although the NLIN(2) method leads to better results when applicable, it is not advised due to its restrictions on the minimum number of colour samples of the training set depending on the number of acquisition channels of the imaging system, which limit its applicability in some of the analysis performed further on this work.

Also in this case, comparing both configurations of the imaging system, better results in terms of accuracy of both colour measurement and spectral reconstruction are obtained using the same PSE, NLIN(2) and PCA methods for the multispectral configuration than for the colorimetric configuration (Tables 6.3 and 6.6).

Table 6.6 *Multispectral Configuration: mean, minimum, maximum and standard deviation of the RMSE values obtained using all possible combinations of the CC charts as training and test sets, and applying the pseudo-inverse method (PSE), the second order non-linear method (NLIN(2)), and the principal component analysis method (PCA).*

	Training / ***Test***	**CCDC** / **CCDC**	**CCDC** / **CCCR**	**CCCR** / **CCCR**	**CCCR** / **CCDC**
PSE	**mean RMSE**	2.942E-02	4.506E-02	2.949E-02	3.966E-02
	min RMSE	0.716E-02	2.358E-02	1.180E-02	1.269E-02
	max RMSE	10.51E-02	7.173E-02	6.591E-02	10.44E-02
	std. dev.	1.296E-02	1.200E-02	1.559E-02	2.246E-02

	Training / ***Test***	**CCDC** / **CCDC**	**CCDC** / **CCCR**	**CCCR** / **CCCR**	**CCCR** / **CCDC**
NLIN(2)	**mean RMSE**	0.732E-02	4.163E-02	Non Applicable	Non Applicable
	min RMSE	0.162E-02	1.599E-02		
	max RMSE	5.049E-02	9.528E-02		
	std. dev.	0.533E-02	2.055E-02		

	Training / ***Test***	**CCDC** / **CCDC**	**CCDC** / **CCCR**	**CCCR** / **CCCR**	**CCCR** / **CCDC**
PCA	**mean RMSE**	3.046E-02	4.588E-02	3.057E-02	4.059E-02
	min RMSE	0.848E-02	2.450E-02	1.286E-02	1.224E-02
	max RMSE	10.55E-02	7.251E-02	6.561E-02	10.63E-02
	std. dev.	1.283E-02	1.256E-02	1.496E-02	2.221E-02

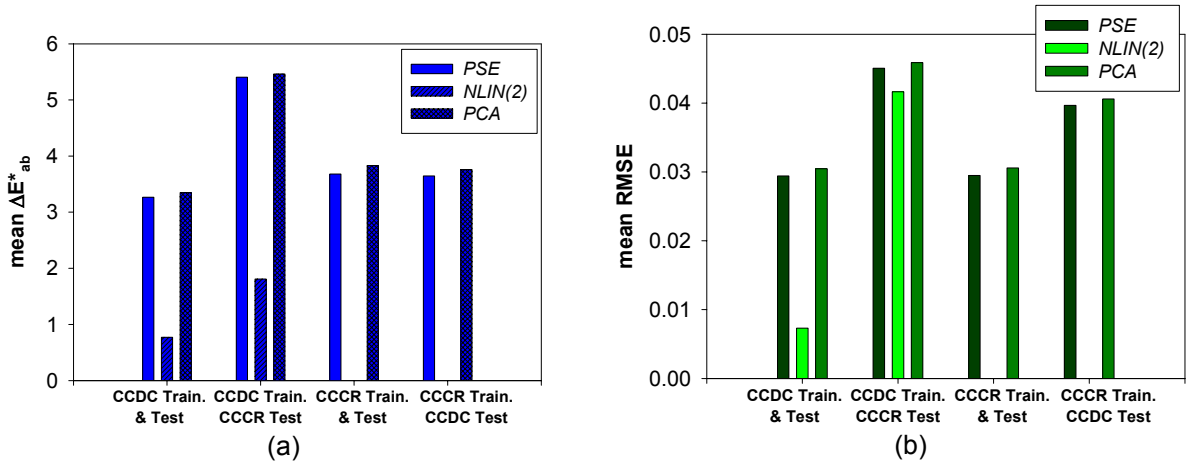

Figure 6.4 *Multispectral Configuration: Bar plots of the mean (a) CIELAB colour difference values and (b) RMSE values obtained using all possible combinations of the CC charts as training and test sets, and applying the methods for spectral reconstruction: the pseudo-inverse method (PSE), the second order non-linear method (NLIN(2)), and the principal component analysis method (PCA).*

Once the most commonly used methods for colour measurement and spectral reconstruction are compared for the colorimetric and the multispectral configurations of the imaging system, the methods that will be used from here on for each configuration are selected taking into account both results obtained and some additional considerations.

First of all, methods selected, one for each configuration, are methods for spectral reconstruction, since these methods allow one to perform not only colour measurement, but also spectral reconstruction of reflectance and/or radiance spectra providing a complete information about colour independently of the illuminant and the colour space used.

Secondly, regarding the methods for spectral reconstruction compared, despite the fact that the better results are globally obtained using the NLIN(2) method, this method is not selected for neither of the two configurations since it presents some restrictions on the minimum number of colour samples of the training set depending on the number of acquisition channels of the imaging system that limit its applicability depending on the training set, mainly for the multispectral configuration.

Finally, the PSE method is selected for the colorimetric configuration. Regarding the multispectral configuration, in spite of the fact that results obtained applying the PSE method and the PCA method are quite similar, the PCA method is selected for the multispectral configuration since it is the most common method used in literature for multispectral imaging systems. Using the PCA method will allow one to compare performances of different multispectral imaging systems without the influence of the method applied.

Regarding the PCA method, the number of principal vectors considered as a basis of reflectance spectra is traditionally chosen in literature to be equal to the number of acquisition channels. In order to complete the comparative study on methods for spectral reconstruction carried out in this section, the analysis of the influence of the number of principal vectors considered as a basis of the reflectance spectra when applying the PCA method on system's performance is presented next for the multispectral configuration.

System's performance is analyzed in terms of accuracy of colour measurement (CIELAB colour difference values) and spectral reconstruction (RMSE values), depending on the number of principal components considered in the PCA basis. Results obtained are presented in Tables 6.7 (1) - (4) and Figures 6.5 and 6.6, for all possible combinations of the CCDC and the CCCR charts used as training and test sets.

Table 6.7 (1) *Multispectral Configuration: mean, minimum, maximum and standard deviation of the CIELAB colour difference values and the RMSE values obtained depending on the number of principal components (PC) considered in the PCA basis, using the CCDC as training and test. Results obtained using a number of principal components equal to the number of acquisition channels (7) are highlighted.*

# PC	mean ΔE^*_{ab}	minimum ΔE^*_{ab}	maximum ΔE^*_{ab}	std.dev. ΔE^*_{ab}	mean RMSE	minimum RMSE	maximum RMSE	std.dev. RMSE
3	6.167	0.522	35.771	4.654	4.061E-02	1.648E-02	1.074E-01	1.465E-02
4	3.733	0.489	12.031	2.498	3.560E-02	1.411E-02	1.084E-01	1.274E-02
5	3.715	0.614	12.186	2.463	3.269E-02	1.260E-02	1.054E-01	1.231E-02
6	3.492	0.330	12.599	2.513	3.116E-02	1.161E-02	1.055E-01	1.266E-02
7	3.349	0.103	12.124	2.558	3.046E-02	8.482E-03	1.055E-01	1.283E-02
8	3.313	0.204	12.177	2.573	2.988E-02	8.217E-03	1.051E-01	1.282E-02
9	3.270	0.218	11.658	2.554	2.952E-02	7.845E-03	1.050E-01	1.294E-02
10	3.265	0.228	11.622	2.558	2.946E-02	7.316E-03	1.050E-01	1.295E-02
15	3.266	0.234	11.495	2.556	2.942E-02	7.172E-03	1.051E-01	1.296E-02
20	3.266	0.234	11.491	2.556	2.942E-02	7.164E-03	1.051E-01	1.296E-02
25	3.266	0.234	11.491	2.556	2.942E-02	7.165E-03	1.051E-01	1.296E-02
30	3.266	0.234	11.491	2.556	2.942E-02	7.164E-03	1.051E-01	1.296E-02
35	3.266	0.234	11.491	2.556	2.942E-02	7.164E-03	1.051E-01	1.296E-02
41	3.266	0.234	11.491	2.556	2.942E-02	7.164E-03	1.051E-01	1.296E-02

Table 6.7 (2) *Multispectral Configuration: mean, minimum, maximum and standard deviation of the CIELAB colour difference values and the RMSE values obtained depending on the number of principal components (PC) considered in the PCA basis, using the CCDC as training and the CCCR as test. Results obtained using a number of principal components equal to the number of acquisition channels (7) are highlighted.*

# PC	mean ΔE^*_{ab}	minimum ΔE^*_{ab}	maximum ΔE^*_{ab}	std.dev. ΔE^*_{ab}	mean RMSE	minimum RMSE	maximum RMSE	std.dev. RMSE
3	9.227	1.865	29.747	6.942	5.445E-02	3.513E-02	1.178E-01	1.865E-02
4	6.049	1.173	20.945	4.331	5.009E-02	2.973E-02	8.187E-02	1.572E-02
5	6.120	1.176	22.417	4.567	4.687E-02	2.451E-02	7.125E-02	1.288E-02
6	5.636	1.022	22.698	4.658	4.618E-02	2.473E-02	7.290E-02	1.276E-02
7	5.463	1.088	21.650	4.500	4.588E-02	2.450E-02	7.251E-02	1.256E-02
8	5.435	1.074	21.765	4.538	4.553E-02	2.361E-02	7.166E-02	1.214E-02
9	5.398	0.992	20.578	4.345	4.519E-02	2.363E-02	7.176E-02	1.209E-02
10	5.400	0.976	20.406	4.323	4.504E-02	2.362E-02	7.180E-02	1.205E-02
15	5.407	0.947	20.127	4.273	4.506E-02	2.358E-02	7.173E-02	1.200E-02
20	5.407	0.946	20.118	4.271	4.506E-02	2.358E-02	7.173E-02	1.200E-02
25	5.407	0.946	20.118	4.271	4.506E-02	2.358E-02	7.173E-02	1.200E-02
30	5.407	0.946	20.118	4.271	4.506E-02	2.358E-02	7.173E-02	1.200E-02
35	5.407	0.946	20.118	4.271	4.506E-02	2.358E-02	7.173E-02	1.200E-02
41	5.407	0.946	20.118	4.271	4.506E-02	2.358E-02	7.173E-02	1.200E-02

Table 6.7 (3) *Multispectral Configuration: mean, minimum, maximum and standard deviation of the CIELAB colour difference values and the RMSE values obtained depending on the number of principal components (PC) considered in the PCA basis, using the CCCR as training and test. Results obtained using a number of principal components equal to the number of acquisition channels (7) are highlighted.*

# PC	mean ΔE^*_{ab}	minimum ΔE^*_{ab}	maximum ΔE^*_{ab}	std.dev. ΔE^*_{ab}	mean RMSE	minimum RMSE	maximum RMSE	std.dev. RMSE
3	8.601	0.940	38.329	7.844	4.495E-02	2.122E-02	8.403E-02	1.380E-02
4	6.468	0.581	15.320	3.768	3.949E-02	1.989E-02	6.784E-02	1.147E-02
5	4.409	0.764	12.409	3.084	3.327E-02	1.369E-02	6.641E-02	1.402E-02
6	3.987	0.311	12.386	3.272	3.143E-02	1.324E-02	6.711E-02	1.482E-02
7	3.831	0.492	12.447	3.201	3.057E-02	1.286E-02	6.561E-02	1.496E-02
8	3.682	0.247	12.440	3.083	2.963E-02	1.171E-02	6.596E-02	1.556E-02
9	3.677	0.275	12.433	3.076	2.963E-02	1.182E-02	6.596E-02	1.550E-02
10	3.677	0.266	12.433	3.049	2.952E-02	1.197E-02	6.589E-02	1.560E-02
15	3.680	0.242	12.439	3.046	2.949E-02	1.180E-02	6.591E-02	1.559E-02
20	3.680	0.242	12.439	3.046	2.949E-02	1.180E-02	6.591E-02	1.559E-02
25	3.680	0.242	12.439	3.046	2.949E-02	1.180E-02	6.591E-02	1.559E-02
30	3.680	0.242	12.439	3.046	2.949E-02	1.180E-02	6.591E-02	1.559E-02
35	3.680	0.242	12.439	3.046	2.949E-02	1.180E-02	6.591E-02	1.559E-02
41	3.680	0.242	12.439	3.046	2.949E-02	1.180E-02	6.591E-02	1.559E-02

Table 6.7 (4) *Multispectral Configuration: mean, minimum, maximum and standard deviation of the CIELAB colour difference values and the RMSE values obtained depending on the number of principal components (PC) considered in the PCA basis, using the CCCR as training and the CCDC as test. Results obtained using a number of principal components equal to the number of acquisition channels (7) are highlighted.*

# PC	mean ΔE^*_{ab}	minimum ΔE^*_{ab}	maximum ΔE^*_{ab}	std.dev. ΔE^*_{ab}	mean RMSE	minimum RMSE	maximum RMSE	std.dev. RMSE
3	8.148	0.588	56.853	5.870	5.070E-02	1.680E-02	1.055E-01	2.245E-02
4	6.180	0.680	21.933	3.748	4.774E-02	1.692E-02	1.077E-01	2.184E-02
5	3.965	0.184	9.852	1.967	4.266E-02	1.324E-02	1.060E-01	2.156E-02
6	3.814	0.280	10.118	2.111	4.118E-02	1.312E-02	1.063E-01	2.199E-02
7	3.759	0.477	10.406	2.185	4.059E-02	1.224E-02	1.063E-01	2.221E-02
8	3.646	0.605	10.575	2.157	3.981E-02	1.270E-02	1.049E-01	2.245E-02
9	3.660	0.606	10.761	2.172	3.970E-02	1.278E-02	1.051E-01	2.248E-02
10	3.653	0.536	10.735	2.168	3.969E-02	1.278E-02	1.051E-01	2.248E-02
15	3.645	0.529	10.614	2.157	3.966E-02	1.268E-02	1.044E-01	2.247E-02
20	3.645	0.528	10.614	2.157	3.966E-02	1.269E-02	1.044E-01	2.246E-02
25	3.645	0.528	10.614	2.157	3.966E-02	1.269E-02	1.044E-01	2.246E-02
30	3.645	0.528	10.614	2.157	3.966E-02	1.269E-02	1.044E-01	2.246E-02
35	3.645	0.528	10.614	2.157	3.966E-02	1.269E-02	1.044E-01	2.246E-02
41	3.645	0.528	10.614	2.157	3.966E-02	1.269E-02	1.044E-01	2.246E-02

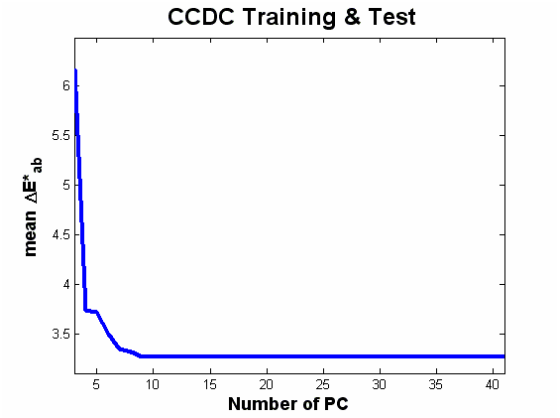

(a)

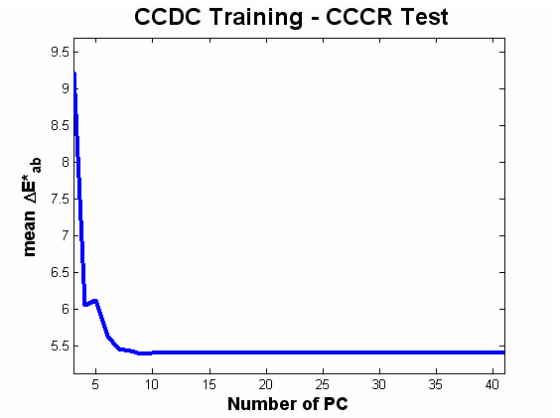

(b)

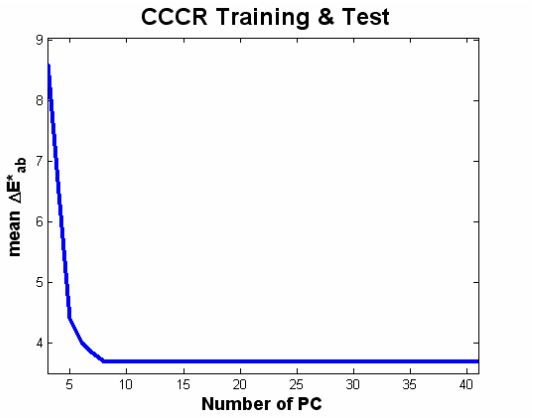

(c)

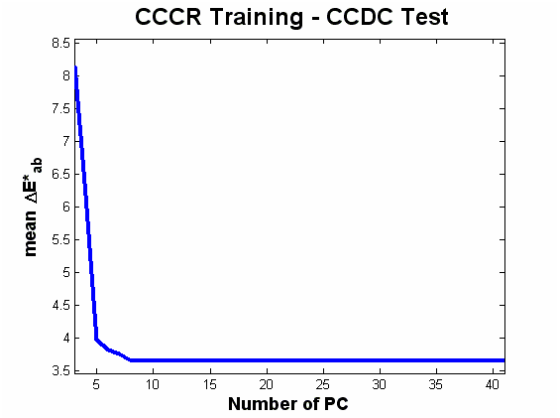

(d)

Figure 6.5 *Multispectral Configuration: mean CIELAB colour difference values plotted versus the number of principal components (PC) considered in the PCA basis, using (a) the CCDC as training and test, (b) the CCDC as training and the CCCR as test, (c) the CCCR as training and test, and (d) the CCCR as training and the CCDC as test.*

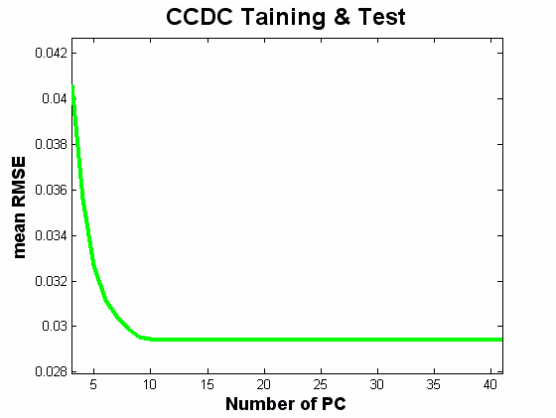

(a)

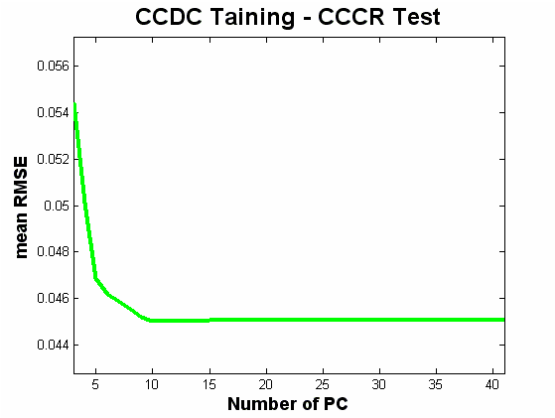

(b)

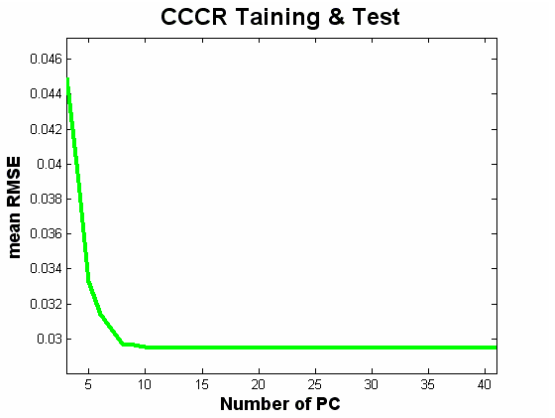

(c)

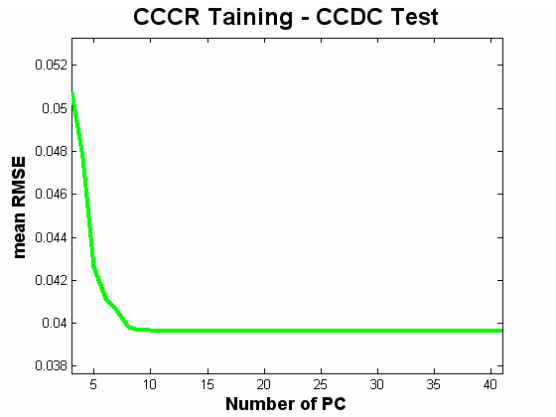

(d)

Figure 6.6 *Multispectral Configuration: mean RMSE values plotted versus the number of principal components (PC) considered in the PCA basis, using (a) the CCDC as training and test, (b) the CCDC as training and the CCCR as test, (c) the CCCR as training and test, and (d) the CCCR as training and the CCDC as test.*

As can be seen from Tables 6.7 (1) - (4) and from Figures 6.5 and 6.6, neither the accuracy of colour measurement nor the accuracy of spectral reconstruction improved significantly by increasing the number of principal components in the PCA basis from 7 principal components on, which is the number of acquisition channels of the multispectral imaging system used. Therefore, the minimum number of principal vectors that must be considered in the PCA basis in order to achieve the best system's performance using the PCA method, both in terms of accuracy of colour measurement and in terms of accuracy of spectral reconstruction, should be equal to the number of acquisition channels, as it is traditionally done in literature.

From here on, the PCA method will be applied as up to now, considering a number of principal components in the PCA basis equal to the number of acquisition channels, i.e. 7 for the multispectral configuration of the imaging system used.

Once the methods that will be used from here on for each configuration are selected, the PSE method for the colorimetric configuration and the PCA method for the multispectral configuration, the repeatability of the two configurations of the imaging system is determined analyzing the fluctuations with respect to the mean of, on one hand, the system's performance in consecutive measurements and, on the other hand, the system's performance in measurements carried out at different times in different days.

Five sets of five consecutive measurements of the CCDC chart carried out at different times in different days are used to evaluate the repeatability of system's performance both in terms of colour measurement and spectral reconstruction.

Considering the performance of colour measurement, the mean fluctuation obtained in consecutive measurements is 0.08% of the mean CIELAB colour difference value for the colorimetric configuration, and 0.16% for the multispectral configuration. The total mean fluctuation considering the five sets of five consecutive measurements carried out at different times in different days is 0.31% for the colorimetric configuration, and 1.15% for the multispectral configuration. Consequently, the percentage of repeatability of the colour measurement performed by the imaging system is approximately 99.7% for the colorimetric configuration, whereas it is approximately 98.9% for the multispectral configuration.

Considering the performance of spectral reconstruction, the mean fluctuation obtained in consecutive measurements is 0.01% of the mean RMSE value for the colorimetric configuration, and 0.20% for the multispectral configuration. The total mean fluctuation considering the five sets of five consecutive measurements carried out at different times in different days is 0.09% for the colorimetric configuration, and 0.54% for the multispectral configuration. Consequently, the percentage of repeatability of the spectral reconstruction performed by the imaging system is almost 100% for the colorimetric configuration, and approximately 99.5% for the multispectral configuration.

As it can be observed, the repeatability of the imaging system is slightly greater for the colorimetric configuration than for the multispectral configuration, both in terms of colour measurement and spectral reconstruction. This can be easily attributed to the type of filters used in each configuration: a set of 7 interference filters (sub-section 2.1.1.2) are used in the multispectral configuration in front of the RGB tunable filter used in the colorimetric configuration.

7 Increasing the Dynamic Range of an Imaging System Based on a CCD Camera: Luminance Adaptation Model

When an imaging system based on a CCD sensor, just as any other optoelectronic imaging sensor, wants to be used as an instrument for measuring, the imaging conditions and/or setting parameters must be such that the system's response at each pixel falls into the linear response zone of the sensor. Considering the system's response depending on the exposure, for fixed imaging conditions and setting parameters, the linear response zone of the imaging sensor corresponds typically to the range between the 8 – 10% and the 90 – 92%, approximately, of the maximum digital response of the imaging system (sub-section 4.1.1). For the 12 bits CCD sensor used in this work, the linear response zone is located between the 330 and the 3700 digital levels, which fixed the useful dynamic range of the imaging system.

On the other hand, one of the main motivations to use imaging systems based on CCD sensors as instruments for measuring is their high spatial resolution, allowing one to perform measurements simultaneously at each pixel of an image. Nevertheless, in real scenes, for a fixed exposure time, it is very probable that digital responses for some of the pixels of the image were not located within the linear response zone of the imaging system due to the large differences in radiance of the different objects imaged. In order to overcome this limitation, basically due to the useful dynamic range of the imaging system, a Luminance Adaptation Model (LAM) is proposed. This LAM allows one to increase the dynamic range of the imaging system by taking images at different exposure times in order to obtain useful digital levels (i.e. digital levels placed within the linear response zone) for all pixels. Different exposure times can be needed for different pixels in the image, depending on the radiance of the object that are imaging. The useful digital levels for the pixels of an image taken at a certain exposure time are transformed into a reference exposure time, common to all pixels in the image, so that all final digital levels at the reference exposure time resulted to be located within the linear range of the system response and become comparable, being the dynamic range of the system increased as a result [Pujol et al., 2006].

For each acquisition channel, the useful digital levels at a certain exposure time are transformed to the final digital levels at a reference exposure time by means of a linear transformation. The coefficients of this transformation, which depend on the exposure time, are determined using the neutral patches of the Munsell Book of Color. For each acquisition channel, the reference exposure time is selected so that the digital levels associated to all Munsell's neutral patches are located within the linear response zone of the system, i.e. are useful digital levels. Apart from the reference exposure time, a set of different exposure times are also considered for each acquisition channel. Images of the Munsell's neutral patches are taken at the reference exposure time, and at the different exposure times for each acquisition channel. The useful digital levels of the Munsell's neutral patches at each exposure time are plotted versus the digital levels of the same Munsell's neutral patches at the reference exposure time, and fitted using a first order least square fitting ($y = ax + b$).

Once the parameters of the fitting, which will be called LAM coefficients, are obtained for each exposure time considered for each acquisition channel, the LAM is applied to the useful digital levels of the colour patches of both the GretagMacbeth ColorChecker DC chart (DC) and the GretagMacbeth ColorChecker Color Rendition chart (CCCR), which are imaged at the same reference and different exposure times. The final digital levels resulting from the LAM application, besides the reflectance spectra of the CCDC's and CCCR's colour samples are used to train the imaging system. The system's performance in terms of accuracy of colour measurement and spectral reconstruction is obtained using all possible combinations of these two charts as training and test sets. Accuracy of colour measurement is evaluated in terms of the CIELAB colour difference, and accuracy of spectral reconstruction is evaluated in terms of the RMSE.

In order to assess the validity of the LAM proposed and to determine if its application allows one to improve the performance of the imaging system in terms of accuracy or, at least, does not worsen it, the CCDC and the CCCR charts are used as training and test sets since it is possible to obtain useful digital levels for all color patches of each chart imaging them at a certain exposure time. Results obtained applying the LAM are compared to results obtained without applying the LAM, for all possible combinations of the CCDC and the CCCR charts as training and test sets, and for the two configurations of the imaging system.

It must be noticed that the LAM coefficients associated to a certain exposure time, just as the reference exposure time and the set of exposure times considered, are specific for the illuminant used. Therefore, a change of the illuminant implies the re-calculation of the LAM coefficients from the Munsell's neutral patches imaged at new different exposure times using the new illuminant.

Next, the LAM coefficients obtained for all exposure times considered for each acquisition channel, and results obtained with and without the application of the LAM are presented for the two configurations of the imaging system.

7.1 Colorimetric Configuration

The LAM coefficients obtained applying a first order least square fitting between the digital levels of the same Munsell's neutral patches at the reference exposure time and at each one of the different exposure times considered, for the R, G and B acquisition channels of the colorimetric configuration, are presented in Table 7.1. The reference exposure time chosen for each acquisition channel is highlighted.

An example of the first order least square fitting applied between the digital levels of the same Munsell's neutral patches at the reference exposure time and at an exposure time of 30ms for the three acquisition channels of the colorimetric configuration, can be seen from Figure 7.1.

Once the LAM coefficients associated to each exposure time for the three acquisition channels of the imaging system are known, images of the CCDC and the CCCR charts are taken at the different exposure times considered in Table 7.1 for each acquisition channel. Then, the LAM is applied to the useful digital levels of the colour samples of the CCDC and the CCCR charts at each exposure time, obtaining the resulting digital levels at the reference exposure time for all colour samples, and for the three acquisition channels. The accuracy of system's performance applying the LAM for all possible combinations of the CCDC and the CCCR charts as training and test sets is compared with the corresponding accuracy of system's performance without applying the LAM, using directly the digital levels for all colour patches of both the CCDC and the CCCR charts obtained from images taken at an exposure time of 10ms for the R and G channels, and 40ms for the B channel. These last

exposure times are such that the digital levels associated to all colour samples of both the CCDC and the CCCR charts are useful.

Table 7.1 *Colorimetric Configuration: parameters of the first order least square fitting (y = ax + b) or LAM coefficients associated to each exposure time (t_{exp}) considered for the R, G, and B channels of the colorimetric configuration. The reference exposure time (t_{ref}) chosen for each acquisition channel is highlighted.*

R CHANNEL				G CHANNEL				B CHANNEL			
t_{exp} (ms)	*a*	*b*	r^2	t_{exp} (ms)	*a*	*b*	r^2	t_{exp} (ms)	*a*	*b*	r^2
10	1.971	-134.031	0.9992	10	1.977	-135.912	0.9992	10	3.955	-429.624	0.9963
20	1.000	0.000	1.0000	20	1.000	0.000	1.0000	20	1.978	-138.946	0.9991
30	0.685	38.134	0.9999	30	0.686	37.709	0.9999	30	1.346	-47.230	0.9999
40	0.511	61.630	0.9996	40	0.511	62.198	0.9996	40	1.000	0.000	1.0000
50	0.410	76.210	0.9992	50	0.410	76.760	0.9992	60	0.681	39.677	0.9999
60	0.345	87.379	0.9988	60	0.346	85.404	0.9989	80	0.510	63.232	0.9996
70	0.296	92.838	0.9986	70	0.297	92.984	0.9986	100	0.406	78.210	0.9992
80	0.259	98.956	0.9984	80	0.258	100.521	0.9983	120	0.337	89.120	0.9987
90	0.230	102.535	0.9983	90	0.229	103.732	0.9981	140	0.290	96.513	0.9983
100	0.207	106.802	0.9981	100	0.207	106.639	0.9980	160	0.254	101.156	0.9980

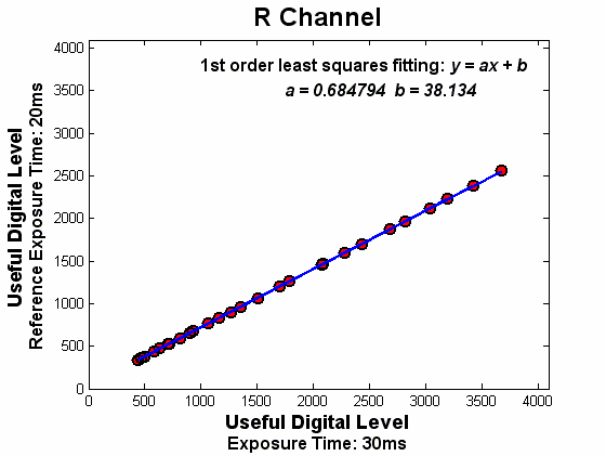

(a)

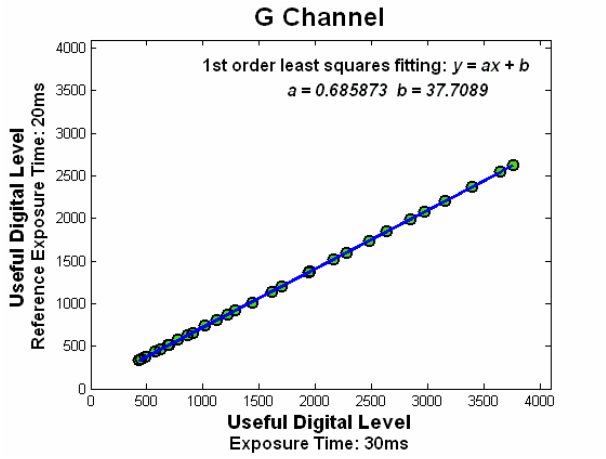

(b)

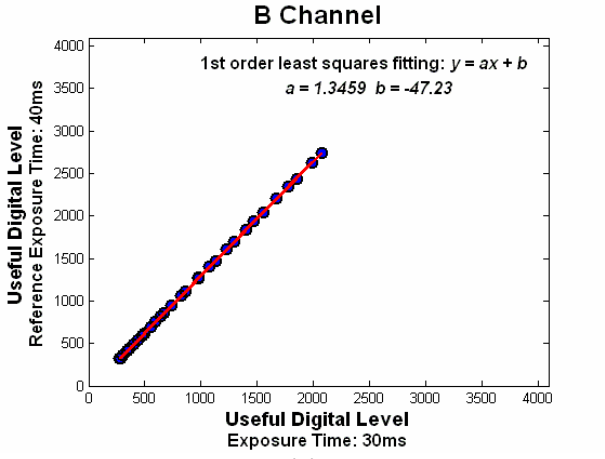

(c)

Figure 7.1 *Colorimetric Configuration: first order least square fitting applied between the digital levels of the same Munsell's neutral patches at the reference exposure time and at an exposure time of 30ms, for the (a) R, (b) G and (c) B acquisition channels of the imaging system. Each point in the plot represents a Munsell's neutral patch.*

Table 7.2 *Colorimetric Configuration: Comparison between the mean, minimum, maximum and standard deviation of the CIELAB colour difference values obtained with (LAM) and without (NO LAM) the application of the Luminance Adaptation Model proposed, for all combinations of the CCDC and CCCR charts used as training and test sets.*

	ΔE^*_{ab} – NO LAM				ΔE^*_{ab} – LAM			
Training	**CCDC**	**CCDC**	**CCCR**	**CCCR**	**CCDC**	**CCDC**	**CCCR**	**CCCR**
Test	**CCDC**	**CCCR**	**CCCR**	**CCDC**	**CCDC**	**CCCR**	**CCCR**	**CCDC**
mean	5.020	7.275	6.051	5.193	3.599	5.279	4.060	3.864
minimum	0.545	0.907	0.548	0.647	0.352	2.225	0.560	0.671
maximum	17.14	19.12	17.22	14.89	10.34	11.15	9.033	11.12
std. dev.	3.554	5.232	4.755	3.008	2.307	2.638	2.443	2.107

Regarding the accuracy of colour measurement, the application of the LAM not only does not worse the accuracy of the system's performance, but also slightly improves it for all combinations of the CCDC and the CCCR charts used as training and test sets (Table 7.2 and Figure 7.2 (a)). Greater improvements are obtained in average when different charts are used as training and test sets.

Considering the accuracy of spectral reconstruction, the application of the LAM slightly improves the accuracy of system's performance for all combinations of the CCDC and the CCCR charts used as training and test sets (Table 7.3 and Figure 7.2 (b)). In this case, the improvement in accuracy is very similar for all combinations of the CCDC and the CCCR charts used as training and test sets.

Table 7.3 *Colorimetric Configuration: Comparison between the mean, minimum, maximum and standard deviation of the RMSE values obtained with (LAM) and without (NO LAM) the application of the Luminance Adaptation Model proposed, for all combinations of the CCDC and CCCR charts used as training and test sets.*

	RMSE – NO LAM				RMSE – LAM			
Training	**CCDC**	**CCDC**	**CCCR**	**CCCR**	**CCDC**	**CCDC**	**CCCR**	**CCCR**
Test	**CCDC**	**CCCR**	**CCCR**	**CCDC**	**CCDC**	**CCCR**	**CCCR**	**CCDC**
mean	4.576E-02	5.801E-02	5.296E-02	5.353E-02	4.256E-02	5.505E-02	5.053E-02	5.081E-02
min	1.388E-02	3.158E-02	2.350E-02	1.685E-02	1.166E-02	3.020E-02	2.463E-02	1.431E-02
max	17.16E-02	17.17E-02	16.24E-02	16.29E-02	17.57E-02	17.54E-02	16.42E-02	16.50E-02
std.dev.	2.229E-02	2.891E-02	2.699E-02	2.376E-02	2.377E-02	3.121E-02	2.819E-02	2.447E-02

These results prove the validity of the LAM proposed in terms of accuracy of both colour measurement and spectral reconstruction for the colorimetric configuration of the imaging system, since its application allows one to increase the dynamic range of the imaging system without any loss or worsening of accuracy in its performance. On the other hand, the application of the LAM proposed can even improve accuracy of system's performance both in terms of colour measurement and spectral reconstruction, as it is the case of this colorimetric configuration.

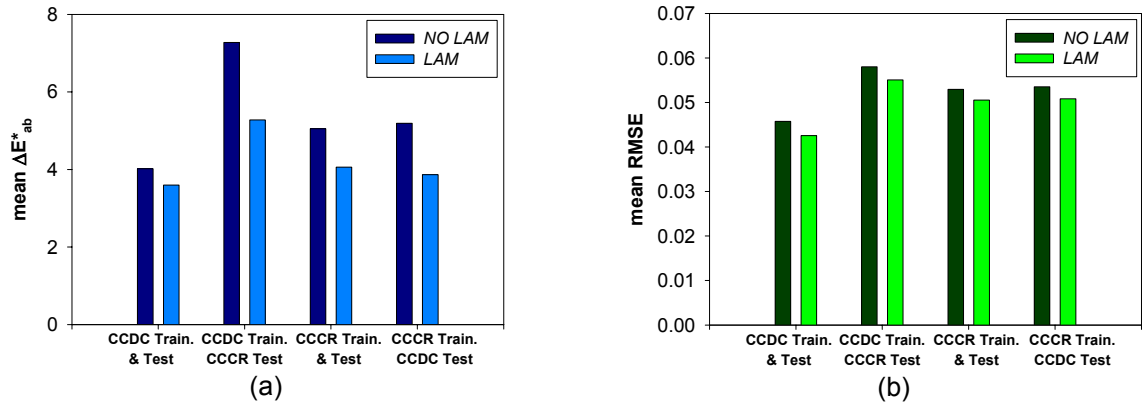

Figure 7.2 *Colorimetric Configuration: Bar plots of the mean (a) CIELAB colour difference values and (b) RMSE values obtained with (LAM) and without (NO LAM) the application of the LAM proposed, for all combinations of the CCDC and the CCCR charts used as training and test sets.*

7.2 Multispectral Configuration

The LAM coefficients associated to the different exposure times considered for each acquisition channel of the multispectral configuration are presented in Tables 7.4 (1) – (2). The reference exposure time chosen for each acquisition channel is highlighted.

Table 7.4 (1) *Multispectral Configuration: parameters of the first order least square fitting (y = ax + b) or LAM coefficients associated to each exposure time (t_{exp}) considered for the 7 channels of the multispectral configuration. Each acquisition channel is denoted by the central wavelength of the interference filter F. The reference exposure time (t_{ref}) chosen for each acquisition channel is highlighted.*

CHANNEL F400			
t_{exp} (ms)	*a*	*b*	r^2
300	1.640	-81.871	0.9998
400	1.238	-28.474	1.0000
500	1.000	0.000	1.0000
750	0.680	35.288	0.9999
1000	0.513	54.819	0.9998
1250	0.407	70.067	0.9997
1500	0.339	77.991	0.9996

CHANNEL F450			
t_{exp} (ms)	*a*	*b*	r^2
25	1.974	-138.241	0.9990
50	1.000	0.000	1.0000
75	0.675	39.023	0.9999
100	0.512	61.510	0.9996
200	0.256	99.506	0.9984
250	0.205	105.579	0.9982
300	0.170	111.627	0.9982

CHANNEL F500			
t_{exp} (ms)	*a*	*b*	r^2
20	1.478	-63.264	0.9998
30	1.000	0.000	1.0000
40	0.760	26.227	1.0000
60	0.512	60.073	0.9997
100	0.308	88.791	0.9990
150	0.206	104.427	0.9987
200	0.153	115.014	0.9987

CHANNEL F550			
t_{exp} (ms)	*a*	*b*	r^2
10	1.974	-136.048	0.9992
20	1.000	0.000	1.0000
30	0.680	38.257	0.9999
50	0.412	76.283	0.9992
100	0.207	106.667	0.9980
125	0.165	113.242	0.9979
150	0.137	119.438	0.9979

Table 7.4 (2) *Multispectral Configuration: parameters of the first order least square fitting (y = ax + b) or LAM coefficients associated to each exposure time (t_{exp}) considered for the 7 channels of the multispectral configuration. Each acquisition channel is denoted by the central wavelength of the interference filter F. The reference exposure time (t_{ref}) chosen for each acquisition channel is highlighted.*

CHANNEL F600			
t_{exp} (ms)	*a*	*b*	r^2
10	1.963	-136.562	0.9991
20	1.000	0.000	1.0000
30	0.673	40.596	0.9999
50	0.408	76.613	0.9992
100	0.205	106.474	0.9980
125	0.164	114.127	0.9978
150	0.138	118.580	0.9978

CHANNEL F650			
t_{exp} (ms)	*a*	*b*	r^2
10	2.958	-286.198	0.9971
20	1.493	-69.326	0.9996
30	1.000	0.000	1.0000
50	0.608	50.635	0.9997
100	0.306	93.174	0.9981
125	0.244	104.062	0.9971
150	0.207	108.372	0.9967

CHANNEL F700			
t_{exp} (ms)	*a*	*b*	r^2
25	5.933	-722.712	0.9943
50	2.995	-286.463	0.9972
75	2.000	-140.473	0.9991
100	1.499	-68.745	0.9997
150	1.000	0.000	1.0000
200	0.756	29.731	0.9999
300	0.517	60.657	0.9996

An example of the first order least square fitting applied between the digital levels of the same Munsell's neutral patches at the reference exposure time and at a different exposure time for the seven acquisition channels of the multispectral configuration, can be seen from Figure 7.3.

Once the LAM coefficients associated to each exposure time for the seven acquisition channels of the imaging system are known, the same procedure used for the colorimetric configuration is followed. Images of the CCDC and the CCCR charts are taken at the different exposure times considered in Tables 7.4 (1) – (2) for each acquisition channel. Then, the LAM is applied obtaining the resulting digital levels at the reference exposure time for all colour samples, and for the seven acquisition channels. Accuracy of system's performance applying the LAM for all possible combinations of the CCDC and the CCCR charts as training and test sets is compared with the corresponding accuracy of system's performance without applying the LAM and imaging the GretagMacbeth ColorChecker charts at the reference exposure time corresponding to each acquisition channel (Tables 7.4 (1) – (2)). Results obtained are presented in Tables 7.5 and 7.6 and in Figure 7.4.

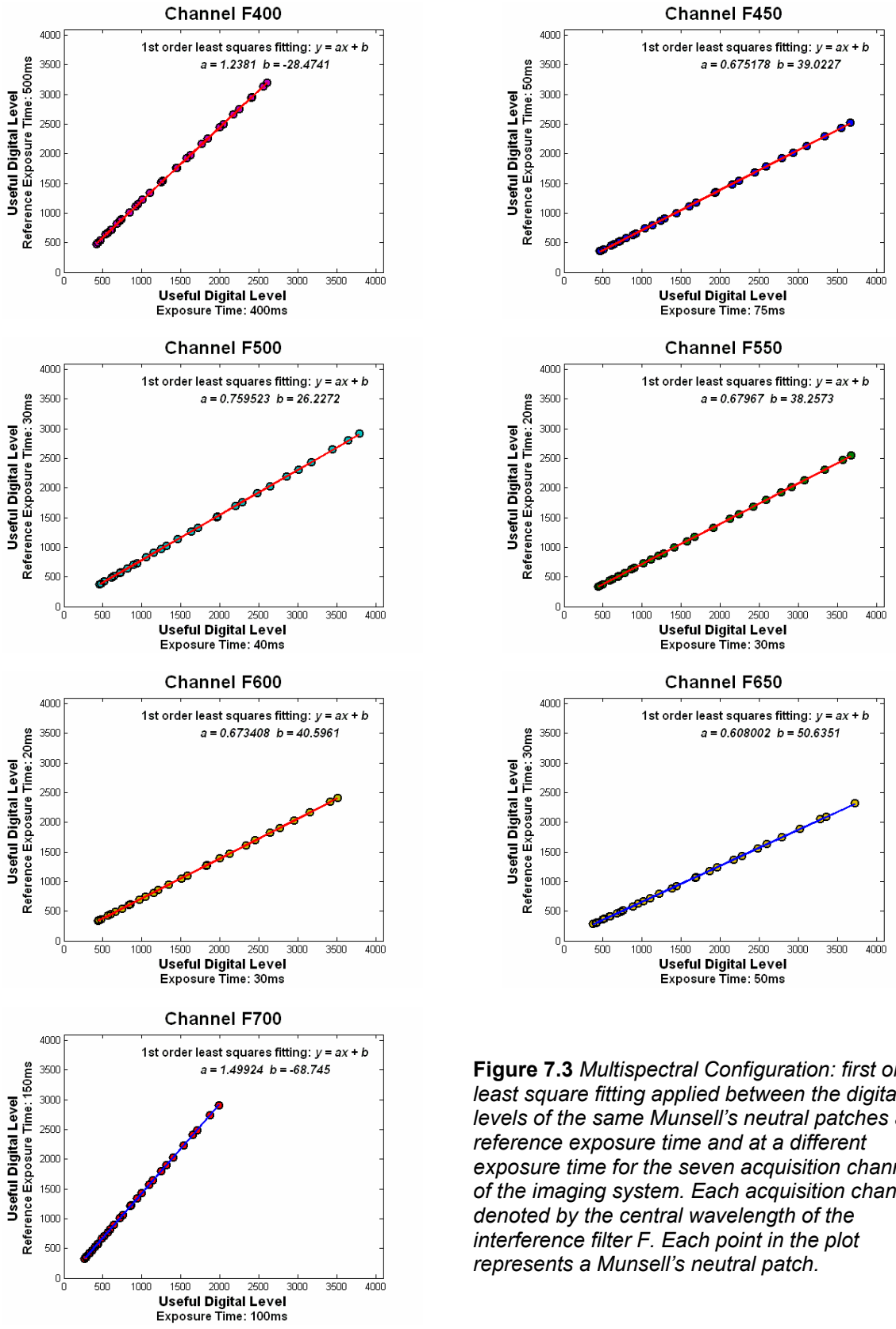

Figure 7.3 *Multispectral Configuration: first order least square fitting applied between the digital levels of the same Munsell's neutral patches at the reference exposure time and at a different exposure time for the seven acquisition channels of the imaging system. Each acquisition channel is denoted by the central wavelength of the interference filter F. Each point in the plot represents a Munsell's neutral patch.*

Regarding the accuracy of colour measurement, very similar results are obtained with and without the application of the LAM for all combinations of the CCDC and the CCCR charts used as training and test sets (Table 7.5 and Figure 7.4 (a)).

Table 7.5 *Multispectral Configuration: Comparison between the mean, minimum, maximum and standard deviation of the CIELAB colour difference values obtained with (LAM) and without (NO LAM) the application of the Luminance Adaptation Model proposed, for the different combinations of the CCDC and CCCR charts used as training and test sets.*

	ΔE^*_{ab} – NO LAM				ΔE^*_{ab} – LAM			
Training	**CCDC**	**CCDC**	**CCCR**	**CCCR**	**CCDC**	**CCDC**	**CCCR**	**CCCR**
Test	**CCDC**	**CCCR**	**CCCR**	**CCDC**	**CCDC**	**CCCR**	**CCCR**	**CCDC**
mean	3.349	5.463	3.831	3.759	3.352	5.429	3.810	3.818
min	0.103	1.088	0.492	0.477	0.124	1.081	0.435	0.522
max	12.124	21.650	12.447	10.406	11.630	20.950	11.975	10.349
std. dev.	2.558	4.500	3.201	2.185	2.489	4.322	3.124	2.030

Considering the accuracy of spectral reconstruction, and similarly to the accuracy of colour measurement, results obtained with and without the application of the LAM are very similar for all combinations of the CCDC and the CCCR charts used as training and test sets (Table 7.6 and Figure 7.4 (b)).

Table 7.6 *Multispectral Configuration: Comparison between the mean, minimum, maximum and standard deviation of the RMSE values obtained with (LAM) and without (NO LAM) the application of the Luminance Adaptation Model proposed, for the different combinations of the CCDC and CCCR charts used as training and test sets.*

	RMSE – NO LAM				RMSE – LAM			
Training	**CCDC**	**CCDC**	**CCCR**	**CCCR**	**CCDC**	**CCDC**	**CCCR**	**CCCR**
Test	**CCDC**	**CCCR**	**CCCR**	**CCDC**	**CCDC**	**CCCR**	**CCCR**	**CCDC**
mean	3.046E-02	4.588E-02	3.057E-02	4.059E-02	3.033E-02	4.563E-02	3.044E-02	4.050E-02
min	0.848E-02	2.450E-02	1.286E-02	1.224E-02	0.817E-02	2.279E-02	1.393E-02	1.288E-02
max	10.55E-02	7.251E-02	6.561E-02	10.63E-02	10.31E-02	7.417E-02	6.616E-02	10.54E-02
std.dev.	1.283E-02	1.256E-02	1.496E-02	2.221E-02	1.262E-02	1.305E-02	1.441E-02	2.175E-02

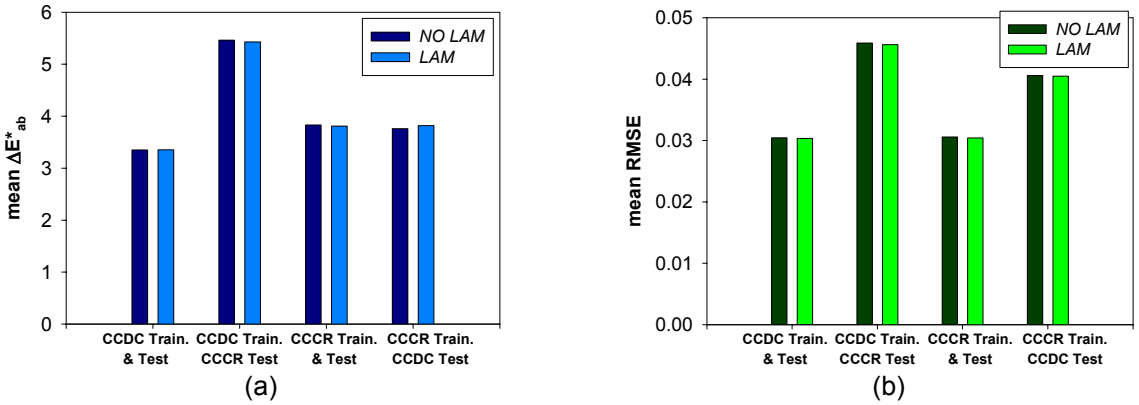

Figure 7.4 *Multispectral Configuration: Bar plots of the mean (a) CIELAB colour difference values and (b) RMSE values obtained with (LAM) and without (NO LAM) the application of the LAM proposed, for all combinations of the CCDC and the CCCR charts used as training and test sets.*

Similarly to the colorimetric configuration, these results prove the validity of the LAM proposed in terms of accuracy of both colour measurement and spectral reconstruction for the multispectral configuration of the imaging system, since its application allows one to increase the dynamic range of the imaging system without any loss or worsening of accuracy in its performance.

Considering results obtained for the two configurations of the imaging system, it can be concluded that the LAM proposed, apart from its proved validity for limited exposure conditions, has been also proved to be a very useful method to increase the dynamic range of the imaging system without any loss or worsening of accuracy in its performance, allowing one to widen its applicability to images having zones with extreme exposure conditions. Consequently, the application of the LAM proposed is greatly advisable mainly on images having zones with an outstandingly wide range of exposures, in order to make useful all zones over the image, either for colour measurement or for spectral reconstruction.

8 Influence of the Number of Samples of the Training Set on Accuracy of Colour Measurement and Spectral Reconstruction

The aim of this section is to analyze the influence of the number of samples of the training set on the accuracy of colour measurement and spectral reconstruction. This study is considered to be the first step in the process of analyzing the accuracy of colour measurement and spectral reconstruction depending on the training set used, in order to be able to determine the most outstanding characteristics of the most suitable training set for both the colorimetric and the multispectral configurations of the imaging system developed previously.

A good training set of an imaging system that want to be used as an instrument for colour measurement and spectral reconstruction, should be representative enough of the kind of samples that the imaging system will measure. Consequently, the training set should have a number and a variety of samples in terms of colour ranges and/or reflectance spectra that allows fulfilling this condition.

The influence of the variety of samples of the training set in terms of colour ranges and/or reflectance spectra on the accuracy of colour measurement and spectral reconstruction performed by the two configurations of the imaging system will be analyzed in next chapters (chapters 10 and 11).

Considering the number of samples and assuming that for all number of samples the variety in terms of colour ranges and/or reflectance spectra is assured, it is direct to suppose that the greater the number of samples will be, the better the accuracy of both colour measurement and spectral reconstruction will be. Nevertheless, is this improvement in accuracy unlimited depending on the increase of the number of colour samples? It is logical to think that it is not, and that there should exist a minimum and/or 'sufficient number of samples' from which on the improvement in accuracy is negligible or nil when increasing the number of samples. On the other hand, the performance of the imaging system must also be independent of the training set. This characteristic can be easily thought to be also related to the features of the training set in terms of its size or its number of colour samples and, subsequently, the variety of colour ranges and/or reflectance spectra. In this section, the performance of the two configurations of the imaging system and their dependence on the training set is analyzed depending on the number of colour samples of the training set.

This study is performed using both the colorimetric and the multispectral configurations of the imaging system and the incandescent lamp illuminant (section 3.3). All training sets considered are made up of a previous selection of the colour samples of the GretagMacbeth ColorChecker DC chart (CCDC, 166 useful colour samples). The GretagMacbeth ColorChecker Color Rendition chart (CCCR, 24 colour samples) is used as test set.

Regarding the selection criterion, none of the criteria commonly used to find the best training set that can be found in literature is used [Harderberg, 1998; Harderberg, 1999; Cheung et al., 2004; Pellegri et al., 2004], as the main aim here is not to find the best training set, but training sets of different size having the greater variety of samples possible. The

selection criterion applied to obtain a training set having the greater variety of samples possible in terms of colour ranges, for each number of samples considered, is based on differences in the a* (Δa*) and b* (Δb*) CIELAB coordinates between each pair of colour samples belonging to the final selected set. Each pair of selected samples must satisfy the condition:

$$\Delta a^* \geq inca \qquad \text{and} \qquad \Delta b^* \geq incb$$

where the values for the *inca* and *incb* variables are chosen so that *inca* = *incb*, for simplicity, and that allow to fix the number of colour samples selected (Table 8.1).

The colorimetric and the multispectral configurations of the imaging system are trained using training sets of sizes between 10 and 166 colour samples in steps of 10 samples (Table 8.1), and their performance is tested using the 24 colour samples of the CCCR chart. The accuracy of colour measurement is evaluated in terms of the mean, minimum, maximum and standard deviation of the CIELAB colour difference between the calculated and the measured tristimulus values of the CCCR's colour samples. The accuracy of spectral reconstruction is evaluated in terms of the mean, minimum, maximum and standard deviation of the RMSE between the reconstructed and the measured reflectance spectra of the CCCR's colour samples.

Table 8.1 *Correspondence between the values of the 'inca' and 'incb' variables used in the selection criterion and the number of colour samples selected from the CCDC chart.*

inca = *incb*	# colour samples	*inca* = *incb*	# colour samples	*inca* = *incb*	# colour samples
17.00	10	3.12	70	1.22	130
9.20	20	2.68	80	0.80	140
6.98	30	2.36	90	0.58	150
5.35	40	2.15	100	0.20	160
4.50	50	1.69	110	0.05	166
4.00	60	1.45	120		

Considering the selection process of the training sets, two different analyses are performed. In the first analysis, the first useful colour sample of the CCDC (colour sample B2) is used as the initial fixed colour sample. Starting from it, the training sets of different sizes are selected among the colour samples of the CCDC chart by applying the selection criterion. In this case, results obtained would show the dependence of the performance of the imaging system on the size of the training set but not on the training set itself, since the training sets selected would be particular for the initial fixed colour sample (colour sample B2), mainly for the lower sizes, and would depend on it. In order to overcome this limitation and be able to analyze the dependence of the system's performance on the training set, a second analysis is performed. In the second analysis, an initial colour sample is selected randomly from the CCDC chart. Starting from it, the rest of colour samples are selected by applying the former selection criterion for all sizes considered (Table 8.1). This process is repeated five times in order to have five training sets for each size selected, obtained from five samples selected randomly from the CCDC chart. The comparison of results obtained using these training sets, which depend on the initial sample considered, will allow one to analyze the influence of the training set on system's performance depending on the number of samples of the training set.

Next, results obtained in the two analyses performed are presented for the colorimetric and the multispectral configurations of the imaging system.

8.1 Colorimetric Configuration

8.1.1 Analysis I: Initial fixed colour sample

As it was said before, the first useful colour sample of the CCDC (colour sample B2) is used in this analysis as the initial fixed colour sample, and starting from it, the rest of colour samples of the training sets for all sizes considered are selected among the colour samples of the CCDC chart by applying the selection criterion.

In this case, as the training sets selected depend on the initial fixed colour sample used, results obtained will indicate the tendency of system's performance depending on the number of samples of the training set, only if it can be assumed that the behaviour of system's performance would be similar when considering training sets of different sizes selected from a different initial colour sample. This assumption and the influence of the training set on system's performance will be analyzed in next sub-section.

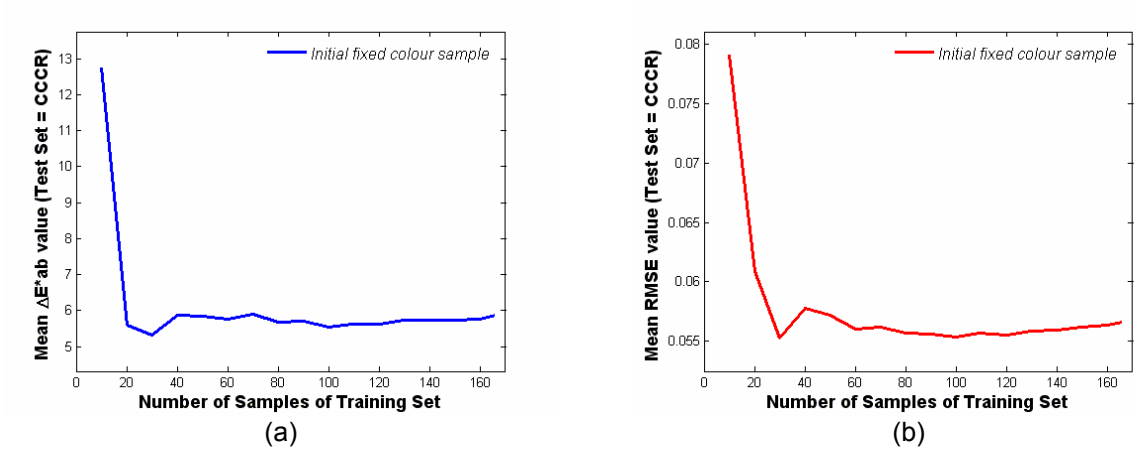

Figure 8.1 *Colorimetric Configuration: (a) mean CIELAB colour difference and (b) mean RMSE values plotted versus the number of colour samples of the training set (initial fixed colour sample).*

As can be seen from Figure 8.1 and from Table 8.2, the improvement on accuracy of both colour measurement and spectral reconstruction, when the number of colour samples of the training set is increased, is limited. This improvement becomes negligible increasing the size of the training set over 60 colour samples approximately, for both the accuracy of colour measurement and the accuracy of spectral reconstruction.

These results point out that there exists a minimum and/or 'sufficient number of colour samples' relatively low for the training set of the imaging system, from which on the increase of the number of samples of the training set does not lead to a noticeable improvement on system's performance.

Table 8.2 *Colorimetric Configuration: mean, minimum, maximum and standard deviation of the CIELAB colour difference and the RMSE values obtained using different sized training sets (initial fixed colour sample) from the CCDC chart and the CCCR chart as test set.*

# colour samples	mean ΔE^*_{ab}	min ΔE^*_{ab}	max ΔE^*_{ab}	std.dev. ΔE^*_{ab}	mean RMSE	min RMSE	max RMSE	std.dev. RMSE
10	12.751	2.179	90.215	19.211	7.905E-02	2.918E-02	1.989E-01	4.352E-02
20	5.606	0.295	12.216	3.278	6.086E-02	2.647E-02	1.671E-01	3.201E-02
30	5.317	1.777	13.503	3.356	5.524E-02	3.307E-02	1.688E-01	2.802E-02
40	5.885	2.577	14.097	3.358	5.779E-02	3.405E-02	1.746E-01	3.053E-02
50	5.852	1.941	14.118	3.511	5.717E-02	2.923E-02	1.742E-01	3.055E-02
60	5.763	2.198	14.110	3.460	5.607E-02	2.762E-02	1.735E-01	3.030E-02
70	5.903	2.256	14.148	3.426	5.616E-02	3.075E-02	1.732E-01	2.989E-02
80	5.681	2.323	13.967	3.431	5.569E-02	2.983E-02	1.720E-01	2.950E-02
90	5.710	2.291	13.891	3.411	5.561E-02	3.035E-02	1.711E-01	2.898E-02
100	5.537	2.089	13.719	3.393	5.534E-02	3.082E-02	1.717E-01	2.929E-02
110	5.628	2.225	13.794	3.333	5.569E-02	3.213E-02	1.706E-01	2.872E-02
120	5.625	2.265	13.837	3.368	5.556E-02	2.987E-02	1.715E-01	2.933E-02
130	5.735	2.312	13.977	3.415	5.586E-02	2.967E-02	1.716E-01	2.945E-02
140	5.726	2.255	13.858	3.409	5.597E-02	3.046E-02	1.710E-01	2.911E-02
150	5.749	2.218	13.879	3.404	5.622E-02	3.152E-02	1.716E-01	2.928E-02
160	5.777	2.219	13.905	3.410	5.633E-02	3.118E-02	1.723E-01	2.963E-02
166	5.886	2.241	13.962	3.414	5.658E-02	3.215E-02	1.728E-01	2.972E-02

8.1.2 Analysis II: Initial randomly selected colour sample

In this second analysis, the initial colour sample is selected randomly from the CCDC chart, and starting from it, the rest of colour samples of the training sets are selected among the colour samples of the CCDC chart by applying the selection criterion for all sizes considered. Five initial colour samples are selected randomly and, from them, the subsequent training sets of the different sizes considered. These training sets will be called 'random' training sets from here on.

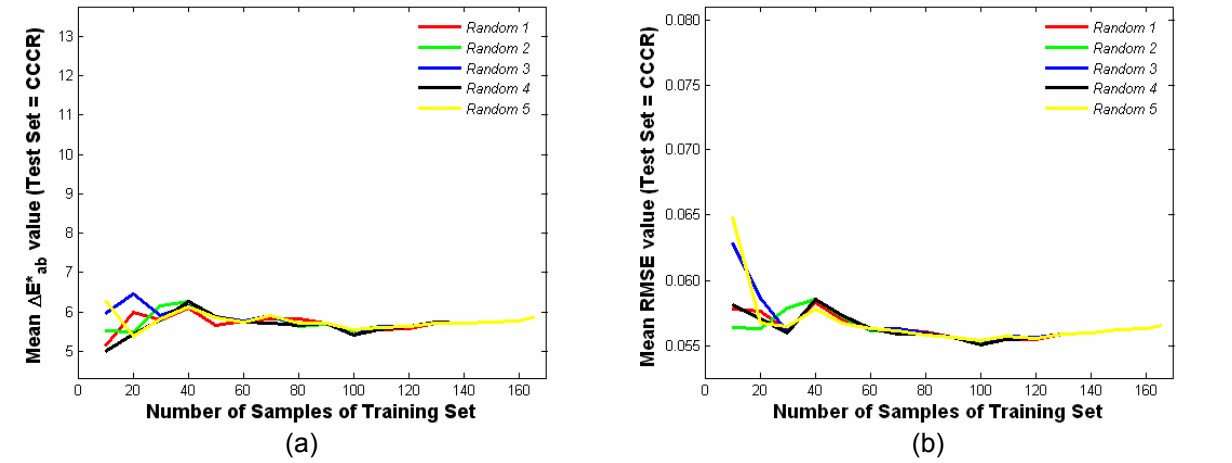

Figure 8.2 *Colorimetric Configuration: (a) mean CIELAB colour difference and (b) mean RMSE values plotted versus the number of colour samples of the training set for the five initial randomly selected colour samples and the subsequent training sets.*

Considering the accuracy of colour measurement, slightly different system's performances are obtained using the five different 'random' training sets for less than 80 colour samples approximately (Figure 8.2 (a)). From 80 samples on, system's performance tends to converge using the five different 'random' training sets at each size, although it still fluctuates depending on the number of samples. The dependence on the training set makes the system's performance fluctuate when using different training sets having the same size. These fluctuations are reduced when the number of colour samples of the training set is increased over 80.

Similarly to the accuracy of colour measurement, regarding the accuracy of spectral reconstruction, slightly different system's performances are obtained using the five different 'random' training sets for less than 80 colour samples approximately (Figure 8.2 (b)). System's performance fluctuates using the five different 'random' training sets with the same size, as a consequence of its dependence on the training set, and tends to converge for the five different 'random' training sets at each size from 80 samples on.

The dependence of system's performance on the training set used can be clearly seen from Figures 8.3 and 8.4, by means of the direct comparison of results obtained using the five different 'random' training sets, for the different sizes considered, in terms of accuracy of both colour measurement (Figure 8.3) and spectral reconstruction (Figure 8.4).

As can be seen from Figure 8.3, in terms of the mean, minimum and maximum CIELAB colour difference values, the smaller the number of samples of the training set is, the greater the fluctuations between the results obtained using the five 'random' training sets are. Similar results are obtained in terms of the mean, minimum and maximum RMSE values (Figure 8.4). The mean and maximum of both the CIELAB colour difference values and the RMSE values present a quite similar behaviour in terms of fluctuations depending on the number of samples of the training set. On the other hand, the minimum values present rather greater fluctuations up to a bigger number of samples of the training set.

The mean, minimum, maximum and standard deviation of the CIELAB colour difference and the RMSE values obtained using the five different 'random' training sets for all sizes considered can be found in Appendix 2 (Tables A2.1 (1) – (3) and A2.2 (1) – (3)). The analysis of these values by means of their mean and standard deviation allows one to quantify the percentage of fluctuation that could be associated to each size of the training set by:

$$\%Fluctuation = 100 \cdot \frac{std.dev.(mean)}{mean} \tag{8.1}$$

Due to the fact that it is really difficult to determine from Figures 8.2, 8.3, and 8.4, the number of samples of the training set from which on the system's performance becomes independent of the training set and does not depend on the number of colour samples, this percentage of fluctuation depending on the number of colour samples of the training set will be used to establish the minimum and/or 'sufficient number of colour samples' for the training set. The percentage of fluctuation for the mean, minimum and maximum of the CIELAB colour difference values and the RMSE values plotted versus the number of samples of the training set can be found in Figures 8.5 and 8.6, respectively.

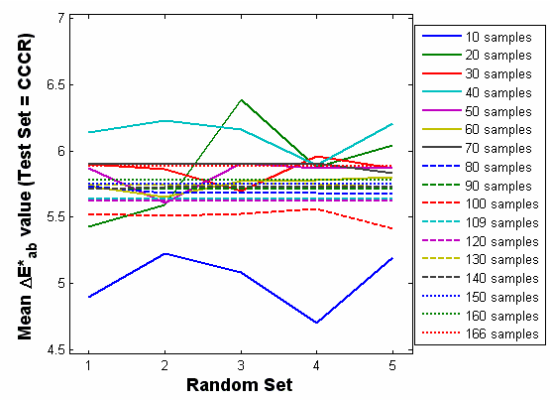

(a)

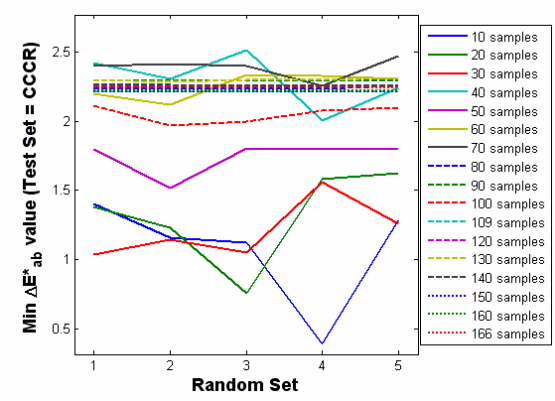

(b)

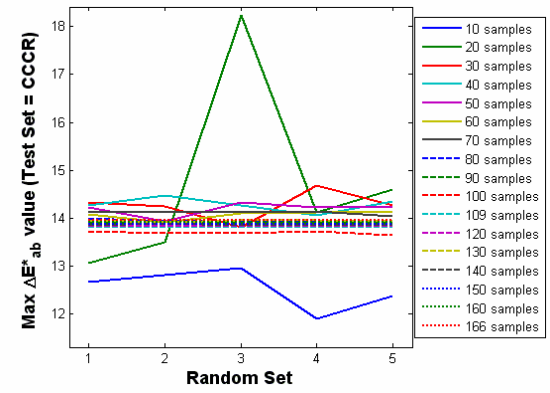

(c)

Figure 8.3 *Colorimetric Configuration: (a) Mean, (b) minimum and (c) maximum CIELAB colour difference values obtained using the five training sets selected from an initial randomly selected CCDC's colour sample, for all sizes of the training set considered, and the CCCR's colour samples as test set.*

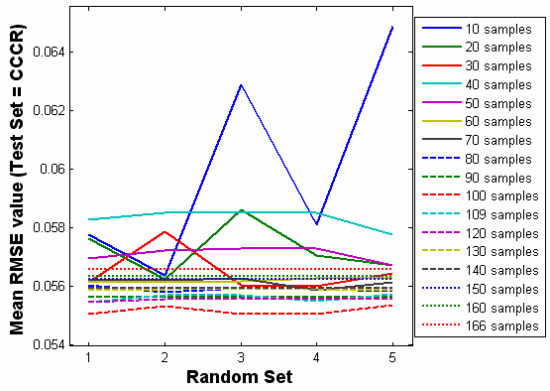

(a)

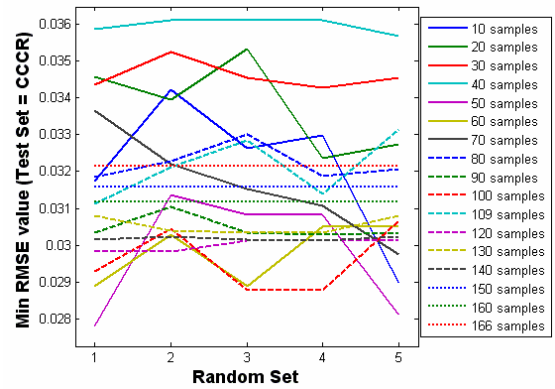

(b)

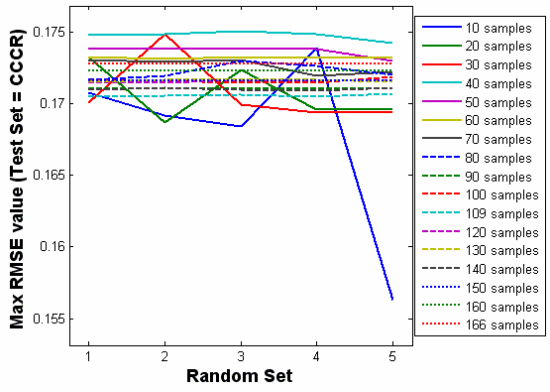

(c)

Figure 8.4 *Colorimetric Configuration: (a) Mean, (b) minimum and (c) maximum RMSE values obtained using the five training sets selected from an initial randomly selected CCDC's colour sample, for all sizes of the training set considered, and the CCCR's colour samples as test set.*

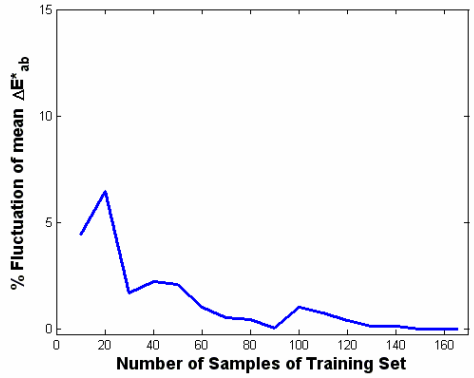

(a)

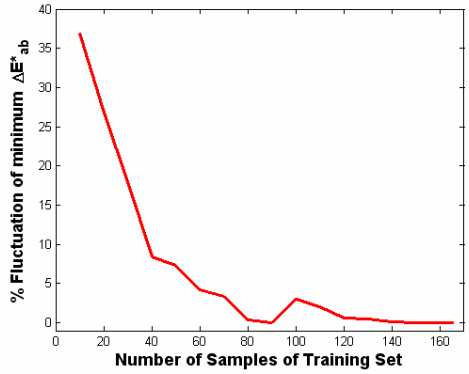

(b)

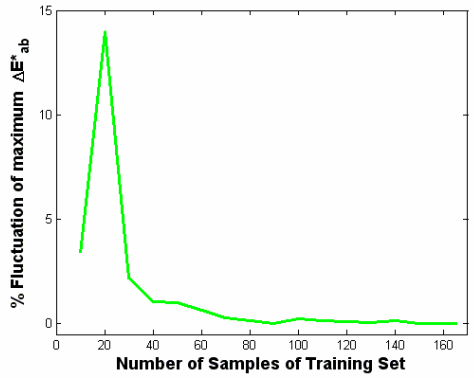

(c)

Figure 8.5 *Colorimetric Configuration: percentage of fluctuation of the (a) mean, (b) minimum and (c) maximum CIELAB colour difference values between results obtained using the five 'random' training sets depending on the number of samples of the training set. The CCCR chart is used as test set.*

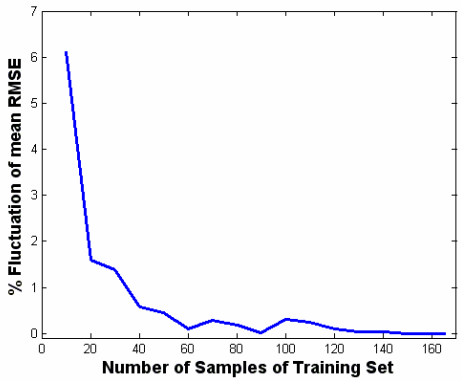

(a)

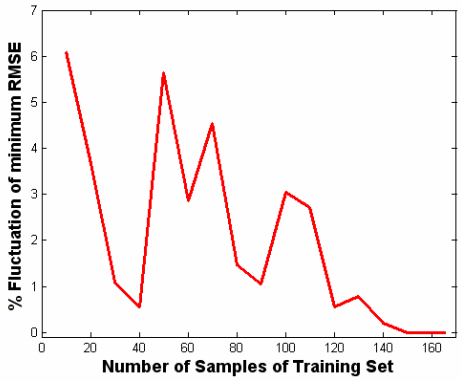

(b)

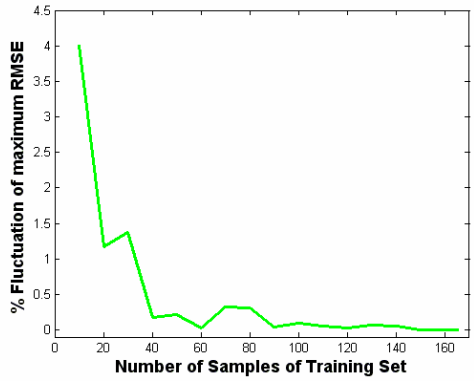

(c)

Figure 8.6 *Colorimetric Configuration: percentage of fluctuation of the (a) mean, (b) minimum and (c) maximum RMSE values between results obtained using the five 'random' training sets depending on the number of samples of the training set. The CCCR chart is used as test set.*

Considering the percentage of fluctuation for the mean, minimum and maximum of the CIELAB colour difference values and the RMSE values depending on the number of samples of the training set (Tables A2.1 (1) – (3) and A2.2 (1) – (3), respectively, in Appendix 2, and Figures 8.5 and 8.6, respectively), the number of colour samples from which on the percentage of fluctuation is negligible can be established in 110 colour samples.

Taking all these results into account, it can be concluded that system's performance seems to become independent of the training set used, in terms of both the number of samples of the training set and the training set itself, when increasing the number of samples over 110. These results hold in terms of accuracy of both colour measurement and spectral reconstruction. Consequently, the minimum and/or 'sufficient number of colour samples' for the training set of the colorimetric configuration of the imaging system would be 110 colour samples.

8.2 Multispectral Configuration

8.2.1 Analysis I: Initial fixed colour sample

Just as for the colorimetric configuration, a first analysis is performed using the first useful colour sample of the CCDC (colour sample B2) as the initial fixed colour sample and, starting from it, the rest of colour samples of the training sets for all sizes considered are selected among the colour samples of the CCDC chart by applying the selection criterion.

Similarly to the colorimetric configuration, the improvement on the accuracy of both colour measurement and spectral reconstruction when increasing the number of colour samples of the training set is limited, and it becomes negligible increasing the size of the training set over 60 colour samples approximately for both the accuracy of colour measurement and the accuracy of spectral reconstruction (Figure 8.7 and Table 8.3).

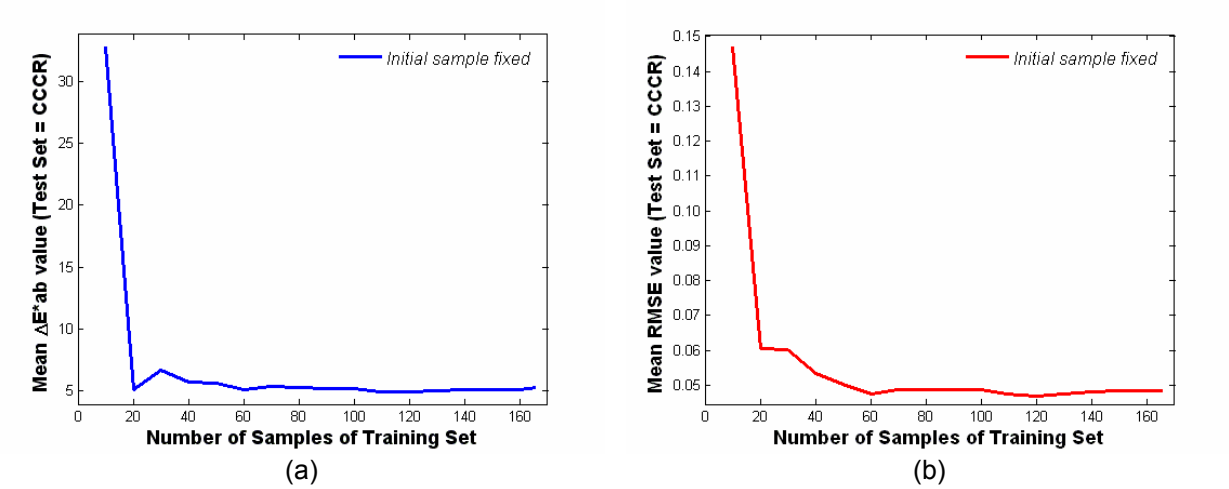

Figure 8.7 *Multispectral Configuration: (a) Mean CIELAB colour difference and (b) mean RMSE values plotted versus the number of colour samples of the training set (initial fixed colour sample).*

Just as before, due to the fact that the training sets selected depend on the initial fixed colour sample used, these results can only be considered as indicative of a tendency of system's performance depending on the number of samples of the training set, if it can be assumed that the behaviour of the system's performance would be similar when considering training sets of different sizes selected from a different initial colour sample.

The dependence of system's performance on the number of colour samples of the training set and on the training set itself is analyzed in next sub-section using five sets of colour samples at each size as training sets, which are selected from an initial randomly selected colour sample of the CCDC chart, and using the CCCR chart as test set.

Table 8.3 *Multispectral Configuration: mean, minimum, maximum and standard deviation of the CIELAB colour difference and the RMSE values obtained using different sized training sets (initial fixed colour sample) from the CCDC chart and the CCCR chart as test set.*

# colour samples	mean ΔE^*_{ab}	min ΔE^*_{ab}	max ΔE^*_{ab}	std.dev. ΔE^*_{ab}	mean RMSE	min RMSE	max RMSE	std.dev. RMSE
10	32.756	2.704	124.469	34.993	1.469E-01	1.541E-02	5.474E-01	1.379E-01
20	5.072	1.524	14.669	3.099	6.050E-02	2.166E-02	1.616E-01	3.235E-02
30	6.712	1.044	31.116	8.048	6.020E-02	2.396E-02	1.546E-01	3.642E-02
40	5.722	1.662	21.737	4.346	5.335E-02	2.683E-02	8.531E-02	1.708E-02
50	5.627	1.679	24.508	4.880	5.033E-02	2.572E-02	9.066E-02	1.654E-02
60	5.135	1.564	21.397	4.177	4.755E-02	2.269E-02	7.803E-02	1.485E-02
70	5.346	1.682	23.328	4.624	4.870E-02	2.063E-02	8.471E-02	1.642E-02
80	5.308	1.633	23.437	4.645	4.865E-02	1.996E-02	8.691E-02	1.676E-02
90	5.218	1.587	22.196	4.353	4.890E-02	2.099E-02	8.267E-02	1.569E-02
100	5.170	1.620	20.424	3.963	4.870E-02	2.271E-02	7.601E-02	1.475E-02
110	4.951	1.320	19.858	3.894	4.742E-02	2.400E-02	7.233E-02	1.389E-02
120	4.924	1.119	19.511	3.802	4.694E-02	2.371E-02	7.195E-02	1.400E-02
130	5.002	1.131	19.894	3.868	4.749E-02	2.378E-02	7.307E-02	1.382E-02
140	5.063	1.235	19.868	3.848	4.818E-02	2.464E-02	7.431E-02	1.389E-02
150	5.107	1.143	20.003	3.871	4.850E-02	2.429E-02	7.595E-02	1.411E-02
160	5.141	1.379	20.339	3.918	4.851E-02	2.380E-02	7.729E-02	1.443E-02
166	5.285	1.794	21.005	3.971	4.835E-02	2.380E-02	7.873E-02	1.457E-02

8.2.2 Analysis II: Initial randomly selected colour sample

In this second analysis, the initial colour sample is selected randomly from the CCDC chart and, starting from it, the rest of colour samples of the training sets are selected among the colour samples of the CCDC chart by applying the selection criterion for all sizes considered. The system's performance using each one of the five 'random' training sets at each size is analyzed depending on the number of samples of the training set.

As can be seen from Figure 8.8, and similarly to the colorimetric configuration, system's performance fluctuates depending on the 'random' training set used for the lower sizes, both in terms of accuracy of colour measurement (Figure 8.8 (a)) and in terms of spectral reconstruction (Figure 8.8 (b)). System's performance seems to converge for the five different 'random' training sets at each size from 80 samples on.

The dependence of system's performance on the training set used for the multispectral configuration can be clearly seen from Figures 8.9 and 8.10, by means of the direct comparison of results obtained using the five different 'random' training sets, for the different sizes considered, in terms of accuracy of both colour measurement (Figure 8.9) and spectral reconstruction (Figure 8.10).

Once more it can be observed that the smaller the number of samples of the training set is, the greater the fluctuations between the results obtained using the five 'random' training sets are for both colour measurements (Figure 8.9) and spectral reconstructions

(Figure 8.10). Similarly to the colorimetric configuration, the mean and maximum values of both the CIELAB colour difference values and the RMSE values present a quite similar behaviour in terms of fluctuations depending on the number of samples of the training set, whereas the minimum values present rather greater fluctuations up to a bigger number of samples of the training set.

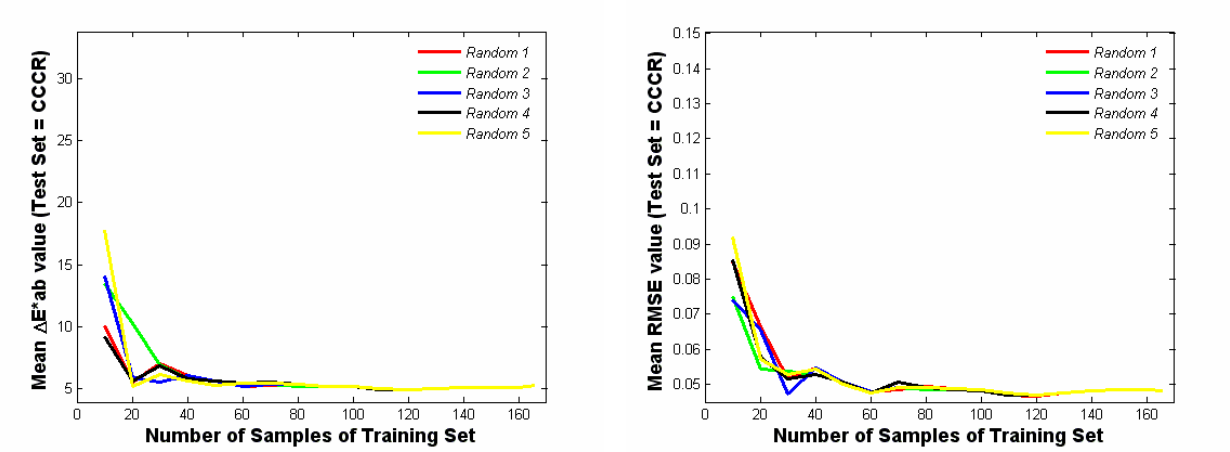

Figure 8.8 *Multispectral Configuration: mean (a) CIELAB colour difference and (b) RMSE values plotted versus the number of colour samples of the training set for the five initial randomly selected colour samples and the subsequent training sets.*

The mean, minimum, maximum and standard deviation of the CIELAB colour difference and the RMSE values obtained using the five 'random' training sets for all sizes considered can be found in Appendix 2 (Tables A2.3 (1) – (3) and A2.4 (1) – (3)).

The percentage of fluctuation defined before (equation (8.1)) is used to determine the number of samples of the training set from which on the system's performance becomes independent of the training set and does not depend on the number of colour samples.

The percentage of fluctuation for the mean, minimum and maximum of the CIELAB colour difference values and the RMSE values plotted versus the number of samples of the training set can be found in Figures 8.11 and 8.12, respectively.

Considering the CIELAB colour difference values, fluctuations in the mean and maximum values become negligible for a number of samples of the training set greater than 100 approximately. On the other hand, the minimum value presents outstanding fluctuations up to 140 samples approximately (Figure 8.11 and Tables A2.3 (1) – (3) in Appendix 2).

Regarding the RMSE values, fluctuations in all mean, minimum and maximum values become negligible for a number of samples of the training set greater than 120 approximately (Figure 8.12 and Tables A2.4 (1) – (3) in Appendix 2).

Taking these results into account, an agreement in terms of accuracy of both colour measurement and spectral reconstruction is reached concluding that system's performance becomes independent of the training set used, in terms of both the number of samples of the training set and the training set itself, when increasing the number of samples over 120 approximately. Consequently, the minimum and/or 'sufficient number of colour samples' for the training set of the multispectral configuration of the imaging system would be 120 colour samples.

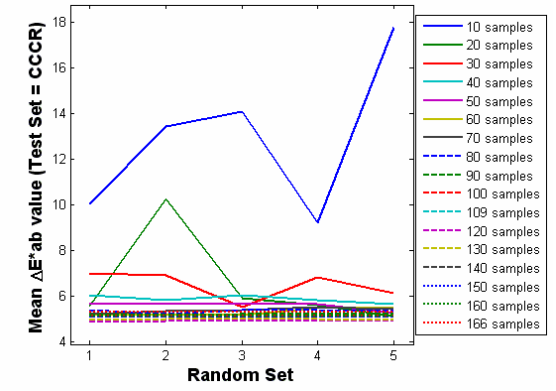

(a)

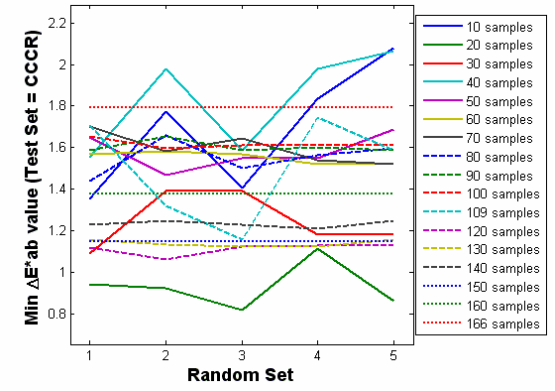

(b)

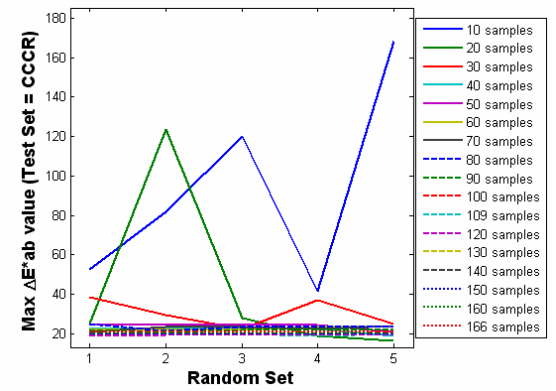

(c)

Figure 8.9 *Multispectral Configuration: (a) mean, (b) minimum and (c) maximum CIELAB colour difference values obtained using the five training sets selected from an initial randomly selected CCDC's colour sample, for all sizes of the training set considered, and the CCCR's colour samples as test set.*

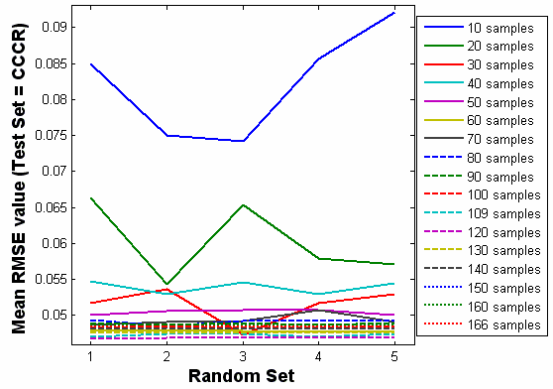

(a)

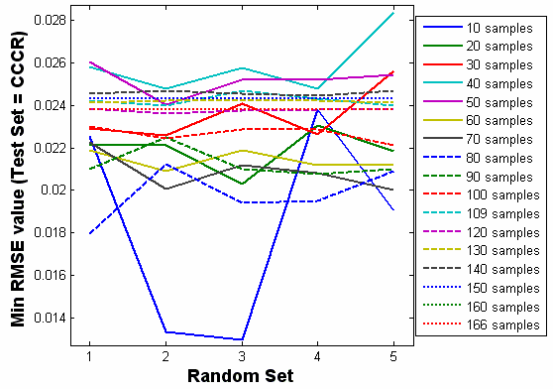

(b)

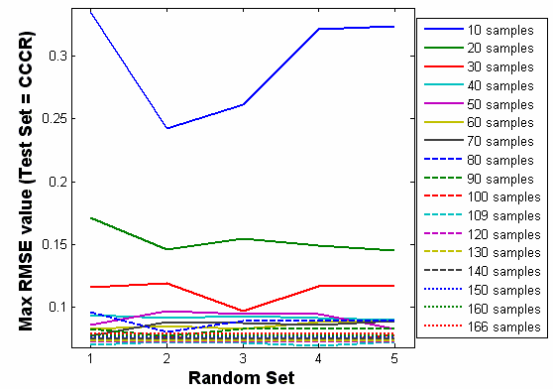

(c)

Figure 8.10 *Multispectral Configuration: (a) mean, (b) minimum and (c) maximum RMSE values obtained using the five training sets selected from an initial randomly selected CCDC's colour sample, for all sizes of the training set considered, and the CCCR's colour samples as test set.*

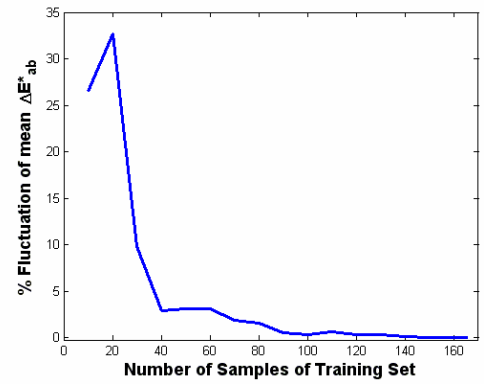

(a)

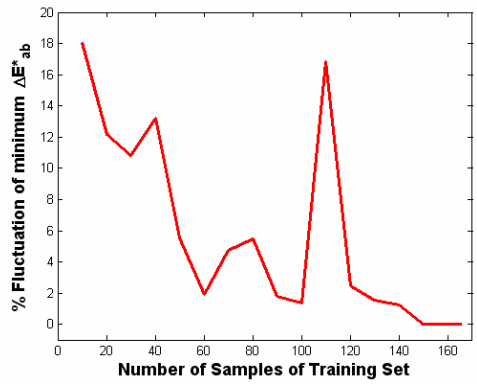

(b)

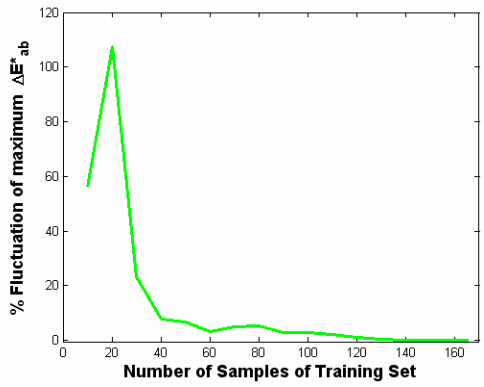

(c)

Figure 8.11 *Multispectral Configuration: percentage of fluctuation of the (a) mean, (b) minimum and (c) maximum CIELAB colour difference values between results obtained using the five 'random' training sets depending on the number of samples of the training set. The CCCR chart is used as test set.*

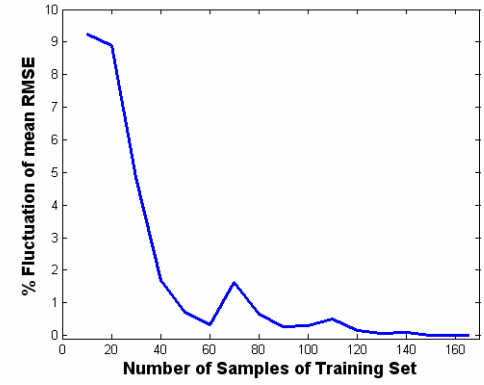

(a)

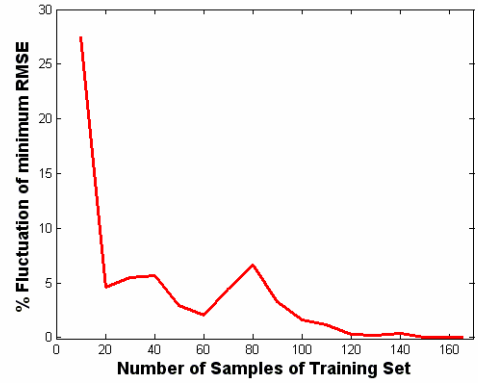

(b)

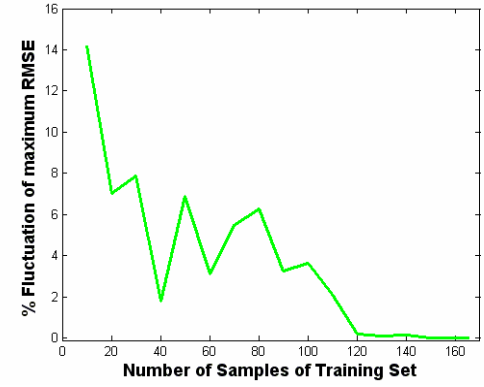

(c)

Figure 8.12 *Multispectral Configuration: percentage of fluctuation of the (a) mean, (b) minimum and (c) maximum RMSE values between results obtained using the five 'random' training sets depending on the number of samples of the training set. The CCCR chart is used as test set.*

9 Influence of Colour Ranges on Accuracy of Colour Measurement and Spectral Reconstruction

Colour measurement and spectral reconstruction performed using both, the colorimetric and the multispectral, configurations of the imaging system are analyzed depending on the colour ranges measured, i.e. sets of colour samples grouped by their hue property, in order to determine if these configurations of the imaging system are especially sensitive to some hues and/or some other colour properties or not.

In order to analyze system's performance, different sets of samples are used as training and test sets. General tendencies of system's performance depending on the colour ranges are firstly evaluated using the GretagMacbeth ColorChecker DC chart (CCDC) as training and test set. Secondly, the 1269 colour patches of the Munsell Book of Color – Matte Collection, classified in 10 Munsell hues (R, YR, Y, GY, G, BG, B, PB, P, RP) and each one of these in 4 sub-hues (2.5, 5, 7.5, 10), are used to analyze the influence of homogeneity in hue of the training set on system's performance. Three combinations of training and test sets of Munsell's colour patches are used in order to vary the degree of homogeneity in hue of the training set. These are: sets of Munsell's colour patches grouped in hues and in sub-hues as training and test sets, sets of Munsell's hues as training sets and sets of Munsell's sub-hues as test sets, and all Munsell's colour patches as training set and sets of Munsell's sub-hues as test sets. Finally, influence of homogeneity in hue of the training set is analyzed considering different sets as training and test sets. This last study is performed using the sets of Munsell's hues as training sets, and the colour samples of the GretagMacbeth ColorChecker DC chart (CCDC) and the GretagMacbeth ColorChecker Color Rendition chart (CCCR), classified in Munsell hues, as test sets.

System's performance is analyzed depending on accuracy of both colour measurement and spectral reconstruction due to the fact that, although general tendency is the better the spectral reconstruction is, the better the colour measurement is, it also occurs that, depending on the colour samples considered, very similar accuracies of spectral reconstruction can be associated to quite different accuracies of colour measurement (Figure 9.1 (a)), or a more accurate spectral reconstruction can be associated to a less accurate colour measurement (Figure 9.1 (b)). These differences in accuracy of colour measurement and spectral reconstruction are explained considering the effect of weighting the reflectance spectra of colour samples by the CIE standard observer colour-matching functions when colour differences are calculated.

Accuracy of colour measurement is evaluated in terms of the mean, minimum, maximum and standard deviation of the mean values of the CIELAB colour differences (ΔE^*_{ab}) between the measured and calculated XYZ tristimulus values. Accuracy of spectral reconstruction is evaluated in terms of the mean, minimum, maximum and standard deviation of the mean values of the Root Mean Square Error (RMSE) between the measured and calculated reflectance spectra.

Furthermore, results obtained are analyzed depending on the colour characteristics of samples measured such as the CIELAB coordinates, and the Munsell hue, value and chroma coordinates.

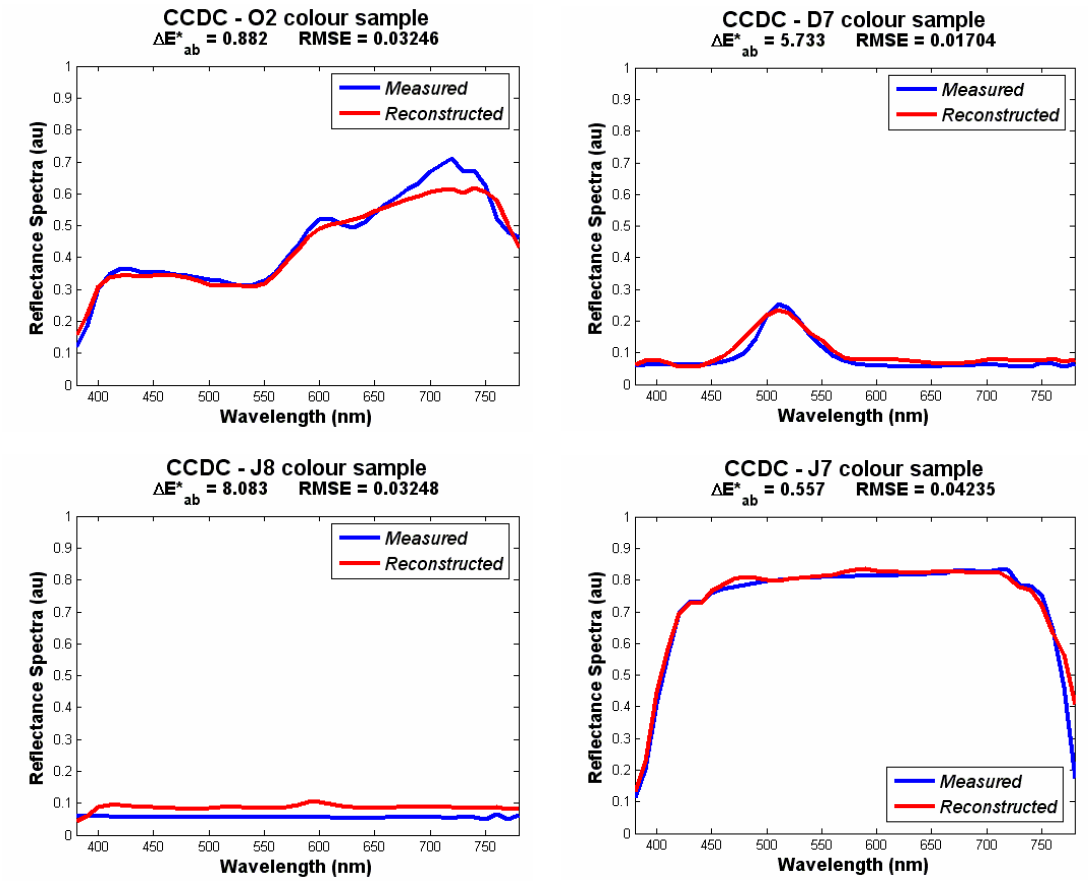

Figure 9.1 *Measured and reconstructed reflectance spectra of the O2, J8, D7, and J7 colour samples of the CCDC chart using the multispectral configuration of the imaging system and the D65 simulator illuminant. (a) O2 and J8 samples: very similar accuracies of spectral reconstruction and quite different accuracies of colour measurement, and (b) D7 and J7 samples: better accuracy of spectral reconstruction does not correspond to better accuracy of colour measurement.*

9.1 General tendencies of system's response depending on the colour ranges

The GretagMacbeth ColorChecker DC chart (CCDC) is widely used in colorimetric characterization of imaging systems because of its wide and adequate selection of colour samples. That is the reason why it is selected to be used to evaluate the general tendencies of system's performance depending on the colour ranges.

Apart from the mean, minimum, maximum and standard deviation values of the CIELAB colour differences (ΔE^*_{ab}) and the RMSEs associated to CCDC's samples, which allow one to evaluate the accuracy of colour measurement and spectral reconstruction, respectively, performed by the system, the CCDC's colour samples are classified in six

groups depending on their CIELAB colour difference and RMSE associated values. These groups are plotted in a*b* and L*C* diagrams in order to facilitate the recognition of any dependence and/or influence of system's accuracy of both colour measurement and spectral reconstruction on the colour ranges.

Next, results obtained for both configurations (colorimetric and multispectral) and for both illuminants used (incandescent lamp and D65 simulator) are presented.

9.1.1 Colorimetric Configuration

As can be seen from Table 9.1, both the CIELAB colour difference and the RMSE values associated to the CCDC's samples present an acceptable average value using both illuminants, although quite high maximum and standard deviation values are obtained. A high standard deviation value is indicative of a wide distribution of values, as it can be seen from Figure 9.2, for the CIELAB colour difference values using both illuminants. The RMSE values presented slightly narrower distributions of values, for both illuminants, than those obtained for the CIELAB colour difference values.

Table 9.1 *Colorimetric Configuration: mean, minimum, maximum and standard deviation of the mean of the ΔE^*_{ab} and RMSE values associated to the CCDC's samples, using the incandescent lamp and D65 simulator illuminants.*

	INCANDESCENT LAMP		D65 SIMULATOR	
	ΔE^*_{ab}	RMSE	ΔE^*_{ab}	RMSE
mean	3.599	4.256E-02	4.719	4.176E-02
minimum	0.352	1.166E-02	0.333	1.581E-02
maximum	10.34	17.57E-02	17.71	14.12E-02
std. dev.	2.307	2.377E-02	3.229	2.109E-02

In terms of colour measurement, better results are obtained using the incandescent lamp illuminant than using the D65 simulator one but, on the contrary, slightly better results are achieved for spectral reconstruction using the D65 simulator illuminant (Table 9.1 and Figure 9.2).

Considering the a*b* and L*C* diagrams for the CCDC's samples grouped depending on their CIELAB colour difference and RMSE values and, as can be seen from Figures 9.3 (a) and 9.3 (b), respectively, there is no correlation between both the CIELAB colour difference values and the RMSE values, and the CIELAB coordinates a* and/or b*. On the other hand, increasing CIELAB colour differences seems to be associated to lower values of L* coordinate, though these tendency is not observed for the RMSE values. These results are common for both illuminants (Figure 9.3 and Figure 9.4).

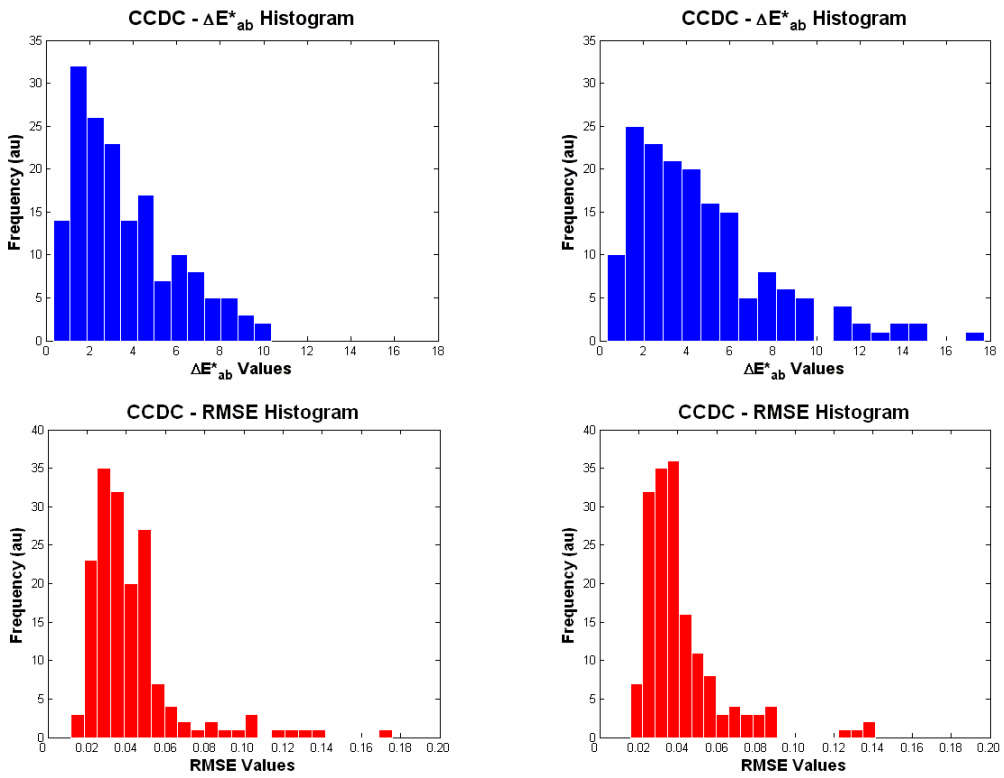

Figure 9.2 *Colorimetric Configuration: histograms of the CIELAB colour difference and the RMSE values associated to the CCDC's samples, using (a) the incandescent lamp and (b) the D65 simulator illuminant.*

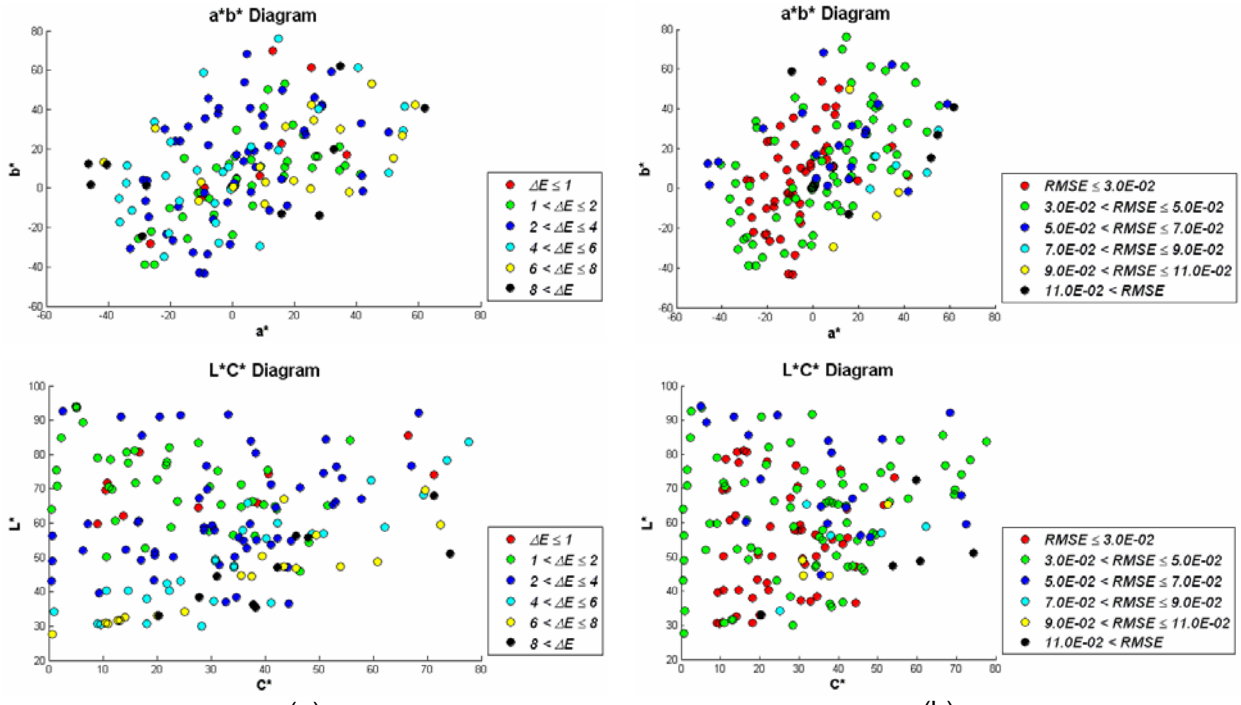

Figure 9.3 *Colorimetric Configuration: a*b* diagram and L*C* diagram for the CCDC's samples grouped in six groups depending on their associated (a) ΔE*ab and (b) RMSE values for the incandescent lamp illuminant.*

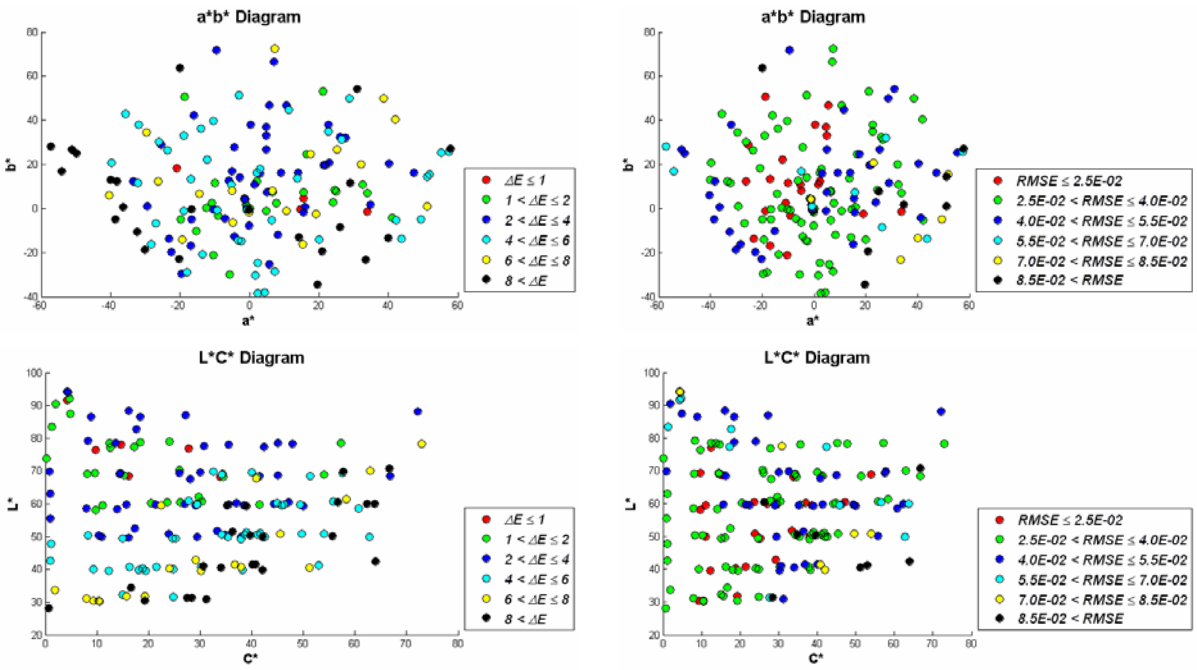

Figure 9.4 *Colorimetric Configuration: a*b* diagram and L*C* diagram for the CCDC's samples grouped in six groups depending on their associated (a) ΔE^*_{ab} and (b) RMSE values for the D65 simulator illuminant.*

9.1.2 Multispectral Configuration

General tendencies of system's performance depending on the colour ranges are equally analyzed for the multispectral configuration using the CCDC chart. Just as for the colorimetric configuration, both the CIELAB colour difference and the RMSE values associated to the CCDC's samples present an acceptable average value but quite high maximum and standard deviation using both illuminants (Table 9.2). These high standard deviation values are related to a wide distribution of values, as can be seen from Figure 9.5 for the CIELAB colour difference values using both illuminants. Slightly narrower distributions are obtained for the RMSE values, mainly for the D65 simulator illuminant.

In this case, unlike the colorimetric configuration, clearly better results are obtained using the D65 simulator illuminant than using the incandescent lamp one, in terms of accuracy of both colour measurement and spectral reconstruction (Table 9.2, Figure 9.5).

Comparing these results to those for the colorimetric configuration, it can be concluded that for the CCDC's samples analyzed, the best combination of system's configuration and illuminant, in terms of accuracy of colour measurement and spectral reconstruction, resulted to be the multispectral configuration and the D65 simulator illuminant. From these results, and taking into account that the CCDC chart is widely known to be a very adequate selection of colour samples to characterize colorimetrically an imaging system, it can be inferred that this combination could provide the best performance of the imaging system in terms of accuracy of colour measurement and spectral reconstruction, globally for any set of colour samples of the same kind (print on paper colour samples). This inference will be analyzed subsequently in this section.

Table 9.2 *Multispectral Configuration: mean, minimum, maximum and standard deviation of the mean of the ΔE^*_{ab} and RMSE values associated to the CCDC's samples, using the incandescent lamp and D65 simulator illuminants.*

	INCANDESCENT LAMP		D65 SIMULATOR	
	ΔE^*_{ab}	RMSE	ΔE^*_{ab}	RMSE
mean	3.352	3.033E-02	2.707	2.762E-02
minimum	0.124	0.817E-02	0.202	1.008E-02
maximum	11.63	10.31E-02	10.04	6.208E-02
std. dev.	2.489	1.262E-02	2.040	1.062E-02

Similarly to the colorimetric configuration, considering the a*b* and L*C* diagrams for the CCDC's samples (Figures 9.6 and 9.7), there is no correlation between both the CIELAB colour difference values and the RMSE values, and the CIELAB coordinates a* and/or b*. On the other hand, it is also observed that increasing CIELAB colour differences seemed to be associated to lower values of L* coordinate, though these tendency is neither observed for the RMSE values. These results are also common for both illuminants (Figures 9.6 and 9.7).

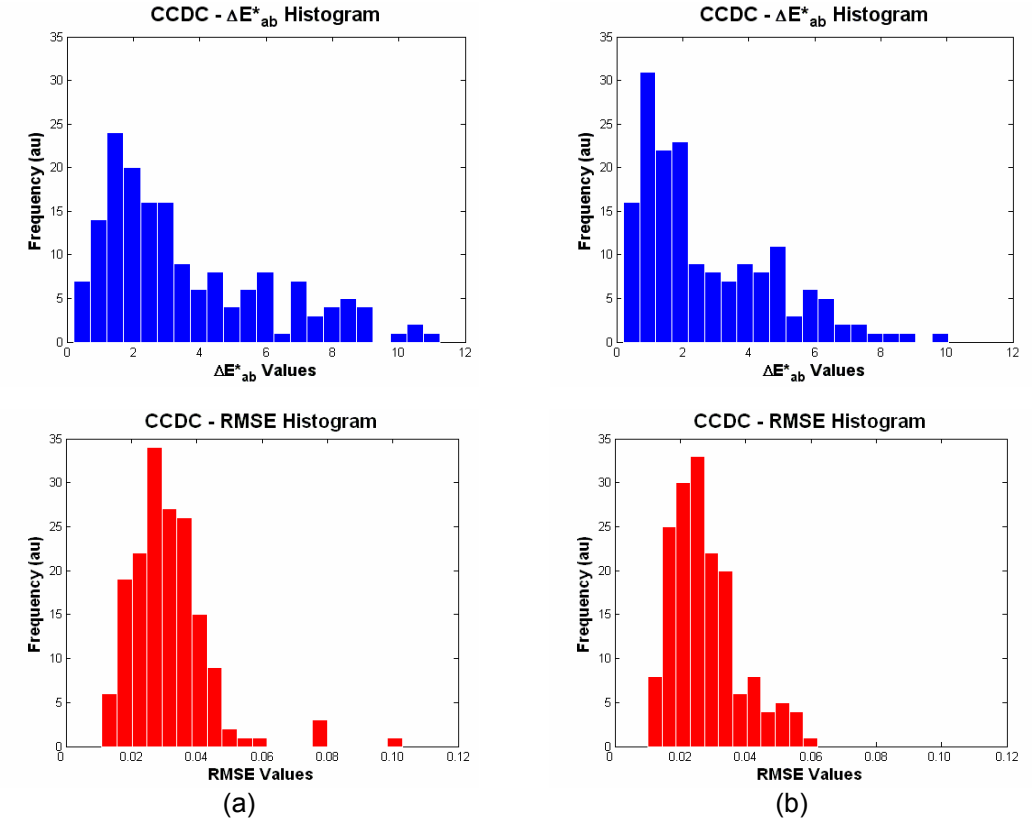

Figure 9.5 *Multispectral Configuration: histograms of the CIELAB colour difference and the RMSE values associated to the CCDC's samples, using (a) the incandescent lamp and (b) the D65 simulator illuminant.*

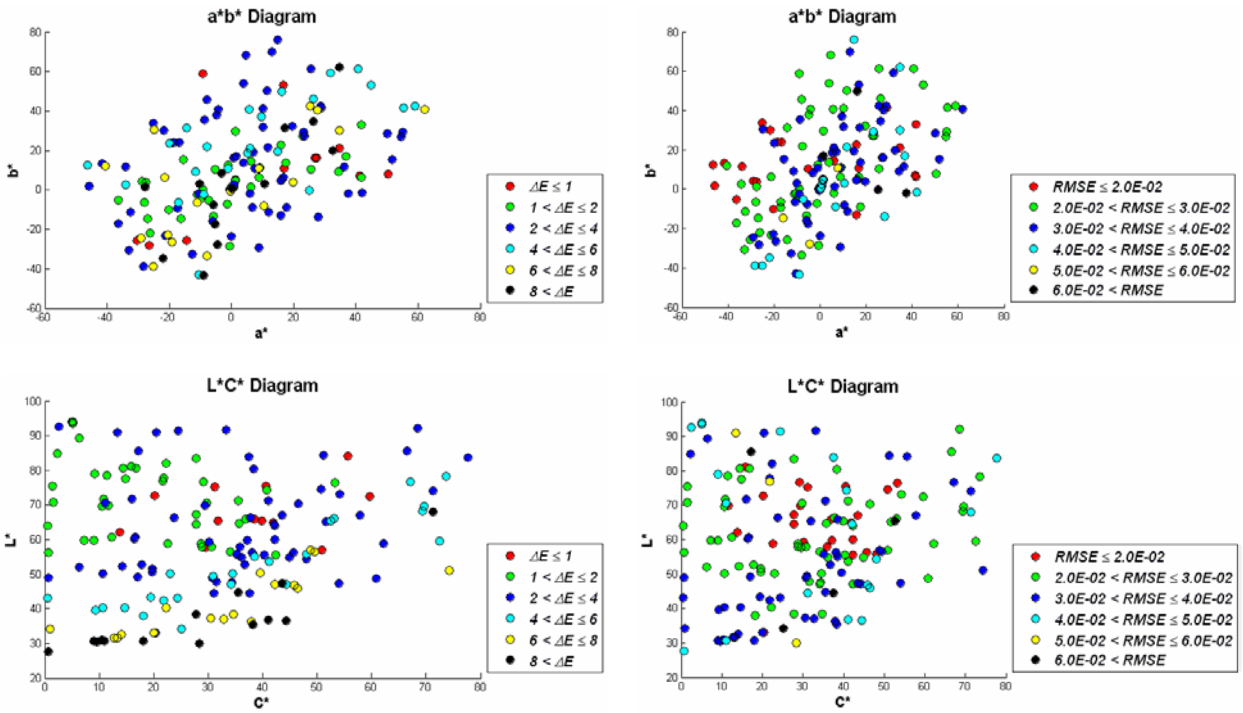

Figure 9.6 *Multispectral Configuration: a*b* diagram and L*C* diagram for the CCDC's samples grouped in six groups depending on their associated (a) ΔE^*_{ab} and (b) RMSE values for the incandescent lamp illuminant.*

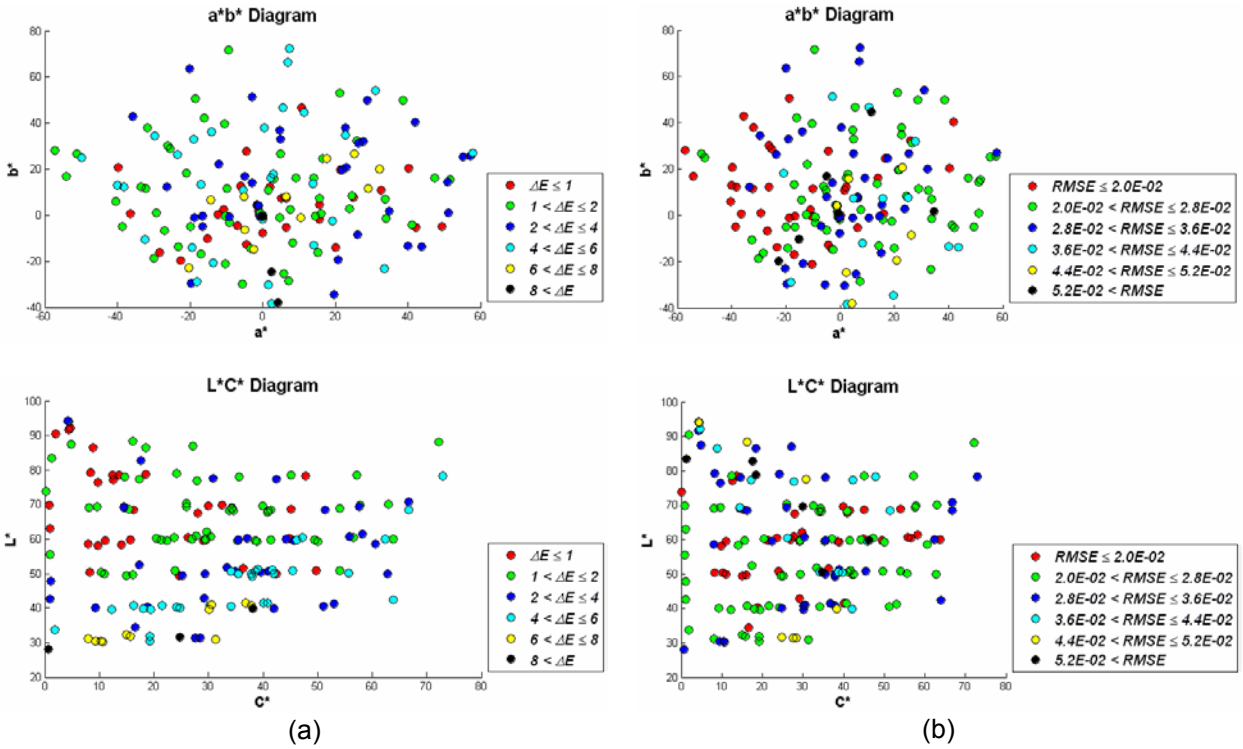

Figure 9.7 *Multispectral Configuration: a*b* diagram and L*C* diagram for the CCDC's samples grouped in six groups depending on their associated (a) ΔE^*_{ab} and (b) RMSE values for the D65 simulator illuminant.*

9.2 Influence of homogeneity in hue of the training set on the accuracy of colour measurement and spectral reconstruction

Results obtained before pointed out that there is no correlation between both the CIELAB colour difference values and the RMSE values and the CIELAB coordinates a* and/or b*, i.e. system's performance seemed to be independent of the colour ranges of samples.

The GretagMacbeth ColorChecker DC chart (CCDC) and GretagMacbeth ColorChecker Color Rendition chart (CCCR) are the training sets used up to know. These charts are widely used in colorimetric characterization of imaging systems because of their more or less wide (CCDC - 166 useful colour samples, CCCR - 24 colour samples) but always appropriate selection of colour samples in order to have a suitable representation of all colour ranges among their samples [Cheung et al., 2004].

Homogeneous training sets in terms of the colour ranges would allow one to carry out a colorimetric characterization of the imaging system per colour ranges. Although system's performance would be very similar between different colour ranges, it could be improved with regard to the system's performance obtained characterizing the imaging system using a multi-colour range training set.

In order to check this hypothesis, the influence of the homogeneity in hue of the training set on accuracy of colour measurement and spectral reconstruction is analyzed. This analysis is carried out using the 1269 colour patches of the Munsell Book of Color – Matte Collection, which are classified in 10 Munsell hues (R, YR, Y, GY, G, BG, B, PB, P, RP) and each one of these in 4 sub-hues (2.5, 5, 7.5, 10). Different combinations of sets of colour patches grouped in hues and sub-hues are used as training and test sets in order to determine the degree of homogeneity to which the system's performance is sensitive.

Sets considered, the number of colour patches at each set, and the range of indexes of colour patches for the Munsell samples used are detailed in Tables 9.3 (1) – (2).

Table 9.3 (1) *Sets of colour patches of the Munsell Book of Color – Matte Collection grouped in hues and sub-hues, number of colour patches at each set and range of indexes for each set.*

	# colour patches	indexes		# colour patches	indexes
2.5R	30	1 – 30	**2.5YR**	29	140 – 168
5R	41	31 – 71	**5YR**	34	169 – 202
7.5R	30	72 – 101	**7.5YR**	26	203 – 228
10R	38	102 – 139	**10YR**	33	229 – 261
All R	139	1 – 139	**All YR**	122	140 – 261
2.5Y	30	262 – 291	**2.5GY**	127	405 – 531
5Y	41	292 – 332	**5GY**	29	405 – 433
7.5Y	32	333 – 364	**7.5GY**	37	434 – 470
10Y	40	365 – 404	**10GY**	26	471 – 496
All Y	143	262 – 404	**All GY**	35	497 - 531
2.5G	26	532 – 557	**2.5BG**	24	647 – 670
5G	33	558 – 590	**5BG**	30	671 – 700
7.5G	25	591 – 615	**7.5BG**	22	701 – 722
10G	31	616 – 646	**10BG**	30	723 – 752
All G	115	532 – 646	**All BG**	106	647 – 752

Table 9.3 (2) *Sets of colour patches of the Munsell Book of Color – Matte Collection grouped in hues and sub-hues, number of colour patches at each set and range of indexes for each set.*

	# colour patches	indexes		# colour patches	indexes
2.5B	22	753 – 774	**2.5PB**	28	865 – 892
5B	31	775 – 805	**5PB**	39	893 – 931
7.5B	25	806 – 830	**7.5PB**	33	932 – 964
10B	34	831 – 864	**10PB**	37	965 - 1001
All B	112	753 – 864	**All PB**	137	865 – 1001
2.5P	28	1002 – 1029	**2.5RP**	31	1133 – 1163
5P	36	1030 – 1065	**5RP**	38	1164 – 1201
7.5P	29	1066 – 1094	**7.5RP**	30	1202 – 1231
10P	38	1095 – 1132	**10RP**	38	1232 – 1269
All P	131	1002 – 1132	**All RP**	137	1133 – 1269

Next, results obtained for the colorimetric and the multispectral configurations using the sets of Munsell's sub-hues and hues as training and test sets are presented.

9.2.1 Colorimetric configuration

Results obtained using all 1269 Munsell's colour patches as training and test set are considered the starting point of this analysis as the less homogeneous training set (Table 9.4.).

Table 9.4. *Colorimetric Configuration: mean, minimum, maximum and standard deviation of the mean of the ΔE^*_{ab} and RMSE values associated to the Munsell's colour patches used as training and test set, using the incandescent lamp and D65 simulator illuminants.*

	INCANDESCENT LAMP		D65 SIMULATOR	
	ΔE^*_{ab}	RMSE	ΔE^*_{ab}	RMSE
mean	8.352	4.125E-02	5.346	4.168E-02
minimum	0.713	1.037E-02	0.215	1.150E-02
maximum	25.026	22.17E-02	19.806	22.75E-02
std. dev.	4.525	2.073E-02	3.441	2.176E-02

In terms of colour measurement, better results are clearly obtained using the D65 simulator illuminant than using the incandescent lamp, unlike results obtained using the CCDC chart as training and test set (Table 9.1). Regarding the spectral reconstruction, very similar results are obtained using both illuminants, although slightly better results are obtained using the incandescent lamp, also unlike results obtained using the CCDC chart (Table 9.1). On the other hand, accuracy of colour measurement is worse for all Munsell's colour patches than for the CCDC chart, using both illuminants, and besides, accuracy of spectral reconstruction is globally slightly better for all Munsell's colour patches than for the CCDC chart, mainly using the incandescent lamp illuminant. These results show that accuracy on colour measurement and spectral reconstruction depends not only on the illuminant but also on the training and test sets considered.

Next, in order to check if system's performance could be improved using homogeneous training sets in terms of hues (colour ranges), with regard to the system's performance obtained characterizing the imaging system using a multi-hue training set (all Munsell's colour patches in this case), accuracy of colour measurement and accuracy of spectral reconstruction are evaluated for different sets of Munsell colour patches homogeneous in hue (Table 9.3), and for both the incandescent lamp and the D65 simulator illuminants.

Considering the accuracy of colour measurement, results obtained for the colorimetric configuration are quite similar between both illuminants (Tables 9.5 (1) – (3)) and there are not outstanding differences between them for any of the Munsell hues and sub-hues. Considering the mean CIELAB colour difference values, slightly differences can be observed between both illuminants and depending on the training and test set considered (Figure 9.8). For example, using the D65 simulator illuminant improved slightly the accuracy of colour measurement performed on the complete YR Munsell hue and its sub-hues, and all sub-hues of the Munsell Y and B hues, but not considering the complete Y and B hues. The slightness of these differences and the fact that they are not consistent for all sets belonging to a same hue do not allow pointing out the appropriateness of one of these illuminants to measure the colour of each Munsell hue when using this configuration of the imaging system.

Regarding the accuracy of spectral reconstruction, results obtained for the colorimetric configuration are also quite similar between both illuminants (Tables 9.6 (1) – (3)). Differences between illuminants for any of the Munsell hues and sub-hues are very slight, and as it occurred for colour measurement, differences in the mean RMSE values also depend on the training and test sets considered (Figure 9.9). In this case, using the incandescent lamp illuminant improves slightly the accuracy of spectral reconstruction performed on the complete R, PB and P Munsell hues and their sub-hues but, just as before, the slightness of these differences and the fact that they are not consistent for the rest of sets belonging to a same hue do not allow to point out the appropriateness of one of these illuminants to perform spectral reconstruction of each Munsell hue when using the colorimetric configuration of the imaging system either.

Table 9.5 (1) *Colorimetric Configuration: mean, minimum, maximum and standard deviation of the mean of the CIELAB colour difference (ΔE^*_{ab}) values of the sub-hues and hues of the Munsell Book of Color – Matte Collection (training & test), using the incandescent lamp and D65 simulator illuminants.*

	INCANDESCENT LAMP					D65 SIMULATOR					
	2.5R	**5R**	**7.5R**	**10R**	**All R**	**2.5R**	**5R**	**7.5R**	**10R**	**All R**	
meanΔE^*_{ab}	3.910	3.936	4.172	3.684	4.361	3.792	3.921	4.265	3.737	4.228	**meanΔE^*_{ab}**
minΔE^*_{ab}	0.580	0.740	0.665	0.364	0.448	0.669	0.426	0.372	0.520	0.268	**minΔE^*_{ab}**
maxΔE^*_{ab}	10.19	10.24	11.28	10.78	12.14	12.52	11.04	10.77	10.97	12.13	**maxΔE^*_{ab}**
stddev ΔE^*_{ab}	2.589	2.523	3.054	2.792	2.942	3.153	2.856	3.061	2.939	3.035	**stddev ΔE^*_{ab}**
	2.5YR	**5YR**	**7.5YR**	**10YR**	**All YR**	**2.5YR**	**5YR**	**7.5YR**	**10YR**	**All YR**	
meanΔE^*_{ab}	3.696	3.937	3.334	3.259	3.758	3.609	3.844	3.251	3.187	3.652	**meanΔE^*_{ab}**
minΔE^*_{ab}	0.458	0.563	0.722	0.786	0.385	0.847	0.521	1.020	0.276	0.168	**minΔE^*_{ab}**
maxΔE^*_{ab}	10.91	10.27	8.502	11.52	11.34	10.59	13.63	8.339	11.36	11.27	**maxΔE^*_{ab}**
stddev ΔE^*_{ab}	2.961	3.114	2.190	2.892	2.780	2.654	3.307	1.892	2.757	2.648	**stddev ΔE^*_{ab}**
	2.5Y	**5Y**	**7.5Y**	**10Y**	**All Y**	**2.5Y**	**5Y**	**7.5Y**	**10Y**	**All Y**	
meanΔE^*_{ab}	3.331	3.651	3.808	3.935	4.105	3.252	3.532	3.500	3.639	4.429	**meanΔE^*_{ab}**
minΔE^*_{ab}	0.357	0.384	0.448	0.565	0.223	0.557	0.471	0.611	0.246	0.455	**minΔE^*_{ab}**
maxΔE^*_{ab}	12.78	13.48	10.82	10.77	17.05	12.52	10.81	10.82	13.67	16.26	**maxΔE^*_{ab}**
stddev ΔE^*_{ab}	2.918	3.001	2.347	2.611	2.782	2.888	2.832	2.479	2.857	2.796	**stddev ΔE^*_{ab}**
	2.5GY	**5GY**	**7.5GY**	**10GY**	**All GY**	**2.5GY**	**5GY**	**7.5GY**	**10GY**	**All GY**	
meanΔE^*_{ab}	3.377	3.424	2.875	3.370	3.882	3.017	3.285	3.303	3.218	4.200	**meanΔE^*_{ab}**
minΔE^*_{ab}	0.327	0.671	0.459	0.289	0.308	0.298	0.742	0.658	0.501	0.378	**minΔE^*_{ab}**
maxΔE^*_{ab}	10.31	9.945	6.819	8.352	12.11	12.10	9.612	13.41	7.561	12.61	**maxΔE^*_{ab}**
stddev ΔE^*_{ab}	2.257	2.331	1.745	2.151	2.487	2.505	2.183	2.559	2.064	2.670	**stddev ΔE^*_{ab}**

Table 9.5 (2) *Colorimetric Configuration: mean, minimum, maximum and standard deviation of the mean of the CIELAB colour difference (ΔE^*_{ab}) values of the sub-hues and hues of the Munsell Book of Color – Matte Collection (training & test), using the incandescent lamp and D65 simulator illuminants.*

	INCANDESCENT LAMP					D65 SIMULATOR					
	2.5G	**5G**	**7.5G**	**10G**	**All G**	**2.5G**	**5G**	**7.5G**	**10G**	**All G**	
meanΔE^*_{ab}	3.480	3.274	3.140	3.780	4.214	3.654	3.765	3.717	3.543	4.407	**meanΔE^*_{ab}**
minΔE^*_{ab}	0.100	0.330	0.185	1.256	0.533	0.360	0.330	0.772	0.447	0.377	**minΔE^*_{ab}**
maxΔE^*_{ab}	9.248	13.77	7.909	9.363	11.16	10.13	11.22	10.54	9.837	12.02	**maxΔE^*_{ab}**
stddev ΔE^*_{ab}	2.346	2.738	2.651	2.166	2.839	2.819	3.082	2.819	2.821	3.177	**stddev ΔE^*_{ab}**
	2.5BG	**5BG**	**7.5BG**	**10BG**	**All BG**	**2.5BG**	**5BG**	**7.5BG**	**10BG**	**All BG**	
meanΔE^*_{ab}	2.813	3.486	3.661	3.942	4.095	2.599	3.541	3.442	3.790	4.636	**meanΔE^*_{ab}**
minΔE^*_{ab}	0.355	0.252	1.105	0.658	0.506	0.421	0.294	1.058	0.447	0.520	**minΔE^*_{ab}**
maxΔE^*_{ab}	8.429	9.529	10.93	10.57	10.88	7.796	10.34	10.06	9.961	12.65	**maxΔE^*_{ab}**
stddev ΔE^*_{ab}	2.399	2.695	2.467	3.021	2.819	2.236	2.732	2.433	2.884	3.090	**stddev ΔE^*_{ab}**
	2.5B	**5B**	**7.5B**	**10B**	**All B**	**2.5B**	**5B**	**7.5B**	**10B**	**All B**	
meanΔE^*_{ab}	3.284	3.783	3.646	3.891	4.037	2.938	3.570	3.579	3.589	4.275	**meanΔE^*_{ab}**
minΔE^*_{ab}	0.641	0.379	0.333	0.320	0.315	0.445	0.343	0.286	0.478	0.257	**minΔE^*_{ab}**
maxΔE^*_{ab}	9.127	10.31	12.27	10.83	11.73	8.341	9.930	11.68	9.363	11.72	**maxΔE^*_{ab}**
stddev ΔE^*_{ab}	2.283	2.833	2.816	3.107	2.745	2.284	2.824	2.787	2.665	2.898	**stddev ΔE^*_{ab}**
	2.5PB	**5PB**	**7.5PB**	**10PB**	**All PB**	**2.5PB**	**5PB**	**7.5PB**	**10PB**	**All PB**	
meanΔE^*_{ab}	3.528	3.766	3.501	2.876	4.269	3.474	3.673	3.906	3.237	4.212	**meanΔE^*_{ab}**
minΔE^*_{ab}	0.695	0.258	0.379	0.343	0.431	0.706	0.192	0.278	0.162	0.277	**minΔE^*_{ab}**
maxΔE^*_{ab}	10.41	11.55	8.429	8.698	12.86	10.11	11.42	9.646	11.82	14.38	**maxΔE^*_{ab}**
stddev ΔE^*_{ab}	2.693	2.865	2.491	2.494	3.023	2.599	2.876	3.026	2.887	3.169	**stddev ΔE^*_{ab}**

Table 9.5 (3) *Colorimetric Configuration: mean, minimum, maximum and standard deviation of the mean of the CIELAB colour difference (ΔE^*_{ab}) values of the sub-hues and hues of the Munsell Book of Color – Matte Collection (training & test), using the incandescent lamp and D65 simulator illuminants.*

	INCANDESCENT LAMP					D65 SIMULATOR					
	2.5P	**5P**	**7.5P**	**10P**	**All P**	**2.5P**	**5P**	**7.5P**	**10P**	**All P**	
meanΔE^*_{ab}	4.213	4.719	3.796	3.955	4.643	4.573	4.865	4.322	4.304	4.691	**meanΔE^*_{ab}**
minΔE^*_{ab}	0.975	0.679	0.442	0.752	0.822	0.588	0.343	0.344	0.685	0.590	**minΔE^*_{ab}**
maxΔE^*_{ab}	13.29	11.26	11.75	11.69	12.12	15.49	11.32	12.34	15.46	14.55	**maxΔE^*_{ab}**
stddev ΔE^*_{ab}	3.636	3.259	3.462	3.223	3.198	4.049	3.556	3.913	3.916	3.613	**stddev ΔE^*_{ab}**
	2.5RP	**5RP**	**7.5RP**	**10RP**	**All RP**	**2.5RP**	**5RP**	**7.5RP**	**10RP**	**All RP**	
meanΔE^*_{ab}	3.039	4.270	3.541	4.279	4.367	3.170	4.248	4.038	3.914	4.436	**meanΔE^*_{ab}**
minΔE^*_{ab}	0.050	0.651	0.834	0.875	0.366	0.470	0.202	0.563	0.292	0.407	**minΔE^*_{ab}**
maxΔE^*_{ab}	11.52	11.22	10.48	10.86	12.18	13.00	12.29	13.43	14.96	12.67	**maxΔE^*_{ab}**
stddev ΔE^*_{ab}	3.077	3.106	2.556	2.758	3.169	3.502	3.652	3.834	3.702	3.351	**stddev ΔE^*_{ab}**

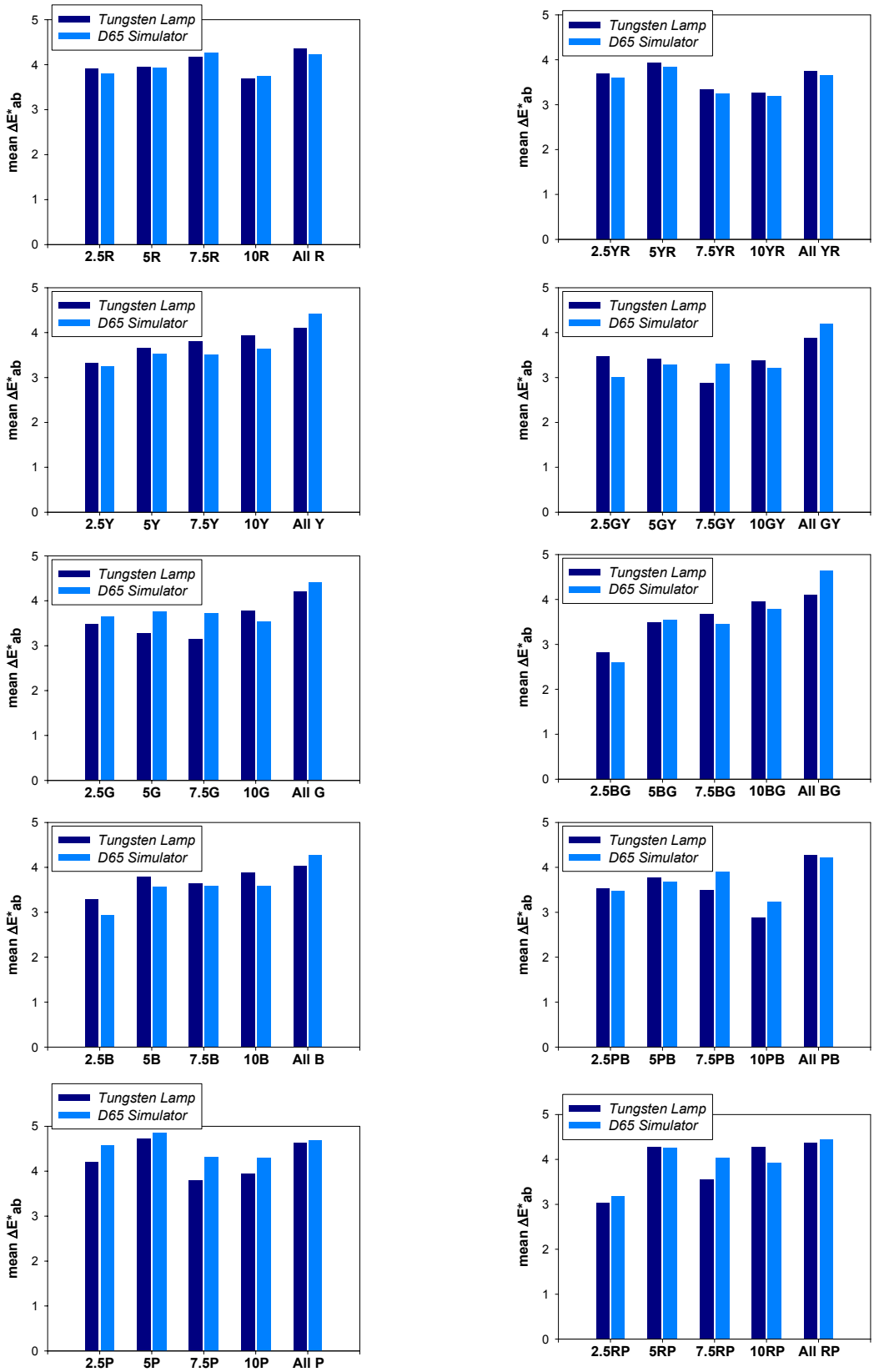

Figure 9.8 *Colorimetric Configuration: Bar plots of the mean ΔE*ab values for all hues (R, YR, Y, GY, G, BG, B, PB, P, RP) and sub-hues of each hue (2.5, 5, 7.5, 10) of the Munsell Book of Color – Matte Collection (training & test), for the incandescent lamp and the D65 simulator illuminants.*

Table 9.6 (1) *Colorimetric Configuration: mean, minimum, maximum and standard deviation of the mean of the RMSE values of the sub-hues and hues of the Munsell Book of Color – Matte Collection (training & test), using the incandescent lamp and D65 simulator illuminants.*

	INCANDESCENT LAMP					D65 SIMULATOR					
	2'5R	**5R**	**7'5R**	**10R**	**All R**	**2'5R**	**5R**	**7'5R**	**10R**	**All R**	
meanRMSE	3.318E-02	3.363E-02	2.941E-02	2.667E-02	3.530E-02	3.565E-02	3.875E-02	3.326E-02	2.680E-02	3.747E-02	**meanRMSE**
minRMSE	0.581E-02	0.759E-02	0.645E-02	0.692E-02	0.815E-02	1.153E-02	0.912E-02	1.093E-02	0.534E-02	1.159E-02	**minRMSE**
maxRMSE	7.646E-02	7.594E-02	7.431E-02	4.781E-02	10.34E-02	8.467E-02	9.397E-02	9.012E-02	4.944E-02	12.48E-02	**maxRMSE**
stddev RMSE	1.61E-02	1.59E-02	1.34E-02	1.09E-02	1.64E-02	1.84E-02	2.24E-02	1.57E-02	1.16E-02	1.97E-02	**stddev RMSE**
	2'5YR	**5YR**	**7'5YR**	**10YR**	**All YR**	**2'5YR**	**5YR**	**7'5YR**	**10YR**	**All YR**	
meanRMSE	2.603E-02	2.579E-02	2.374E-02	2.464E-02	2.802E-02	2.765E-02	2.643E-02	2.485E-02	2.389E-02	2.918E-02	**meanRMSE**
minRMSE	0.899E-02	0.635E-02	0.603E-02	0.578E-02	0.696E-02	0.625E-02	0.797E-02	0.976E-02	0.361E-02	0.507E-02	**minRMSE**
maxRMSE	5.942E-02	4.537E-02	5.552E-02	4.438E-02	5.740E-02	6.524E-02	4.718E-02	6.128E-02	4.267E-02	6.522E-02	**maxRMSE**
stddev RMSE	1.07E-02	1.16E-02	1.37E-02	1.08E-02	1.12E-02	1.25E-02	1.19E-02	1.22E-02	1.11E-02	1.22E-02	**stddev RMSE**
	2'5Y	**5Y**	**7'5Y**	**10Y**	**All Y**	**2'5Y**	**5Y**	**7'5Y**	**10Y**	**All Y**	
meanRMSE	2.681E-02	2.744E-02	2.904E-02	2.705E-02	3.490E-02	2.425E-02	2.974E-02	3.039E-02	2.743E-02	3.621E-02	**meanRMSE**
minRMSE	0.514E-02	0.542E-02	0.906E-02	0.721E-02	0.947E-02	0.763E-02	0.492E-02	0.954E-02	0.690E-02	0.964E-02	**minRMSE**
maxRMSE	5.433E-02	6.772E-02	7.665E-02	6.479E-02	7.205E-02	5.541E-02	6.484E-02	8.593E-02	6.719E-02	7.967E-02	**maxRMSE**
stddev RMSE	1.33E-02	1.46E-02	1.47E-02	1.31E-02	1.23E-02	1.35E-02	1.49E-02	1.65E-02	1.40E-02	1.32E-02	**stddev RMSE**
	2'5GY	**5GY**	**7'5GY**	**10GY**	**All GY**	**2'5GY**	**5GY**	**7'5GY**	**10GY**	**All GY**	
meanRMSE	2.336E-02	2.548E-02	1.840E-02	2.467E-02	3.008E-02	2.165E-02	2.691E-02	1.893E-02	2.307E-02	3.119E-02	**meanRMSE**
minRMSE	0.748E-02	0.699E-02	0.742E-02	0.71E-02	1.026E-02	0.291E-02	0.619E-02	0.869E-02	0.527E-02	0.714E-02	**minRMSE**
maxRMSE	5.503E-02	7.460E-02	3.933E-02	5.758E-02	5.859E-02	5.240E-02	7.969E-02	3.210E-02	5.143E-02	6.183E-02	**maxRMSE**
stddev RMSE	1.27E-02	1.45E-02	0.822E-03	1.14E-02	1.25E-02	1.17E-02	1.47E-02	0.685E-02	1.19E-02	1.33E-02	**stddev RMSE**

Table 9.6 (2) *Colorimetric Configuration: mean, minimum, maximum and standard deviation of the mean of the RMSE values of the sub-hues and hues of the Munsell Book of Color – Matte Collection (training & test), using the incandescent lamp and D65 simulator illuminants.*

	INCANDESCENT LAMP					D65 SIMULATOR					
	2'5G	**5G**	**7'5G**	**10G**	**All G**	**2'5G**	**5G**	**7'5G**	**10G**	**All G**	
meanRMSE	2.009E-02	2.058E-02	1.973E-02	2.195E-02	2.539E-02	2.100E-02	2.284E-02	2.275E-02	2.085E-02	2.622E-02	**meanRMSE**
minRMSE	0.376E-02	0.633E-02	0.248E-02	0.761E-02	0.743E-02	0.259E-02	0.933E-02	0.563E-02	0.732E-02	0.792E-02	**minRMSE**
maxRMSE	5.352E-02	4.803E-02	5.230E-02	3.650E-02	6.975E-02	5.985E-02	4.711E-02	5.878E-02	4.076E-02	6.831E-02	**maxRMSE**
stddev RMSE	1.09E-02	0.966E-02	1.22E-02	0.750E-02	1.17E-02	1.37E-02	1.03E-02	1.44E-02	0.874E-02	1.25E-02	**stddev RMSE**
	2'5BG	**5BG**	**7'5BG**	**10BG**	**All BG**	**2'5BG**	**5BG**	**7'5BG**	**10BG**	**All BG**	
meanRMSE	1.733E-02	2.218E-02	2.191E-02	2.589E-02	2.616E-02	1.568E-02	2.279E-02	2.185E-02	2.568E-02	2.672E-02	**meanRMSE**
minRMSE	0.254E-02	0.373E-02	0.865E-02	0.532E-02	0.725E-02	0.412E-02	0.509E-02	0.819E-02	0.363E-02	0.638E-02	**minRMSE**
maxRMSE	4.239E-02	5.793E-02	3.775E-02	6.498E-02	7.259E-02	3.791E-02	5.748E-02	3.955E-02	6.569E-02	7.271E-02	**maxRMSE**
stddev RMSE	0.971E-02	1.16E-02	1.05E-02	1.42E-02	1.19E-02	0.884E-02	1.23E-02	1.04E-02	1.46E-02	1.24E-02	**stddev RMSE**
	2'5B	**5B**	**7'5B**	**10B**	**All B**	**2'5B**	**5B**	**7'5B**	**10B**	**All B**	
meanRMSE	2.129E-02	2.557E-02	2.600E-02	2.729E-02	2.862E-02	2.120E-02	2.515E-02	2.598E-02	2.680E-02	2.866E-02	**meanRMSE**
minRMSE	0.480E-02	0.572E-02	0.734E-02	0.612E-02	0.727E-02	0.403E-02	0.647E-02	0.632E-02	0.571E-02	0.517E-02	**minRMSE**
maxRMSE	4.109E-02	5.210E-02	5.279E-02	6.408E-02	6.195E-02	4.527E-02	5.456E-02	5.584E-02	6.597E-02	6.350E-02	**maxRMSE**
stddev RMSE	1.09E-02	1.28E-02	1.18E-02	1.21E-02	1.13E-02	1.15E-02	1.31E-02	1.23E-02	1.25E-02	1.15E-02	**stddev RMSE**
	2'5PB	**5PB**	**7'5PB**	**10PB**	**All PB**	**2'5PB**	**5PB**	**7'5PB**	**10PB**	**All PB**	
meanRMSE	2.619E-02	2.680E-02	2.480E-02	2.249E-02	3.050E-02	2.634E-02	2.741E-02	2.798E-02	2.260E-02	3.067E-02	**meanRMSE**
minRMSE	0.861E-02	0.786E-02	0.879E-02	0.589E-0	0.619E-02	1.032E-02	0.809E-02	0.741E-02	0.522E-02	0.643E-02	**minRMSE**
maxRMSE	4.603E-02	4.708E-02	8.986E-02	4.951E-02	8.307E-02	5.061E-02	5.045E-02	8.977E-02	4.965E-02	8.197E-02	**maxRMSE**
stddev RMSE	1.06E-02	1.04E-02	1.43E-02	1.06E-02	1.24E-02	1.06E-02	1.22E-02	1.51E-02	1.05E-02	1.22E-02	**stddev RMSE**

Table 9.6 (3) *Colorimetric Configuration: mean, minimum, maximum and standard deviation of the mean of the RMSE values of the sub-hues and hues of the Munsell Book of Color – Matte Collection (training & test), using the incandescent lamp and D65 simulator illuminants.*

	INCANDESCENT LAMP					D65 SIMULATOR					
	2'5P	**5P**	**7'5P**	**10P**	**All P**	**2'5P**	**5P**	**7'5P**	**10P**	**All P**	
meanRMSE	3.201E-02	3.764E-02	3.718E-02	2.958E-02	4.812E-02	3.541E-02	4.186E-02	4.009E-02	3.102E-02	4.820E-02	**meanRMSE**
minRMSE	0.702E-02	1.441E-02	0.829E-02	0.661E-02	0.914E-02	1.172E-02	1.383E-02	0.953E-02	0.826E-02	0.714E-02	**minRMSE**
maxRMSE	10.99E-02	13.34E-02	17.28E-02	10.60E-02	20.97E-02	12.23E-02	16.20E-02	17.39E-02	14.80E-02	20.83E-02	**maxRMSE**
stddev RMSE	1.99E-02	2.08E-02	3.03E-02	1.69E-02	3.10E-02	2.30E-02	2.60E-02	3.14E-02	2.44E-02	3.12E-02	**stddev RMSE**
	2'5RP	**5RP**	**7'5RP**	**10RP**	**All RP**	**2'5RP**	**5RP**	**7'5RP**	**10RP**	**All RP**	
meanRMSE	2.244E-02	3.054E-02	3.170E-02	3.953E-02	3.619E-02	2.379E-02	2.966E-02	3.052E-02	3.683E-02	3.771E-02	**meanRMSE**
minRMSE	0.591E-02	0.544E-02	0.609E-02	0.921E-02	0.979E-02	0.284E-02	1.355E-02	0.670E-02	0.579E-02	0.967E-02	**minRMSE**
maxRMSE	5.270E-02	5.748E-02	8.063E-02	16.05E-02	15.87E-02	6.071E-02	6.319E-02	7.712E-02	14.54E-02	16.69E-02	**maxRMSE**
stddev RMSE	1.10E-02	1.25E-02	1.69E-02	2.61E-02	1.87E-02	1.28E-02	1.40E-02	1.57E-02	2.73E-02	2.05E-02	**stddev RMSE**

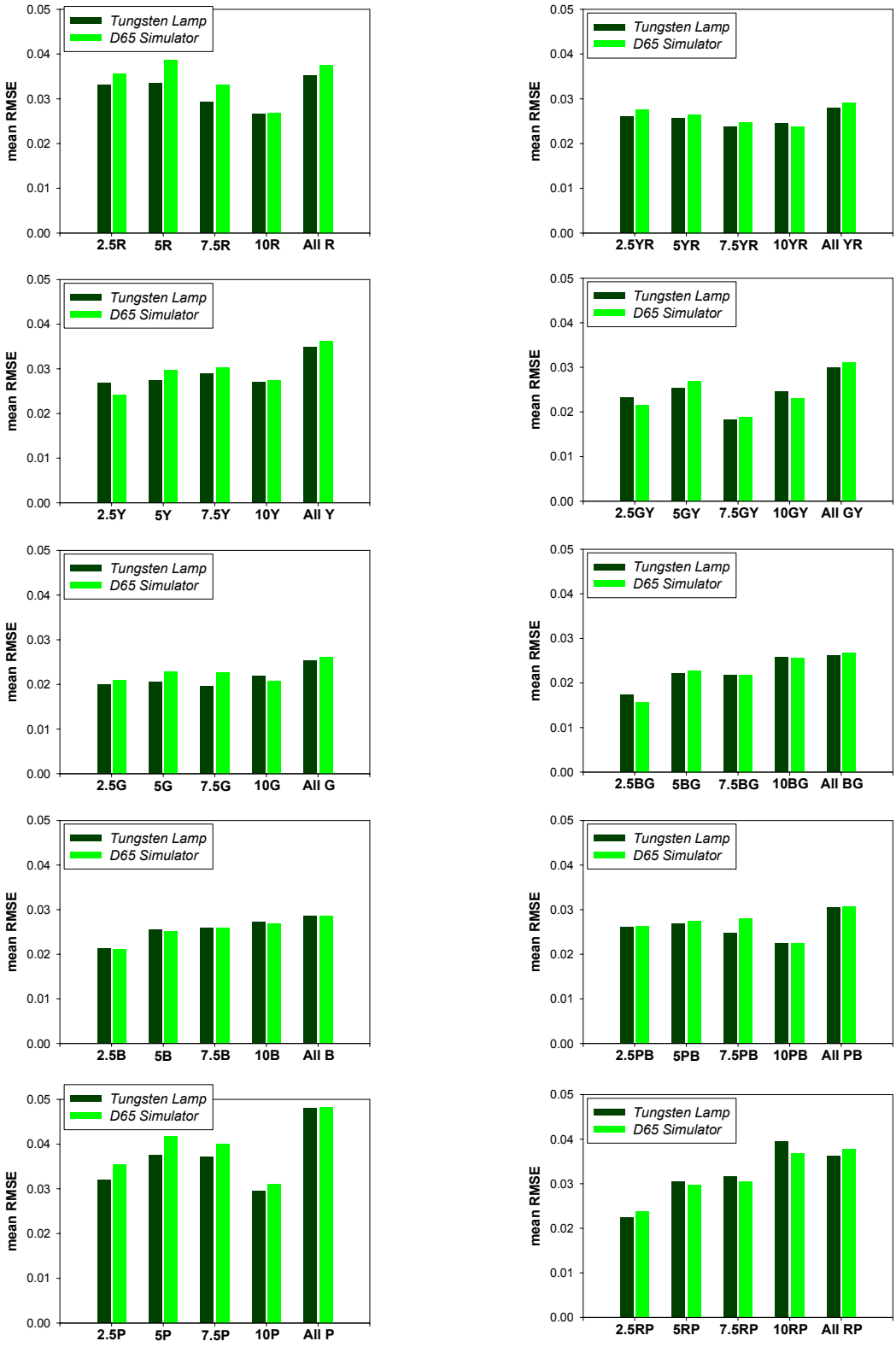

Figure 9.9 *Colorimetric Configuration: Bar plots of the mean RMSE values for all hues (R, YR, Y, GY, G, BG, B, PB, P, RP) and sub-hues of each hue (2.5, 5, 7.5, 10) of the Munsell Book of Color – Matte Collection (training & test), for the incandescent lamp and the D65 simulator illuminants.*

Comparison between results obtained using all Munsell's colour patches as training and test set (Table 9.4.), and results obtained using the sets of Munsell hues and sub-hues as training and test sets (Tables 9.5 (1) – (3) and Tables 9.6 (1) – (3)), makes it obvious that

homogeneity in hue of the training set allow improving the accuracy of both colour measurement and spectral reconstruction for both the incandescent lamp and the D65 simulator illuminants used.

9.2.2 Multispectral Configuration

Just as for the colorimetric configuration, results obtained using all 1269 Munsell's colour patches as training and test set are considered the starting point of this analysis as the less homogeneous training set (Table 9.7). For this multispectral configuration, better results are obtained using the D65 simulator illuminant than using the incandescent lamp in terms of accuracy of both colour measurement and spectral reconstruction, similarly to results obtained using the CCDC chart as training and test set (Table 9.2). On the other hand, and similarly to the colorimetric configuration, accuracy of colour measurement is worse for all Munsell's colour patches than for the CCDC chart using both illuminants. Accuracy of spectral reconstruction is slightly better in average for all Munsell's colour patches than for the CCDC chart using the D65 simulator illuminant, and slightly worse using the incandescent lamp illuminant. These results also show that accuracy on colour measurement and spectral reconstruction for this multispectral configuration depends not only on the illuminant but also on the training and test sets considered.

Table 9.7 *Multispectral Configuration: mean, minimum, maximum and standard deviation of the mean of the ΔE^*_{ab} and RMSE values associated to the Munsell's colour patches used as training and test set, using the incandescent lamp and D65 simulator illuminants.*

	INCANDESCENT LAMP		D65 SIMULATOR	
	ΔE^*_{ab}	RMSE	ΔE^*_{ab}	RMSE
mean	7.670	3.457E-02	3.360	2.654E-02
minimum	0.231	0.435E-02	0.164	0.313E-02
maximum	20.842	18.91E-03	22.163	18.94E-02
std. dev.	3.908	1.990E-02	2.612	1.610E-02

Next, accuracy of colour measurement and accuracy of spectral reconstruction are evaluated for different sets of Munsell colour patches homogeneous in hue (Table 9.3), for both the incandescent lamp and the D65 simulator illuminants.

Regarding the accuracy of colour measurement, unlike the colorimetric configuration, results obtained for the multispectral configuration are notably different between both illuminants (Table 9.8 (1) – (3)). For all Munsell hues and sub-hues considered as training and test sets, better results are obtained using the D65 simulator illuminant.

Considering the mean CIELAB colour difference values, differences between illuminants also depend on the hue and/or sub-hue considered as training and test set (Figure 9.10), but for all of them the D65 simulator illuminant allows a better system's performance on colour measurement than the incandescent lamp illuminant.

On the other hand, comparing both configurations in terms of the accuracy of colour measurement (Tables 9.5 (1) – (3) and 9.8 (1) – (3), Figures 9.8 and 9.10), the best results are obtained with the multispectral configuration, which allows to improve the accuracy on colour measurement notably for all Munsell hues and sub-hues used as training and test sets. This improvement also depends on the hue and sub-hue considered, but is common for all of them.

Table 9.8 (1) *Multispectral Configuration: mean, minimum, maximum and standard deviation of the mean of the CIELAB colour difference (ΔE^*_{ab}) values of the sub-hues and hues of the Munsell Book of Color – Matte Collection (training & test), using the incandescent lamp and D65 simulator illuminants.*

	INCANDESCENT LAMP					D65 SIMULATOR					
	2.5R	**5R**	**7.5R**	**10R**	**All R**	**2.5R**	**5R**	**7.5R**	**10R**	**All R**	
meanΔE^*_{ab}	2.839	3.210	3.642	2.388	4.009	2.129	1.742	2.016	2.418	2.681	**meanΔE^*_{ab}**
minΔE^*_{ab}	0.320	0.484	0.500	0.403	0.355	0.418	0.439	0.367	0.484	0.118	**minΔE^*_{ab}**
maxΔE^*_{ab}	8.615	10.055	9.330	7.105	13.537	7.211	5.613	6.502	7.517	8.344	**maxΔE^*_{ab}**
stddev ΔE^*_{ab}	2.333	2.653	2.494	1.685	3.086	1.709	1.315	1.662	1.678	1.826	**stddev ΔE^*_{ab}**
	2.5YR	**5YR**	**7.5YR**	**10YR**	**All YR**	**2.5YR**	**5YR**	**7.5YR**	**10YR**	**All YR**	
meanΔE^*_{ab}	2.087	2.585	1.892	1.947	3.285	1.612	1.818	1.733	1.727	2.300	**meanΔE^*_{ab}**
minΔE^*_{ab}	0.293	0.359	0.498	0.292	0.611	0.335	0.329	0.178	0.402	0.208	**minΔE^*_{ab}**
maxΔE^*_{ab}	6.867	9.457	4.918	6.401	8.659	5.891	4.595	4.572	6.188	8.788	**maxΔE^*_{ab}**
stddev ΔE^*_{ab}	1.556	2.217	1.213	1.350	1.988	1.365	1.191	1.157	1.349	1.550	**stddev ΔE^*_{ab}**
	2.5Y	**5Y**	**7.5Y**	**10Y**	**All Y**	**2.5Y**	**5Y**	**7.5Y**	**10Y**	**All Y**	
meanΔE^*_{ab}	2.347	2.756	2.743	2.718	3.325	1.830	1.937	1.536	1.494	2.130	**meanΔE^*_{ab}**
minΔE^*_{ab}	0.279	0.645	0.409	0.767	0.407	0.400	0.174	0.318	0.281	0.135	**minΔE^*_{ab}**
maxΔE^*_{ab}	8.295	7.588	8.485	7.034	11.233	8.885	5.592	5.839	3.036	8.565	**maxΔE^*_{ab}**
stddev ΔE^*_{ab}	2.089	1.922	1.849	1.801	2.265	1.735	1.209	1.059	0.769	1.454	**stddev ΔE^*_{ab}**
	2.5GY	**5GY**	**7.5GY**	**10GY**	**All GY**	**2.5GY**	**5GY**	**7.5GY**	**10GY**	**All GY**	
meanΔE^*_{ab}	2.006	3.047	1.929	2.572	2.772	1.606	1.754	1.305	1.456	1.932	**meanΔE^*_{ab}**
minΔE^*_{ab}	0.343	0.940	0.347	0.319	0.310	0.163	0.580	0.290	0.167	0.206	**minΔE^*_{ab}**
maxΔE^*_{ab}	5.226	8.641	5.932	9.254	9.400	4.828	4.702	3.690	5.604	5.344	**maxΔE^*_{ab}**
stddev ΔE^*_{ab}	1.182	1.907	1.319	1.938	1.741	1.050	1.109	0.721	1.073	1.093	**stddev ΔE^*_{ab}**

Table 9.8 (2) *Multispectral Configuration: mean, minimum, maximum and standard deviation of the mean of the CIELAB colour difference (ΔE^*_{ab}) values of the sub-hues and hues of the Munsell Book of Color – Matte Collection (training & test), using the incandescent lamp and D65 simulator illuminants.*

	INCANDESCENT LAMP					D65 SIMULATOR					
	2.5G	**5G**	**7.5G**	**10G**	**All G**	**2.5G**	**5G**	**7.5G**	**10G**	**All G**	
meanΔE^*_{ab}	2.195	3.006	2.262	3.080	3.239	1.375	1.870	1.662	2.291	2.213	**meanΔE^*_{ab}**
minΔE^*_{ab}	0.406	0.456	0.641	0.402	0.263	0.354	0.432	0.284	0.472	0.315	**minΔE^*_{ab}**
maxΔE^*_{ab}	6.561	7.996	7.454	8.234	8.563	3.222	4.929	5.974	6.608	7.589	**maxΔE^*_{ab}**
stddev ΔE^*_{ab}	1.777	2.234	1.431	2.186	1.855	1.009	1.234	1.307	1.672	1.473	**stddev ΔE^*_{ab}**
	2.5BG	**5BG**	**7.5BG**	**10BG**	**All BG**	**2.5BG**	**5BG**	**7.5BG**	**10BG**	**All BG**	
meanΔE^*_{ab}	1.999	2.583	1.716	1.784	2.810	1.775	2.019	1.699	1.777	2.148	**meanΔE^*_{ab}**
minΔE^*_{ab}	0.592	0.317	0.320	0.369	0.370	0.202	0.134	0.484	0.043	0.308	**minΔE^*_{ab}**
maxΔE^*_{ab}	9.560	8.414	4.169	5.068	12.992	7.541	6.107	4.537	5.579	9.545	**maxΔE^*_{ab}**
stddev ΔE^*_{ab}	2.066	2.091	1.164	1.352	2.237	1.751	1.654	1.121	1.413	1.669	**stddev ΔE^*_{ab}**
	2.5B	**5B**	**7.5B**	**10B**	**All B**	**2.5B**	**5B**	**7.5B**	**10B**	**All B**	
meanΔE^*_{ab}	1.421	2.088	2.364	2.016	2.655	1.393	1.799	1.706	1.404	1.860	**meanΔE^*_{ab}**
minΔE^*_{ab}	0.275	0.276	0.237	0.110	0.475	0.267	0.155	0.348	0.280	0.231	**minΔE^*_{ab}**
maxΔE^*_{ab}	3.929	8.429	6.530	6.935	7.987	3.978	6.921	5.369	4.717	6.533	**maxΔE^*_{ab}**
stddev ΔE^*_{ab}	0.829	1.743	1.793	1.781	1.806	1.068	1.544	1.266	1.061	1.374	**stddev ΔE^*_{ab}**
	2.5PB	**5PB**	**7.5PB**	**10PB**	**All PB**	**2.5PB**	**5PB**	**7.5PB**	**10PB**	**All PB**	
meanΔE^*_{ab}	2.194	2.721	2.612	1.953	3.444	1.713	2.026	1.915	1.535	2.448	**meanΔE^*_{ab}**
minΔE^*_{ab}	0.320	0.250	0.188	0.203	0.318	0.118	0.242	0.106	0.168	0.209	**minΔE^*_{ab}**
maxΔE^*_{ab}	7.502	7.949	8.142	8.690	11.479	6.357	6.979	5.094	5.983	8.166	**maxΔE^*_{ab}**
stddev ΔE^*_{ab}	1.787	1.744	2.076	1.902	3.009	1.398	1.429	1.304	1.243	1.955	**stddev ΔE^*_{ab}**

Table 9.8 (3) *Multispectral Configuration: mean, minimum, maximum and standard deviation of the mean of the CIELAB colour difference (ΔE^*_{ab}) values of the sub-hues and hues of the Munsell Book of Color – Matte Collection (training & test), using the incandescent lamp and D65 simulator illuminants.*

	INCANDESCENT LAMP					**D65 SIMULATOR**					
	2.5P	**5P**	**7.5P**	**10P**	**All P**	**2.5P**	**5P**	**7.5P**	**10P**	**All P**	
meanΔE^*_{ab}	1.980	2.507	2.129	2.081	2.694	1.349	2.375	1.806	1.542	2.294	**meanΔE^*_{ab}**
minΔE^*_{ab}	0.190	0.332	0.370	0.233	0.370	0.275	0.218	0.428	0.194	0.247	**minΔE^*_{ab}**
maxΔE^*_{ab}	5.618	6.372	6.991	7.363	8.977	4.024	9.985	5.092	4.880	9.889	**maxΔE^*_{ab}**
stddev ΔE^*_{ab}	1.623	1.869	1.768	1.814	2.103	0.931	2.107	1.325	1.220	1.938	**stddev ΔE^*_{ab}**
	2.5RP	**5RP**	**7.5RP**	**10RP**	**All RP**	**2.5RP**	**5RP**	**7.5RP**	**10RP**	**All RP**	
meanΔE^*_{ab}	1.934	2.296	2.055	2.700	2.996	1.819	1.957	2.104	2.640	2.437	**meanΔE^*_{ab}**
minΔE^*_{ab}	0.411	0.224	0.478	0.538	0.396	0.432	0.236	0.443	0.555	0.130	**minΔE^*_{ab}**
maxΔE^*_{ab}	5.826	7.544	4.757	8.842	9.681	5.570	7.394	7.167	8.371	8.685	**maxΔE^*_{ab}**
stddev ΔE^*_{ab}	1.522	1.834	1.271	1.895	2.067	1.348	1.737	1.675	1.999	1.936	**stddev ΔE^*_{ab}**

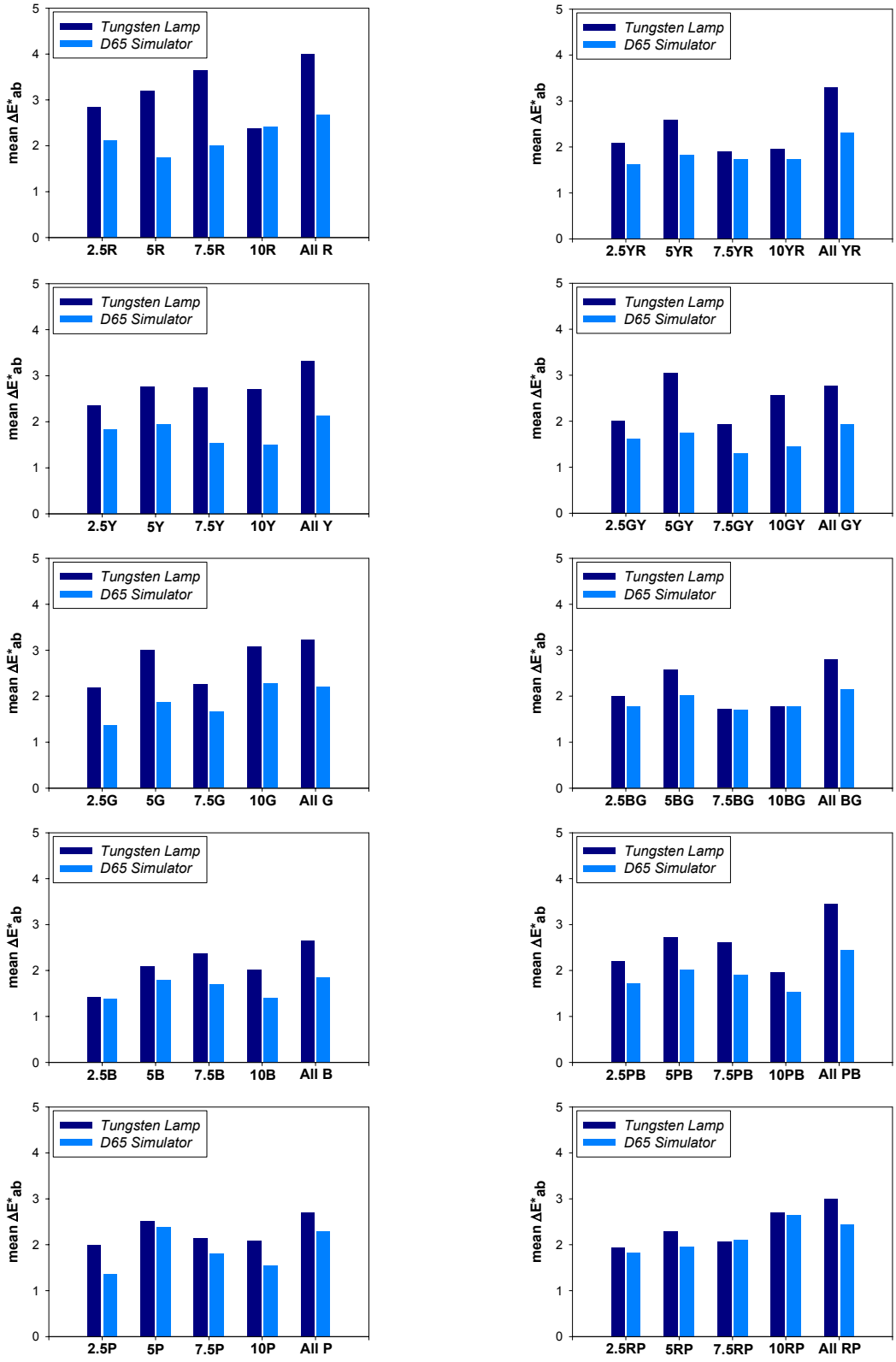

Figure 9.10 *Multispecral Configuration: Bar plots of the mean ΔE^*_{ab} values for all hues (R, YR, Y, GY, G, BG, B, PB, P, RP) and sub-hues of each hue (2.5, 5, 7.5, 10) of the Munsell Book of Color – Matte Collection (training & test), for the incandescent lamp and the D65 simulator illuminants.*

Table 9.9 (1) *Multispectral Configuration: mean, minimum, maximum and standard deviation of the mean of the RMSE values of the sub-hues and hues of the Munsell Book of Color – Matte Collection (training & test), using the incandescent lamp and D65 simulator illuminants.*

	INCANDESCENT LAMP					D65 SIMULATOR					
	2'5R	**5R**	**7'5R**	**10R**	**All R**	**2'5R**	**5R**	**7'5R**	**10R**	**All R**	
meanRMSE	1.858E-02	2.075E-02	2.253E-02	1.726E-02	2.680E-02	1.711E-02	1.633E-02	1.474E-02	1.822E-02	2.173E-02	**meanRMSE**
minRMSE	0.627E-02	0.445E-02	0.447E-02	0.358E-02	0.429E-0	0.536E-02	0.417E-02	0.282E-02	0.579E-02	0.301E-02	**minRMSE**
maxRMSE	4.784E-02	5.139E-02	4.182E-02	4.057E-02	5.716E-02	5.400E-02	4.382E-02	3.310E-02	4.102E-02	5.967E-02	**maxRMSE**
stddev RMSE	1.04E-02	1.14E-02	1.03E-02	0.924E-02	1.23E-02	1.00E-02	1.01E-02	0.758E-02	0.881E-02	1.11E-02	**stddev RMSE**
	2'5YR	**5YR**	**7'5YR**	**10YR**	**All YR**	**2'5YR**	**5YR**	**7'5YR**	**10YR**	**All YR**	
meanRMSE	1.690E-02	1.773E-02	1.153E-02	1.146E-02	2.525E-02	1.573E-02	1.483E-02	1.074E-02	1.057E-02	1.909E-02	**meanRMSE**
minRMSE	0.624E-02	0.794E-02	0.517E-02	0.344E-02	0.599E-02	0.518E-02	0.551E-02	0.294E-02	0.295E-02	0.387E-02	**minRMSE**
maxRMSE	4.481E-02	4.702E-02	2.718E-02	2.891E-02	6.767E-02	3.354E-02	3.299E-02	1.942E-02	2.992E-02	5.178E-02	**maxRMSE**
stddev RMSE	1.05E-02	1.01E-02	0.475E-02	0.609E-02	1.25E-02	0.732E-02	0.739E-02	0.489E-02	0.593E-02	1.08E-02	**stddev RMSE**
	2'5Y	**5Y**	**7'5Y**	**10Y**	**All Y**	**2'5Y**	**5Y**	**7'5Y**	**10Y**	**All Y**	
meanRMSE	1.614E-02	1.952E-02	2.281E-02	2.034E-02	2.628E-02	1.512E-02	1.528E-02	1.672E-02	1.562E-02	1.978E-02	**meanRMSE**
minRMSE	0.319E-02	0.586E-02	0.492E-02	0.751E-02	0.566E-02	0.299E-02	0.275E-02	0.492E-02	0.499E-02	0.353E-02	**minRMSE**
maxRMSE	3.832E-02	4.335E-02	6.275E-02	5.822E-02	8.054E-02	3.391E-02	3.731E-02	5.605E-02	5.459E-02	6.089E-02	**maxRMSE**
stddev RMSE	0.951E-02	1.00E-02	1.50E-02	1.10E-02	1.38E-02	0.851E-02	0.958E-02	1.19E-02	1.05E-02	1.25E-02	**stddev RMSE**
	2'5GY	**5GY**	**7'5GY**	**10GY**	**All GY**	**2'5GY**	**5GY**	**7'5GY**	**10GY**	**All GY**	
meanRMSE	1.728E-02	2.623E-02	1.491E-02	1.915E-02	2.225E-02	1.560E-02	1.628E-02	1.328E-02	1.063E-02	1.638E-02	**meanRMSE**
minRMSE	0.421E-02	1.146E-02	0.487E-02	0.502E-02	0.654E-02	0.332E-02	0.328E-02	0.493E-02	0.302E-02	0.284E-02	**minRMSE**
maxRMSE	4.865E-02	6.552E-02	3.108E-02	3.476E-02	7.457E-02	5.036E-02	5.719E-02	2.391E-02	3.488E-02	5.945E-02	**maxRMSE**
stddev RMSE	1.13E-02	1.45E-02	0.729E-02	0.845E-02	1.22E-02	1.01E-02	1.11E-02	0.586E-02	0.667E-02	0.977E-02	**stddev RMSE**

Table 9.9 (2) *Multispectral Configuration: mean, minimum, maximum and standard deviation of the mean of the RMSE values of the sub-hues and hues of the Munsell Book of Color – Matte Collection (training & test), using the incandescent lamp and D65 simulator illuminants.*

	INCANDESCENT LAMP					D65 SIMULATOR					
	2'5G	**5G**	**7'5G**	**10G**	**All G**	**2'5G**	**5G**	**7'5G**	**10G**	**All G**	
meanRMSE	1.394E-02	1.792E-02	1.270E-02	1.725E-02	2.032E-02	0.736E-02	1.022E-02	1.085E-02	1.421E-02	1.414E-02	**meanRMSE**
minRMSE	0.452E-02	0.456E-02	0.419E-02	0.529E-02	0.496E-02	0.253E-02	0.348E-02	0.239E-02	0.523E-02	0.241E-02	**minRMSE**
maxRMSE	3.851E-02	4.314E-02	3.032E-02	3.472E-02	5.579E-02	2.307E-02	1.929E-02	2.400E-02	2.590E-02	4.855E-02	**maxRMSE**
stddev RMSE	0.913E-02	1.08E-02	0.599E-02	0.907E-02	1.09E-02	0.472E-02	0.452E-02	0.541E-02	0.668E-02	0.741E-02	**stddev RMSE**
	2'5BG	**5BG**	**7'5BG**	**10BG**	**All BG**	**2'5BG**	**5BG**	**7'5BG**	**10BG**	**All BG**	
meanRMSE	0.954E-02	1.479E-02	0.881E-02	0.942E-02	1.607E-02	0.761E-02	1.149E-02	0.861E-02	0.999E-02	1.220E-02	**meanRMSE**
minRMSE	0.341E-02	0.343E-02	0.258E-02	0.246E-02	0.434E-02	0.231E-02	0.351E-02	0.494E-02	0.233E-02	0.334E-02	**minRMSE**
maxRMSE	2.228E-02	3.414E-02	2.206E-02	2.244E-02	4.863E-02	1.939E-02	2.686E-02	2.327E-02	2.315E-02	3.622E-02	**maxRMSE**
stddev RMSE	0.476E-02	0.803E-02	0.467E-02	0.506E-02	0.869E-02	0.502E-02	0.679E-02	0.469E-02	0.523E-02	0.689E-02	**stddev RMSE**
	2'5B	**5B**	**7'5B**	**10B**	**All B**	**2'5B**	**5B**	**7'5B**	**10B**	**All B**	
meanRMSE	0.813E-02	1.198E-02	1.104E-02	1.152E-02	1.609E-02	0.893E-02	1.034E-02	0.905E-02	1.016E-02	1.244E-02	**meanRMSE**
minRMSE	0.204E-02	0.343E-02	0.394E-02	0.487E-02	0.466E-02	0.278E-02	0.296E-02	0.319E-02	0.408E-02	0.361E-02	**minRMSE**
maxRMSE	1.745E-02	3.219E-02	2.537E-02	2.666E-02	3.434E-02	1.838E-02	2.496E-02	1.916E-02	1.736E-02	3.418E-02	**maxRMSE**
stddev RMSE	0.447E-02	0.733E-02	0.603E-02	0.533E-02	0.752E-02	0.432E-02	0.611E-02	0.462E-02	0.402E-02	0.543E-02	**stddev RMSE**
	2'5PB	**5PB**	**7'5PB**	**10PB**	**All PB**	**2'5PB**	**5PB**	**7'5PB**	**10PB**	**All PB**	
meanRMSE	1.050E-02	1.544E-02	1.605E-02	1.453E-02	2.096E-02	0.950E-02	1.243E-02	1.362E-02	1.192E-02	1.607E-02	**meanRMSE**
minRMSE	0.315E-02	0.488E-02	0.444E-02	0.354E-02	0.378E-02	0.333E-02	0.444E-02	0.355E-02	0.381E-02	0.413E-02	**minRMSE**
maxRMSE	2.209E-02	3.074E-02	4.003E-02	3.700E-02	8.699E-02	1.957E-02	2.705E-02	4.306E-02	2.534E-02	7.479E-02	**maxRMSE**
stddev RMSE	0.543E-02	0.683E-02	0.973E-02	0.798E-02	1.26E-02	0.456E-02	0.505E-02	0.882E-02	0.608E-02	0.976E-02	**stddev RMSE**

Table 9.9 (3) *Multispectral Configuration: mean, minimum, maximum and standard deviation of the mean of the RMSE values of the sub-hues and hues of the Munsell Book of Color – Matte Collection (training & test), using the incandescent lamp and D65 simulator illuminants.*

	INCANDESCENT LAMP					D65 SIMULATOR					
	2'5P	**5P**	**7'5P**	**10P**	**All P**	**2'5P**	**5P**	**7'5P**	**10P**	**All P**	
meanRMSE	2.522E-02	2.796E-02	2.823E-02	1.954E-02	2.850E-02	2.045E-02	2.629E-02	2.761E-02	1.670E-02	2.571E-02	**meanRMSE**
minRMSE	0.509E-02	0.429E-02	0.761E-02	0.545E-02	0.686E-02	0.456E-02	0.293E-02	0.662E-02	0.405E-02	0.445E-02	**minRMSE**
maxRMSE	9.211E-02	11.28E-02	14.90E-02	9.713E-02	17.60E-02	9.028E-02	10.63E-02	15.49E-02	8.073E-02	17.01E-02	**maxRMSE**
stddev RMSE	1.91E-02	2.04E-02	2.72E-02	1.62E-02	2.30E-02	1.82E-02	1.95E-02	2.78E-02	1.44E-02	2.21E-02	**stddev RMSE**
	2'5RP	**5RP**	**7'5RP**	**10RP**	**All RP**	**2'5RP**	**5RP**	**7'5RP**	**10RP**	**All RP**	
meanRMSE	1.400E-02	1.897E-02	1.558E-02	2.129E-02	2.247E-02	1.341E-02	1.448E-02	1.546E-02	1.973E-02	1.874E-02	**meanRMSE**
minRMSE	0.369E-02	0.503E-02	0.606E-02	0.748E-02	0.543E-02	0.575E-02	0.492E-02	0.691E-02	0.589E-02	0.197E-02	**minRMSE**
maxRMSE	3.348E-02	4.803E-02	5.440E-02	5.121E-02	10.55E-02	2.967E-02	4.237E-02	5.381E-02	4.454E-02	10.51E-02	**maxRMSE**
stddev RMSE	7.90E-02	1.04E-02	1.04E-02	1.08E-02	1.32E-02	0.607E-02	0.762E-02	0. 992E-02	0.946E-02	1.27E-02	**stddev RMSE**

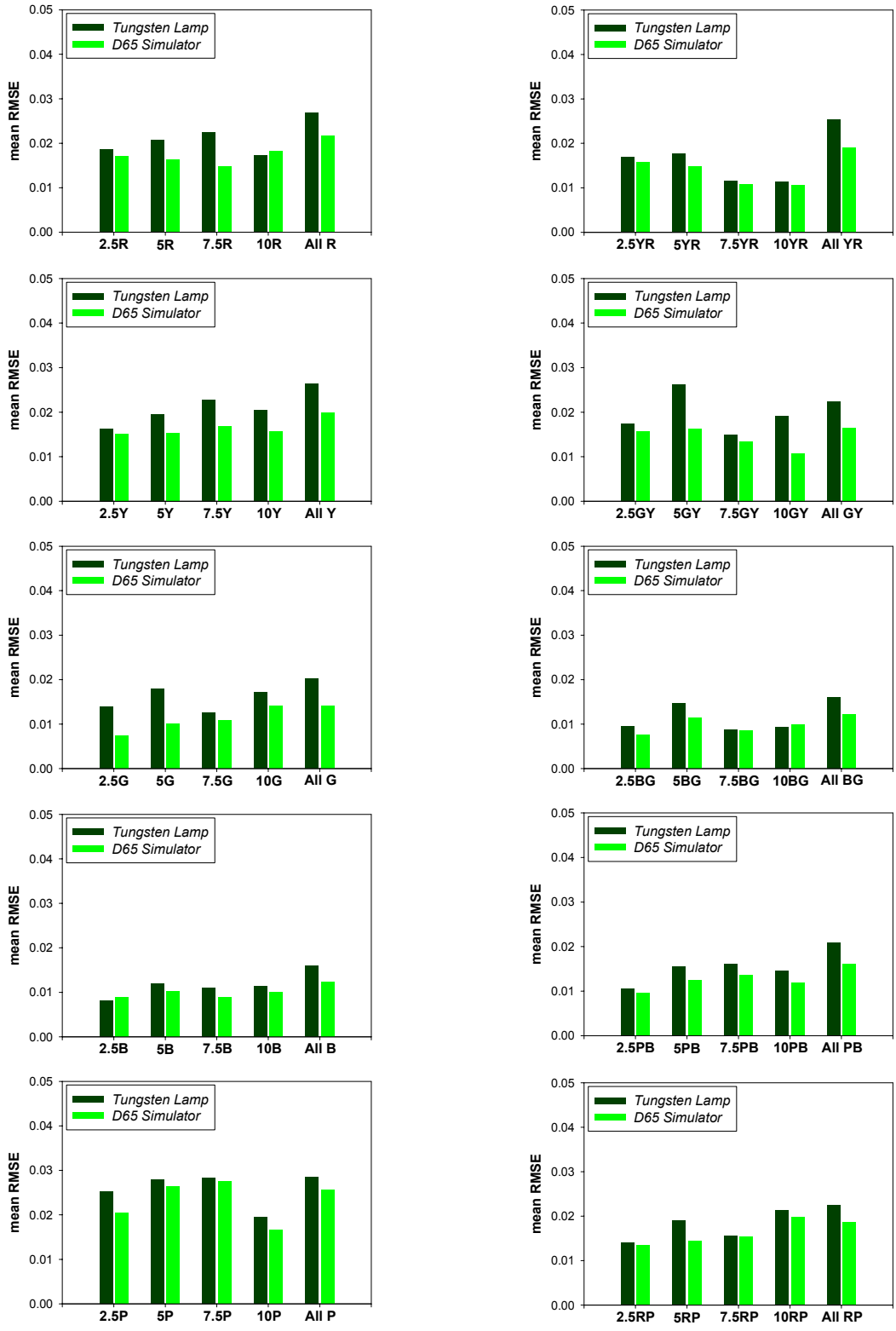

Figure 9.11 *Multispectral Configuration: Bar plots of the mean RMSE values for all hues (R, YR, Y, GY, G, BG, B, PB, P, RP) and sub-hues of each hue (2.5, 5, 7.5, 10) of the Munsell Book of Color – Matte Collection (training & test), for the incandescent lamp and the D65 simulator illuminants.*

Regarding the accuracy of spectral reconstruction, and again unlike the colorimetric configuration, results obtained for the multispectral configuration are also notably different

between both illuminants (Tables 9.9 (1) – (3)). For all Munsell hues and sub-hues considered as training and test sets, better results are also obtained using the D65 simulator illuminant (Tables 9.9 (1) – (3) and Figure 9.11).

Considering the mean RMSE values, and similarly to the CIELAB colour difference values, differences between illuminants depend on the hue and/or sub-hue considered as training and test set (Figure 9.11), but for all of them, unlike it happened with the colorimetric configuration, the D65 simulator illuminant allows a better system's performance on spectral reconstruction than the incandescent lamp illuminant.

On the other hand, comparing both configurations in terms of the accuracy of spectral reconstruction (Tables 9.6 (1) – (3) and 9.9 (1) – (3), Figures 9.9 and 9.11), the best results are also obtained with the multispectral configuration, which allows to improve the accuracy on spectral reconstruction notably for all Munsell hues and sub-hues used as training and test sets. Similarly to the accuracy on colour measurement, this improvement also depends on the hue and sub-hue considered, but is common for all of them.

Just as for the colorimetric configuration, comparison between results obtained using all Munsell's colour patches as training and test set (Table 9.7), and results obtained using the sets of Munsell hues and sub-hues as training and test sets (Tables 9.8 (1) – (3) and Tables 9.9 (1) – (3)), makes it obvious that homogeneity in hue of the training set allows to improve the accuracy of both colour measurement and spectral reconstruction for both the incandescent lamp and the D65 simulator illuminants used.

Comparing results obtained for both configurations and using, on one hand, all sets of Munsell's hues as training and test sets (Tables 9.5 (1) – (3), 9.6 (1) – (3), 9.8 (1) – (3), and 9.9 (1) – (3)) and, on the other hand, the CCDC's colour samples as training and test sets (Tables 9.1 and 9.2), some conclusions can be drawn with regard to the influence of homogeneity in hue of the training set on the accuracy of colour measurement and spectral reconstruction for these two sets of colour samples.

First, in terms of accuracy of colour measurement, and commonly for the two illuminants used, the homogeneity in hue of the training set, using sets of Munsell's hues and sub-hues as training and test sets, does not lead to an outstanding and widespread improvement with regard to results obtained using the CCDC chart as a multi-colour range training set, neither for the colorimetric configuration (Tables 9.1 and 9.5 (1) – (3)) nor for the multispectral configuration (Tables 9.2 and 9.8 (1) – (3)). This improvement is not common to all hues and/or sub-hues, and depends on the concrete training set considered. On the other hand, an outstanding improvement in accuracy of colour measurement is obtained using sets of Munsell's hues and sub-hues as training and test sets instead of using all Munsell's colour patches as training and test set (Tables 9.4 and 9.5 (1) – (3), and Tables 9.7 and 9.8 (1) – (3)).

Secondly, very similar results are obtained in terms of accuracy of spectral reconstruction, and also commonly for the two illuminants used. The homogeneity in hue of the training set, using sets of Munsell's hues and sub-hues as training and test sets, also does not improve outstandingly the accuracy of spectral reconstruction for all hues and/or sub-hues used as training and test sets, with regard to results obtained using the CCDC chart as a multi-colour range training set, neither for the colorimetric configuration (Tables 9.1 and 9.6 (1) – (3)) nor for the multispectral configuration (Tables 9.2 and 9.9 (1) – (3)). Just as for the accuracy of colour measurement, the improvement in accuracy of spectral reconstruction is not common to all hues and/or sub-hues, and depends on the concrete training set considered. On the other hand, an outstanding improvement in accuracy of spectral reconstruction is also obtained using sets of Munsell's hues and sub-hues as training and test sets instead of using all Munsell's colour patches as training and test set (Tables 9.4 and 9.6 (1) – (3), and Tables 9.7 and 9.9 (1) – (3)).

Summing up, firstly, comparing results obtained using all Munsell's colour patches and sets of Munsell's colour patches grouped in hues and sub-hues as training and test sets, homogeneity in hue of the training set leads to an outstanding improvement on the accuracy of both colour measurement and spectral reconstruction for all colour ranges. Secondly, comparing results obtained using a multi-colour range CCDC chart and sets of Munsell's hues and sub-hues as training and test sets, homogeneity in hue of the training set does not assure an improvement in accuracy neither of colour measurement nor of spectral reconstruction, for all colour ranges.

Finally, bearing in mind that these results are not general as same sets of colour samples are used as training and test sets, the two sets of colour samples compared (CCDC chart and Munsell Book of Color – Matte Collection) are quite different and are used independently, and for the CCDC chart an analysis of the influence of the homogeneity in hue of the training set is not possible because the low number of samples for some hues, it can be concluded that homogeneity in hue of the training set improves outstandingly the accuracy of colour measurement and spectral reconstruction when the original set of samples is large enough to group its samples in sets of different hues to be used as training sets.

9.2.3 Influence of the degree of homogeneity in hue of the training set using different combinations of training and test sets of Munsell's colour patches

So far in this analysis of the influence of homogeneity in hue of the training set, same sets of colour samples have been used as training and test sets, being the training sets the most homogeneous in hue possible considering the classification in hue of Munsell's colour patches.

In this section, two combinations of training and test sets of Munsell's colour patches are used in order to vary the degree of homogeneity in hue of the training set with regard to results obtained previously. These are: sets of Munsell's hues as training sets and sets of Munsell's sub-hues and hues as test sets, and all Munsell's colour patches as training set and sets of Munsell's sub-hues and hues as test sets. For these combinations, test sets are always included on training sets, but this last ones also include other sets of samples, such as the rest of sub-hues for each hue in the first combination, and the rest of Munsell's colour patches in the second combination, becoming less homogeneous in hue than sets of Munsell's sub-hues used previously.

In this study, and from here on, the best proved combination of system's configuration and illuminant, which is multispectral configuration and D65 simulator illuminant, will be used.

Results obtained considering sets of Munsell's sub-hues and hues as test sets, and sets of Munsell's hues and all Munsell's colour patches as training sets, are shown in Tables 9.10 (1) – (3) and 9.11 (1) – (3). As can be seen from these tables, and comparing these results with those obtained using the same training and test sets (Tables 9.8 (1) – (3) and 9.9 (1) – (3)), increasing the non-homogeneity in hue of the training set decreases outstandingly the accuracy of both colour measurement (Tables 9.10 (1) – (3)) and spectral reconstruction (Tables 9.11 (1) – (3)). These results become more obvious when considering the mean CIELAB colour difference and the mean RMSE values, plotted for each hue and sub-hue set and using the same sub-hue, the corresponding hue, and all Munsell's colour patches as training sets (Figures 9.12 and 9.13).

Taking these results into account, it can be concluded that, for the Munsell's colour patches, the more homogeneous the training set is, the better results obtained are in terms of accuracy of both colour measurement and spectral reconstruction.

Table 9.10 (1) *Mean, minimum, maximum and standard deviation of the mean of the CIELAB colour difference (ΔE^*_{ab}) values of the sets of Munsell sub-hues, using the sets of Munsell hues and all Munsell colour patches as training sets.*

	Training Set: MUNSELL R					Training Set: All MUNSELL					
	2.5R	**5R**	**7.5R**	**10R**	**All R**	**2.5R**	**5R**	**7.5R**	**10R**	**All R**	
meanΔE^*_{ab}	2.661	2.325	2.963	2.857	2.681	3.875	3.516	4.453	3.669	3.838	**meanΔE^*_{ab}**
minΔE^*_{ab}	0.269	0.118	0.314	0.557	0.118	0.492	0.736	1.069	1.033	0.492	**minΔE^*_{ab}**
maxΔE^*_{ab}	8.171	7.796	8.344	7.603	8.344	11.430	11.086	10.336	8.630	11.430	**maxΔE^*_{ab}**
stddev ΔE^*_{ab}	1.887	1.812	2.091	1.559	1.826	2.644	2.801	2.919	2.065	2.608	**stddev ΔE^*_{ab}**

	Training Set: MUNSELL YR					Training Set: All MUNSELL					
	2.5YR	**5YR**	**7.5YR**	**10YR**	**All YR**	**2.5YR**	**5YR**	**7.5YR**	**10YR**	**All YR**	
meanΔE^*_{ab}	2.441	2.169	2.211	2.379	2.300	3.534	3.329	3.843	3.569	3.552	**meanΔE^*_{ab}**
minΔE^*_{ab}	0.208	0.458	0.404	0.382	0.208	1.018	0.455	0.639	0.479	0.455	**minΔE^*_{ab}**
maxΔE^*_{ab}	7.613	6.365	5.898	8.788	8.788	10.023	8.399	9.491	11.140	11.140	**maxΔE^*_{ab}**
stddev ΔE^*_{ab}	1.726	1.360	1.447	1.700	1.550	2.447	1.952	2.523	2.597	2.357	**stddev ΔE^*_{ab}**

	Training Set: MUNSELL Y					Training Set: All MUNSELL					
	2.5Y	**5Y**	**7.5Y**	**10Y**	**All Y**	**2.5Y**	**5Y**	**7.5Y**	**10Y**	**All Y**	
meanΔE^*_{ab}	2.109	2.271	2.237	1.915	2.130	3.774	3.513	3.265	2.920	3.346	**meanΔE^*_{ab}**
minΔE^*_{ab}	0.700	0.308	0.586	0.135	0.135	0.755	0.164	0.739	0.533	0.164	**minΔE^*_{ab}**
maxΔE^*_{ab}	7.378	7.625	8.565	6.808	8.565	10.896	11.826	10.346	7.475	11.826	**maxΔE^*_{ab}**
stddev ΔE^*_{ab}	1.380	1.535	1.670	1.254	1.454	2.640	2.621	2.220	1.887	2.348	**stddev ΔE^*_{ab}**

	Training Set: MUNSELL GY					Training Set: All MUNSELL					
	2.5GY	**5GY**	**7.5GY**	**10GY**	**All GY**	**2.5GY**	**5GY**	**7.5GY**	**10GY**	**All GY**	
meanΔE^*_{ab}	1.898	2.013	1.955	1.858	1.932	2.846	3.018	3.245	2.646	2.923	**meanΔE^*_{ab}**
minΔE^*_{ab}	0.206	0.215	0.781	0.511	0.206	0.355	1.130	0.875	0.630	0.355	**minΔE^*_{ab}**
maxΔE^*_{ab}	4.643	5.329	5.344	4.928	5.344	7.463	7.213	7.252	7.045	7.463	**maxΔE^*_{ab}**
stddev ΔE^*_{ab}	1.084	1.175	1.046	1.084	1.093	1.995	1.759	1.875	1.452	1.756	**stddev ΔE^*_{ab}**

Table 9.10 (2) *Mean, minimum, maximum and standard deviation of the mean of the CIELAB colour difference (ΔE^*_{ab}) values of the sets of Munsell sub-hues, using the sets of Munsell hues and all Munsell colour patches as training sets.*

	Training Set: MUNSELL G					Training Set: All MUNSELL					
	2.5G	**5G**	**7.5G**	**10G**	**All G**	**2.5G**	**5G**	**7.5G**	**10G**	**All G**	
meanΔE^*_{ab}	1.963	2.170	2.295	2.404	2.213	2.997	2.722	2.735	2.929	2.843	**meanΔE^*_{ab}**
minΔE^*_{ab}	0.315	0.398	0.462	0.457	0.315	0.894	0.441	0.411	0.436	0.411	**minΔE^*_{ab}**
maxΔE^*_{ab}	5.434	7.253	7.589	6.474	7.589	6.702	7.522	9.121	8.222	9.121	**maxΔE^*_{ab}**
stddev ΔE^*_{ab}	1.123	1.656	1.612	1.446	1.473	1.737	1.960	2.201	2.079	1.978	**stddev ΔE^*_{ab}**

	Training Set: MUNSELL BG					Training Set: All MUNSELL					
	2.5BG	**5BG**	**7.5BG**	**10BG**	**All BG**	**2.5BG**	**5BG**	**7.5BG**	**10BG**	**All BG**	
meanΔE^*_{ab}	2.169	2.246	2.331	1.900	2.148	2.658	3.302	3.533	3.384	3.227	**meanΔE^*_{ab}**
minΔE^*_{ab}	0.568	0.308	0.751	0.369	0.308	0.491	1.018	0.809	0.788	0.491	**minΔE^*_{ab}**
maxΔE^*_{ab}	9.545	7.503	5.708	5.585	9.545	7.427	8.602	7.277	7.916	8.602	**maxΔE^*_{ab}**
stddev ΔE^*_{ab}	2.093	1.765	1.390	1.415	1.669	2.129	2.238	1.863	2.505	2.215	**stddev ΔE^*_{ab}**

	Training Set: MUNSELL B					Training Set: All MUNSELL					
	2.5B	**5B**	**7.5B**	**10B**	**All B**	**2.5B**	**5B**	**7.5B**	**10B**	**All B**	
meanΔE^*_{ab}	1.928	1.982	1.860	1.706	1.860	3.912	3.603	4.212	3.491	3.766	**meanΔE^*_{ab}**
minΔE^*_{ab}	0.614	0.258	0.472	0.231	0.231	0.484	0.188	0.461	0.507	0.188	**minΔE^*_{ab}**
maxΔE^*_{ab}	4.362	6.272	6.533	5.543	6.533	8.775	10.330	11.116	10.273	11.116	**maxΔE^*_{ab}**
stddev ΔE^*_{ab}	1.157	1.559	1.450	1.311	1.374	2.554	2.922	3.463	2.970	2.973	**stddev ΔE^*_{ab}**

	Training Set: MUNSELL PB					Training Set: All MUNSELL					
	2.5PB	**5 PB**	**7.5 PB**	**10 PB**	**All PB**	**2.5PB**	**5 PB**	**7.5 PB**	**10 PB**	**All PB**	
meanΔE^*_{ab}	2.070	2.559	2.817	2.290	2.448	4.294	4.816	4.241	2.313	3.895	**meanΔE^*_{ab}**
minΔE^*_{ab}	0.230	0.209	0.402	0.444	0.209	0.282	0.447	0.824	0.718	0.282	**minΔE^*_{ab}**
maxΔE^*_{ab}	7.287	7.982	8.127	8.166	8.166	15.663	15.735	15.832	8.357	15.832	**maxΔE^*_{ab}**
stddev ΔE^*_{ab}	1.531	1.883	2.386	1.897	1.955	4.186	4.251	3.875	1.596	3.704	**stddev ΔE^*_{ab}**

Table 9.10 (3) *Mean, minimum, maximum and standard deviation of the mean of the CIELAB colour difference (ΔE^*_{ab}) values of the sets of Munsell sub-hues, using the sets of Munsell hues and all Munsell colour patches as training sets.*

	Training Set: MUNSELL P					Training Set: All MUNSELL					
	2.5P	**5P**	**7.5P**	**10P**	**All P**	**2.5P**	**5P**	**7.5P**	**10P**	**All P**	
meanΔE^*_{ab}	1.868	2.819	2.200	2.181	2.294	2.350	4.033	3.521	2.946	3.245	**meanΔE^*_{ab}**
minΔE^*_{ab}	0.294	0.247	0.483	0.260	0.247	0.629	0.374	0.354	0.280	0.280	**minΔE^*_{ab}**
maxΔE^*_{ab}	5.456	9.889	8.074	6.674	9.889	5.769	22.163	18.077	11.765	22.163	**maxΔE^*_{ab}**
stddev ΔE^*_{ab}	1.363	2.562	1.764	1.688	1.938	1.431	4.302	3.610	2.493	3.221	**stddev ΔE^*_{ab}**

	Training Set: MUNSELL RP					Training Set: All MUNSELL					
	2.5RP	**5RP**	**7.5RP**	**10RP**	**All RP**	**2.5RP**	**5RP**	**7.5RP**	**10RP**	**All RP**	
meanΔE^*_{ab}	1.996	2.308	2.675	2.738	2.437	2.697	2.632	3.118	3.169	2.902	**meanΔE^*_{ab}**
minΔE^*_{ab}	0.602	0.130	0.341	0.540	0.130	1.014	0.576	1.046	0.583	0.576	**minΔE^*_{ab}**
maxΔE^*_{ab}	7.726	8.498	6.761	8.685	8.685	7.530	8.489	6.849	8.641	8.641	**maxΔE^*_{ab}**
stddev ΔE^*_{ab}	1.602	2.091	1.869	2.065	1.936	1.765	2.086	1.661	2.241	1.971	**stddev ΔE^*_{ab}**

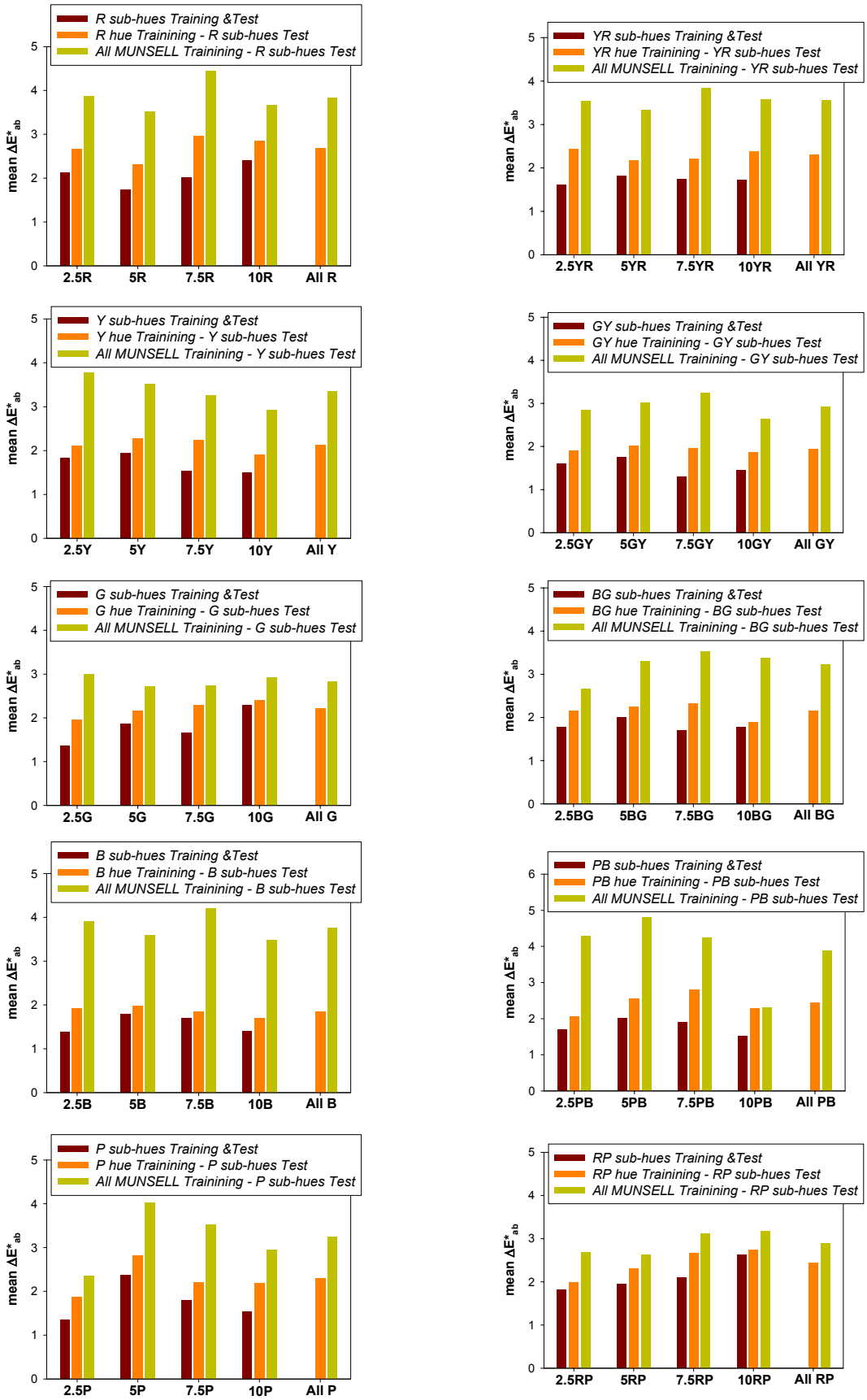

Figure 9.12 *Bar plots of the mean ΔE^*_{ab} values for all hues (R, YR, Y, GY, G, BG, B, PB, P, RP) and sub-hues of each hue (2.5, 5, 7.5, 10) of the Munsell Book of Color – Matte Collection, for the training sets: Munsell sub-hues, Munsell hues, and all Munsell's colour patches.*

Table 9.11 (1) *Mean, minimum, maximum and standard deviation of the mean of the RMSE values of the sets of Munsell sub-hues, using the sets of Munsell hues and all Munsell's colour patches as training sets.*

	Training Set: MUNSELL R					Training Set: All MUNSELL				
	2.5R	**5R**	**7.5R**	**10R**	**All R**	**2.5R**	**5R**	**7.5R**	**10R**	**All R**
meanRMSE	2.235E-02	2.090E-02	2.095E-02	2.277E-02	2.173E-02	3.667E-02	2.543E-02	3.029E-02	2.809E-02	2.963E-02
minRMSE	0.627E-02	0.371E-02	0.301E-02	0.643E-02	0.301E-02	5.351E-03	6.657E-03	1.060E-02	1.039E-02	5.351E-03
maxRMSE	4.278E-02	5.366E-02	4.663E-02	5.967E-02	5.967E-02	1.044E-01	5.908E-02	5.778E-02	6.260E-02	1.044E-01
stddev RMSE	1.013E-02	1.162E-02	0.929E-02	1.263E-02	1.11E-02	2.111E-02	1.319E-02	1.258E-02	1.220E-02	1.530E-02

	Training Set: MUNSELL YR					Training Set: All MUNSELL				
	2.5YR	**5YR**	**7.5YR**	**10YR**	**All YR**	**2.5YR**	**5YR**	**7.5YR**	**10YR**	**All YR**
meanRMSE	2.056E-02	2.063E-02	1.714E-02	1.777E-02	1.909E-02	2.685E-02	3.122E-02	2.628E-02	2.522E-02	2.751E-02
minRMSE	0.609E-02	0.427E-02	0.391E-02	0.387E-02	0.387E-02	6.128E-03	1.498E-02	7.354E-03	7.555E-03	6.128E-03
maxRMSE	5.167E-02	5.030E-02	4.543E-02	5.178E-02	5.178E-02	3.945E-02	7.031E-02	5.531E-02	5.540E-02	7.031E-02
stddev RMSE	1.110E-02	1.127E-02	1.067E-02	1.038E-02	1.08E-02	1.021E-02	1.281E-02	1.211E-02	1.042E-02	1.156E-02

	Training Set: MUNSELL Y					Training Set: All MUNSELL				
	2.5Y	**5Y**	**7.5Y**	**10Y**	**All Y**	**2.5Y**	**5Y**	**7.5Y**	**10Y**	**All Y**
meanRMSE	2.143E-02	1.935E-02	2.190E-02	1.730E-02	1.978E-02	2.912E-02	2.859E-02	3.360E-02	2.756E-02	2.963E-02
minRMSE	0.626E-02	0.463E-02	0.589E-02	0.353E-02	0.353E-02	8.114E-03	1.127E-02	1.113E-02	9.436E-03	8.114E-03
maxRMSE	5.690E-02	6.089E-02	5.362E-02	5.930E-02	6.089E-02	4.887E-02	6.430E-02	6.469E-02	6.008E-02	6.469E-02
stddev RMSE	1.289E-02	1.295E-02	1.282E-02	1.151E-02	1.25E-02	1.175E-02	1.440E-02	1.364E-02	1.197E-02	1.312E-02

	Training Set: MUNSELL GY					Training Set: All MUNSELL				
	2.5GY	**5GY**	**7.5GY**	**10GY**	**All GY**	**2.5GY**	**5GY**	**7.5GY**	**10GY**	**All GY**
meanRMSE	1.890E-02	1.736E-02	1.590E-02	1.362E-02	1.638E-02	2.841E-02	2.873E-02	2.772E-02	2.585E-02	2.766E-02
minRMSE	0.415E-02	0.439E-02	0.544E-02	0.284E-02	0.284E-02	8.555E-03	7.461E-03	1.381E-02	5.837E-03	5.837E-03
maxRMSE	4.712E-02	5.945E-02	3.310E-02	3.519E-02	5.945E-02	5.996E-02	7.886E-02	5.632E-02	6.395E-02	7.886E-02
stddev RMSE	1.048E-02	1.249E-02	0.645E-02	0.729E-02	0.977E-02	1.515E-02	1.590E-02	9.219E-03	1.622E-02	1.458E-02

Table 9.11 (2) *Mean, minimum, maximum and standard deviation of the mean of the RMSE values of the sets of Munsell sub-hues, using the sets of Munsell hues and all Munsell's colour patches as training sets.*

	Training Set: MUNSELL G					Training Set: All MUNSELL				
	2.5G	**5G**	**7.5G**	**10G**	**All G**	**2.5G**	**5G**	**7.5G**	**10G**	**All G**
meanRMSE	1.274E-02	1.290E-02	1.516E-02	1.579E-02	1.414E-02	2.144E-02	1.901E-02	1.987E-02	1.912E-02	1.978E-02
minRMSE	0.507E-02	0.529E-02	0.581E-02	0.241E-02	0.241E-02	6.722E-03	4.590E-03	7.811E-03	6.165E-03	4.590E-03
maxRMSE	2.474E-02	3.591E-02	4.855E-02	3.814E-02	4.855E-02	4.523E-02	5.191E-02	6.202E-02	3.258E-02	6.202E-02
stddev RMSE	0.544E-02	0.621E-02	0.938E-02	0.807E-02	0.741E-02	8.652E-03	9.735E-03	1.195E-02	6.714E-03	9.266E-03

	Training Set: MUNSELL BG					Training Set: All MUNSELL				
	2.5BG	**5BG**	**7.5BG**	**10BG**	**All BG**	**2.5BG**	**5BG**	**7.5BG**	**10BG**	**All BG**
meanRMSE	0.983E-02	1.334E-02	1.367E-02	1.187E-02	1.220E-02	1.788E-02	2.064E-02	2.448E-02	2.063E-02	2.081E-02
minRMSE	0.487E-02	0.334E-02	0.569E-02	0.447E-02	0.334E-02	8.781E-03	6.325E-03	1.352E-02	5.806E-03	5.806E-03
maxRMSE	2.414E-02	3.622E-02	3.125E-02	2.428E-02	3.622E-02	3.160E-02	3.905E-02	4.337E-02	3.436E-02	4.337E-02
stddev RMSE	0.568E-02	0.881E-02	0.684E-02	0.523E-02	0.689E-02	6.809E-03	8.002E-03	9.415E-03	8.433E-03	8.367E-03

	Training Set: MUNSELL B					Training Set: All MUNSELL				
	2.5B	**5B**	**7.5B**	**10B**	**All B**	**2.5B**	**5B**	**7.5B**	**10B**	**All B**
meanRMSE	1.406E-02	1.246E-02	1.175E-02	1.188E-02	1.244E-02	2.334E-02	2.305E-02	3.119E-02	2.459E-02	2.539E-02
minRMSE	0.443E-02	0.361E-02	0.376E-02	0.368E-02	0.361E-02	8.567E-03	5.261E-03	6.305E-03	5.740E-03	5.261E-03
maxRMSE	3.418E-02	2.640E-02	2.303E-02	2.481E-02	3.418E-02	3.587E-02	5.547E-02	6.599E-02	7.193E-02	7.193E-02
stddev RMSE	0.631E-02	0.548E-02	0.541E-02	0.478E-02	0.543E-02	7.686E-03	1.134E-02	1.590E-02	1.619E-02	1.374E-02

	Training Set: MUNSELL PB					Training Set: All MUNSELL				
	2.5PB	**5 PB**	**7.5 PB**	**10 PB**	**All PB**	**2.5PB**	**5 PB**	**7.5 PB**	**10 PB**	**All PB**
meanRMSE	1.344E-02	1.581E-02	1.704E-02	1.746E-02	1.607E-02	2.781E-02	3.197E-02	2.846E-02	2.027E-02	2.712E-02
minRMSE	0.413E-02	0.418E-02	0.462E-02	0.477E-02	0.413E-02	5.235E-03	7.700E-03	6.672E-03	4.467E-03	4.467E-03
maxRMSE	3.106E-02	3.563E-02	7.479E-02	4.338E-02	7.479E-02	8.338E-02	8.619E-02	8.905E-02	4.533E-02	8.905E-02
stddev RMSE	0.711E-02	0.865E-02	1.315E-02	0.901E-02	0.976E-02	1.970E-02	2.014E-02	1.948E-02	9.863E-03	1.804E-02

Table 9.11 (3) *Mean, minimum, maximum and standard deviation of the mean of the RMSE values of the sets of Munsell sub-hues, using the sets of Munsell hues and all Munsell's colour patches as training sets.*

	Training Set: MUNSELL P					Training Set: All MUNSELL				
	2.5P	**5P**	**7.5P**	**10P**	**All P**	**2.5P**	**5P**	**7.5P**	**10P**	**All P**
meanRMSE	2.635E-02	2.748E-02	2.975E-02	2.049E-02	2.571E-02	3.203E-02	3.263E-02	3.443E-02	2.330E-02	3.019E-02
minRMSE	0.613E-02	0.445E-02	0.747E-02	0.555E-02	0.445E-02	5.120E-03	4.745E-03	6.416E-03	5.783E-03	4.745E-03
maxRMSE	8.675E-02	12.20E-02	17.01E-02	8.984E-02	17.01E-02	1.193E-01	1.624E-01	1.894E-01	1.055E-01	1.894E-01
stddev RMSE	1.877E-02	2.214E-02	3.146E-02	1.438E-02	2.21E-02	2.513E-02	3.011E-02	3.598E-02	1.628E-02	2.738E-02

	Training Set: MUNSELL RP					Training Set: All MUNSELL				
	2.5RP	**5RP**	**7.5RP**	**10RP**	**All RP**	**2.5RP**	**5RP**	**7.5RP**	**10RP**	**All RP**
meanRMSE	1.697E-02	1.781E-02	1.947E-02	2.052E-02	1.874E-02	2.238E-02	2.358E-02	2.974E-02	2.573E-02	2.525E-02
minRMSE	0.512E-02	0.313E-02	0.475E-02	0.197E-02	0.197E-02	9.128E-03	6.063E-03	7.034E-03	3.133E-03	3.133E-03
maxRMSE	3.762E-02	4.980E-02	7.014E-02	10.51E-02	10.51E-02	4.550E-02	1.070E-01	7.341E-02	7.809E-02	1.070E-01
stddev RMSE	0.732E-02	1.111E-02	1.241E-02	1.713E-02	1.27E-02	9.888E-03	1.904E-02	1.723E-02	1.611E-02	1.616E-02

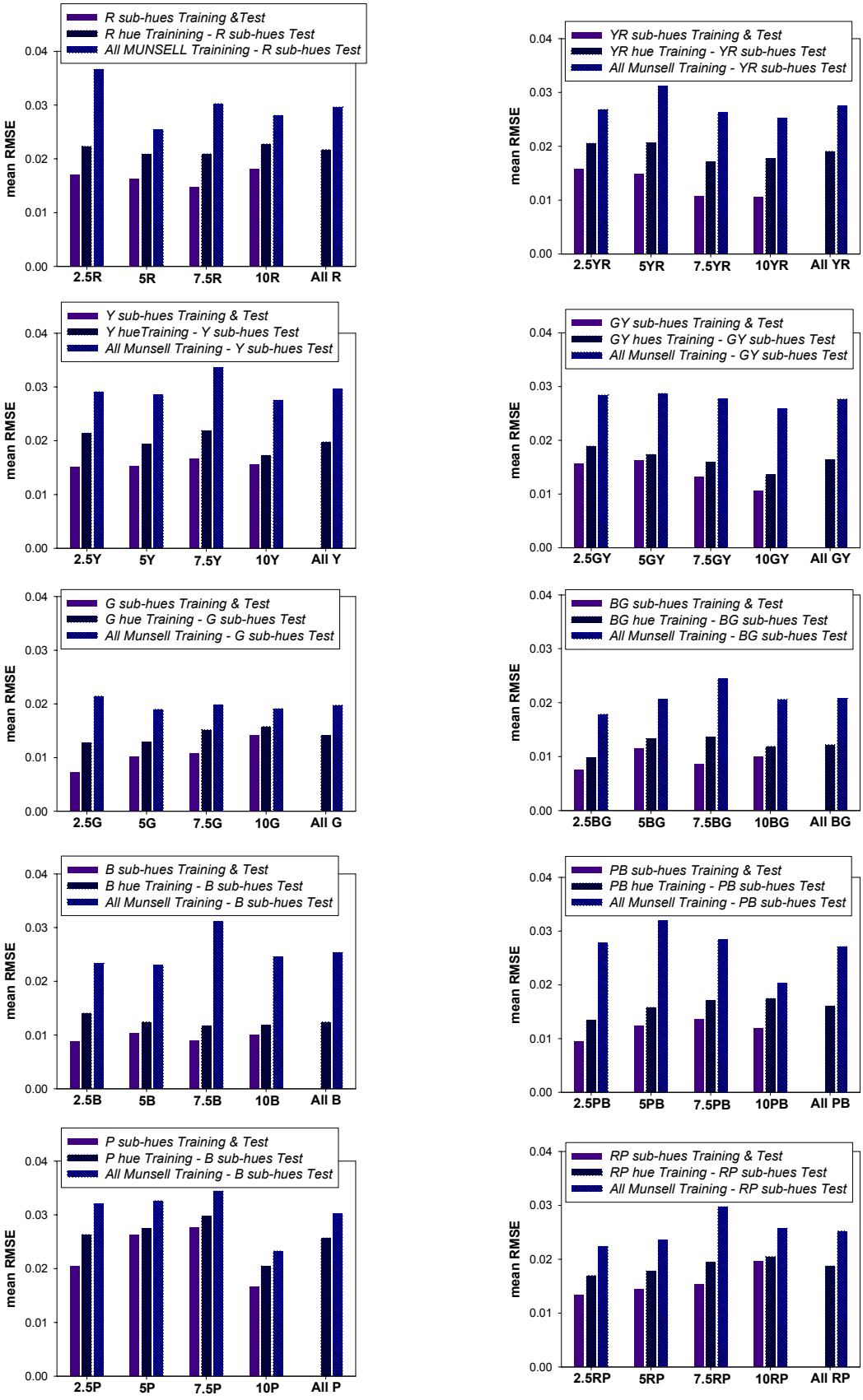

Figure 9.13 *Bar plots of the mean RMSE values for all hues (R, YR, Y, GY, G, BG, B, PB, P, RP) and sub-hues of each hue (2.5, 5, 7.5, 10) of the Munsell Book of Color – Matte Collection, for the training sets: Munsell sub-hues, Munsell hues, and all Munsell's colour patches.*

9.2.4 Influence of homogeneity in hue of the training set using different sets as training and test sets

In order to finish this study on influence of homogeneity in hue of the training set, different sets of colour samples are used as training and test sets: sets of Munsell's hues are used as training sets, and colour samples of the GretagMacbeth ColorChecker DC chart (CCDC) classified in Munsell hues are used as test sets. As mentioned before, this study is carried out using the multispectral configuration of the imaging system and the D65 simulator illuminant.

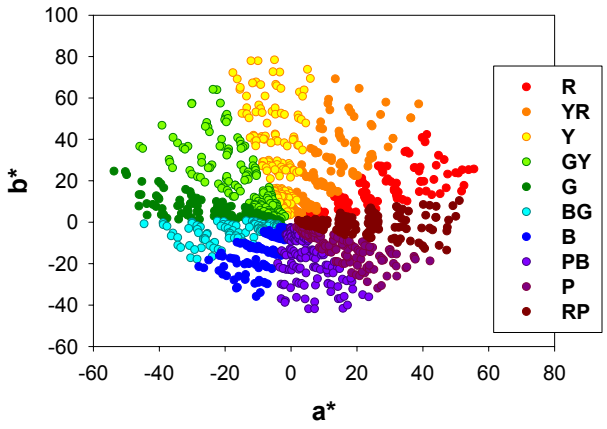

Figure 9.14 *a*b* diagram for the colour patches of the Munsell Book of Color – Matte Collection.*

Considering that the Munsell hue is equivalent to the CIELAB hue angle h_{ab}, which is claculated from the a* and b* CIELAB coordinates, the CCDC's colour samples are classified in Munsell hues manually by plotting each sample on the a*b* diagram for the colour patches of the Munsell Book of Color (Figure 9.14), and determining the corresponding hue depending on the a*b* zone where the sample is located.

All Munsell's colour patches are used as training set for colour samples placed near the a*b* origin, where it is difficult to determine the corresponding hue. Classification of CCDC's colour samples on Munsell hues is shown in Table 9.12.

Table 9.12 *Classification of CCDC's colour samples in Munsell hues. For colour samples in the boundary between two hues and/or out of the Munsell a*b* domain, these are indicated in brackets*

R	B2, D2, E2, F2, G2, H2, K2, N2, O2 (R - RP), P2 (R - RP), F3, L3, M3 (R - RP), N3, Q3 (R - YR), I4
YR	Q2, R2 (YR - R), B3, C3, D3, E3 (YR - R), G3 (YR – R), H3 (YR - R), I3, J3, K3, O3, P3 (YR - R), R3 (YR - Y), B4 (YR - Y), C4, E4 (YR - Y), G4, H4 (YR - R), J4, K4, L4, M4, N4, O4 (YR - Y), P4 (YR - Y), Q4, R4, Q5
Y	S2, S3 (Y - GY), D4, F4 (Y - YR), M5, N5, O5 (Y - YR), P5 (Y - YR), R5, G6 (Y – GY), Q9, R9, R10 (Y - YR)
GY	B5, C5, D5, E5 (GY - Y), F5, G5, H5, B6, C6 (GY – G), D6, E6, F6 (GY- Y), H6 (GY - Y), G7 (GY – G), H7, R7, Q8, R8 (GY - Y)
G	P6 (G - BG), R6, B7 (G – GY), C7 (G – GY), D7 E7, F7 (G – GY), M7 (G – GY out of MUNSELL a*b* domain), N7 (out of MUNSELL a*b* domain), O7 (G – GY), P7, Q7, O9 (G – BG), Q10 (G – BG)
BG	M6, N6, O6, Q6, B8 (BG - G), C8, D8 (BG - G), E8, G8 (BG – B), H8 (BG – B), M8 (BG – B), M9, N9 (BG – B), P9 (BG – B), Q11 (BG - G), R11 (BG - G)
B	F8 (B - BG), N8, B9, E9, F9, G9, H9, I9, K9, L9
PB	O8, P8 (PB - B), C9 (PB - B), D9, J9 (PB - B), F10, G10, H10, I10, J10, K10
P	L10, M10, N10, O10, P10, O11, P11 (P - BP)
RP	C2 (RP - P), I2, J2, L2 (RP - P), M2, B11 (RP - P), C11, D11 (RP - P), E11 (RP - P), F11, G11, H11, I11, J11, K11, L11, M11 (RP - P), N11
All Hues	I5, J5, K5, L5, I6, J6, K6, L6, I7, J7, K7, L7, I8, J8

Results obtained for the CCDC's colour samples classified in Munsell hues, using the sets of Munsell's hues, the CCDC chart itself, and all Munsell's colour patches as training sets, are shown in Tables 9.13 and 9.14.

Table 9.13 *Mean, minimum, maximum and standard deviation of the ΔE^*_{ab} values of the sets of CCDC's colour samples classified in Munsell hues, using the sets of the corresponding Munsell hues, the CCDC chart itself, and all Munsell's colour patches as training sets.*

Training Set	Munsell R	CCDC	All Munsell	Munsell YR	CCDC	All Munsell
meanΔE^*_{ab}	4.574	2.565	6.334	4.201	2.665	4.704
minΔE^*_{ab}	2.666	0.792	2.836	1.451	0.369	2.242
maxΔE^*_{ab}	7.086	7.783	12.658	11.032	6.902	8.179
std. dev. ΔE^*_{ab}	1.265	2.065	2.487	1.904	1.883	1.468

Training Set	Munsell Y	CCDC	All Munsell	Munsell GY	CCDC	All Munsell
meanΔE^*_{ab}	5.272	3.093	6.239	4.475	3.093	4.528
minΔE^*_{ab}	1.144	0.520	2.313	1.938	0.569	2.090
maxΔE^*_{ab}	13.664	5.959	11.083	7.074	7.190	6.572
std. dev. ΔE^*_{ab}	3.098	1.648	2.642	1.457	1.903	1.243

Training Set	Munsell G	CCDC	All Munsell	Munsell BG	CCDC	All Munsell
meanΔE^*_{ab}	5.488	2.724	5.514	3.876	1.984	4.332
minΔE^*_{ab}	3.299	0.481	3.490	1.799	0.647	1.718
maxΔE^*_{ab}	8.880	7.235	8.196	5.898	4.541	8.386
std. dev. ΔE^*_{ab}	1.556	2.103	1.510	1.221	1.294	1.701

Training Set	Munsell B	CCDC	All Munsell	Munsell PB	CCDC	All Munsell
meanΔE^*_{ab}	4.301	3.722	5.961	3.566	4.016	4.963
minΔE^*_{ab}	3.011	0.780	2.831	2.375	0.656	1.860
maxΔE^*_{ab}	5.903	6.395	9.654	5.498	10.041	10.194
std. dev. ΔE^*_{ab}	0.935	2.301	2.247	1.043	3.287	2.914

Training Set	Munsell P	CCDC	All Munsell	Munsell RP	CCDC	All Munsell
meanΔE^*_{ab}	3.127	2.357	4.940	3.509	2.148	4.254
minΔE^*_{ab}	2.017	0.202	2.721	0.810	0.689	2.241
maxΔE^*_{ab}	4.572	5.199	10.641	4.926	6.511	7.156
std. dev. ΔE^*_{ab}	0.937	1.961	2.644	0.989	1.650	1.207

Training Set	Munsell All	CCDC	All Munsell
meanΔE^*_{ab}	3.235	2.050	3.235
minΔE^*_{ab}	0.621	0.265	0.621
maxΔE^*_{ab}	5.176	8.084	5.176
std. dev. ΔE^*_{ab}	1.240	2.265	1.240

Table 9.14 *Mean, minimum, maximum and standard deviation of the RMSE values of the sets of CCDC's colour samples classified in Munsell hues, using the sets of the corresponding Munsell hues, the CCDC chart itself, and all Munsell's colour patches as training sets.*

Training Set	Munsell R	CCDC	All Munsell	Munsell YR	CCDC	All Munsell
meanRMSE	6.189E-02	2.384E-02	6.894E-02	4.717E-02	2.337E-02	4.610E-02
minRMSE	1.741E-02	8.827E-03	2.622E-02	6.953E-03	7.601E-03	1.175E-02
maxRMSE	9.793E-02	4.700E-02	1.072E-01	1.150E-01	4.242E-02	1.048E-01
std. dev. RMSE	2.054E-02	8.860E-03	1.990E-02	2.807E-02	1.023E-02	2.726E-02

Training Set	Munsell Y	CCDC	All Munsell	Munsell GY	CCDC	All Munsell
meanRMSE	4.283E-02	2.891E-02	4.530E-02	2.989E-02	2.185E-02	3.296E-02
minRMSE	6.112E-03	1.190E-02	1.268E-02	1.503E-02	7.844E-03	1.326E-02
maxRMSE	6.747E-02	5.488E-02	1.037E-01	5.645E-02	3.883E-02	7.718E-02
std. dev. RMSE	2.147E-02	1.105E-02	2.698E-02	1.131E-02	9.549E-03	1.893E-02

Training Set	Munsell G	CCDC	All Munsell	Munsell BG	CCDC	All Munsell
meanRMSE	3.175E-02	1.649E-02	3.563E-02	3.050E-02	1.796E-02	2.844E-02
minRMSE	9.299E-03	7.421E-03	1.146E-02	7.881E-03	9.540E-03	6.938E-03
maxRMSE	4.284E-02	3.182E-02	6.468E-02	5.988E-02	2.896E-02	6.594E-02
std. dev. RMSE	1.065E-02	6.735E-03	1.511E-02	1.783E-02	5.407E-03	1.793E-02

Training Set	Munsell B	CCDC	All Munsell	Munsell PB	CCDC	All Munsell
meanRMSE	3.275E-02	2.586E-02	3.283E-02	3.338E-02	2.885E-02	3.170E-02
minRMSE	1.086E-02	1.012E-02	1.475E-02	8.335E-03	8.245E-03	2.034E-02
maxRMSE	5.622E-02	4.700E-02	5.262E-02	5.447E-02	5.576E-02	5.463E-02
std. dev. RMSE	1.724E-02	1.184E-02	1.428E-02	1.594E-02	1.507E-02	1.138E-02

Training Set	Munsell P	CCDC	All Munsell	Munsell RP	CCDC	All Munsell
meanRMSE	3.102E-02	1.867E-02	4.472E-02	4.902E-02	2.051E-02	5.955E-02
minRMSE	8.011E-03	7.922E-03	6.650E-03	1.148E-02	9.484E-03	1.107E-02
maxRMSE	4.737E-02	2.946E-02	6.713E-02	7.326E-02	3.036E-02	9.506E-02
std. dev. RMSE	1.452E-02	7.534E-03	2.181E-02	1.981E-02	6.753E-03	2.528E-02

Training Set	Munsell All	CCDC	All Munsell
meanRMSE	4.578E-02	2.270E-02	4.578E-02
minRMSE	6.945E-03	9.044E-03	6.945E-03
maxRMSE	9.521E-02	4.805E-02	9.521E-02
std. dev. RMSE	2.733E-02	1.194E-02	2.733E-02

As can be seen, best results are always obtained globally (in terms of mean values) when the same set of colour samples is used as training and test set. Nevertheless, this is neither a general nor a realistic situation if the imaging system is pretended to be used as an instrument for measuring colour and/or reconstructing reflectance spectra. In a more general and realistic case, the imaging system would be characterized using a training set the most similar to and representative possible of colour samples to be subsequently measured, but not necessarily using these same samples. This is the reason why different sets of colour samples

are used as training and test sets in this last stage of this study on influence of homogeneity in hue of the training set. On the other hand, the Munsell's colour patches are used as an alternative training set to the CCDC chart, whose appropriateness for colorimetric characterization of imaging systems has been widely proved, due to the fact that most of the CCDC's colour samples fall inside the L*a*b* domain of the Munsell's colour patches.

Considering results obtained using different training and test sets, better results in terms of accuracy of both colour measurement (Table 9.13) and spectral reconstruction (Table 9.14), are globally obtained when CCDC's colour samples are classified in Munsell hues, and system is trained using the sets of Munsell's hues, than using all Munsell's colour patches to train the imaging system. These results can be seen from Figure 9.15, where the mean ΔE^*_{ab} and the mean RMSE values are plotted for the three training sets considered: sets of Munsell's hues, the CCDC chart, and all Munsell's colour patches. It can also be observed that the improvement in accuracy of colour measurement and spectral reconstruction achieved using the sets of Munsell hues as training sets instead of using all Munsell's colour patches depends on the hue considered (Figure 9.15).

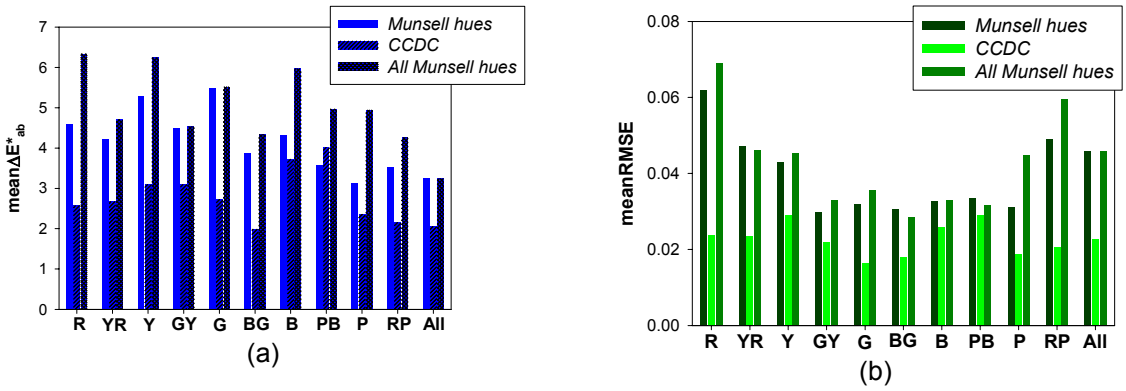

Figure 9.15 *Bar plots of the mean (a) ΔE^*_{ab} values and (b) RMSE values for the sets of CCDC's colour samples classified in Munsell hues, using the sets of the corresponding Munsell hues, the CCDC chart itself, and all Munsell's colour patches as training sets.*

From these results it can be concluded that, using different training and test sets, the homogeneity in hue of the training set tends to improve the accuracy of both colour measurement and spectral reconstruction, in general for all hues, with regard to results obtained using a multi-colour range training set, as it is, in this case, the set of all Munsell's colour patches.

On the other hand, regarding the classification of the CCDC's colour samples in Munsell hues and the use of the sets of Munsell hues as training sets, it is important to notice that quite a lot of the CCDC's colour samples are located on zones of the CIELAB space where there are not Munsell's colour patches (Figure 9.16). This is due to the fact that the Munsell's colour patches present 'discrete' values of the Munsell value coordinate, progressing from very light to very dark colours in equal intervals, and the values of the L* coordinate for the Munsell's colour patches, which would be the equivalent in the CIELAB colour space to the Munsell value dimension, are arranged, as a result, in 'discrete' bands (Figure 9.16).

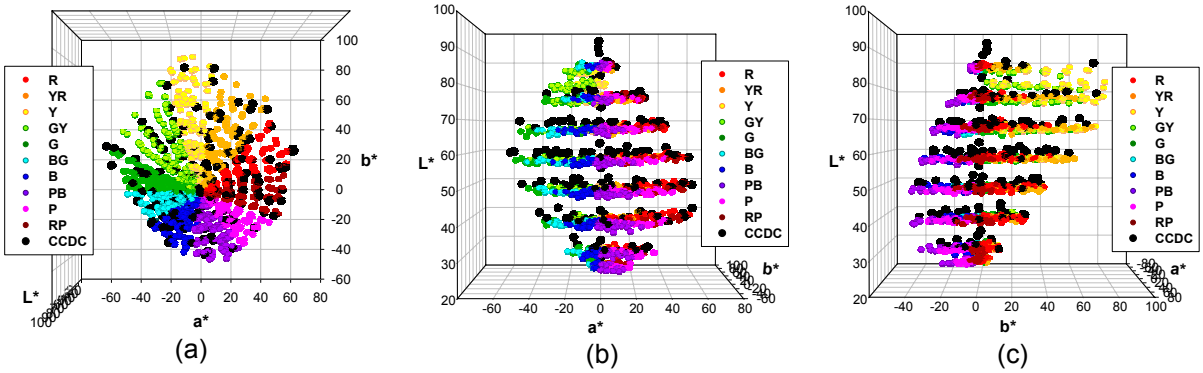

Figure 9.16 *L*a*b* diagram for the colour patches of the Munsell Book of Color – Matte Collection and the CCDC's colour samples, on (a) top, (b) front, and (c) lateral perspectives.*

Consequently, although being classified in some Munsell hue considering their a* and b* coordinates, for some CCDC's samples there are not Munsell's colour patches with similar L* values to train the imaging system. This could be the reason why most of the colour samples associated to the lowest accuracies of colour measurement and spectral reconstruction (biggest ΔE^*_{ab} and RMSE values) obtained using the sets of Munsell's hues as training sets, are samples placed on zones of the CIELAB where there is a lack of Munsell's colour patches, and/or border zones between Munsell hues and/or Munsell's L*a*b* domain (Figure 9.17 and Figure 9.18).

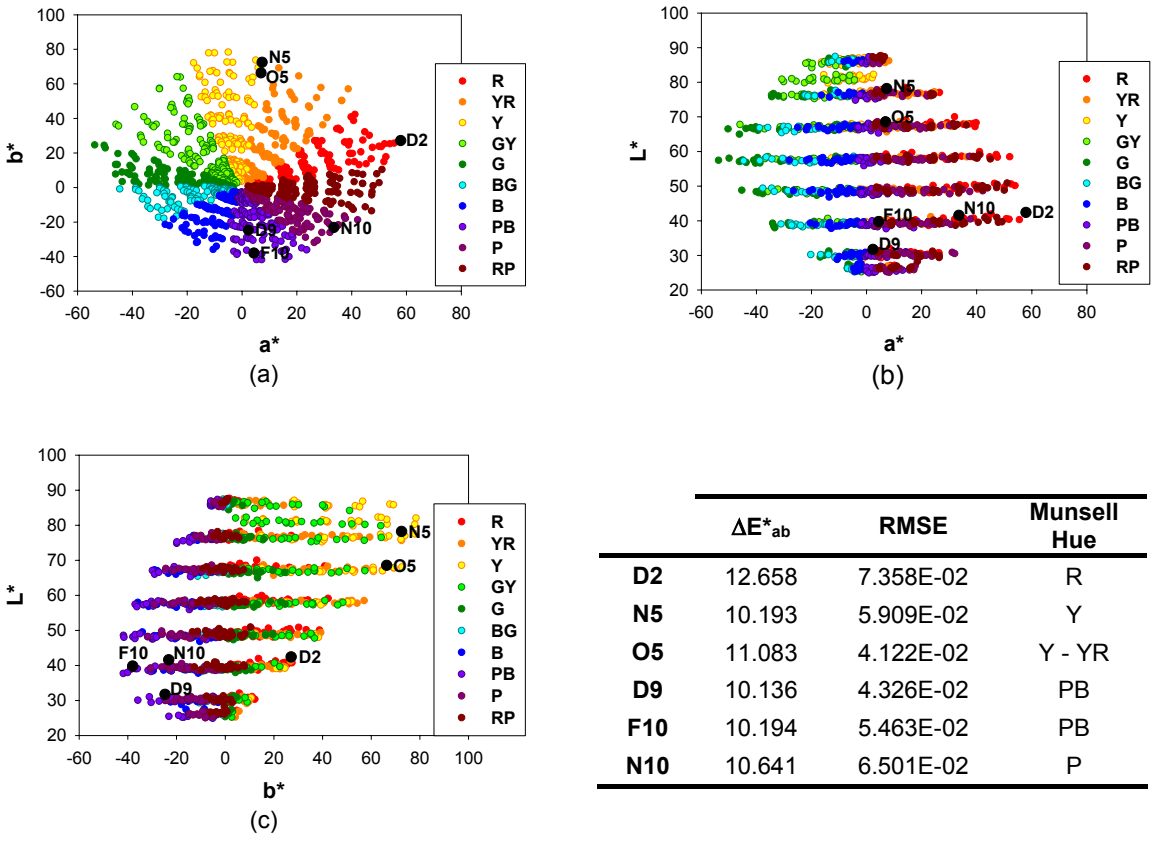

	ΔE^*_{ab}	RMSE	Munsell Hue
D2	12.658	7.358E-02	R
N5	10.193	5.909E-02	Y
O5	11.083	4.122E-02	Y - YR
D9	10.136	4.326E-02	PB
F10	10.194	5.463E-02	PB
N10	10.641	6.501E-02	P

Figure 9.17 *(a) a*b* diagram, (b) L*a* diagram, and (c) L*b* diagram for the Munsell's colour patches and the CCDC's colour samples having the biggest ΔE^*_{ab} values. The ΔE^*_{ab} and RMSE values associated to these samples are shown in the table beside.*

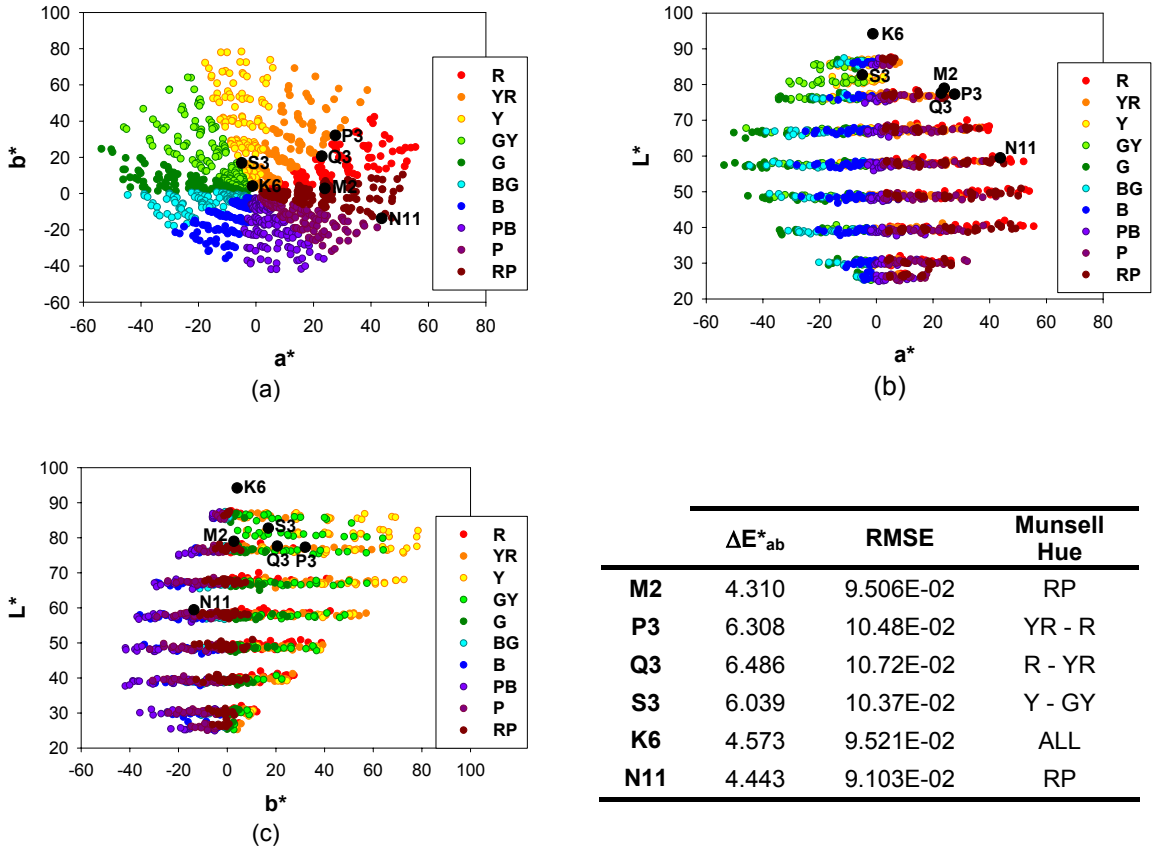

	ΔE^*_{ab}	RMSE	Munsell Hue
M2	4.310	9.506E-02	RP
P3	6.308	10.48E-02	YR - R
Q3	6.486	10.72E-02	R - YR
S3	6.039	10.37E-02	Y - GY
K6	4.573	9.521E-02	ALL
N11	4.443	9.103E-02	RP

Figure 9.18 *(a) a*b* diagram, (b) L*a* diagram, and (c) L*b* diagram for the Munsell's colour patches and the CCDC's colour samples having the biggest RMSE values. The ΔE^*_{ab} and RMSE values associated to these samples are shown in the table beside.*

These results point out that, on one hand, the *a*b* classification method* applied, which considered the location of the CCDC's colour samples on the a*b* diagram of the Munsell's colour patches as the criterion to associate a Munsell hue to each colour sample, is not fine enough and does not work for some samples (samples on border zones of Munsell hues and/or out of Munsell a*b* domain). In this aspect, a more sophisticated classification method should be developed, taking into account more and/or other characteristics of colour samples in order to improve this hue classification, such as the three L*a*b* CIELAB coordinates (or the $L^*C^*h_{ab}$) to define the concrete volume in the CIELAB space occupied by each Munsell hue, or the reflectance spectra which contain all information about colour. On the other hand, the complete training set (comprised by the training sets homogeneous in hue) should be improved to cover the whole CIELAB space of the samples to be used as test set in order to be able to train the imaging system in the widest way possible hue by hue. This improvement of the training sets homogeneous in hue is left for future work.

Regarding the classification method, two different classification methods are subsequently developed and applied. The first of these two methods is based on the CIELAB colour difference values (ΔE^*_{ab}) between all colour patches of the sets of Munsell's hues and each CCDC's colour sample, and is called the *ΔE^*_{ab} classification method*. The second method is based on the RMSE between the reflectance spectra of the colour patches of the sets of Munsell's hues and the reflectance spectrum of each CCDC's colour sample, and is

called the *RMSE classification method*. A detailed description of these two methods and results obtained applying them are presented below.

In the *ΔE^*_{ab} classification method*, the CIELAB colour difference (ΔE^*_{ab}) between each CCDC's colour sample and all colour patches belonging to a Munsell hue are calculated. The mean value of these ΔE^*_{ab} values is associated to the Munsell hue, and the CCDC's colour sample is classified in the Munsell hue having the minimum mean ΔE^*_{ab} value between all colour patches of the Munsell hue and the CCDC's colour sample. Unlike the *a*b* classification method*, in this case the three L*a*b* CIELAB coordinates are considered in the classification process and all CCDC's colour samples are classified in one of the Munsell's hues.

Results obtained for the CCDC's colour samples classified in Munsell hues by applying the *ΔE^*_{ab} classification method*, using the sets of Munsell's hues, the CCDC chart itself, and all Munsell's colour patches as training sets, are shown in Tables 9.15 and 9.16.

Table 9.15 *ΔE^*_{ab} classification method: mean, minimum, maximum and standard deviation of the ΔE^*_{ab} values of the sets of CCDC's colour samples classified in Munsell hues, using the sets of Munsell hues, the CCDC chart itself, and all Munsell's colour patches as training sets.*

Training Set	Munsell R	CCDC	All Munsell	Munsell YR	CCDC	All Munsell
meanΔE^*_{ab}	4.267	2.944	5.921	4.302	2.662	4.794
minΔE^*_{ab}	2.427	0.755	2.723	1.385	0.484	2.242
maxΔE^*_{ab}	7.086	7.783	12.658	11.032	4.946	8.179
std. dev. ΔE^*_{ab}	1.277	2.206	2.524	2.190	1.472	1.615

Training Set	Munsell Y	CCDC	All Munsell	Munsell GY	CCDC	All Munsell
meanΔE^*_{ab}	5.748	2.256	6.390	4.035	2.432	4.486
minΔE^*_{ab}	2.500	0.369	3.406	1.168	0.265	2.418
maxΔE^*_{ab}	13.664	5.959	11.083	8.501	5.769	6.572
std. dev. ΔE^*_{ab}	2.790	1.695	2.401	1.870	1.607	1.300

Training Set	Munsell G	CCDC	All Munsell	Munsell BG	CCDC	All Munsell
meanΔE^*_{ab}	5.460	2.683	5.244	4.131	2.673	4.550
minΔE^*_{ab}	3.506	0.569	2.090	1.799	0.481	1.718
maxΔE^*_{ab}	8.880	5.733	8.196	7.112	7.235	8.386
std. dev. ΔE^*_{ab}	1.616	1.746	1.717	1.516	2.157	1.728

Training Set	Munsell B	CCDC	All Munsell	Munsell PB	CCDC	All Munsell
meanΔE^*_{ab}	3.726	2.908	4.447	3.590	4.823	5.402
minΔE^*_{ab}	0.898	0.366	0.621	2.375	1.124	1.860
maxΔE^*_{ab}	5.903	8.084	9.654	5.342	10.041	10.194
std. dev. ΔE^*_{ab}	1.198	2.453	2.107	0.971	3.464	3.614

Training Set	Munsell P	CCDC	All Munsell	Munsell RP	CCDC	All Munsell
meanΔE^*_{ab}	3.314	2.790	4.651	3.505	2.062	4.221
minΔE^*_{ab}	2.017	0.202	2.527	0.810	0.689	2.241
maxΔE^*_{ab}	4.572	6.511	10.641	4.926	6.902	6.438
std. dev. ΔE^*_{ab}	0.902	2.200	2.425	0.956	1.742	0.917

Results obtained applying the ΔE^*_{ab} *classification method* and using the sets of Munsell's hues as training sets (Tables 9.15 and 9.16) cannot be directly compared to those obtained applying the *a*b* classification method* (Tables 9.13 and 9.14) since the CCDC's colour samples could be classified in different Munsell's hues depending on the classification method applied, but must be compared considering them relative to results obtained using the CCDC chart itself, and all Munsell's colour patches as training sets.

Table 9.16 ΔE^*_{ab} *classification method*: *mean, minimum, maximum and standard deviation of the mean of the RMSE values of the sets of CCDC's and CCCR's colour samples classified in Munsell hues, using the sets of the corresponding Munsell hues, the CCDC and CCCR charts respectively, and all Munsell's colour patches as training sets.*

Training Set	Munsell R	CCDC	All Munsell	Munsell YR	CCDC	All Munsell
meanRMSE	6.554E-02	2.545E-02	6.569E-02	6.304E-02	2.833E-02	6.095E-02
minRMSE	1.479E-02	1.201E-02	1.229E-02	8.738E-03	1.100E-02	1.463E-02
maxRMSE	1.304E-01	4.377E-02	1.032E-01	1.210E-01	5.760E-02	1.170E-01
std. dev. RMSE	3.361E-02	8.856E-03	3.351E-02	3.493E-02	1.156E-02	3.356E-02

Training Set	Munsell Y	CCDC	All Munsell	Munsell GY	CCDC	All Munsell
meanRMSE	7.339E-02	3.006E-02	7.126E-02	6.543E-02	3.064E-02	6.408E-02
minRMSE	3.898E-02	1.634E-02	4.062E-02	2.091E-02	1.476E-02	1.707E-02
maxRMSE	1.128E-01	5.137E-02	1.102E-01	1.515E-01	6.208E-02	1.294E-01
std. dev. RMSE	2.156E-02	9.076E-03	2.338E-02	3.929E-02	1.270E-02	3.638E-02

Training Set	Munsell G	CCDC	All Munsell	Munsell BG	CCDC	All Munsell
meanRMSE	3.025E-02	1.906E-02	3.151E-02	2.845E-02	2.231E-02	2.886E-02
minRMSE	1.425E-02	1.455E-02	1.575E-02	1.162E-02	1.008E-02	9.342E-03
maxRMSE	4.957E-02	2.901E-02	5.824E-02	5.744E-02	5.494E-02	5.868E-02
std. dev. RMSE	1.026E-02	4.262E-03	1.330E-02	1.313E-02	9.600E-03	1.429E-02

Training Set	Munsell B	CCDC	All Munsell	Munsell PB	CCDC	All Munsell
meanRMSE	4.044E-02	2.837E-02	3.946E-02	4.554E-02	3.784E-02	4.154E-02
minRMSE	1.180E-02	1.029E-02	1.166E-02	1.890E-02	2.015E-02	2.702E-02
maxRMSE	1.056E-01	5.644E-02	1.147E-01	6.766E-02	4.820E-02	5.260E-02
std. dev. RMSE	2.502E-02	1.074E-02	2.347E-02	1.774E-02	9.686E-03	9.565E-03

Training Set	Munsell P	CCDC	All Munsell	Munsell RP	CCDC	All Munsell
meanRMSE	3.660E-02	3.250E-02	4.810E-02	6.806E-02	2.891E-02	7.344E-02
minRMSE	1.221E-02	1.859E-02	1.505E-02	1.370E-02	1.778E-02	1.323E-02
maxRMSE	5.484E-02	5.022E-02	7.646E-02	1.206E-01	5.330E-02	1.066E-01
std. dev. RMSE	1.606E-02	1.137E-02	2.362E-02	2.914E-02	8.283E-03	2.775E-02

In terms of accuracy of colour measurement, quite similar results are obtained applying the *a*b* classification method* (Table 9.13) and the ΔE^*_{ab} *classification method* (Table 9.15). Considering results obtained using different training and test sets, better results are globally obtained when CCDC's colour samples are classified in Munsell hues, and the system is trained using the sets of Munsell's hues, than using all Munsell's colour patches as training set. These results can also be seen from Figure 9.19 (a), where the mean ΔE^*_{ab} values

are plotted for the three training sets considered. The improvement in accuracy of colour measurement using the sets of Munsell hues as training sets instead of using all Munsell's colour patches depends on the hue considered (Figure 9.19 (a)).

Regarding the accuracy of spectral reconstruction, slightly different results are obtained applying the *a*b* classification method* (Table 9.14) and the *ΔE^*_{ab} classification method* (Table 9.16). Considering results obtained using different training and test sets, quite similar results are globally obtained classifying the CCDC's colour samples in Munsell's hues and using the sets of Munsell's hues as training sets, and using all Munsell's colour patches as training set, unlike the globally better results obtained classifying the CCDC's colour samples in Munsell's hues obtained applying the *a*b* classification method*. These results can be seen from Figure 9.19 (b), where the mean RMSE values are plotted for each Munsell's hue using the three training sets considered.

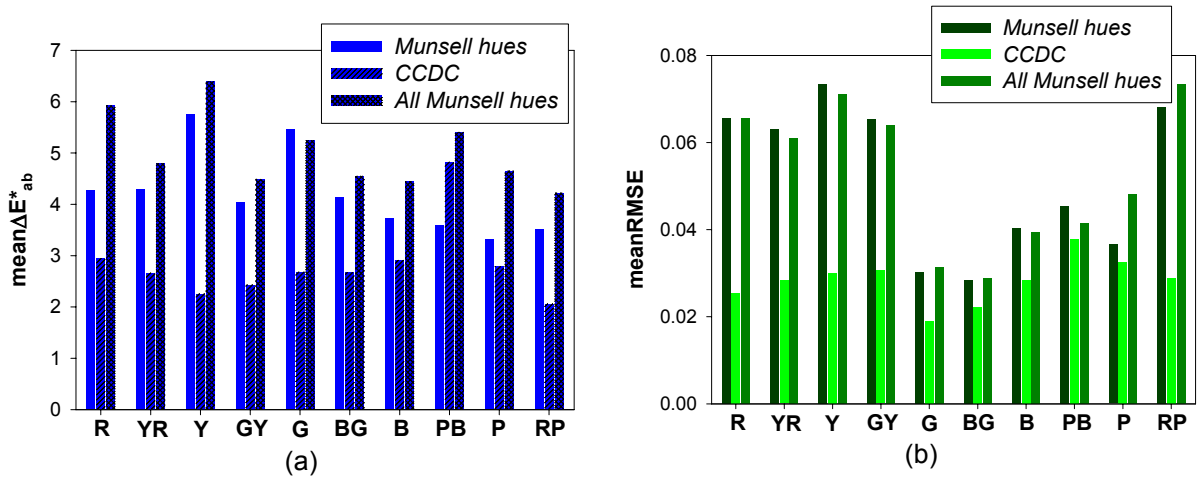

Figure 9.19 *ΔE^*_{ab} classification method*: *bar plots of the mean (a) ΔE^*_{ab} values and (b) RMSE values for the sets of CCDC's colour samples classified in Munsell hues, using the sets of Munsell hues, the CCDC chart itself, and all Munsell's colour patches as training sets.*

In the *RMSE classification method*, the RMSE between the reflectance spectrum of each CCDC's colour sample and the reflectance spectra of all colour patches belonging to a Munsell hue are calculated. The mean value of these RMSE values is associated to the Munsell hue, and the CCDC's colour sample is classified in the Munsell hue having the minimum mean RMSE value between the reflectance spectra of all colour patches of the Munsell hue and the reflectance spectrum of the CCDC's colour sample. In this case the reflectance spectra, from which all colorimetric information about the colour samples can be computed, are directly considered in the classification process and all CCDC's colour samples are classified in one of the Munsell's hues.

Results obtained for the CCDC's colour samples classified in Munsell hues by applying the *RMSE classification method*, using the sets of Munsell's hues, the CCDC chart itself, and all Munsell's colour patches as training sets, are shown in Tables 9.17 and 9.18.

Also in this case, results obtained applying the *RMSE classification method* and using the sets of Munsell's hues as training sets (Tables 9.17 and 9.18) cannot be directly compared to those obtained applying either the *ΔE^*_{ab} classification method* (Tables 9.15 and 9.16) nor the *a*b* classification method* (Tables 9.13 and 9.14), since the CCDC's colour samples could be classified in different Munsell's hues depending on the classification method applied. Results must be compared considering them relative to results obtained using the CCDC chart itself, and all Munsell's colour patches as training sets.

In terms of accuracy of colour measurement, quite similar results are obtained applying the three classification methods (Tables 9.13, 9.15, and 9.17). As can be seen from Figure 9.20 (a), considering results obtained using different training and test sets, better results are globally obtained when CCDC's colour samples are classified in Munsell hues, and the sets of Munsell's hues are used as training sets, than using all Munsell's colour patches as training set.

Table 9.17 *RMSE classification method: mean, minimum, maximum and standard deviation of the mean of the ΔE^*_{ab} values of the sets of CCDC's colour samples classified in Munsell hues, using the sets of the corresponding Munsell hues, the CCDC chart itself, and all Munsell's colour patches as training sets.*

Training Set	Munsell R	CCDC	All Munsell	Munsell YR	CCDC	All Munsell
meanΔE^*_{ab}	5.408	2.450	5.895	5.774	2.471	5.360
minΔE^*_{ab}	2.427	0.689	2.512	3.058	0.792	3.304
maxΔE^*_{ab}	10.948	6.138	12.658	11.032	5.959	11.083
std. dev. ΔE^*_{ab}	2.291	1.581	2.869	2.317	1.576	1.833

Training Set	Munsell Y	CCDC	All Munsell	Munsell GY	CCDC	All Munsell
meanΔE^*_{ab}	4.697	1.515	4.927	4.069	1.175	4.359
minΔE^*_{ab}	0.480	0.265	2.241	1.456	0.366	2.831
maxΔE^*_{ab}	13.664	4.128	10.193	7.074	2.222	6.037
std. dev. ΔE^*_{ab}	3.317	0.950	1.921	1.713	0.588	0.995

Training Set	Munsell G	CCDC	All Munsell	Munsell BG	CCDC	All Munsell
meanΔE^*_{ab}	5.614	3.810	4.543	4.865	3.237	5.792
minΔE^*_{ab}	1.344	0.497	0.621	2.952	0.656	3.060
maxΔE^*_{ab}	16.174	10.041	10.136	6.634	8.778	10.194
std. dev. ΔE^*_{ab}	3.065	2.307	1.896	0.894	2.539	2.337

Training Set	Munsell B	CCDC	All Munsell	Munsell PB	CCDC	All Munsell
meanΔE^*_{ab}	5.238	2.178	5.627	3.613	0.940	2.728
minΔE^*_{ab}	4.824	0.647	4.346	3.000	0.202	1.860
maxΔE^*_{ab}	5.903	4.808	7.422	4.312	1.495	4.097
std. dev. ΔE^*_{ab}	0.377	1.633	1.099	0.660	0.666	1.200

Training Set	Munsell P	CCDC	All Munsell	Munsell RP	CCDC	All Munsell
meanΔE^*_{ab}	3.248	2.132	4.522	3.958	2.988	5.440
minΔE^*_{ab}	2.017	0.755	2.362	3.360	2.422	4.443
maxΔE^*_{ab}	4.800	4.690	10.641	4.555	3.555	6.438
std. dev. ΔE^*_{ab}	1.058	1.281	2.692	0.845	0.801	1.410

Regarding the accuracy of spectral reconstruction, similar results are obtained applying the *RMSE classification method* (Table 9.18) and the *ΔE^*_{ab} classification method* (Table 9.16), and slightly different to those obtained applying the *a*b* classification method* (Table 9.14). Similarly to results obtained applying the *ΔE^*_{ab} classification method*, and as can be seen from Figure 9.20 (b), quite similar results are globally obtained classifying the CCDC's colour samples in Munsell's hues and using the sets of Munsell's hues as training set and using all Munsell's colour patches as training set, unlike the globally better results obtained classifying the CCDC's colour samples in Munsell's hues obtained applying the *a*b* classification method*.

Table 9.18 *RMSE classification method: mean, minimum, maximum and standard deviation of the mean of the RMSE values of the sets of CCDC's and CCCR's colour samples classified in Munsell hues, using the sets of the corresponding Munsell hues, the CCDC and CCCR charts respectively, and all Munsell's colour patches as training sets.*

Training Set	Munsell R	CCDC	All Munsell	Munsell YR	CCDC	All Munsell
meanRMSE	8.090E-02	2.840E-02	7.918E-02	6.983E-02	2.509E-02	6.685E-02
minRMSE	2.961E-02	2.081E-02	2.595E-02	3.523E-02	1.100E-02	3.426E-02
maxRMSE	1.304E-01	5.330E-02	9.800E-02	1.096E-01	5.760E-02	1.085E-01
std. dev. RMSE	2.790E-02	9.603E-03	2.327E-02	2.462E-02	1.025E-02	2.559E-02

Training Set	Munsell Y	CCDC	All Munsell	Munsell GY	CCDC	All Munsell
meanRMSE	9.489E-02	3.653E-02	9.678E-02	5.552E-02	2.732E-02	5.766E-02
minRMSE	4.586E-02	1.636E-02	6.197E-02	2.876E-02	1.536E-02	4.062E-02
maxRMSE	1.540E-01	6.208E-02	1.294E-01	8.225E-02	5.494E-02	8.393E-02
std. dev. RMSE	2.813E-02	1.152E-02	1.864E-02	1.803E-02	1.173E-02	1.106E-02

Training Set	Munsell G	CCDC	All Munsell	Munsell BG	CCDC	All Munsell
meanRMSE	3.108E-02	2.321E-02	2.655E-02	3.277E-02	2.507E-02	3.523E-02
minRMSE	9.279E-03	1.008E-02	9.342E-03	1.320E-02	1.029E-02	2.017E-02
maxRMSE	6.613E-02	4.619E-02	5.824E-02	5.744E-02	4.820E-02	5.868E-02
std. dev. RMSE	1.311E-02	6.590E-03	1.235E-02	1.185E-02	1.020E-02	1.266E-02

Training Set	Munsell B	CCDC	All Munsell	Munsell PB	CCDC	All Munsell
meanRMSE	6.204E-02	3.280E-02	4.669E-02	5.426E-02	2.721E-02	3.633E-02
minRMSE	4.795E-02	1.758E-02	3.595E-02	4.402E-02	2.015E-02	2.702E-02
maxRMSE	7.549E-02	5.415E-02	5.471E-02	6.498E-02	3.572E-02	4.219E-02
std. dev. RMSE	1.204E-02	1.250E-02	8.435E-03	1.049E-02	7.887E-03	8.154E-03

Training Set	Munsell P	CCDC	All Munsell	Munsell RP	CCDC	All Munsell
meanRMSE	4.685E-02	3.472E-02	5.737E-02	6.943E-02	3.864E-02	8.574E-02
minRMSE	3.689E-02	1.201E-02	3.061E-02	5.656E-02	3.829E-02	7.739E-02
maxRMSE	5.484E-02	5.022E-02	7.646E-02	8.230E-02	3.898E-02	9.408E-02
std. dev. RMSE	6.792E-03	1.334E-02	1.520E-02	1.820E-02	4.850E-04	1.180E-02

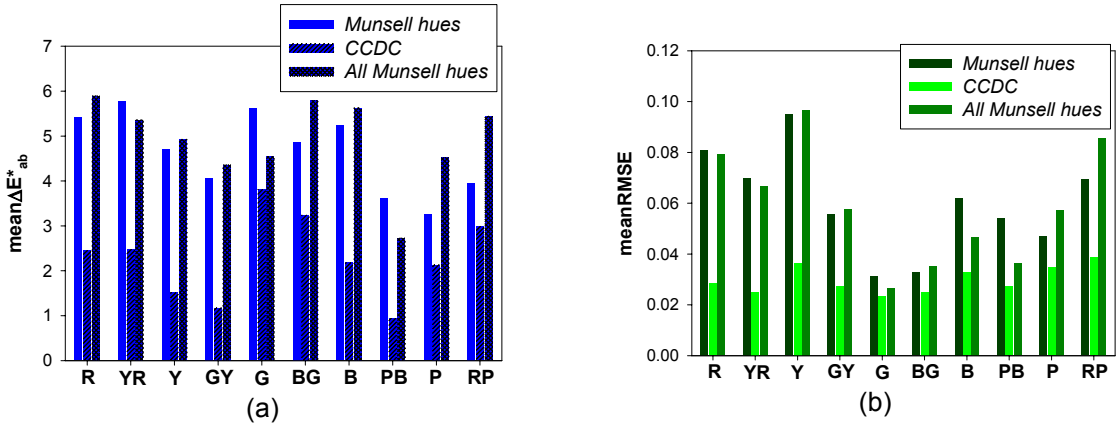

Figure 9.20 *RMSE classification method: bar plots of the mean (a) ΔE^*_{ab} values and (b) RMSE values for the sets of CCDC's colour samples classified in Munsell hues, using the sets of the corresponding Munsell hues, the CCDC chart itself, and all Munsell's colour patches as training sets.*

In order to compare directly the system's performance using the sets of Munsell's hues as training sets and the CCDC's colour samples classified in Munsell's hues by applying the three classification methods as test sets, the mean, minimum, maximum and standard deviation of the ΔE^*_{ab} values and the RMSE values obtained for all CCDC's colour samples are computed (Table 9.19 and Figures 9.21 and 9.22). As can be seen from Table 9.19 and from Figures 9.21 and 9.22, the best results are globally obtained using the *a*b* classification method* to classify the CCDC's colour samples in Munsell'es hues.

Table 9.19 *Mean, minimum, maximum and standard deviation of the ΔE^*_{ab} and the RMSE values for all CCDC's colour samples classified in Munsell's hues by the a*b* classification method, the ΔE^*_{ab} classification method and the RMSE classification method, and using the sets of Munsell's hues as training sets.*

	a*b* classif. meth.	***ΔE^*_{ab} classif. meth.***	***RMSE classif. meth.***
meanΔE^*_{ab}	4.190	4.207	5.101
minΔE^*_{ab}	0.621	0.810	0.480
maxΔE^*_{ab}	13.66	13.66	16.17
std. dev. ΔE^*_{ab}	1.686	1.756	2.611
meanRMSE	5.232E-02	5.296E-02	5.500E-02
minRMSE	1.004E-02	8.738E-03	9.279E-03
maxRMSE	1.304E-01	1.515E-01	1.540E-01
std. dev. RMSE	3.071E-02	3.143E-02	3.080E-02

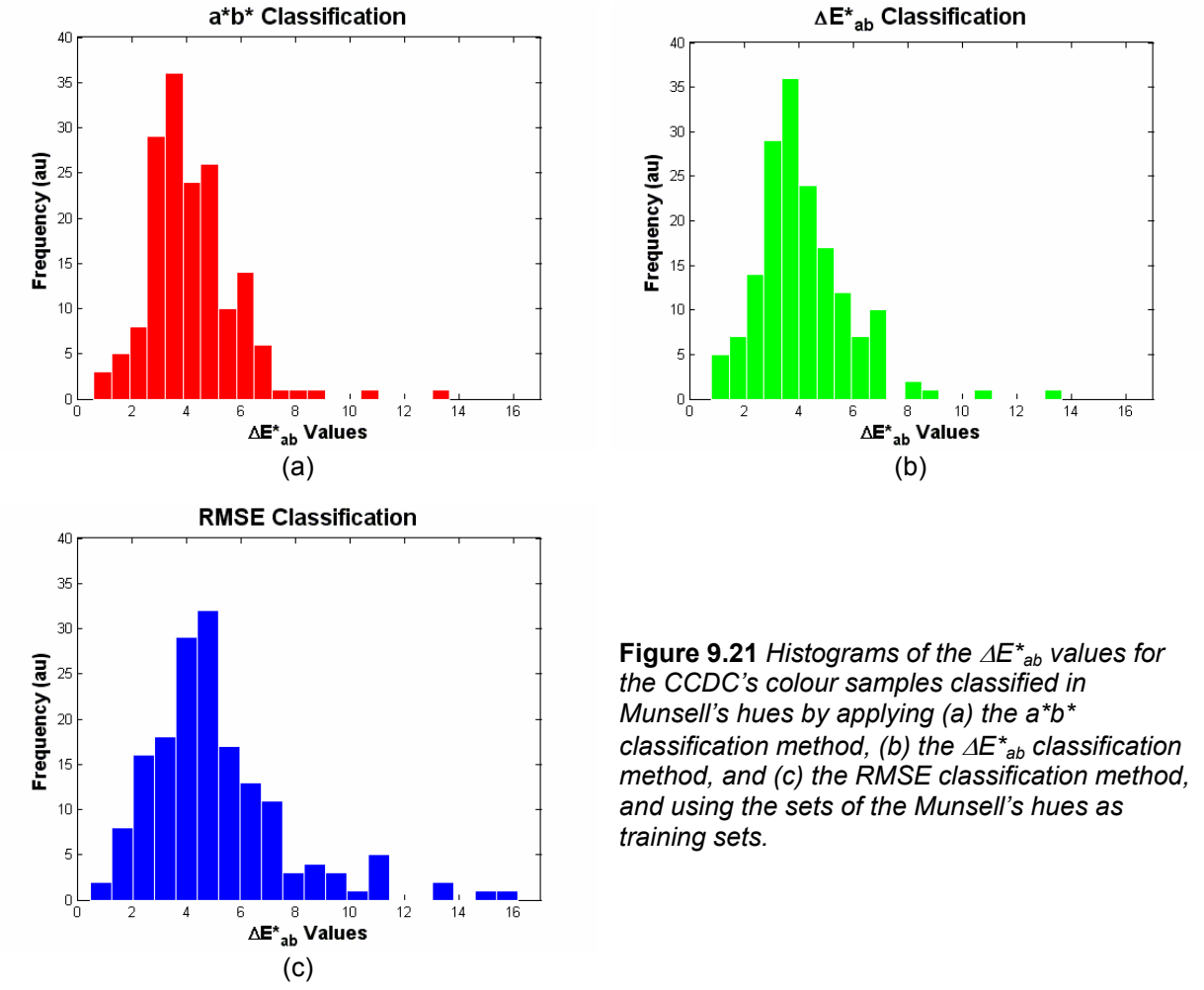

Figure 9.21 *Histograms of the ΔE^*_{ab} values for the CCDC's colour samples classified in Munsell's hues by applying (a) the a*b* classification method, (b) the ΔE^*_{ab} classification method, and (c) the RMSE classification method, and using the sets of the Munsell's hues as training sets.*

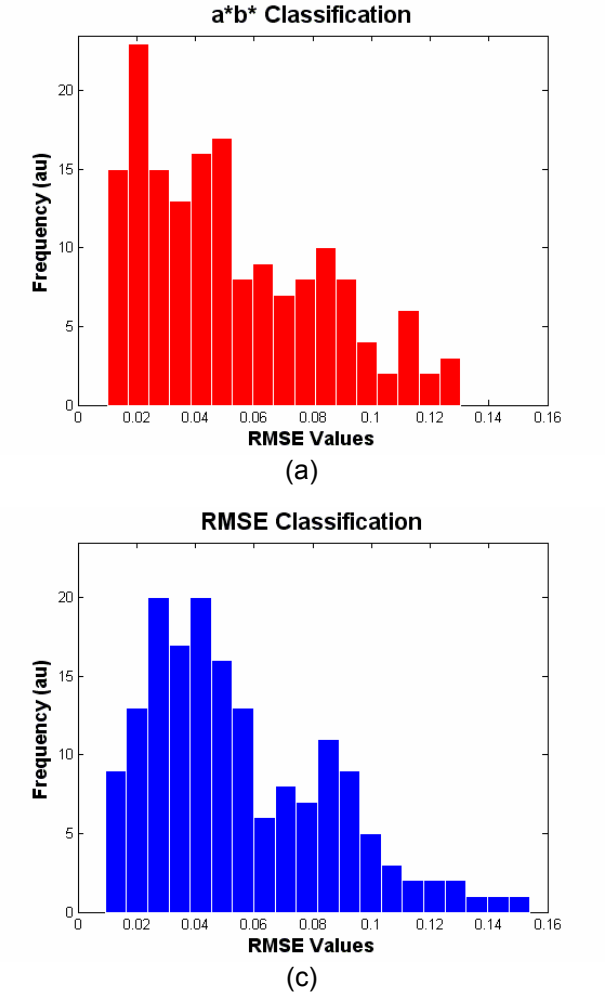

Figure 9.22 *Histograms of the RMSE values for the CCDC's colour samples classified in Munsell's hues by applying (a) the a*b* classification method, (b) the ΔE^*_{ab} classification method, and (c) the RMSE classification method, and using the sets of the Munsell's hues as training sets.*

Taking these results into account it can be concluded that, using different training and test sets, the homogeneity in hue of the training set and the classification of the colour samples of the test set in hues tends to improve the accuracy of both colour measurement and spectral reconstruction, in general for all hues, with regard to results obtained using a multi-colour range training set, as it is, in this case, the set of all Munsell's colour patches.

On the other hand, the complete training set (comprised by the training sets homogeneous in hue) should be improved to cover the whole CIELAB space and/or the reflectance spectra space of the samples to be used as test set in order to be able to train the imaging system in the widest way possible hue by hue. This improvement of the training sets homogeneous in hue is left for future work.

Finally, regarding the classification of the colour samples of the test set in hues, three classification methods are tested, and the best performance is obtained by applying the *a*b* classification method*. The main aim of these methods is to classify the colour samples of a known test set in hues in order to obtain the best system's performance and prove that system's performance is improved when different training sets homogeneous in hue are used. These methods require the previous knowledge of the colour samples of the test set (CIELAB coordinates, reflectance spectra) which is neither a general nor a realistic situation if the imaging system is pretended to be used as an instrument for measuring colour and/or reconstructing reflectance spectra. Future work should be oriented to develop a classification method of the colour samples to be measured based on the corresponding digital responses obtained directly from the multispectral imaging system.

9.3 Accuracy of colour measurement and spectral reconstruction depending on the Munsell Value and Chroma coordinates

Previously in section 9.1, general tendencies of system's performance depending on the colour ranges, and evaluated using the CCDC chart as training and test set, were presented for both configurations (colorimetric and multispectral) and for both illuminants used (incandescent lamp and D65 simulator).

Commonly for both configurations and for both illuminants, no correlation was observed between both the CIELAB colour difference values and the RMSE values, and the CIELAB coordinates a* and/or b*. On the other hand, increasing CIELAB colour differences seemed to be associated to lower values of L* coordinate.

Considering the subsequent analysis carried out in section 9.2 using the colour patches of the Munsell Book of Color – Matte Collection as training and test set, no correlation was observed either between both the CIELAB colour difference values and the RMSE values and, in this case, the Munsell hues and/or sub-hues, which could be considered equivalent to the CIELAB hue angle h_{ab} in the Munsell Colour System (Figure 9.23).

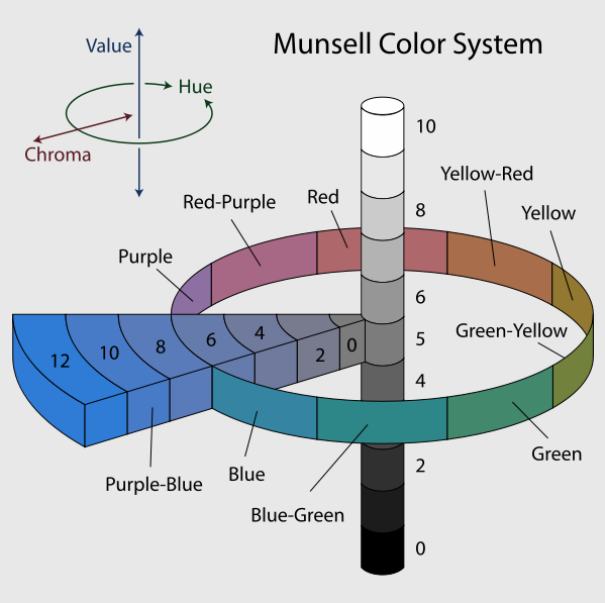

Figure 9.23 *The Munsell color system, showing: a circle of hues at value 5 chroma 6; the neutral values from 0 to 10; and the chromas of purple-blue (5PB) at value 5. (Source: http://en.wikipedia.org/wiki/Munsell_color_system)*

The Munsell Colour System is a colour space that specifies colours based on three colour dimensions: hue, value (lightness), and chroma (color purity or colorfulness). The Munsell hue would be equivalent to the CIELAB hue angle (h_{ab}), the Munsell chroma, which is the the difference from gray at a given hue and lightness in the Munsell color system, would be equivalent to the CIELAB chroma (C*), and the Munsell value the equivalent to the CIELAB L* coordinate (Figure 9.23).

Therefore, in order to complete the analysis of system's performance carried out using the Munsell's colour patches, the accuracy of colour measurement and spectral reconstruction is analyzed depending on the Munsell value and chroma coordinates using the Munsell's colour patches grouped in hues and sub-hues as training and test sets, equivalently to the analysis carried outt depending on the CIELAB L* and C* coordinates when using the CCDC chart. This analysis is carried out for both configurations (colorimetric and multispectral) and for both illuminants used (incandescent lamp and D65 simulator).

In order to determine if there is any kind of correlation between the accuracy of colour measurement and spectral reconstruction and the Munsell value and chroma coordinates, the CIELAB colour difference and the RMSE associated to the colour patches with a same chroma are plotted for each Munsell sub-hue as a function of the value coordinate for all chroma values of each sub-hue. Some examples of these plots are shown in Figures 9.24 (ΔE^*_{ab} vs value for all chroma values) and 9.25 (RMSE vs value for all chroma values). The plots of the CIELAB colour difference and the RMSE values for all Munsell sub-hues (2.5, 5, 7.5, 10) of each Munsell hue (R, YR, Y, GY, G, BG, B, PB, P, RP), for both the colorimetric

and the multispectral configurations, and using both the incandescent lamp and the D65 simulator illuminants, can be found in Appendixes 3 and 4, respectively.

In terms of accuracy of colour measurement, a general tendency is detected for all Munsell sub-hues, both system's configurations and both illuminants. Apart from the great fluctuations between samples having a same Munsell chroma value, it can be seen that the CIELAB colour differences tend to decrease with an increasing value of the Munsell value coordinate, for all possible Munsell chroma values and for all Munsell sub-hues. In general, it could be said that larger CIELAB colour differences are obtained for samples having a Munsell value V < 5 – 6, and CIELAB colour differences tend to increase slightly for samples having a Munsell Value V > 7 – 8 (Figure 9.24). This general tendency is also followed by the RMSE values, although there is not such a decrease in the RMSE values with an increasing value of the Munsell value coordinate as there is for the CIELAB colour differences (Figure 9.25). On the other hand, the RMSE values also tend to increase slightly for samples having a Munsell Value V > 7 – 8 (Figure 9.25), as it occurrs for the CIELAB colour differences.

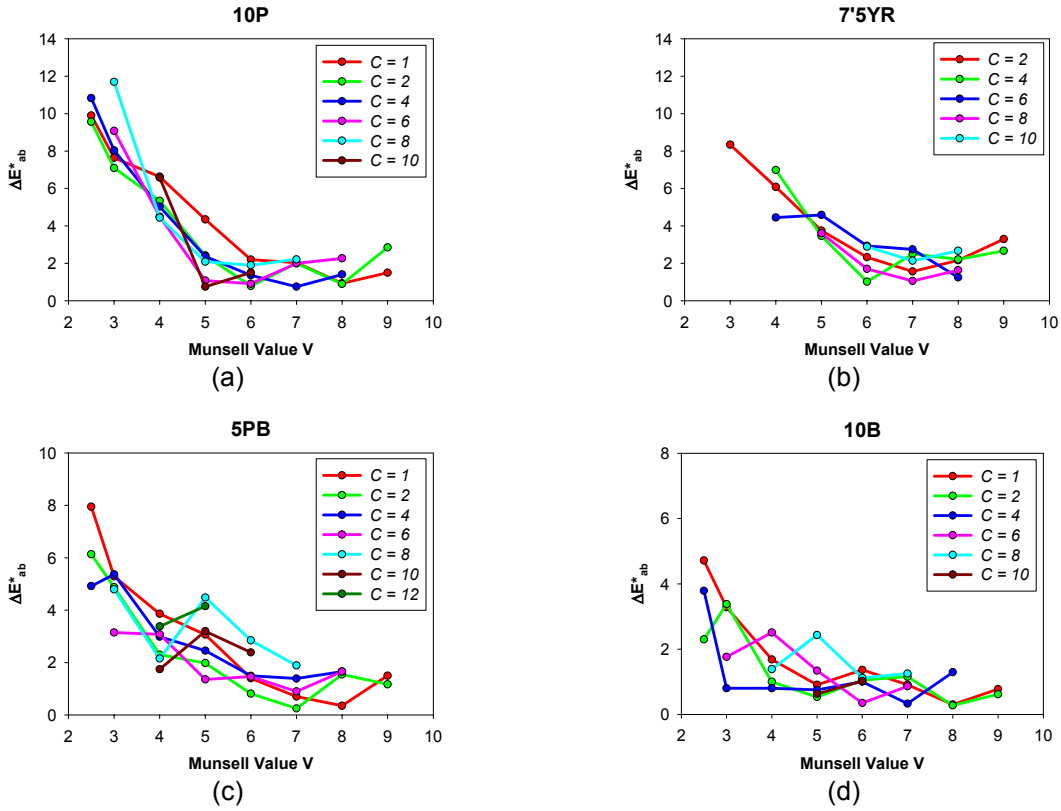

Figure 9.24 *ΔE^*_{ab} values vs Munsell value for all Munsell chroma values for the (a) 10P sub-hue using the colorimetric configuration + incandescent lamp, (b) 7.5YR sub-hue using the colorimetric configuration + D65 simulator, (c) 5PB sub-hue using the multispectral configuration + incandescent lamp, and (d) 10B sub-hue using the multispectral configuration + D65 simulator.*

Considering that the Munsell value coordinate, of the Munsell Color System, would be equivalent to the CIELAB L* coordinate, of the CIE 1976 (L*, a*, b*) colour space, these results agree with those obtained in section 9.1 using the CCDC as training and test set, where increasing CIELAB colour differences seemed to be associated to lower values of L* coordinate, for both system's configurations and the two illuminants used. Here, increasing CIELAB colour differences seem to be associated to lower values of the Munsell value, equivalent to lower L* values. On the other hand, it is also observed that CIELAB colour differences and also RMSE values tend to increase for the highest Munsell values, that is, the

lightest colour patches, which was not observed for the CCDC's colour samples depending on the L* coordinate.

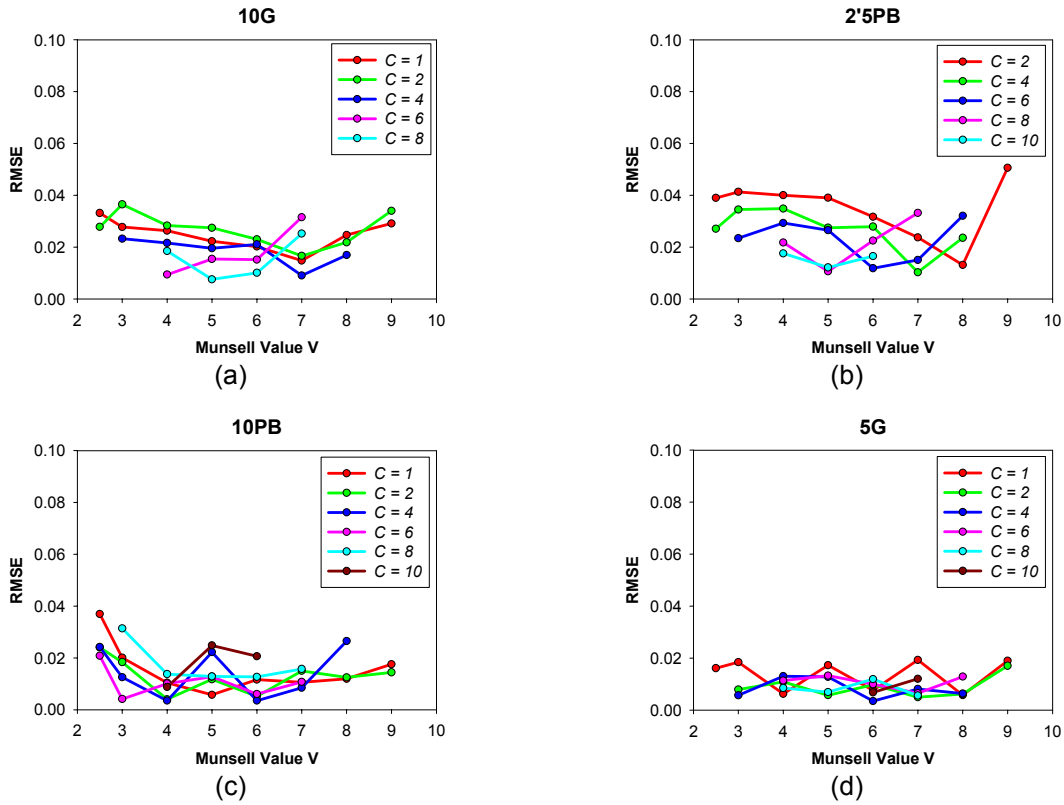

Figure 9.25 *RMSE values vs Munsell value for all Munsell chroma for the (a) 10G sub-hue using the colorimetric configuration and the incandescent lamp illuminant, (b) 2.5PB sub-hue using the colorimetric configuration + D65 simulator, (c) 10PB sub-hue using the multispectral configuration + incandescent lamp, and (d) 5G sub-hue using the multispectral configuration + D65 simulator.*

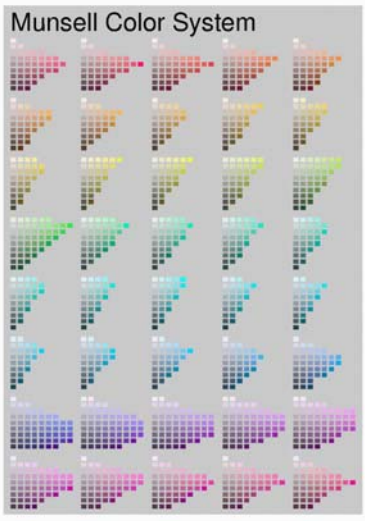

Figure 9.26 *Munsell Color System (Source: http://www.uni-mannheim.de/fakul/psycho/irtel/colsys/Munsell.html)*

The greater and the lower values of the Munsell value coordinate are associated to the lower Munsell chroma values, that is, correspond to the lower colourful patches (Figure 9.26), whose reflectance spectra are quite flat and have no outstanding characteristics in their shape at any wavelength range (Figure 9.27 (a) and (b)).

For the sets of Munsell sub-hues used as training sets homogeneous in hue, most of the colour patches have Munsell chroma values greater than 2, and Munsell values lower than 8 and greater than 3, that is, are colourful colour patches (with some characteristic shape in reflectance spectra) with an intermediate lightness level. This can be seen, as an example, from Figure 9.27 for the 10B Munsell sub-hue. This lack of less colourful and low light and high light colour patches is probably the reason why the accuracy, mainly of colour measurement, is worse for these colour patches.

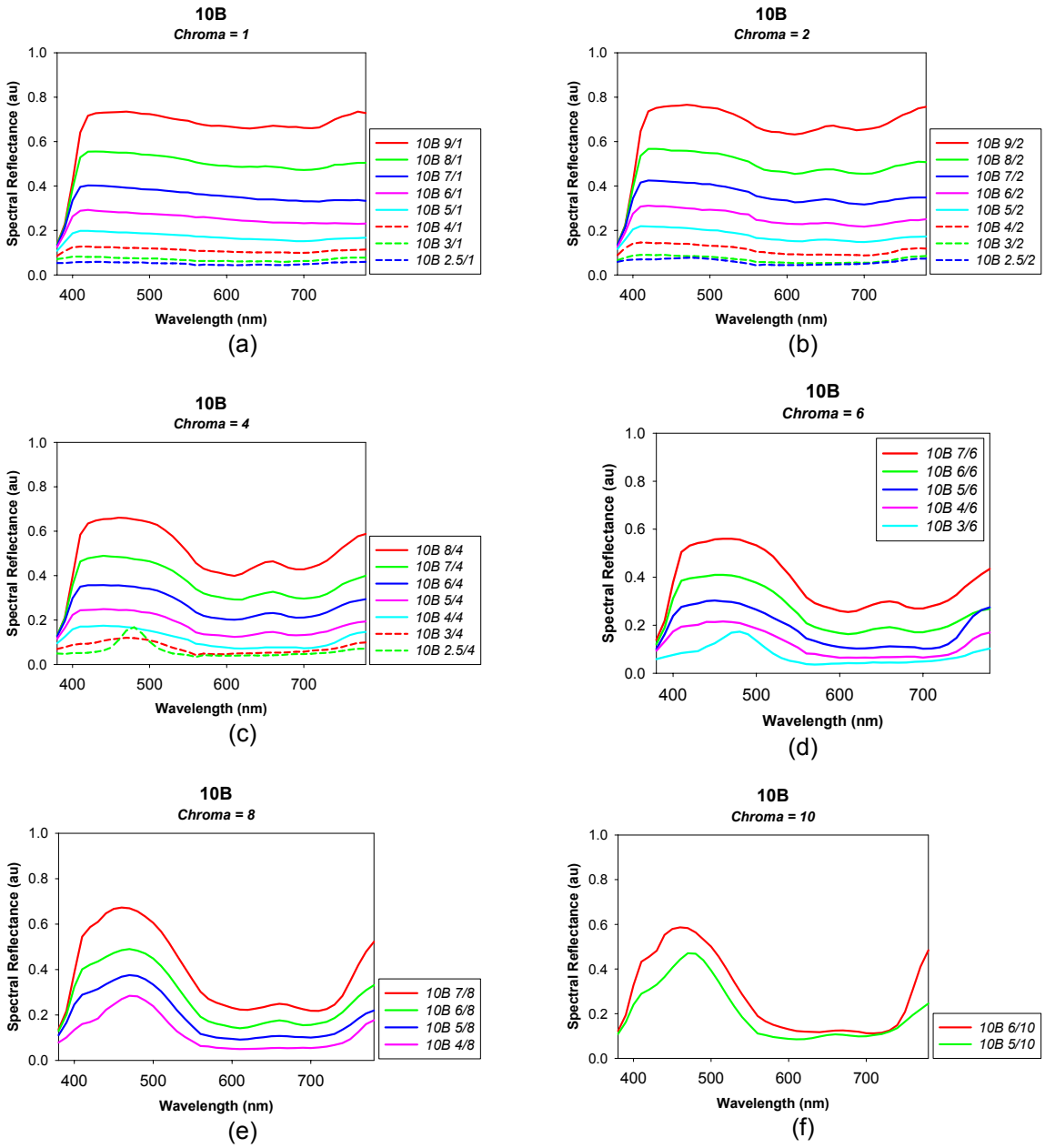

Figure 9.27 *Reflectance spectra for the colour patches of the 10B Munsell sub-hue, grouped by Munsell chroma values: (a) chroma = 1, (b) chroma = 2, (c) chroma = 4, (d) chroma = 6, (e) chroma = 8 and (f) chroma = 10.*

Regarding the accuracy of spectral reconstruction, it is not directly related to the accuracy of colour measurement for each colour sample due to the influence of the CIE standard observer colour-matching functions on the calculation of its CIELAB coordinates. In accuracy of spectral reconstruction, assessed by the RMSE value, the mismatching between the measured and the reconstructed spectra is averaged equally weighted over the whole visible range, whereas in accuracy of colour measurements the CIE standard colour-matching functions introduce an spectral weight in the calculation of the CIELAB coordinates that can exaggerate or reduce the mismatching resulting of the spectral reconstruction depending on the wavelength range (Figure 9.28). This would also explain the fact that the RMSE value is not as sensitive to the Munsell value coordinate as the ΔE^*_{ab} is, for the low light and lower colourful patches (low Munsell value and chroma).

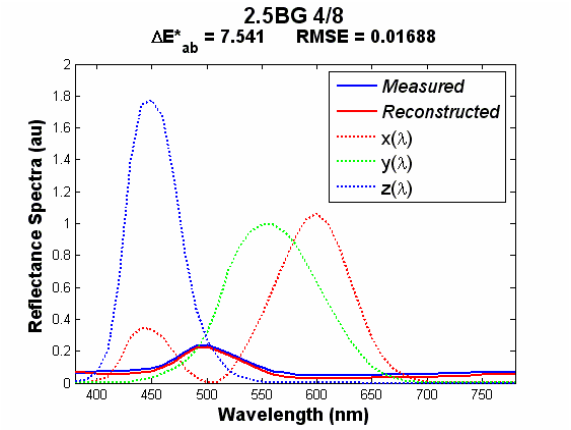

(a)

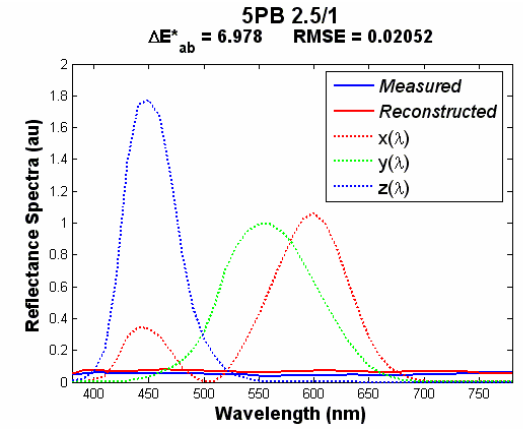

(b)

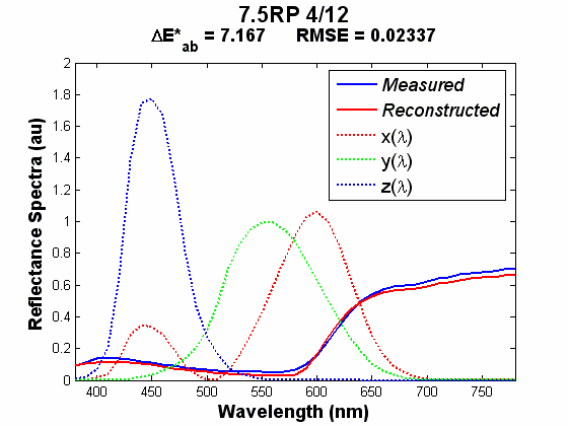

(c)

Figure 9.28 *Plot of the measured and reconstructed reflectance spectra, and the CIE standard observer colour matching-functions (x, y, z) for the (a) 2.5BG 4/8, (b) 5PB 2.5/1, and (c) 7.5RP 4/12 Munsell colour patches.*

10 Influence of Reflectance Spectra on Accuracy of Colour Measurement and Spectral Reconstruction

In this section, the accuracy of colour measurement and spectral reconstruction is analyzed depending on the reflectance spectra of the colour samples measured, in order to determine if any kind of correlation between them exists.

This study is performed using the best proved combination of system's configuration and illuminant, which is multispectral configuration and D65 simulator illuminant, and the GretagMacbeth ColorChecker DC chart (CCDC) and the 1269 colour patches of the Munsell Book of Color – Matte Collection, classified in 10 Munsell hues (R, YR, Y, GY, G, BG, B, PB, P, RP) and each one of these in 4 sub-hues (2.5, 5, 7.5, 10), as training and test sets. The same set of colour samples is used as training and test set in order to analyze the system's performance in the optimum conditions independently of the effect introduced by using different training and test sets.

First of all, in order to determine general tendencies, the reflectance spectra of the colour samples having the five worse and the best CIELAB colour difference and RMSE values are compared for the CCDC's colour samples in Figure 10.1, and for the Munsell's colour patches grouped in hues and sub-hues in Figure 10.2 for the R hue, and in Appendix A5.1 for the rest of Munsell's hues. The Munsell's colour samples plotted for each hue and sub-hue are listed in Appendix A5.2 with their corresponding ΔE^*_{ab} and RMSE values.

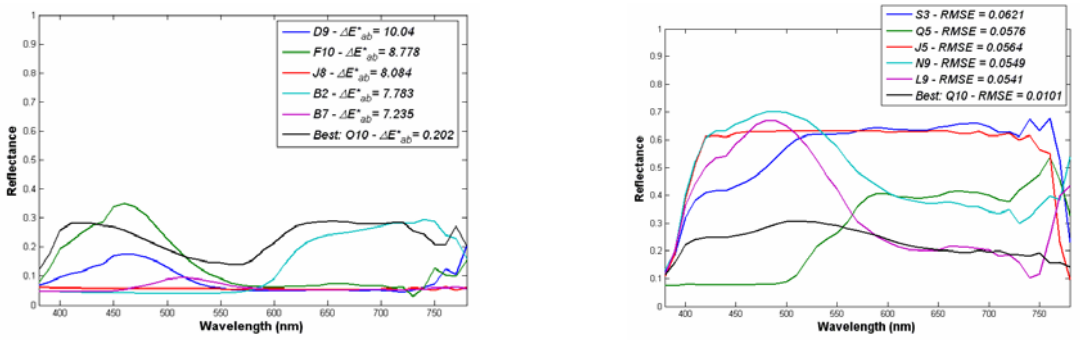

(a) (b)

Figure 10.1 *Reflectance spectra of the CCDC's colour samples having the five worse and the best (a) ΔE^*_{ab} and (b) RMSE values.*

As can be seen from Figures 10.1 and 10.2 (Appendix A5.1), considering the accuracy of colour measurement the main difference between reflectance spectra associated to the colour samples having the five worse ΔE^*_{ab} and the one associated to the colour sample having the best ΔE^*_{ab} seems to be the Area Under the Curve (AUC) of the reflectance spectrum. Although increasing ΔE^*_{ab} values do not seem to be directly related to decreasing values of the AUC of the corresponding reflectance spectra for all colour samples considered,

it always happens that the colour sample having the smallest ΔE^*_{ab} value seems to have the greater AUC.

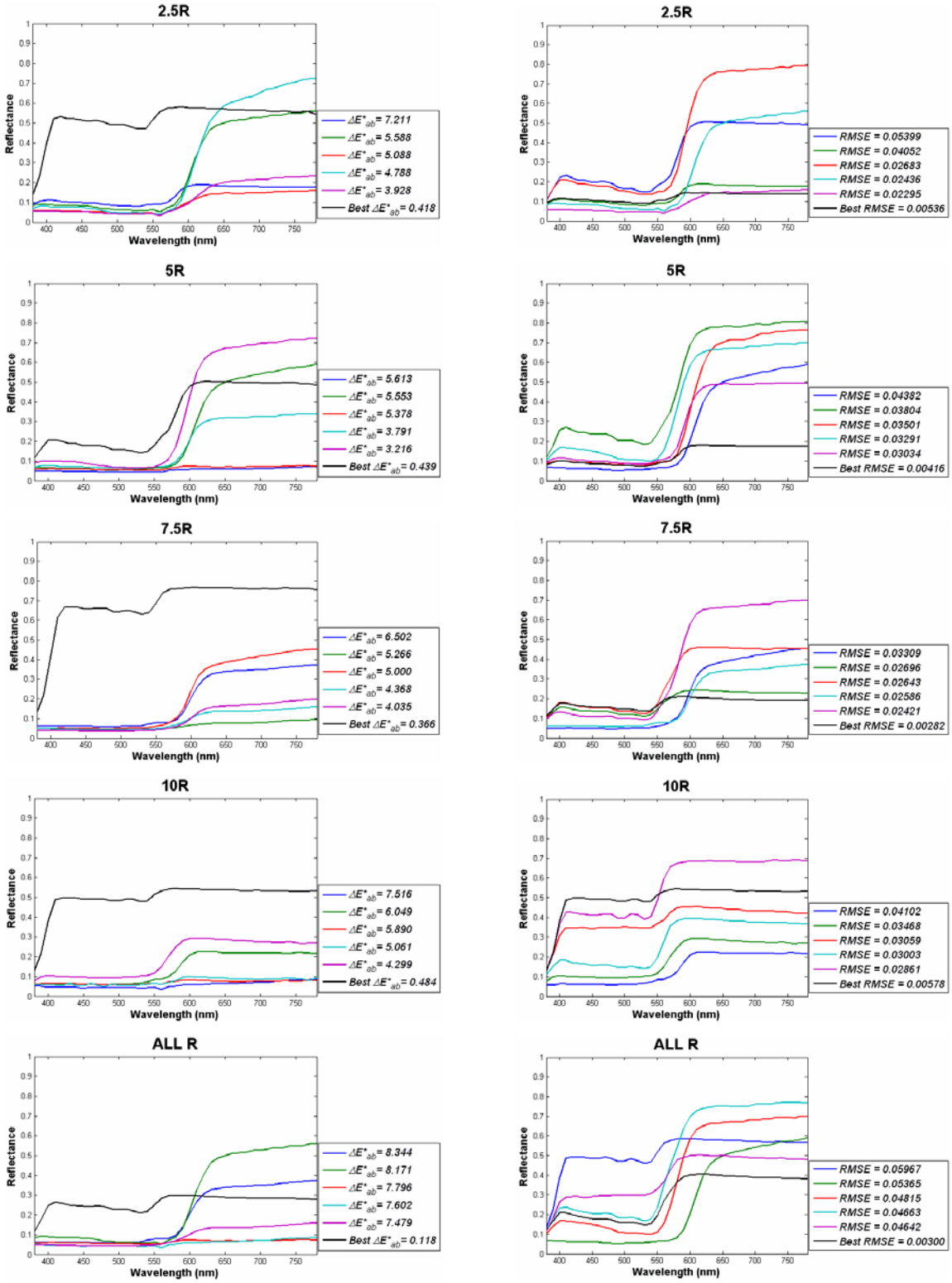

(a) (b)

Figure 10.2 *Reflectance spectra of the Munsell's colour patches of the R hue grouped in the 2.5R, 5R, 7.5R, and 10R sub-hues, and all R hue, with the five worse and the best (a) ΔE^*_{ab} and (b) RMSE values.*

Regarding the accuracy of spectral reconstruction, the smoothness of the reflectance spectrum seems to be the main difference between reflectance spectra associated to the colour samples having the five worse RMSE values and the one associated to the colour sample having the best RMSE value. Just as for the accuracy of colour measurement, although increasing RMSE values do not seem to be directly associated to sharper and/or less smooth reflectance spectra for all colour samples considered, the colour sample having the smallest RMSE value always seems to have the smoothest reflectance spectrum.

Taking these preliminary results into account, the accuracy of colour measurement and spectral reconstruction are analyzed depending on, on one hand, the area under the curve (AUC) of the reflectance spectra and, on the other hand, the smoothness of the reflectance spectra by means of their Discrete Fourier Transform (DFT), which is usually used in spectral analysis to determine the smoothness of curves.

10.1 Accuracy of colour measurement and spectral reconstruction depending on the area under the curve of the reflectance spectra

The accuracy of colour measurement and spectral reconstruction are analyzed depending on the AUC of the reflectance spectra by plotting the ΔE^*_{ab} and the RMSE values versus the AUC of the reflectance spectra for the CCDC's colour samples (Figure 10.3), and for the Munsell's colour patches grouped in hues and sub-hues (Figure 10.4: Munsell's G hue, and Appendix 6: all Munsell's hues).

As can be seen from Figure 10.3 for the CCDC's colour samples, from Figure 10.4 for the Munsell's G hue, and from Appendix 6 for the rest of Munsell's hues, a general tendency for the increasing ΔE^*_{ab} values to be associated to colour samples having a reflectance spectrum with lower AUCs exists, and vice versa, decreasing ΔE^*_{ab} values tend to be associated to colour samples having a reflectance spectrum with higher AUCs. This is only a general tendency and no direct relationship can be established between the ΔE^*_{ab} values and the AUCs of the reflectance spectra of the corresponding colour samples.

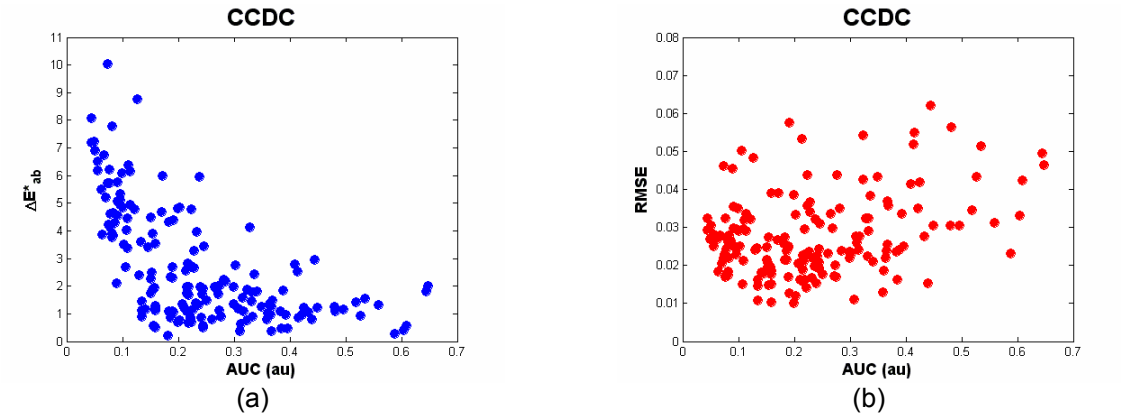

Figure 10.3 *Plots of the (a) ΔE^*_{ab} and (b) RMSE values versus the AUC of the reflectance spectra for the CCDC's colour samples.*

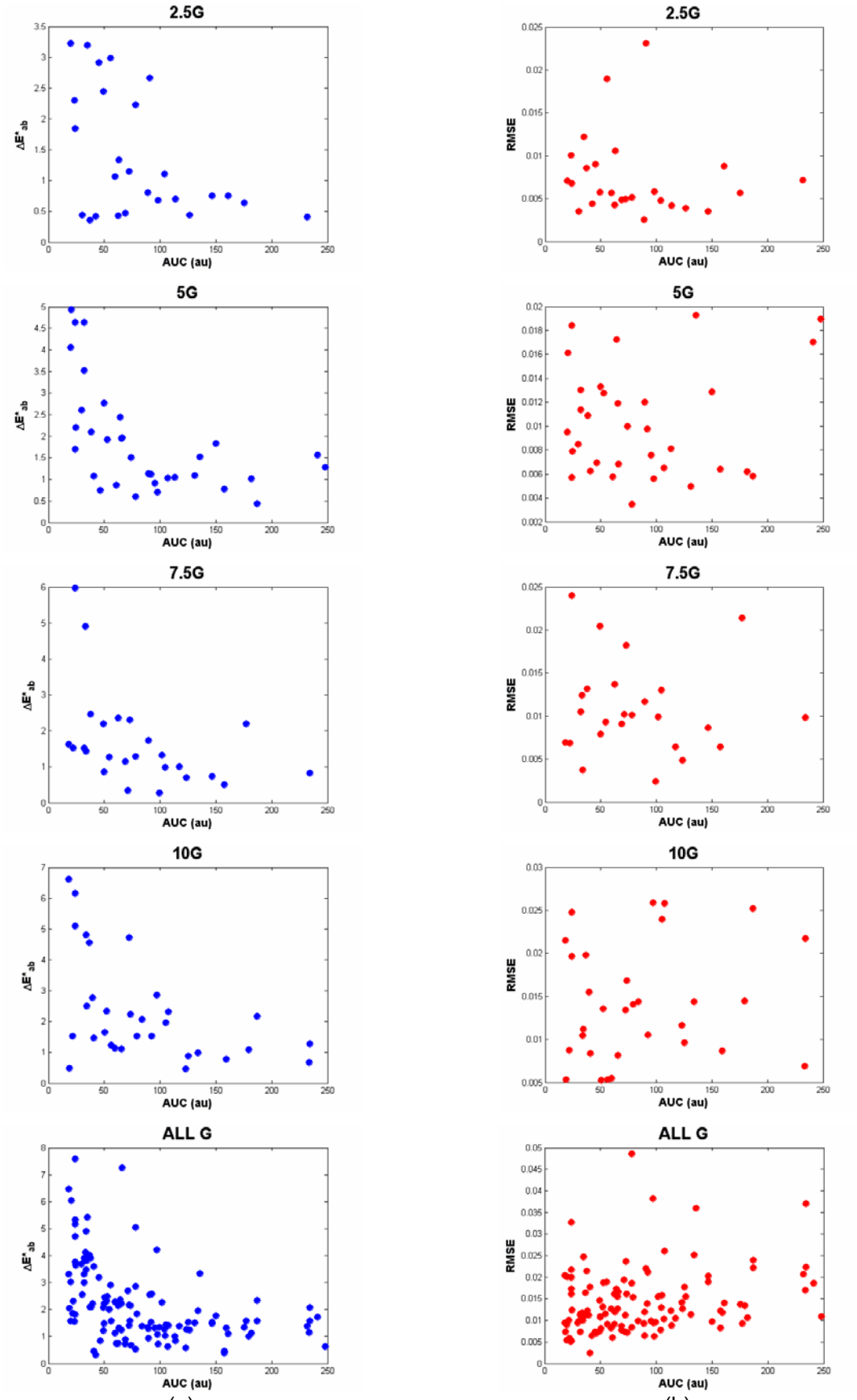

Figure 10.4 *(a) ΔE*$_{ab}$ and (b) RMSE values plotted vs the AUC of the reflectance spectra for the Munsell's colour patches of the G hue grouped in sub-hues, and all G hue.*

On the other hand, any tendency is observed considering the RMSE values plotted versus the AUCs of the reflectance spectra of the corresponding colour samples, and a cloud of points over the range of RMSE and AUC values is obtained for the CCDC's colour samples (Figure 10.3 (b)), for the Munsell's G hue (Figure 10.4 (b)) and for the rest of Munsell's hues (Appendix 6).

These results confirm the preliminary results obtained before through the comparison of the reflectance spectra associated to the colour samples having the five worse and the best ΔE^*_{ab} and RMSE values, for the CCDC chart (Figure 10.1) and for the Munsell's colour patches grouped in hues and sub-hues (Figure 10.2 and Appendix 5): the accuracy of colour measurement tends to improve for colour samples with higher AUCs of their reflectance spectra, whereas this tendency is not observed for the accuracy of spectral reconstruction. On the other hand, any direct relationship cannot be established either between the accuracy of colour measurement and the AUC of the reflectance spectra of colour samples.

Finally, taking into account the formulas used to calculate the CIE XYZ tristimulus values from the reflectance spectra of a colour sample (equations (10.1)) and the formulas to calculate the CIELAB L*a*b* coordinates from the XYZ tristimulus values (equations (10.2)), the higher the AUC of the reflectance spectra is, the higher the CIE XYZ tristimulus values are and, consequently, the higher the CIELAB L* coordinate is, but nothing can be said about the CIELAB a* and b* coordinates.

$$\begin{aligned} X &= \int_0^\infty I(\lambda)\cdot Refl(\lambda)\cdot \bar{x}(\lambda)\cdot d\lambda \\ Y &= \int_0^\infty I(\lambda)\cdot Refl(\lambda)\cdot \bar{y}(\lambda)\cdot d\lambda \\ Z &= \int_0^\infty I(\lambda)\cdot Refl(\lambda)\cdot \bar{z}(\lambda)\cdot d\lambda \end{aligned} \tag{10.1}$$

where $I(\lambda)$ represents the spectral power distribution of the illuminant, $Refl(\lambda)$ represents reflectance spectrum of the colour sample, $\bar{x}(\lambda)$, $\bar{y}(\lambda)$, $\bar{z}(\lambda)$ represent the CIE standard observer colour-matching functions.

$$\begin{aligned} L^* &= 116\cdot f(Y/Y_W) - 16 \\ a^* &= 500\cdot\left[f(X/X_W) - f(Y/Y_W)\right] \\ b^* &= 200\cdot\left[f(Y/Y_W) - f(Z/Z_W)\right] \end{aligned} \tag{10.2}$$

where X_W, Y_W, Z_W are the CIE XYZ tristimulus values of the reference white and $f(t)$ is:

$$\begin{aligned} f(t) &= t^{1/3} && \text{if} \quad t > 0.008856 \\ f(t) &= 7.787\cdot t + 16/116 && \text{otherwise} \end{aligned}$$

Therefore, results obtained in chapter 9 are confirmed here in connection with the fact that increasing CIELAB colour differences seem to be associated to lower values of L* coordinate, though this tendency is not observed for the RMSE values, and that there is no correlation between both the CIELAB colour difference values and the RMSE values, and the CIELAB coordinates a* and/or b*. Even though any direct relationship cannot be established, accuracy of colour measurement tends to improve for the colour samples with higher AUCs of their reflectance spectra. This tendency is not observed in terms of the accuracy of spectral reconstruction.

10.2 Accuracy of colour measurement and spectral reconstruction depending on the Discrete Fourier Transform of the reflectance spectra

Fourier analysis is a family of mathematical techniques, all based on decomposing signals into sinusoids, and the Discrete Fourier Transform (DFT) is one of the specific forms of Fourier analysis. The DFT requires an input function that is discrete and whose non-zero values have a limited (finite) duration and it only evaluates enough frequency components to reconstruct the finite segment that is analyzed. Its inverse transform cannot reproduce the entire time domain, unless the input happens to be periodic (forever). Therefore it is often said that the DFT is a transform for Fourier analysis of finite-domain discrete-time functions. Since the input function is a finite sequence of real or complex numbers, the DFT is ideal for processing information stored in computers. In particular, the DFT is widely employed in signal processing and related fields to analyze the frequencies contained in a sampled signal, to solve partial differential equations, and to perform other operations such as convolutions.

The DFT transforms the sequence of N complex numbers $x_0, ..., x_{N-1}$ into the sequence of N complex numbers $X_0, ..., X_{N-1}$ according to the formula:

$$X_k = \sum_{n=0}^{N-1} x_n \exp\left\{-\frac{2\pi}{N} ikn\right\} \qquad k = 0, ..., N-1 \qquad (10.3)$$

The inverse discrete Fourier transform (IDFT) is given by equation:

$$x_n = \frac{1}{N} \sum_{k=0}^{N-1} X_k \exp\left\{\frac{2\pi}{N} ikn\right\} \qquad n = 0, ..., N-1 \qquad (10.4)$$

The complex numbers X_k represent the amplitude and phase of the different sinusoidal components of the input 'signal' x_n. The DFT computes the X_k from the x_n, while the IDFT shows how to compute the x_n as a sum of sinusoidal components $X_k \exp\{2\pi ikn/N\}/N$ with a frequency $2\pi k/N$. By writing X_k in polar form, the sinusoid amplitude is immediately obtained from $|X_k|$ and the phase from the complex argument.

The input signal is usually said to be in the time domain. This is because the most common type of signal entering the DFT is composed of samples taken at regular intervals of time. But any kind of sampled data can be used, regardless of how it was acquired. The term 'time domain' in Fourier analysis may actually refer to samples taken over time, or it might be a general reference to any discrete signal that is being decomposed. The term 'frequency domain' is used to describe the amplitude and phase of the different components.

In this case, the reflectance spectra of the colour samples are considered the input signals: data sampled between the [380,780]nm wavelength range in equal intervals of 10nm. Consequently, the Nyquist frequency, which is defined as the half of the sampling frequency, is $0.05nm^{-1}$, and the fundamental frequency, which is the smallest repeating unit of a signal, is $(1/400)nm^{-1}$.

The DFTs of the reflectance spectra are calculated for all CCDC's colour samples and all Munsell's colour patches, grouped in hues and sub-hues. The amplitude of the DFT's components of the reflectance spectra of the colour samples having the five worse and the best ΔE^*_{ab} and RMSE values can be seen from Figure 10.5 for the CCDC's colour samples, from Figure 10.6 for the sub-hues and the complete Munsell's GY hue, and from Appendix A7.1 for the rest of Munsell's colour patches. The Munsell's colour samples plotted for each

hue and sub-hue are listed in Appendix A5.2 with their corresponding ΔE^*_{ab} and RMSE values.

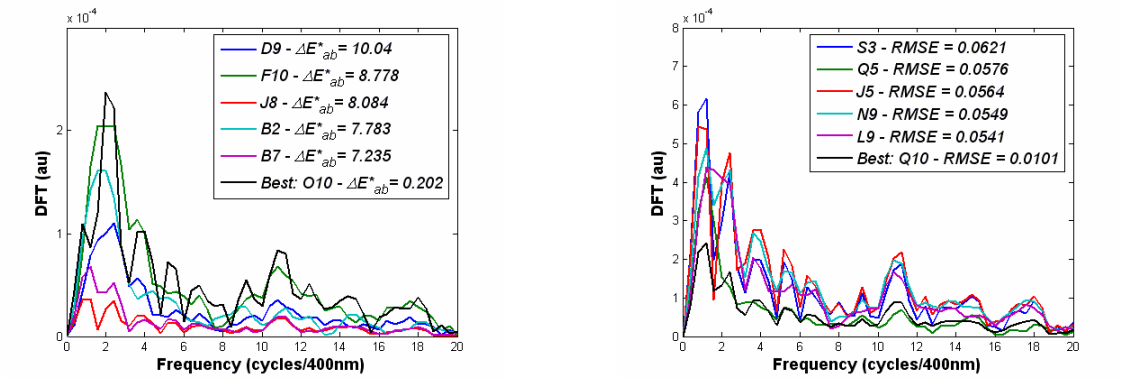

Figure 10.5 *Amplitude of the DFT's components of the reflectance spectra of the CCDC's colour samples with the five worse and the best (a) ΔE^*_{ab} and (b) RMSE values.*

The DFT is used to analyze the smoothness of the reflectance spectra due to the fact that the smoother a signal is, the less number of contributing harmonics are necessary to compute it, i.e., the more rapid is the decreasing of the amplitude of the DFT's components when increasing their order.

No correlation is observed between the ΔE^*_{ab} values and the plots of the corresponding amplitudes of the DFT's components of the reflectance spectra (Figure 10.5 (a) and Figure 10.6 (a)) but, on the contrary, the best RMSE values seem to be associated to a rapidly decreasing amplitude of the DFT's components, according to the preliminary results obtained.

In order to confirm these results in a more clear way, the contribution of the different harmonics to the DFT and the accumulated contribution of harmonics are calculated for the CCDC's and Munsell's colour samples having the five worse and the best ΔE^*_{ab} and RMSE values.

Considering that vectors $\exp\{2\pi ikn/N\}$ form an orthogonal basis over the set of N-dimensional complex vectors:

$$\sum_{n=0}^{N}\left(\exp\left\{\frac{2\pi}{N}ikn\right\}\right)\cdot\left(\exp\left\{-\frac{2\pi}{N}ik'n\right\}\right)=N\delta_{kk'} \qquad (10.5)$$

where the $\delta_{kk'}$ is the Kronecker delta, the contribution of the kth harmonic to the complete signal (C_k) can be calculated as the percentage given by the ratio of the power of the kth harmonic to the sum of the powers of all harmonics:

$$C_k = 100\cdot\frac{|X_k|^2}{\sum_{k'=0}^{N-1}|X_{k'}|^2} \qquad (10.6)$$

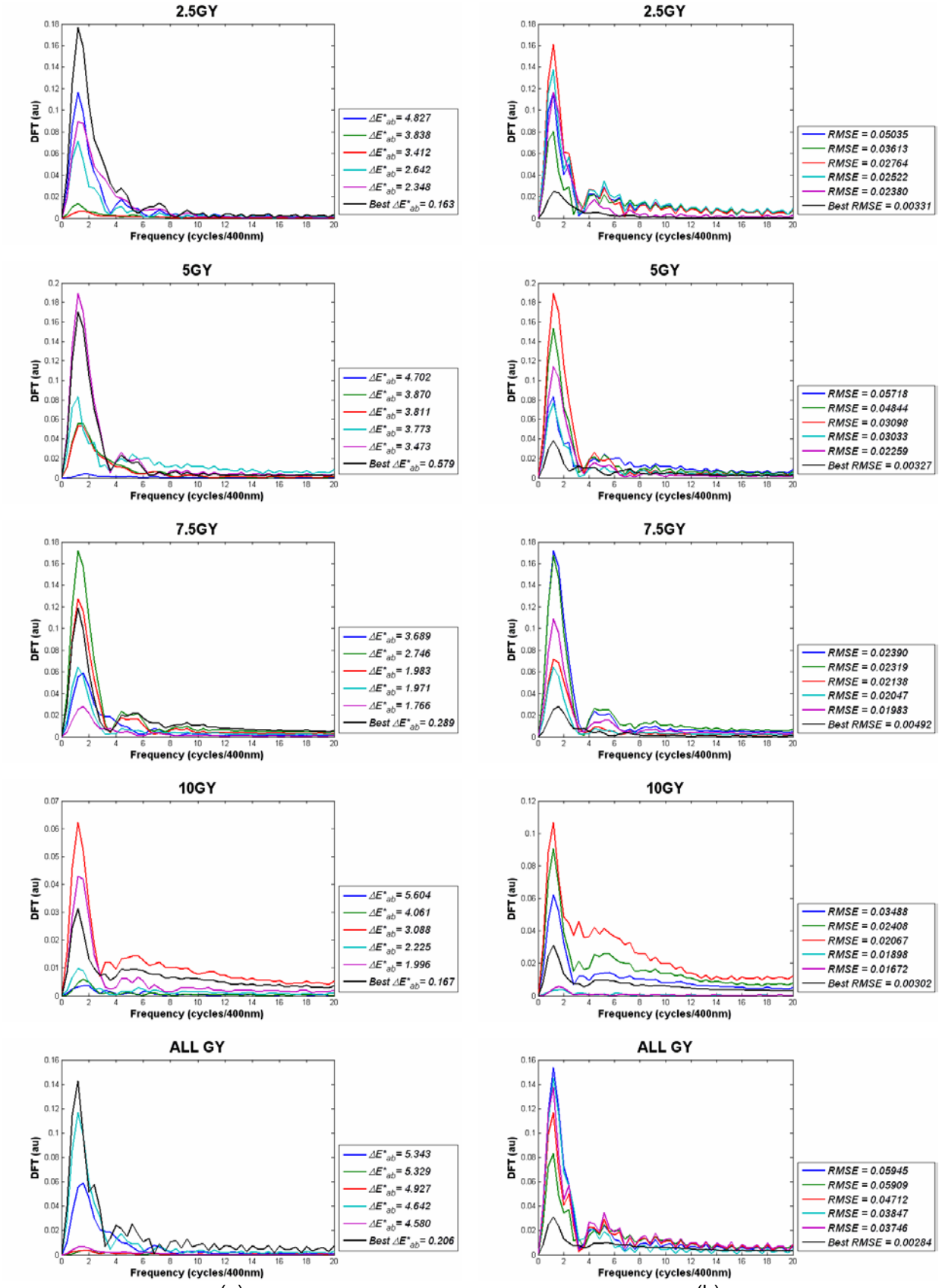

Figure 10.6 *Amplitude of the DFT's components of the reflectance spectra of the Munsell's colour patches of the GY hue grouped in the 2.5GY, 5GY, 7.5GY, and 10GY sub-hues, and all GY hue, having the five worse and the best (a) ΔE^*_{ab} and (b) RMSE values.*

Then, the Accumulated Contribution of the first M harmonics (AC_M) is given by:

$$AC_M = \sum_{k=0}^{M-1} C_k = 100 \cdot \frac{\sum_{k=0}^{M-1} |X_k|^2}{\sum_{k'=0}^{N-1} |X_{k'}|^2} \tag{10.7}$$

The accumulated contribution of the harmonics is plotted versus their frequency for the CCDC's (Figure 10.7) and Munsell's colour samples (Figure 10.8 for the Munsell's GY hue, Appendix A7.2 for all Munsell's hues) having the five worse and the best ΔE^*_{ab} and RMSE values in order to determine if any correlation can be established between the ΔE^*_{ab} and/or the RMSE values and the rapidity of the increase of the accumulated contribution of harmonics.

As can be seen from Figure 10.7 for the CCDC's colour samples, from Figure 10.8 for the Munsell's GY hue, and from Appendix A7.2 for the rest of Munsell's hues, any direct correlation cannot be established between neither the ΔE^*_{ab} nor the RMSE values and the increase of the accumulated contribution of harmonics. As it was expected, very different increases of the accumulated contribution of harmonics are obtained when considering the five worse and the best ΔE^*_{ab} values (Figure 10.7 (a), Figure 10.8 (a) and Appendix A7.2 (a)), according to the fact that the best ΔE^*_{ab} is not so related to the shape of the reflectance spectra as it is to the area under the curve. On the other hand, the expected relationship between the best RMSE values and the smoothness of the reflectance spectra, represented by a higher rapidity of the increase of the accumulated contribution of harmonics, is observed for the most, but not all, colour samples considered (Figure 10.7 (b) Figure 10.8 (b) and Appendix A7.2 (b)).

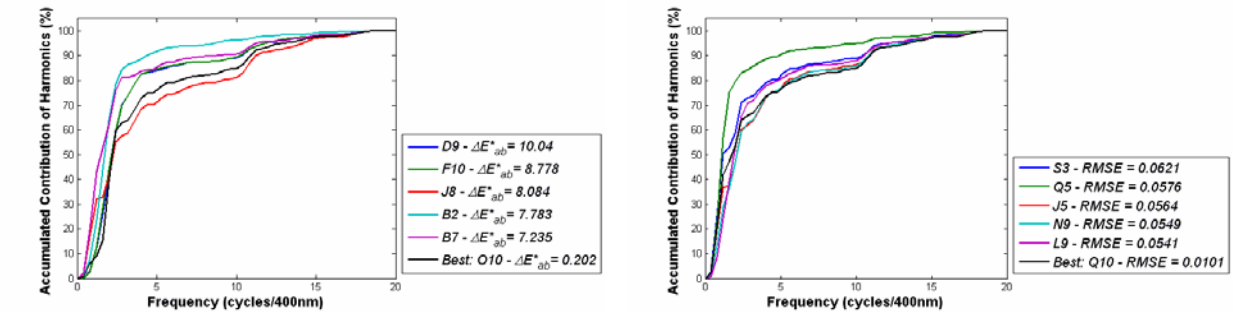

Figure 10.7 *Accumulated contribution of the DFT's harmonics for the CCDC's colour samples having the five worse and the best (a) ΔE^*_{ab} and (b) RMSE values.*

These results allow to conclude that, in spite of the fact that any general correlation cannot be established between accuracy of spectral reconstruction and the smoothness of a reflectance spectrum, best accuracy of spectral reconstruction is frequently associated to a smooth reflectance spectrum. On the other hand, accuracy of colour measurement seems to be independent of the shape and/or the smoothness of the reflectance spectra.

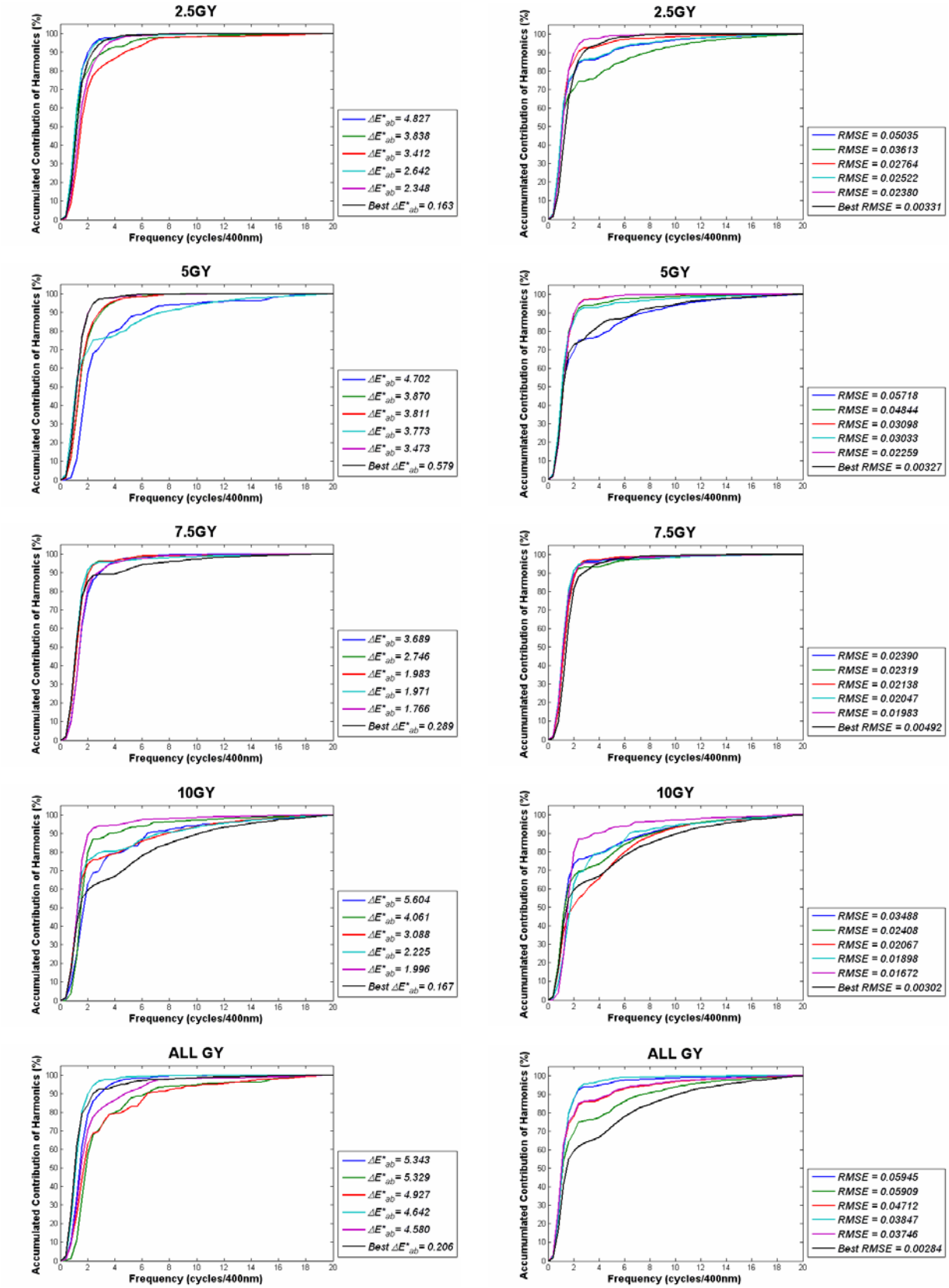

Figure 10.8 *Accumulated contribution of the DFT's harmonics for the Munsell's colour patches of the GY hue grouped in the 2.5GY, 5GY, 7.5GY, and 10GY sub-hues, and all GY hue, having the five worse and the best (a) ΔE^*_{ab} and (b) RMSE values.*

11 Simulation Study of an Optimum and Commercially Available Multispectral Imaging System for Colour Measurement and Spectral Reconstruction

Once the multispectral imaging system developed has been thoroughly analyzed and its limitations in terms of accuracy of colour measurement and spectral reconstruction have been established, the next stage would be to determine if any other number and/or combination of commercially available interference filters would allow to improve, at least theoretically, the accuracy of the multispectral imaging system in terms of colour measurement and spectral reconstruction. For this purpose, a simulation study of an optimum multispectral imaging system for colour measurement and spectral reconstruction is presented in this chapter.

The multispectral imaging system developed and used throughout this work comprises, as it was previously presented in section 3.4, a 12-bits cooled monochrome CCD camera model QImaging QICAM Fast1394 (Q12), an objective lens model Nikon AF Nikkor 28 – 105 mm, and a motorized filter wheel placed between them with seven CVI Laser interference filters covering the whole visible range of the spectrum. The supplier specifications for these interference filters, which are usually considered to be approximately gaussian, are: peak positions or central wavelengths (CWLs) at 400nm, 450nm, 500nm, 550nm, 600nm, 650nm, and 700nm, full widths at half maximum (FWHMs) of 40nm for all of them, and peak transmittances of 35%, 45%, and 50% depending on the CWL (Appendix 8).

The selection of the interference filters used was based on results about the theoretical optimum filters obtained previously by our research group on multispectral systems for reflectance reconstruction in the near-infrared region [Vilaseca, 2005; Vilaseca et al., 2006 – 2]. The extrapolation of these results to the visible region of the spectrum led to select a set of gaussian interference filters having equidistant peak positions covering the whole visible range, equal FWHMs that allow a slight overlapping between them, and the higher transmittance possible. Among the commercially available interference filters, the seven CVI Laser interference filters selected fulfilled all these requirements.

Next, a simulation study of an optimum multispectral imaging system for colour measurement and spectral reconstruction is presented. This study is performed considering the spectral response of the Q12 CCD camera (Figure 11.1) and a database of commercially available interference filters (Appendix 8), selected among the databases of Edmund Optics, OptoSigma and CVI Laser (only filters having a FWHM $\geq$ 10nm and a peak transmittance $\geq$ 35% were selected), which are considered to be approximately gaussian.

Considering the linear model of a CCD camera, the digital response to a light stimulus at each pixel of the kth acquisition channel of a multispectral imaging system can be expressed as:

$$P_k = \sum_{\lambda=380}^{780} E(\lambda) \cdot R(\lambda) \cdot X_k(\lambda) \cdot \Delta\lambda \tag{11.1}$$

where $E(\lambda)$ is the spectral power distribution of the light source, $R(\lambda)$ is the spectral reflectance of the imaged colour sample, and $X_k(\lambda)$ is the spectral response of the *k*th acquisition channel that comprises the CCD sensor spectral response ($S(\lambda)$) and the spectral transmittance of the interference filter ($T_k(\lambda)$) (equation (11.2)).

$$X_k(\lambda) = S(\lambda) \cdot T_k(\lambda) \tag{11.2}$$

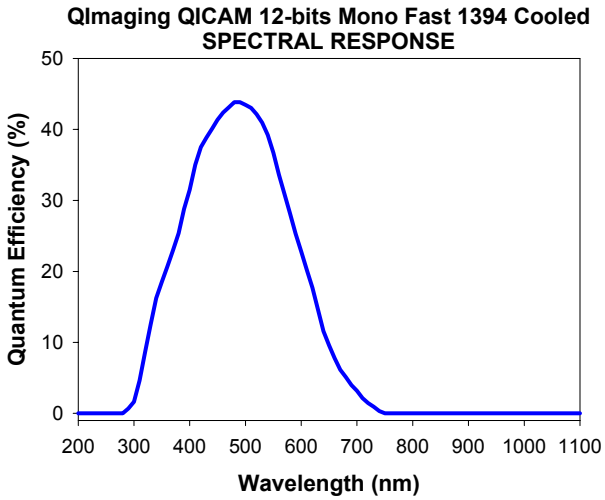

Figure 11.1 *Spectral response of the 12 bits cooled monochrome CCD camera model QImaging QICAM Fast1394.*

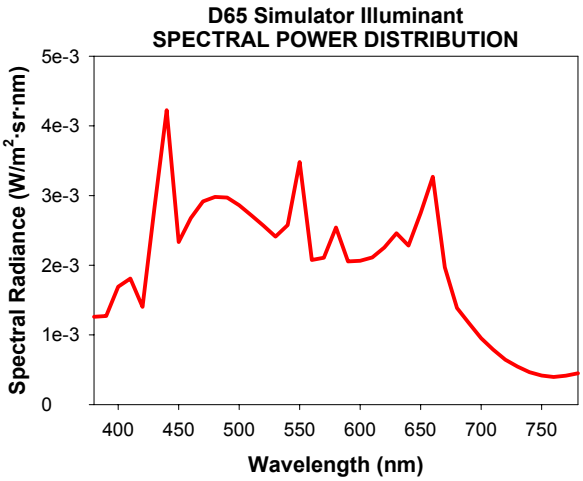

Figure 11.2. *Spectral power distribution of the D65 simulator illuminant.*

The simulation study carried out consists of an exhaustive search of the optimum set of interference filters considering all possible combinations of the filters on the database used (Appendix 8), for a fixed number of filters or acquisition channels. The costs functions used to find the optimum set of filters are the CIELAB colour difference for the accuracy of colour measurement, and the RMSE for the accuracy of spectral reconstruction. Imaging systems having 3, 4, 5, 6, 7, 8, and 9 acquisition channels are simulated.

For each number of acquisition channels considered, the digital response of the imaging system is simulated using the spectral power distribution $E(\lambda)$ of the D65 simulation illuminant (Figure 11.2) as the light source, the spectral response of the Q12 CCD camera as the CCD sensor spectral response $S(\lambda)$ (Figure 11.1), and the reflectance spectra of the CCDC's colour samples as the imaged colour samples $R(\lambda)$. The interference filter's transmittances $T_k(\lambda)$ are simulated to be Gaussian with the central wavelength (CWL), FWHM, and peak transmittance (PT) provided by suppliers (Appendix 8).

For each set of filters tested, the digital response of each acquisition channel of the imaging system is calculated using the equation (11.1). Considering the main noise sources that could remain and affect the system's response once corrected, some noise is then added in order the simulated digital response to be as similar to the real one as possible. First, a gaussian noise of zero mean and the same variance as the real Q12 CCD camera had after noise correction is added. The mean variance of the CCD camera after noise correction is

4.86E-05, which corresponds to a SNR of 43dB. Secondly, the quantization noise corresponding to a 12 bits analog-to-digital converter is applied. After that, the simulated system's responses are related to the reflectance spectra of the CCDC's colour samples, which will be used as the training and test set of the simulated system, by means of applying the PCA to the set of reflectance spectra and obtaining the transformation matrix that relates directly the system's digital responses to the coefficients of the reflectance spectrum on the PCA basis for each colour sample. Once the transformation matrix is obtained, the reconstructed reflectance spectra are calculated straightforward and next the accuracy of colour measurement and spectral reconstruction that could be theoretically achieved by each set of filters.

The optimum combination of filters is obtained for sets of 3, 4, 5, 6, 7, 8, and 9 interference filters, both in terms of accuracy of colour measurement and in terms of accuracy of spectral reconstruction. Next, the simulated spectral transmittances (gaussian shape), the specifications of the filters (CWL, FWHM, and PT) and the accuracy of the system's performance are presented for the four best combinations of filters in Figures 11.3 (1) – (7) and 11.4 (1) – (7), and Tables 11.1 and 11.2, in terms of accuracy of both colour measurement and spectral reconstruction, respectively, for the sets of 3, 4, 5, 6, 7, 8, and 9 interference filters analyzed.

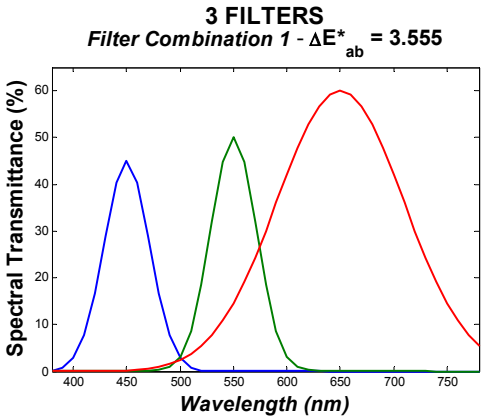

	CWL (nm)	FWHM (nm)	PT (%)
Filter 1	450	25	45
Filter 2	550	25	50
Filter 3	650	70	60

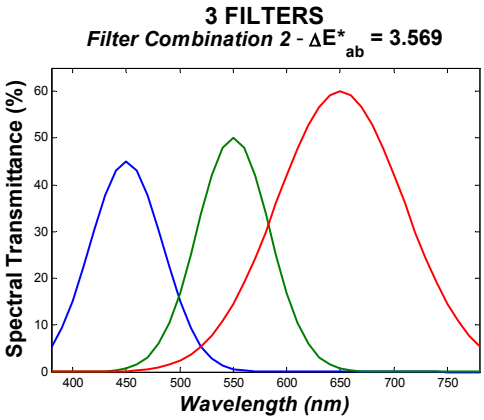

	CWL (nm)	FWHM (nm)	PT (%)
Filter 1	450	40	45
Filter 2	550	40	50
Filter 3	650	70	60

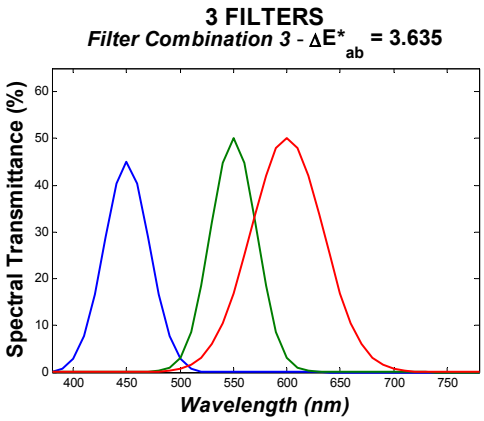

	CWL (nm)	FWHM (nm)	PT (%)
Filter 1	450	25	45
Filter 2	550	25	50
Filter 3	600	40	50

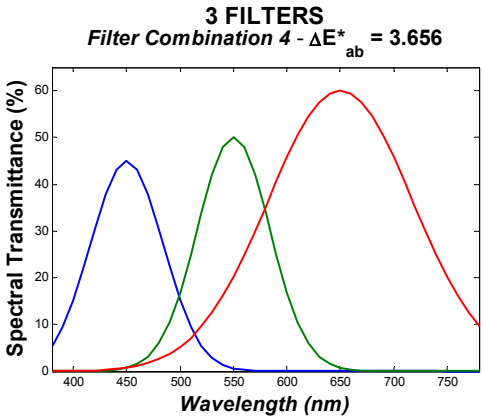

	CWL (nm)	FWHM (nm)	PT (%)
Filter 1	450	40	45
Filter 2	550	40	50
Filter 3	650	80	60

Figure 11.3 (1) *Simulated spectral transmittances (gaussian shape) and mean ΔE^*_{ab} value obtained for the four best sets of 3 interference filters in terms of accuracy of colour measurement. The specifications of the filters (CWL, FWHM, PT) are detailed in the table beside each figure.*

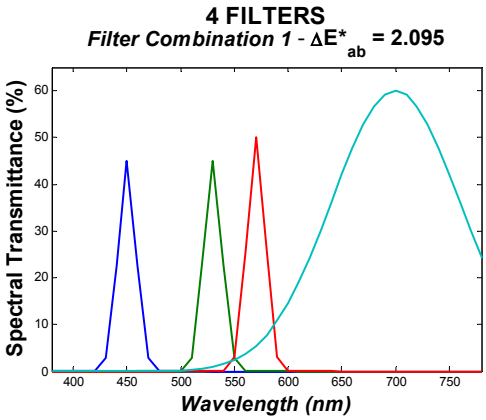

	CWL (nm)	FWHM (nm)	PT (%)
Filter 1	450	10	45
Filter 2	530	10	45
Filter 3	570	10	50
Filter 4	700	70	60

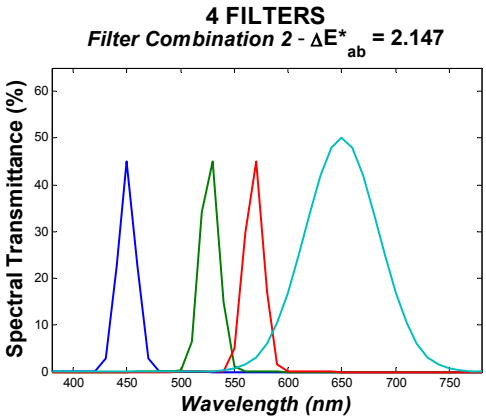

	CWL (nm)	FWHM (nm)	PT (%)
Filter 1	450	10	45
Filter 2	527	10	45
Filter 3	568	10	45
Filter 4	650	40	50

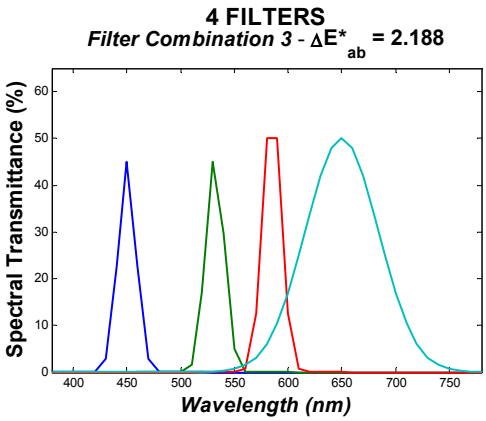

	CWL (nm)	FWHM (nm)	PT (%)
Filter 1	450	10	45
Filter 2	532	10	45
Filter 3	585	10	50
Filter 4	650	40	50

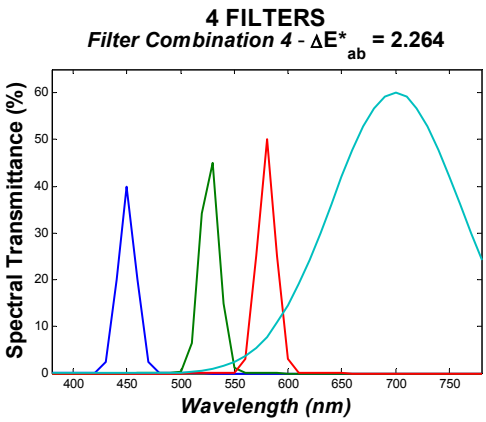

	CWL (nm)	FWHM (nm)	PT (%)
Filter 1	450	10	40
Filter 2	527	10	45
Filter 3	580	10	50
Filter 4	700	70	60

Figure 11.3 (2) *Simulated spectral transmittances (gaussian shape) and mean ΔE^*_{ab} value obtained for the four best sets of 4 interference filters in terms of accuracy of colour measurement. The specifications of the filters (CWL, FWHM, PT) are detailed in the table beside each figure.*

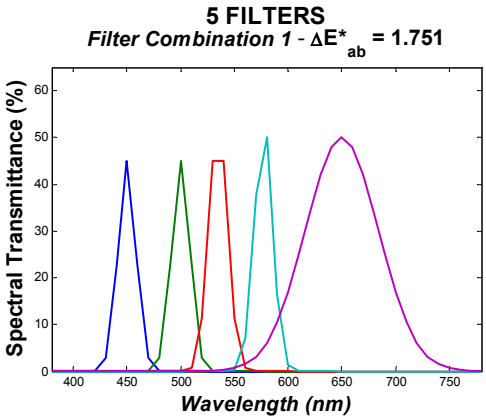

	CWL (nm)	FWHM (nm)	PT (%)
Filter 1	450	10	45
Filter 2	500	10	45
Filter 3	535	10	45
Filter 4	577	10	50
Filter 5	650	40	50

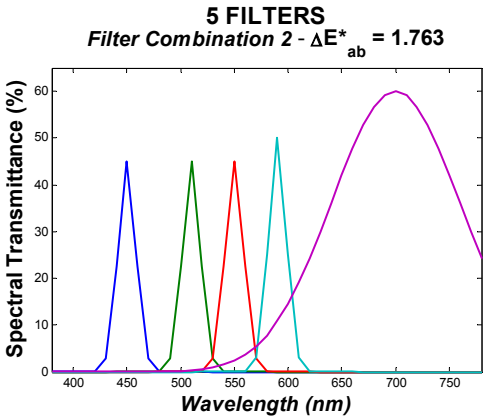

	CWL (nm)	FWHM (nm)	PT (%)
Filter 1	450	10	45
Filter 2	510	10	45
Filter 3	550	10	45
Filter 4	590	10	50
Filter 5	700	70	60

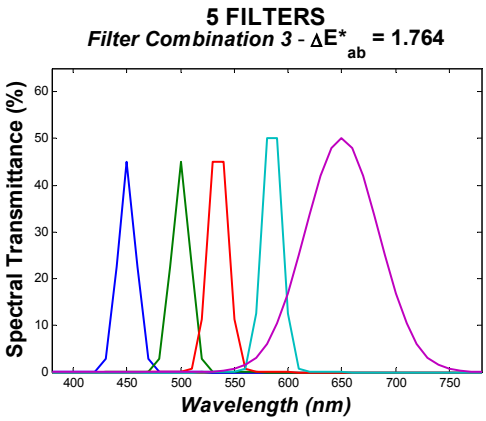

	CWL (nm)	FWHM (nm)	PT (%)
Filter 1	450	10	45
Filter 2	500	10	45
Filter 3	535	10	45
Filter 4	585	10	50
Filter 5	650	40	50

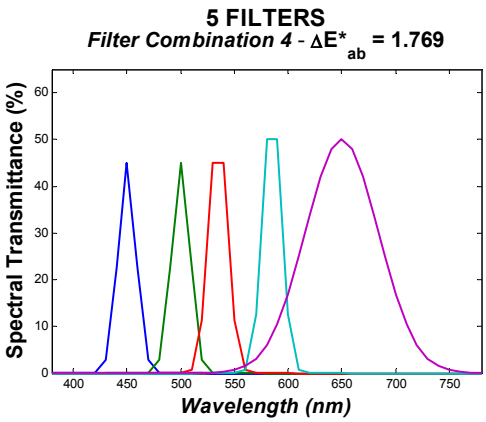

	CWL (nm)	FWHM (nm)	PT (%)
Filter 1	450	10	45
Filter 2	500	10	45
Filter 3	535	10	45
Filter 4	585	10	50
Filter 5	650	40	50

Figure 11.3 (3) *Simulated spectral transmittances (gaussian shape) and mean ΔE^*_{ab} value obtained for the four best sets of 5 interference filters in terms of accuracy of colour measurement. The specifications of the filters (CWL, FWHM, PT) are detailed in the table beside each figure.*

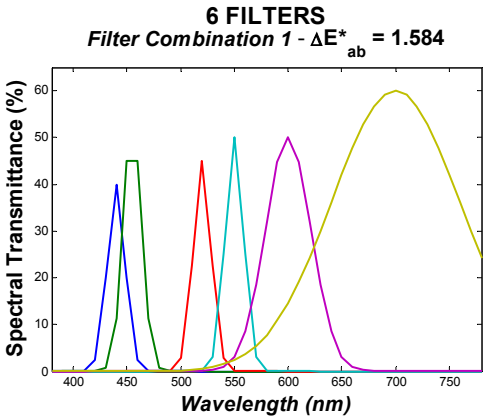

	CWL (nm)	FWHM (nm)	PT (%)
Filter 1	440	10	40
Filter 2	455	10	45
Filter 3	520	10	45
Filter 4	550	10	50
Filter 5	600	25	50
Filter 6	700	70	60

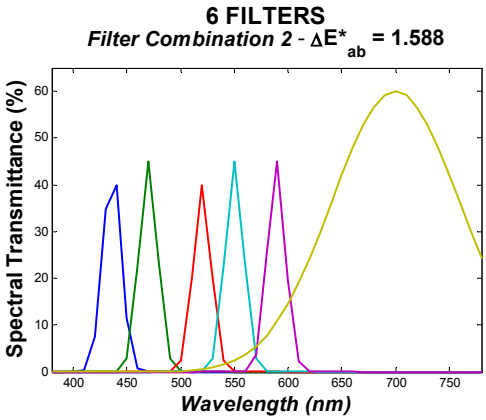

	CWL (nm)	FWHM (nm)	PT (%)
Filter 1	436	10	40
Filter 2	470	10	45
Filter 3	520	10	40
Filter 4	550	10	45
Filter 5	589	10	45
Filter 6	700	70	60

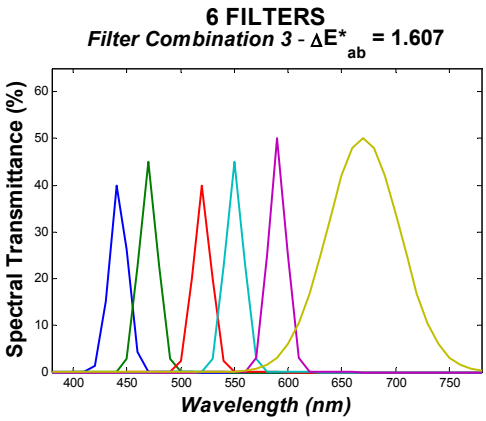

	CWL (nm)	FWHM (nm)	PT (%)
Filter 1	442	10	40
Filter 2	470	10	45
Filter 3	520	10	40
Filter 4	550	10	45
Filter 5	590	10	50
Filter 6	670	40	50

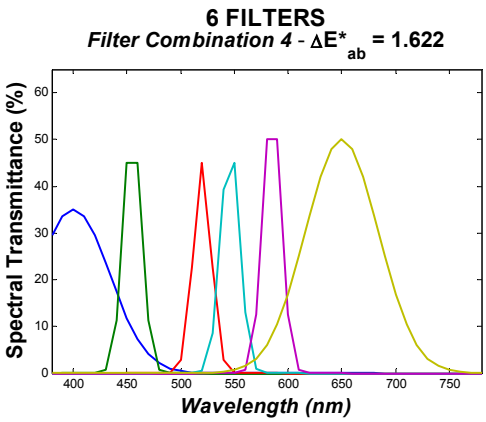

	CWL (nm)	FWHM (nm)	PT (%)
Filter 1	400	40	35
Filter 2	455	10	45
Filter 3	520	10	45
Filter 4	546	10	45
Filter 5	585	10	50
Filter 6	650	40	50

Figure 11.3 (4) *Simulated spectral transmittances (gaussian shape) and mean ΔE^*_{ab} value obtained for the four best sets of 6 interference filters in terms of accuracy of colour measurement. The specifications of the filters (CWL, FWHM, PT) are detailed in the table beside each figure.*

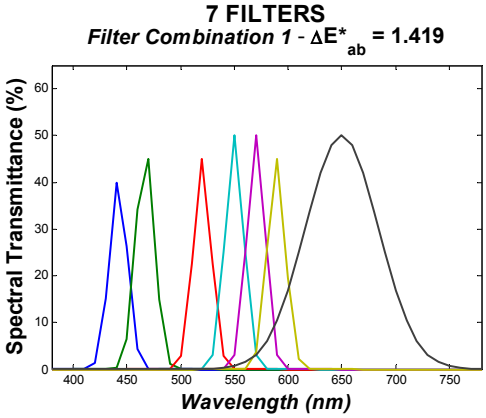

	CWL (nm)	FWHM (nm)	PT (%)
Filter 1	442	10	40
Filter 2	467	10	45
Filter 3	520	10	45
Filter 4	550	10	50
Filter 5	570	10	50
Filter 6	589	10	45
Filter 7	650	40	50

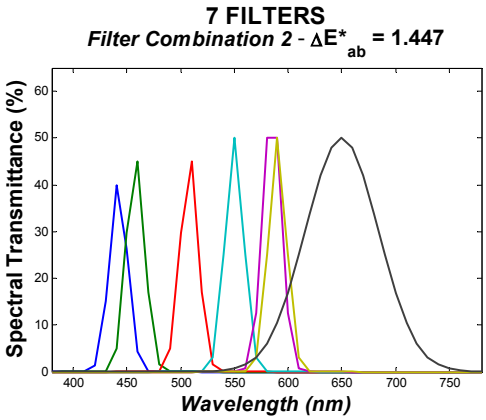

	CWL (nm)	FWHM (nm)	PT (%)
Filter 1	442	10	40
Filter 2	458	10	45
Filter 3	508	10	45
Filter 4	550	10	50
Filter 5	585	10	50
Filter 6	590	10	50
Filter 7	650	40	50

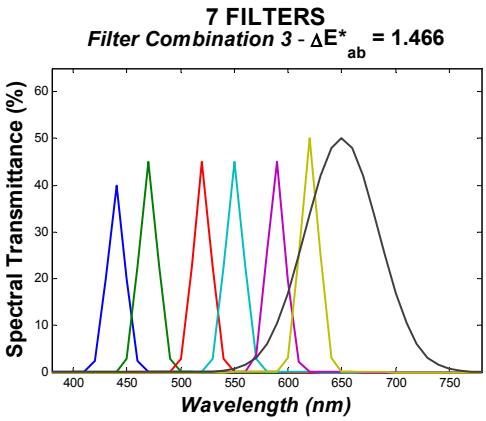

	CWL (nm)	FWHM (nm)	PT (%)
Filter 1	440	10	40
Filter 2	470	10	45
Filter 3	520	10	45
Filter 4	550	10	45
Filter 5	589	10	45
Filter 6	620	10	50
Filter 7	650	40	50

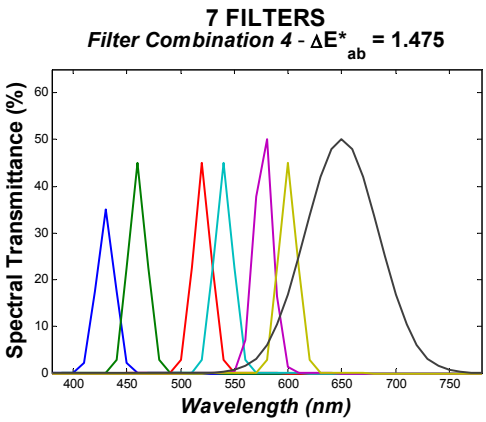

	CWL (nm)	FWHM (nm)	PT (%)
Filter 1	430	10	35
Filter 2	460	10	45
Filter 3	520	10	45
Filter 4	540	10	45
Filter 5	577	10	50
Filter 6	600	10	45
Filter 7	650	40	50

Figure 11.3 (5) *Simulated spectral transmittances (gaussian shape) and mean ΔE^*_{ab} value obtained for the four best sets of 7 interference filters in terms of accuracy of colour measurement. The specifications of the filters (CWL, FWHM, PT) are detailed in the table beside each figure.*

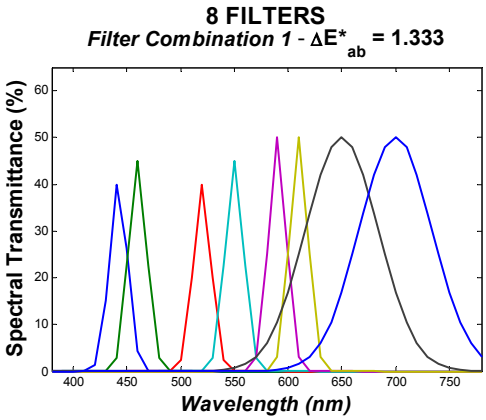

	CWL (nm)	FWHM (nm)	PT (%)
Filter 1	442	10	40
Filter 2	460	10	45
Filter 3	520	10	40
Filter 4	550	10	45
Filter 5	590	10	50
Filter 6	610	10	50
Filter 7	650	40	50
Filter 8	700	40	50

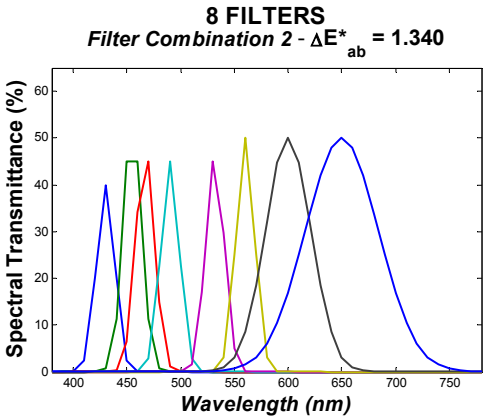

	CWL (nm)	FWHM (nm)	PT (%)
Filter 1	430	10	40
Filter 2	455	10	45
Filter 3	467	10	45
Filter 4	490	10	45
Filter 5	532	10	45
Filter 6	560	10	50
Filter 7	600	25	50
Filter 8	650	40	50

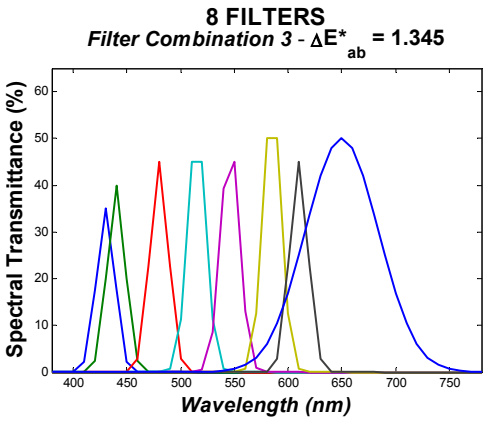

	CWL (nm)	FWHM (nm)	PT (%)
Filter 1	430	10	35
Filter 2	440	10	40
Filter 3	480	10	45
Filter 4	515	10	45
Filter 5	546	10	45
Filter 6	585	10	50
Filter 7	610	10	45
Filter 8	650	40	50

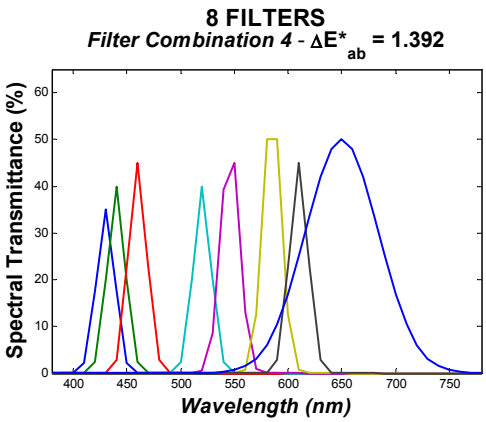

	CWL (nm)	FWHM (nm)	PT (%)
Filter 1	430	10	35
Filter 2	440	10	40
Filter 3	460	10	45
Filter 4	520	10	40
Filter 5	546	10	45
Filter 6	585	10	50
Filter 7	610	10	45
Filter 8	650	40	50

Figure 11.3 (6) *Simulated spectral transmittances (gaussian shape) and mean ΔE^*_{ab} value obtained for the four best sets of 8 interference filters in terms of accuracy of colour measurement. The specifications of the filters (CWL, FWHM, PT) are detailed in the table beside each figure.*

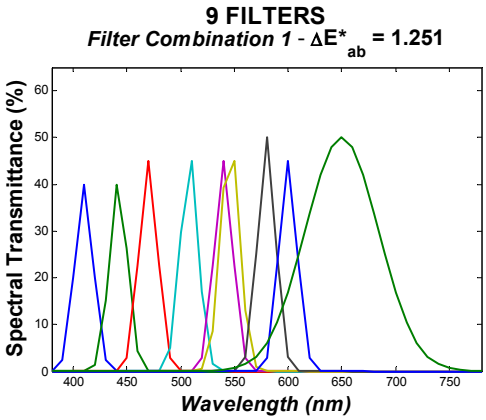

	CWL (nm)	FWHM (nm)	PT (%)
Filter 1	410	10	40
Filter 2	442	10	40
Filter 3	470	10	45
Filter 4	508	10	45
Filter 5	540	10	45
Filter 6	546	10	45
Filter 7	580	10	50
Filter 8	600	10	45
Filter 9	650	40	50

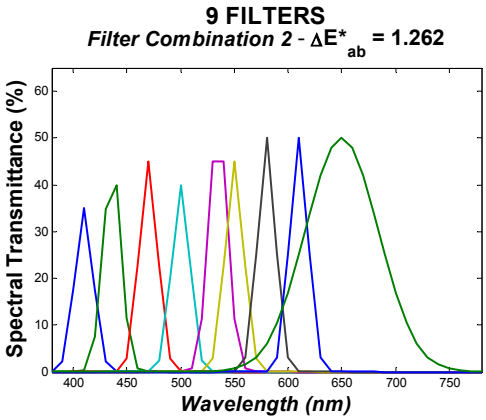

	CWL (nm)	FWHM (nm)	PT (%)
Filter 1	410	10	35
Filter 2	436	10	40
Filter 3	470	10	45
Filter 4	500	10	40
Filter 5	535	10	45
Filter 6	550	10	45
Filter 7	580	10	50
Filter 8	610	10	50
Filter 9	650	40	50

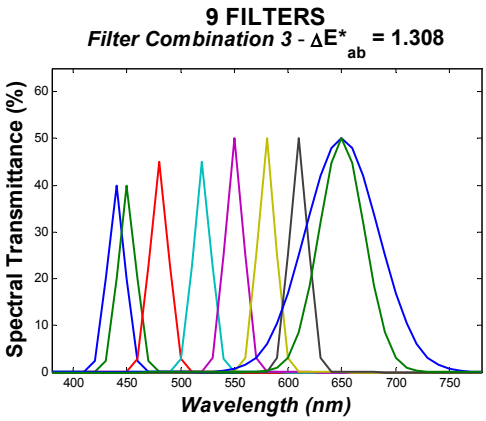

	CWL (nm)	FWHM (nm)	PT (%)
Filter 1	440	10	40
Filter 2	450	10	40
Filter 3	480	10	45
Filter 4	520	10	45
Filter 5	550	10	50
Filter 6	580	10	50
Filter 7	610	10	50
Filter 8	650	40	50
Filter 9	650	25	50

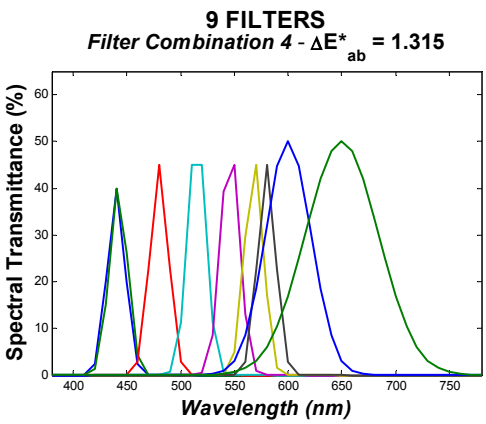

	CWL (nm)	FWHM (nm)	PT (%)
Filter 1	440	10	40
Filter 2	442	10	40
Filter 3	480	10	45
Filter 4	515	10	45
Filter 5	546	10	45
Filter 6	568	10	45
Filter 7	580	10	45
Filter 8	600	25	50
Filter 9	650	40	50

Figure 11.3 (7) *Simulated spectral transmittances (gaussian shape) and mean ΔE^*_{ab} value obtained for the four best sets of 9 interference filters in terms of accuracy of colour measurement. The specifications of the filters (CWL, FWHM, PT) are detailed in the table beside each figure.*

Table 11.1 *Mean, minimum, maximum and standard deviation values of the CIELAB ΔE^*_{ab} colour difference obtained using the four best combinations of 3, 4, 5, 6, 7, 8, and 9 interference filters in terms of accuracy of colour measurement (CCDC training and test).*

		meanΔE^*_{ab}	minΔE^*_{ab}	maxΔE^*_{ab}	std. dev. ΔE^*_{ab}
3 FILTERS	***Filter Comb. 1***	3.556	0.216	14.326	2.829
	Filter Comb. 2	3.570	0.199	13.468	2.764
	Filter Comb. 3	3.635	0.466	11.665	2.383
	Filter Comb. 4	3.657	0.196	14.590	2.831

		meanΔE^*_{ab}	minΔE^*_{ab}	maxΔE^*_{ab}	std. dev. ΔE^*_{ab}
4 FILTERS	***Filter Comb. 1***	2.095	0.198	7.276	1.369
	Filter Comb. 2	2.147	0.371	10.518	1.517
	Filter Comb. 3	2.189	0.125	8.520	1.492
	Filter Comb. 4	2.265	0.062	9.305	1.732

		meanΔE^*_{ab}	minΔE^*_{ab}	maxΔE^*_{ab}	std. dev. ΔE^*_{ab}
5 FILTERS	***Filter Comb. 1***	1.751	0.277	7.861	1.293
	Filter Comb. 2	1.763	0.090	7.163	1.178
	Filter Comb. 3	1.764	0.157	7.009	1.236
	Filter Comb. 4	1.770	0.106	7.590	1.253

		meanΔE^*_{ab}	minΔE^*_{ab}	maxΔE^*_{ab}	std. dev. ΔE^*_{ab}
6 FILTERS	***Filter Comb. 1***	1.585	0.146	6.640	1.155
	Filter Comb. 2	1.588	0.144	8.048	1.149
	Filter Comb. 3	1.607	0.260	6.522	1.154
	Filter Comb. 4	1.623	0.164	7.604	1.127

		meanΔE^*_{ab}	minΔE^*_{ab}	maxΔE^*_{ab}	std. dev. ΔE^*_{ab}
7 FILTERS	***Filter Comb. 1***	1.420	0.118	4.179	0.888
	Filter Comb. 2	1.447	0.149	4.906	0.965
	Filter Comb. 3	1.466	0.070	6.482	1.049
	Filter Comb. 4	1.475	0.054	5.753	1.012

		meanΔE^*_{ab}	minΔE^*_{ab}	maxΔE^*_{ab}	std. dev. ΔE^*_{ab}
8 FILTERS	***Filter Comb. 1***	1.334	0.098	4.714	0.896
	Filter Comb. 2	1.341	0.053	4.965	0.934
	Filter Comb. 3	1.345	0.109	4.587	0.914
	Filter Comb. 4	1.393	0.065	5.139	0.879

		meanΔE^*_{ab}	minΔE^*_{ab}	maxΔE^*_{ab}	std. dev. ΔE^*_{ab}
9 FILTERS	***Filter Comb. 1***	1.252	0.118	5.102	0.944
	Filter Comb. 2	1.263	0.117	4.612	0.821
	Filter Comb. 3	1.309	0.075	4.019	0.878
	Filter Comb. 4	1.315	0.110	5.048	0.980

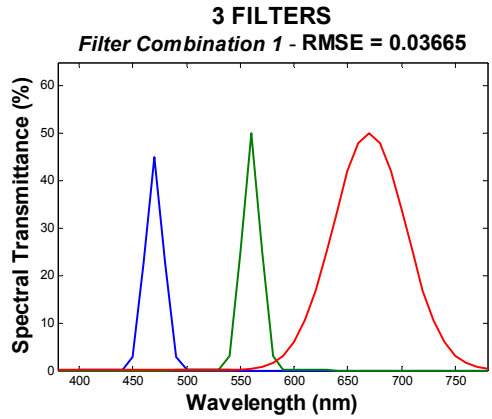

	CWL (nm)	FWHM (nm)	PT (%)
Filter 1	470	10	45
Filter 2	560	10	50
Filter 3	670	40	50

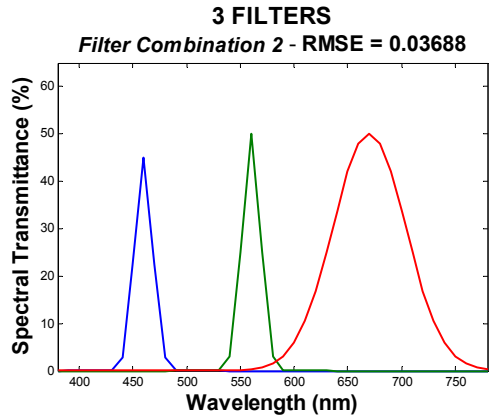

	CWL (nm)	FWHM (nm)	PT (%)
Filter 1	460	10	45
Filter 2	560	10	50
Filter 3	670	40	50

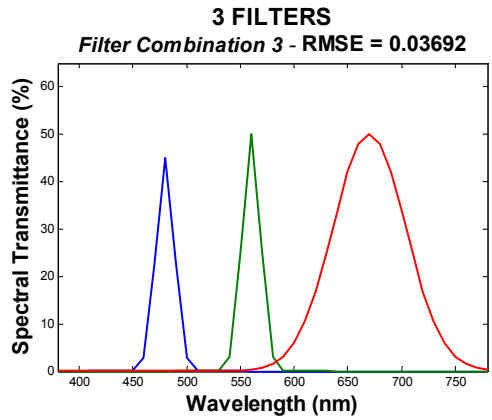

	CWL (nm)	FWHM (nm)	PT (%)
Filter 1	480	10	45
Filter 2	560	10	50
Filter 3	670	40	50

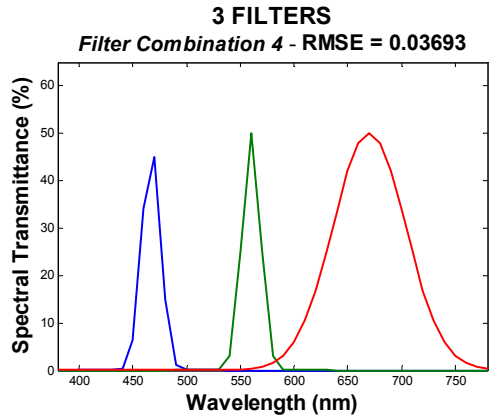

	CWL (nm)	FWHM (nm)	PT (%)
Filter 1	467	10	45
Filter 2	560	10	50
Filter 3	670	40	50

Figure 11.4 (1) *Simulated spectral transmittances (gaussian shape) and mean RMSE value obtained for the four best sets of 3 interference filters in terms of accuracy of spectral reconstruction. The specifications of the filters (CWL, FWHM, PT) are detailed in the table beside each figure.*

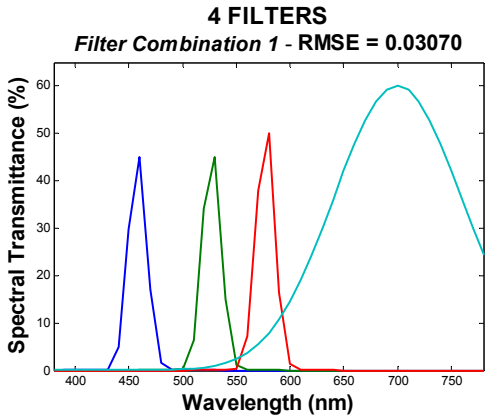

	CWL (nm)	FWHM (nm)	PT (%)
Filter 1	458	10	45
Filter 2	527	10	45
Filter 3	577	10	50
Filter 4	700	70	60

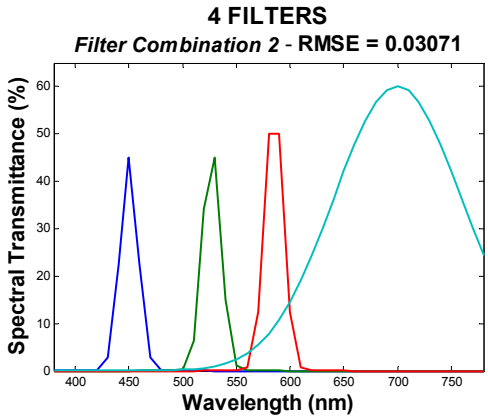

	CWL (nm)	FWHM (nm)	PT (%)
Filter 1	450	10	45
Filter 2	527	10	45
Filter 3	585	10	50
Filter 4	700	70	60

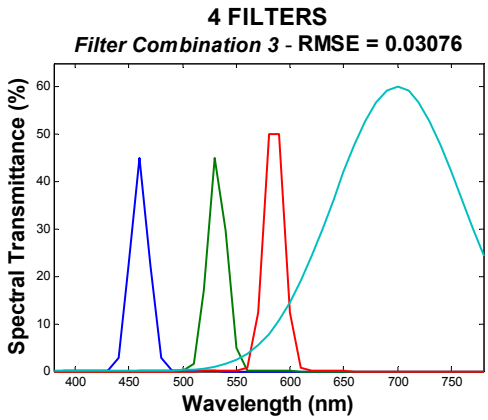

	CWL (nm)	FWHM (nm)	PT (%)
Filter 1	460	10	45
Filter 2	532	10	45
Filter 3	585	10	50
Filter 4	700	70	60

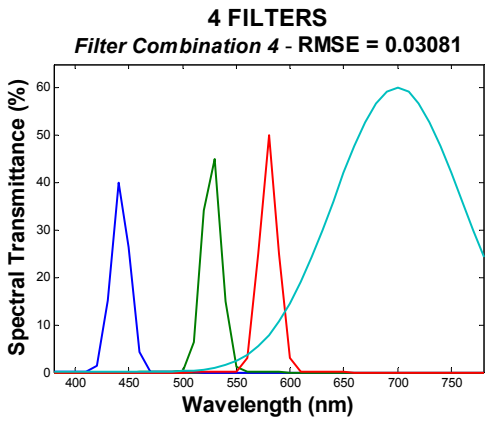

	CWL (nm)	FWHM (nm)	PT (%)
Filter 1	442	10	40
Filter 2	527	10	45
Filter 3	580	10	50
Filter 4	700	70	60

Figure 11.4 (2) *Simulated spectral transmittances (gaussian shape) and mean RMSE value obtained for the four best sets of 4 interference filters in terms of accuracy of spectral reconstruction. The specifications of the filters (CWL, FWHM, PT) are detailed in the table beside each figure.*

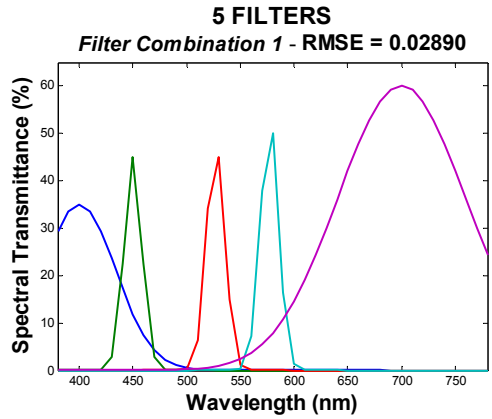

	CWL (nm)	FWHM (nm)	PT (%)
Filter 1	400	40	35
Filter 2	450	10	45
Filter 3	527	10	45
Filter 4	577	10	50
Filter 5	700	70	60

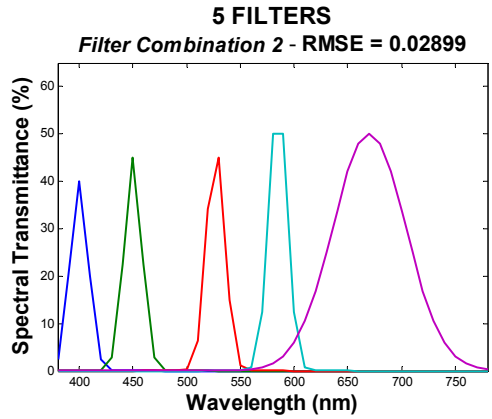

	CWL (nm)	FWHM (nm)	PT (%)
Filter 1	400	10	40
Filter 2	450	10	45
Filter 3	527	10	45
Filter 4	585	10	50
Filter 5	670	40	50

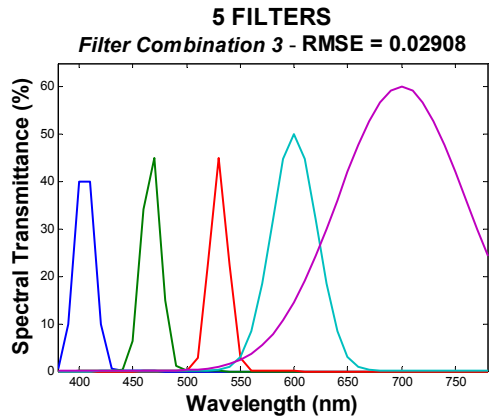

	CWL (nm)	FWHM (nm)	PT (%)
Filter 1	405	10	40
Filter 2	467	10	45
Filter 3	530	10	45
Filter 4	600	25	50
Filter 5	700	70	60

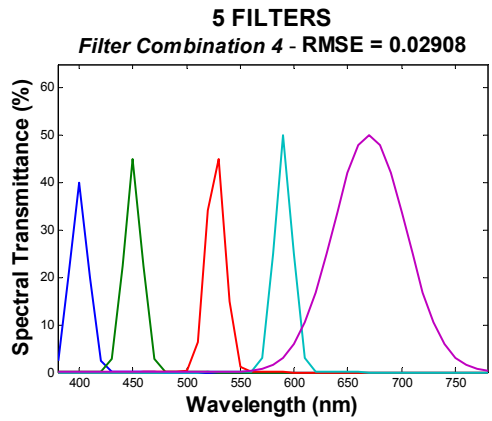

	CWL (nm)	FWHM (nm)	PT (%)
Filter 1	400	10	40
Filter 2	450	10	45
Filter 3	527	10	45
Filter 4	590	10	50
Filter 5	670	40	50

Figure 11.4 (3) *Simulated spectral transmittances (gaussian shape) and mean RMSE value obtained for the four best sets of 5 interference filters in terms of accuracy of spectral reconstruction. The specifications of the filters (CWL, FWHM, PT) are detailed in the table beside each figure.*

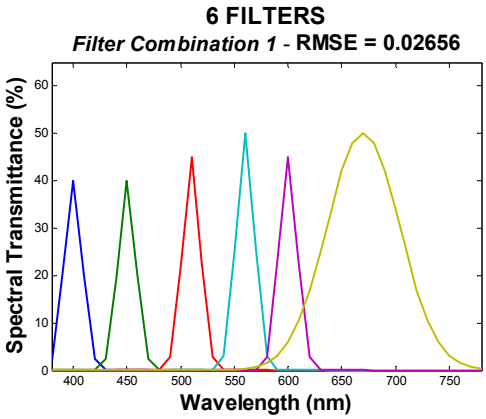

	CWL (nm)	FWHM (nm)	PT (%)
Filter 1	400	10	40
Filter 2	450	10	40
Filter 3	510	10	45
Filter 4	560	10	50
Filter 5	600	10	45
Filter 6	670	40	50

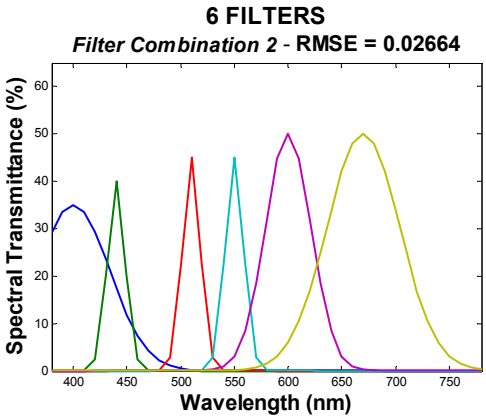

	CWL (nm)	FWHM (nm)	PT (%)
Filter 1	400	40	35
Filter 2	440	10	40
Filter 3	510	10	45
Filter 4	550	10	45
Filter 5	600	25	50
Filter 6	670	40	50

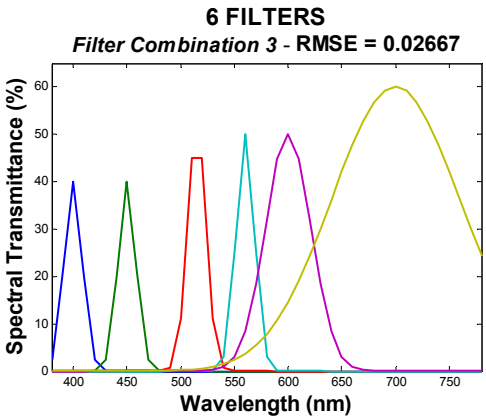

	CWL (nm)	FWHM (nm)	PT (%)
Filter 1	400	10	40
Filter 2	450	10	40
Filter 3	515	10	45
Filter 4	560	10	50
Filter 5	600	25	50
Filter 6	700	70	60

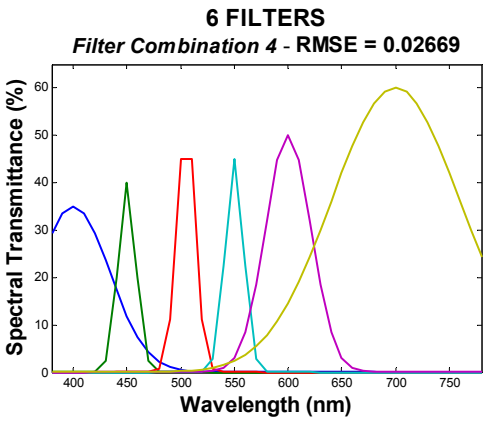

	CWL (nm)	FWHM (nm)	PT (%)
Filter 1	400	40	35
Filter 2	450	10	40
Filter 3	505	10	45
Filter 4	550	10	45
Filter 5	600	25	50
Filter 6	700	70	60

Figure 11.4 (4) *Simulated spectral transmittances (gaussian shape) and mean RMSE value obtained for the four best sets of 6 interference filters in terms of accuracy of spectral reconstruction. The specifications of the filters (CWL, FWHM, PT) are detailed in the table beside each figure.*

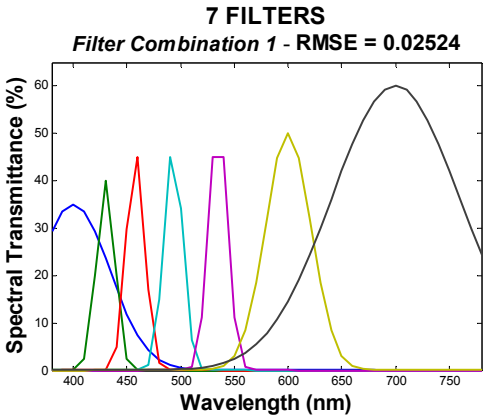

	CWL (nm)	FWHM (nm)	PT (%)
Filter 1	400	40	35
Filter 2	430	10	40
Filter 3	458	10	45
Filter 4	493	10	45
Filter 5	535	10	45
Filter 6	600	25	50
Filter 7	700	70	60

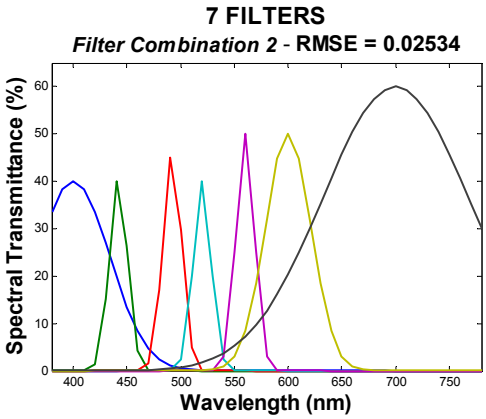

	CWL (nm)	FWHM (nm)	PT (%)
Filter 1	400	40	40
Filter 2	442	10	40
Filter 3	492	10	45
Filter 4	520	10	40
Filter 5	560	10	50
Filter 6	600	25	50
Filter 7	700	80	60

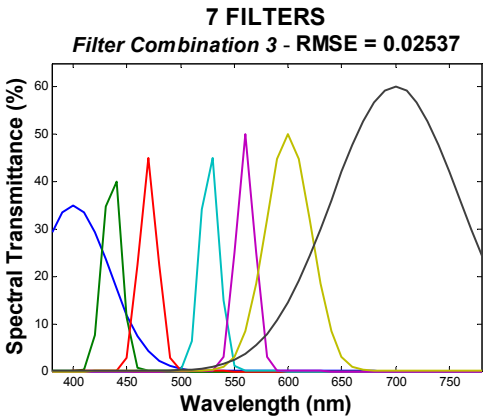

	CWL (nm)	FWHM (nm)	PT (%)
Filter 1	400	40	35
Filter 2	436	10	40
Filter 3	470	10	45
Filter 4	527	10	45
Filter 5	560	10	50
Filter 6	600	25	50
Filter 7	700	70	60

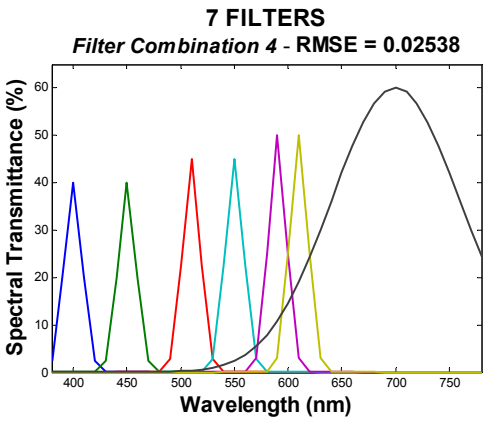

	CWL (nm)	FWHM (nm)	PT (%)
Filter 1	400	10	40
Filter 2	450	10	40
Filter 3	510	10	45
Filter 4	550	10	45
Filter 5	590	10	50
Filter 6	610	10	50
Filter 7	700	70	60

Figure 11.4 (5) *Simulated spectral transmittances (gaussian shape) and mean RMSE value obtained for the four best sets of 7 interference filters in terms of accuracy of spectral reconstruction. The specifications of the filters (CWL, FWHM, PT) are detailed in the table beside each figure.*

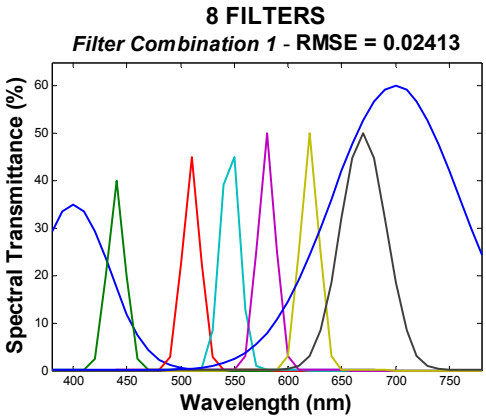

	CWL (nm)	FWHM (nm)	PT (%)
Filter 1	400	40	35
Filter 2	440	10	40
Filter 3	510	10	45
Filter 4	546	10	45
Filter 5	580	10	50
Filter 6	620	10	50
Filter 7	670	25	50
Filter 8	700	70	60

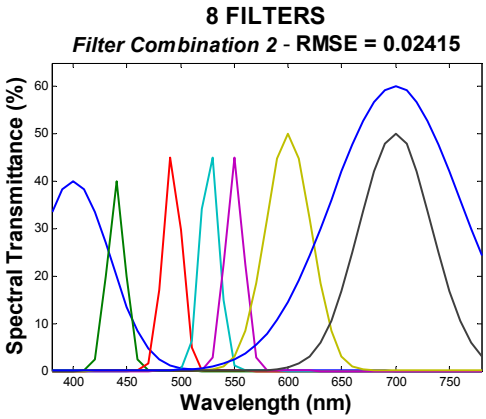

	CWL (nm)	FWHM (nm)	PT (%)
Filter 1	400	40	40
Filter 2	440	10	40
Filter 3	492	10	45
Filter 4	527	10	45
Filter 5	550	10	45
Filter 6	600	25	50
Filter 7	700	40	50
Filter 8	700	70	60

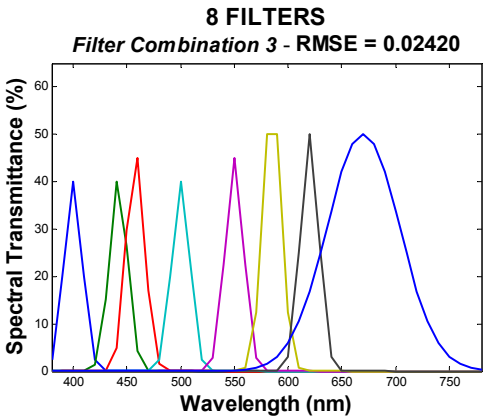

	CWL (nm)	FWHM (nm)	PT (%)
Filter 1	400	10	40
Filter 2	442	10	40
Filter 3	458	10	45
Filter 4	500	10	40
Filter 5	550	10	45
Filter 6	585	10	50
Filter 7	620	10	50
Filter 8	670	40	50

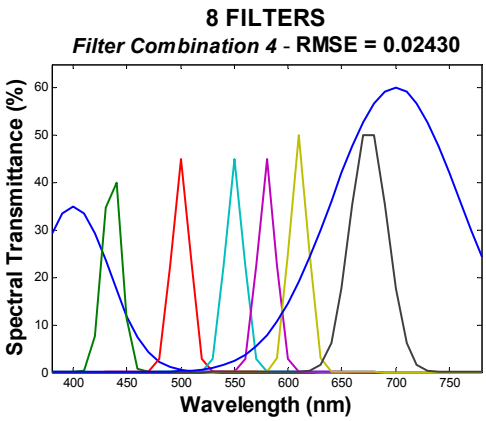

	CWL (nm)	FWHM (nm)	PT (%)
Filter 1	400	40	35
Filter 2	436	10	40
Filter 3	500	10	45
Filter 4	550	10	45
Filter 5	580	10	45
Filter 6	610	10	50
Filter 7	675	20	50
Filter 8	700	70	60

Figure 11.4 (6) *Simulated spectral transmittances (gaussian shape) and mean RMSE value obtained for the four best sets of 8 interference filters in terms of accuracy of spectral reconstruction. The specifications of the filters (CWL, FWHM, PT) are detailed in the table beside each figure.*

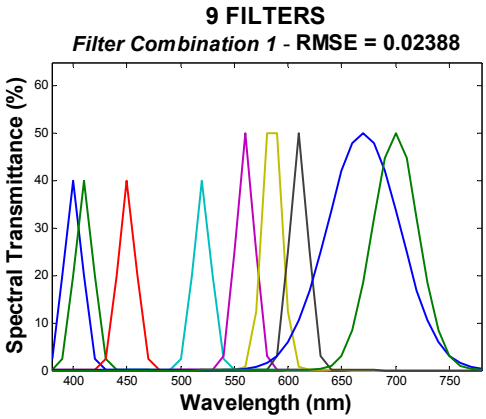

	CWL (nm)	FWHM (nm)	PT (%)
Filter 1	400	10	40
Filter 2	410	10	40
Filter 3	450	10	40
Filter 4	520	10	40
Filter 5	560	10	50
Filter 6	585	10	50
Filter 7	610	10	50
Filter 8	670	40	50
Filter 9	700	25	50

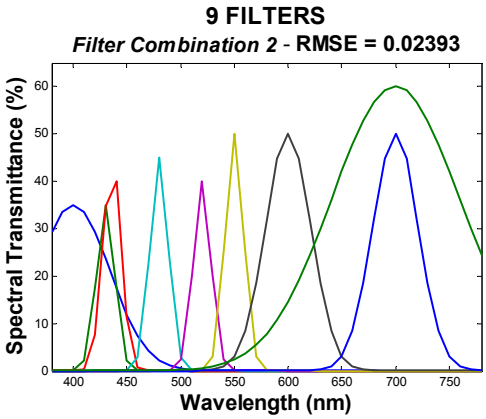

	CWL (nm)	FWHM (nm)	PT (%)
Filter 1	400	40	35
Filter 2	430	10	35
Filter 3	436	10	40
Filter 4	480	10	45
Filter 5	520	10	40
Filter 6	550	10	50
Filter 7	600	25	50
Filter 8	700	25	50
Filter 9	700	70	60

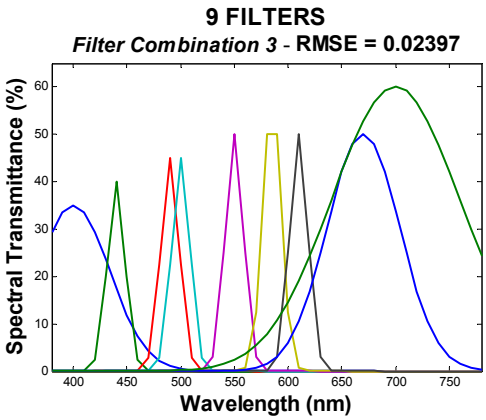

	CWL (nm)	FWHM (nm)	PT (%)
Filter 1	400	40	35
Filter 2	440	10	40
Filter 3	490	10	45
Filter 4	500	10	45
Filter 5	550	10	50
Filter 6	585	10	50
Filter 7	610	10	50
Filter 8	670	40	50
Filter 9	700	70	60

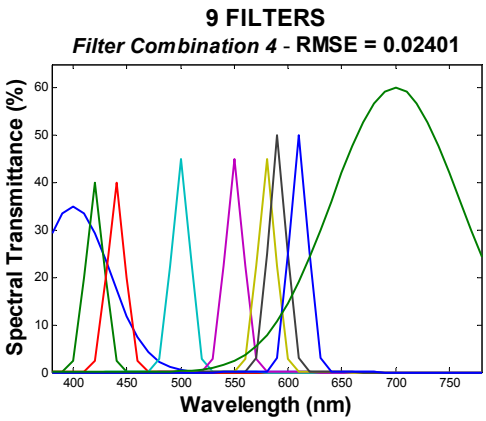

	CWL (nm)	FWHM (nm)	PT (%)
Filter 1	400	40	35
Filter 2	420	10	40
Filter 3	440	10	40
Filter 4	500	10	45
Filter 5	550	10	45
Filter 6	580	10	45
Filter 7	590	10	50
Filter 8	610	10	50
Filter 9	700	70	60

Figure 11.4 (7) *Simulated spectral transmittances (gaussian shape) and mean RMSE value obtained for the four best sets of 9 interference filters in terms of accuracy of spectral reconstruction. The specifications of the filters (CWL, FWHM, PT) are detailed in the table beside each figure.*

Table 11.2 *Mean, minimum, maximum and standard deviation values of the RMSE obtained using the four best combinations of 3, 4, 5, 6, 7, 8, and 9 interference filters in terms of accuracy of spectral reconstruction.*

		meanRMSE	minRMSE	maxRMSE	std. dev. RMSE
3 FILTERS	***Filter Comb. 1***	3.665E-02	0.776E-02	13.60E-02	1.831E-02
	Filter Comb. 2	3.688E-02	1.032E-02	14.64E-02	1.897E-02
	Filter Comb. 3	3.692E-02	0.866E-02	13.71E-02	1.810E-02
	Filter Comb. 4	3.693E-02	1.024E-02	13.88E-02	1.852E-02

		meanRMSE	minRMSE	maxRMSE	std. dev. RMSE
4 FILTERS	***Filter Comb. 1***	3.071E-02	0.733E-02	12.92E-02	1.629E-02
	Filter Comb. 2	3.072E-02	0.812E-02	14.09E-02	1.643E-02
	Filter Comb. 3	3.077E-02	0.832E-02	12.37E-02	1.574E-02
	Filter Comb. 4	3.081E-02	0.988E-02	13.91E-02	1.624E-02

		meanRMSE	minRMSE	maxRMSE	std. dev. RMSE
5 FILTERS	***Filter Comb. 1***	2.891E-02	0.709E-02	11.89E-02	1.508E-02
	Filter Comb. 2	2.899E-02	0.812E-02	12.51E-02	1.509E-02
	Filter Comb. 3	2.908E-02	0.967E-02	11.14E-02	1.349E-02
	Filter Comb. 4	2.909E-02	0.787E-02	11.85E-02	1.466E-02

		meanRMSE	minRMSE	maxRMSE	std. dev. RMSE
6 FILTERS	***Filter Comb. 1***	2.656E-02	0.932E-02	11.09E-02	1.412E-02
	Filter Comb. 2	2.664E-02	0.853E-02	11.26E-02	1.380E-02
	Filter Comb. 3	2.668E-02	0.789E-02	10.56E-02	1.312E-02
	Filter Comb. 4	2.670E-02	0.808E-02	11.18E-02	1.416E-02

		meanRMSE	minRMSE	maxRMSE	std. dev. RMSE
7 FILTERS	***Filter Comb. 1***	2.524E-02	0.798E-02	11.38E-02	1.411E-02
	Filter Comb. 2	2.535E-02	0.856E-0	11.31E-02	1.403E-02
	Filter Comb. 3	2.537E-02	0.769E-02	11.08E-02	1.356E-02
	Filter Comb. 4	2.539E-02	0.914E-02	10.51E-02	1.366E-02

		meanRMSE	minRMSE	maxRMSE	std. dev. RMSE
8 FILTERS	***Filter Comb. 1***	2.413E-02	0.721E-02	9.174E-02	1.217E-02
	Filter Comb. 2	2.415E-02	0.628E-02	10.48E-02	1.337E-02
	Filter Comb. 3	2.420E-02	0.739E-02	10.98E-02	1.351E-02
	Filter Comb. 4	2.431E-02	0.666E-02	8.998E-02	1.290E-02

		meanRMSE	minRMSE	maxRMSE	std. dev. RMSE
9 FILTERS	***Filter Comb. 1***	2.389E-02	0.718E-02	8.986E-02	1.316E-02
	Filter Comb. 2	2.394E-02	0.777E-02	9.927E-02	1.292E-02
	Filter Comb. 3	2.397E-02	0.598E-02	10.18E-02	1.418E-02
	Filter Comb. 4	2.402E-02	0.535E-02	10.47E-02	1.410E-02

Regarding the accuracy of colour measurement, as can be seen from Figures 11.3 (1) – (7) and from Table 11.1, several combinations of interference filters lead to quite similar results. It is noticeable that, commonly to all optimum filter combinations obtained for all numbers of filters, the selected filters with a CWL between 650nm and 780nm (red zone of the visible spectrum) tend to have a larger FWHM than the rest of filters of the set, and one of the larger peak transmittances available. This is probably to compensate for the low spectral response of the CCD camera in this region compared to its spectral response over the rest of the visible spectrum (Figure 11.1).

Comparing results obtained using the real colorimetric configuration (Table 11.3), with 3 liquid crystal tunable filters (whose transmittances cannot be measured since the tuning between filters can only be controlled through the camera), with the simulated colorimetric configuration with the 3 optimum interference filters (Table 11.1), it can be said that several combinations of 3 interference filters can improve theoretically the system's performance in terms of accuracy of colour measurement. Anyway, this result can only be considered as a theoretical hypothesis due to the fact that, on one hand, the spectral transmittances of the liquid crystal tunable filters are not available and, consequently, the real system's performance cannot be simulated to compare both simulations, and on the other hand, interference filters used in the simulation are considered to be approximately gaussian, whereas the spectral transmittance of the real ones are quite different from the theoretical gaussian shape (Figure 11.5).

Table 11.3 *Mean, minimum, maximum and standard deviation values of the CIELAB ΔE^*_{ab} colour difference obtained using the real colorimetric configuration, with 3 liquid crystal tunable filters, and the real multispectral configuration, with 7 interference filters, of the imaging system (CCDC training and test).*

	meanΔE^*_{ab}	minΔE^*_{ab}	maxΔE^*_{ab}	std. dev. ΔE^*_{ab}
Colorimetric Configuration 3 TUNABLE FILTERS	4.719	0.333	17.71	3.229
Multispectral Configuration 7 INTERFERENCE FILTERS	2.707	0.202	10.04	2.040

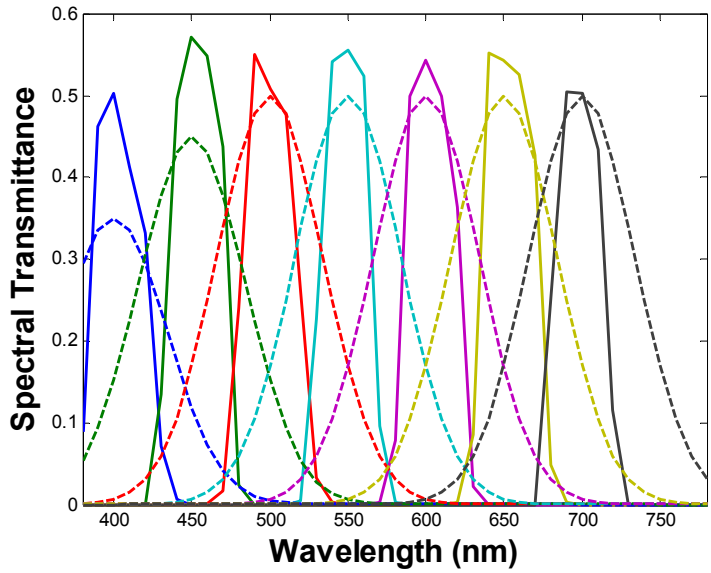

Figure 11.5 *Spectral transmittances of the 7 interference filters used in the multispectral configuration of the imaging system. Continuous lines correspond to the real measured spectral transmittances of the filters, and dashed lines correspond to the gaussian simulations considering the specifications (CWL, FWHM, and PT) provided by the supplier (CVI Laser).*

Considering a multispectral imaging system with 7 acquisition channels, results obtained using the real multispectral configuration with 7 filters (Table 11.3) are also improved theoretically using several combinations of 7 interference filters (Table 11.1). In this case, the real spectral transmittances of the filters used are known and, as can be observed from Figure 11.5, they are quite different from the gaussian simulations used in the theoretical calculations considering the specifications provided by the supplier (CWL, FWHM, and PT). The real filters presented narrower spectral transmittances with larger peak transmittance values in most cases. In order to check how these differences have affected results obtained from simulations using gaussian filters, system's response is simulated using both the real transmittances and the gaussian simulations represented in Figure 11.5 (Table 11.4). Results obtained using the real transmittances are similar to those obtained using the real multispectral configuration of the imaging system, while results obtained using the gaussian simulations of the filter's transmittances are noticeably worse (Table 11.4).

Table 11.4 *Mean, minimum, maximum and standard deviation values of the CIELAB ΔE^*_{ab} colour difference obtained in the theoretical simulation of the system's performance using the real transmittances of the 7 interference filters and their gaussian simulations (CCDC training and test).*

	meanΔE^*_{ab}	minΔE^*_{ab}	maxΔE^*_{ab}	std. dev. ΔE^*_{ab}
REAL TRANSMITTANCES	2.104	0.349	17.237	2.221
GAUSSIAN SIMULATIONS	6.400	0.521	29.383	4.955

Similar results are obtained in terms of accuracy of spectral reconstruction. As can be observed from Figures 11.4 (1) – (7) and from Table 11.2, several combinations of interference filters also lead to almost equal results. The selected filters with CWLs between 650nm and 780nm (red zone of the visible spectrum) also tend to have larger FWHMs than the rest of filters of the set, and one of the larger peak transmittances available. However, in this case filters are not placed as uniformly as the optimum filters obtained in terms of accuracy of colour measurement.

Comparing results obtained using the real colorimetric configuration (Table 11.5), with 3 liquid crystal tunable filters, with the simulated colorimetric configuration with the 3 optimum interference filters (Table 11.2), several combinations of 3 interference filters can also slightly improve theoretically the system's performance in terms of spectral reconstruction. In this case, the improvement in system's performance is smaller that the one obtained in terms of accuracy of colour measurement. Nevertheless, just as before, this result can only be considered as a theoretical hypothesis.

Table 11.5 *Mean, minimum, maximum and standard deviation values of RMSE obtained using the real colorimetric configuration, with 3 liquid crystal tunable filters, and the real multispectral configuration, with 7 interference filters, of the imaging system (CCDC training and test).*

	meanRMSE	minRMSE	maxRMSE	std. dev. RMSE
Colorimetric Configuration 3 TUNABLE FILTERS	4.176E-02	1.581E-02	14.12E-02	2.109E-02
Multispectral Configuration 7 INTERFERENCE FILTERS	2.762E-02	1.008E-02	6.208E-02	1.062E-02

Results obtained using the real multispectral configuration with 7 filters (Table 11.5) are also slightly improved theoretically using several combinations of 7 interference filters

(Table 11.2). In this case, differences between the real transmittances of the filters and their gaussian simulations also affect results obtained from the system's performance simulation (Table 11.6) but not as much as they do in terms of accuracy of colour measurement. Results obtained using the real transmittances are slightly worse than those obtained using the gaussian simulations of the filter's transmittances (Table 11.6). In both cases results obtained from the simulation of the system's response are worse than those obtained using the real multispectral configuration of the imaging system (Table 11.5 and Table 11.6).

Table 11.6 *Mean, minimum, maximum and standard deviation values of the RMSE obtained in the theoretical simulation of the system's performance using the real transmittances of the 7 interference filters and their gaussian simulations (CCDC training and test).*

	meanRMSE	minRMSE	maxRMSE	std. dev. RMSE
REAL TRANSMITTANCES	3.138E-02	1.040E-02	10.49E-02	1.588E-02
GAUSSIAN SIMULATIONS	4.397E-02	1.350E-02	12.86E-02	2.073E-02

Finally, considering results obtained from simulations of system's performance depending on the number of interference filters considered, system's performance is improved in terms of accuracy of both colour measurement and spectral reconstruction with an increasing number of interference filters. Nevertheless, as it can be observed from Figure 11.6, this improvement is limited and tends to be insignificant for more than 8 filters, but it must be bore in mind that these results are obtained using the CCDC chart as training and test set. Using another training set, results could be notably different.

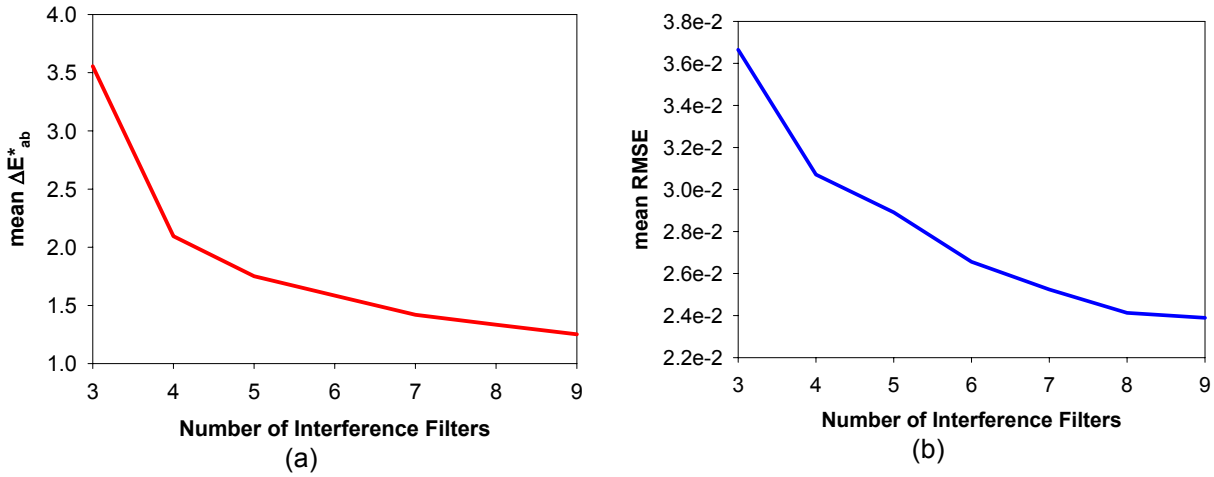

Figure 11.6 *(a) Mean ΔE^*_{ab} for the optimum set of filters in terms of accuracy of colour measurement versus the number of filters. (b) Mean RMSE for the optimum set of filters in terms of accuracy of spectral reconstruction versus the number of filters.*

Taking all these results into account it can be concluded that when designing a multispectral imaging system, a simulation study of the optimum multispectral imaging system considering the commercially available filters, either in terms of accuracy of colour measurement or in terms of accuracy of spectral reconstruction, can be very useful in order to get an idea of the specific characteristics of the optimum filters, but not decisive in the sense that results of simulations depend greatly on the real spectral transmittances of filters, which not always can be easily simulated from the specifications provided by suppliers. Optimum

filters tend to make up for the spectral response of the CCD camera over the whole visible range, but considering the drawback the unknown real spectral transmittances of filters supposes, the selection of a set of gaussian interference filters having equidistant peak positions covering the whole visible range, equal FWHMs that allow a slight overlapping between them, and the higher transmittance possible, as it was done in this work, constitutes an acceptable option to obtain a worthy multispectral imaging system.

Regarding the number of filters, although increasing the number of filters tends to improve theoretically the accuracy of the system's performance, it also introduces experimental errors involving a longer sequence of measurements, increases the mechanical complexity of the experimental setup to fit the filters in a wheel or a similar assembly and automate it, and also increases the final cost of the system. Therefore, some kind of compromise should also be reached among real accuracy, complexity, and cost.

12 Application of the Multispectral Imaging System Developed: Colour Measurement and Spectral Reconstruction of Textile Samples

Once the multispectral imaging system developed for colour measurement has been fully characterized, its applicability is tested not only using standardized colour charts, such as the ones used so far (the GretagMacbeth ColorChecker Color Rendition (CCCR) and DC (CCDC) charts, and the Munsell Book of Color – Matte Collection), but also using real samples. In this section the performance of the multispectral imagining system developed is tested using a set of textile samples provided by the INTEXTER (Institute of Textile Research and Industrial Cooperation of Terrassa) and the D65 simulator illuminant.

The performance of colour measurement and spectral reconstruction of textile samples is one of the numerous applications of a multispectral imaging system like the one designed and developed in this work (sub-section 2.1.3). The good performance of the multispectral imaging system in measuring colour and reconstructing spectra of real samples different from the standardized colour charts used to characterize it, such as the textile samples considered, will prove its versatility to be used in different and real applications.

The set of textile samples considered is constituted by 56 textile samples grouped in 28 pairs. These pairs of textile samples were made specifically to test the applicability of colour difference formulas to textile samples, particularly the CIELAB colour difference formula. Hence, these samples have characteristic spectra, quite similar between pairs, which make them rather difficult to be distinguished and to be measured and reconstructed accurately without confusion between pairs. Differences between the two samples in a pair (called A and B) are quite slight for most of them (Table 12.5), as it can be deduced from their reflectance spectra (Figure 12.1 and Appendix 9). The reflectance spectra of the 28 pairs of textile samples used were measured using a MACBETH ColorEye 7000 Spectrophotometer, and can be found in Appendix 9 (Figure A9 (1) – (3)).

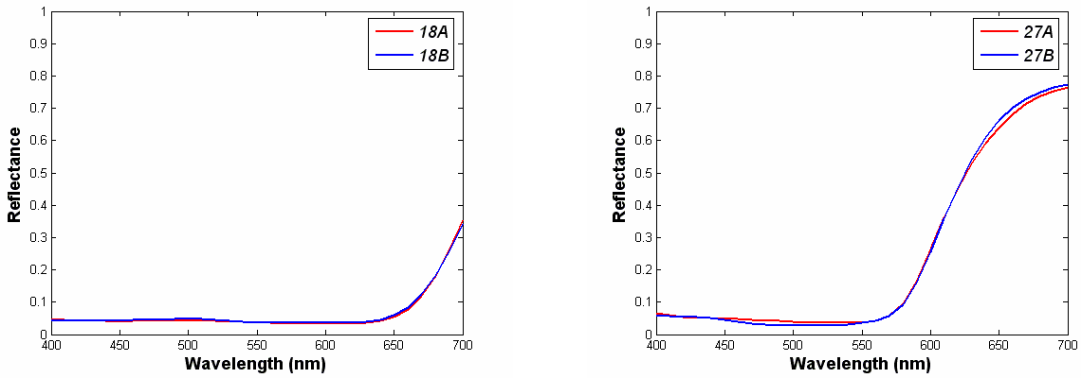

Figure 12.1 *Reflectance spectra of (a) the pair 18 with a* ΔE^*_{ab} = 0.750 *and a RMSE* = 3.971E-03 *between them, and (b) the pair 27 with a* ΔE^*_{ab} = 3.018 *and a RMSE* = 1.001E-02 *between them.*

Two different studies are carried out in this section: a study on the accuracy of system's performance in terms of colour measurement and spectral reconstruction of the textile samples, and a study on the accuracy of system's performance in detecting both the colour and the spectral differences between the pairs of textile samples.

Just as it has been done so far, accuracy of colour measurement is evaluated in terms of the mean, minimum, maximum and standard deviation of the mean values of the CIELAB colour differences (ΔE^*_{ab}) between the measured and the calculated XYZ tristimulus values, and accuracy of spectral reconstruction is evaluated in terms of the mean, minimum, maximum and standard deviation of the mean values of the Root Mean Square Error (RMSE) between the measured and the recovered reflectance spectra.

12.1 Accuracy of system's performance in terms of colour measurement and spectral reconstruction of the textile samples

In this first study, the multispectral configuration of the imaging system is used to reconstruct the reflectance spectra and measure the colour of the textile samples using different training sets. The textile samples (TS), the CCDC chart, and all Munsell's colour patches are used as training sets. Furthermore, the textile samples are classified in Munsell's hues by applying the *a*b* classification method* (sub-section 9.2.4), and their reflectance spectra are also reconstructed using the sets of Munsell's hues as training sets.

Global results for all textile samples in terms of accuracy of colour measurement and spectral reconstruction, for the different training sets used, are presented in Tables 12.1 and 12.2, respectively.

Table 12.1 *Mean, minimum, maximum and standard deviation of the CIELAB colour difference values of the textile samples (TS) using the TS themselves, the CCDC chart, the sets of Munsell's hues (classifying the TS in Munsell's hues), and all Munsell's colour patches as training sets.*

Training	TS	CCDC	MUNSELL Hues	All MUNSELL
Test	TS	TS	TS	TS
mean ΔE^*_{ab}	3.758	5.991	4.442	6.081
min ΔE^*_{ab}	0.095	0.741	1.500	0.978
max ΔE^*_{ab}	12.54	15.39	11.51	14.15
std. dev. ΔE^*_{ab}	3.213	3.902	2.772	3.612

Table 12.2 *Mean, minimum, maximum and standard deviation of the RMSE values of the textile samples (TS) using the TS themselves, the CCDC chart, the sets of Munsell's hues* (*classifying the TS in Munsell's hues), and all Munsell's colour patches as training sets.*

Training	TS	CCDC	MUNSELL Hues	All MUNSELL
Test	TS	TS	TS	TS
mean RMSE	1.861E-02	4.252E-02	3.432E-02	3.489E-02
min RMSE	0.313E-02	1.310E-02	1.012E-02	0.918E-02
max RMSE	3.993E-02	8.245E-02	6.451E-02	8.198E-02
std. dev. RMSE	0.958E-02	1.623E-02	1.386E-02	1.432E-02

As it was expected, best results both in terms of accuracy of colour measurement and in terms of accuracy of spectral reconstruction are obtained using the textile samples as

training and test set. When different training and test sets are used, the best results are obtained using the sets of Munsell's hues as training set, and classifying the textile samples in hues to reconstruct them. These results confirm that results obtained in sub-section 9.2.4 are applicable not only to standardized colour samples, but also to real samples.

Next, results obtained for the textile samples classified in Munsell's hues in terms of accuracy of colour measurement and spectral reconstruction, are presented in Tables 12.3 and 12.4, respectively, and in Figure 12.2 for the different training sets used.

Classifying the textile samples in Munsell's hues and using different training and test sets, the best results both in terms of accuracy of colour measurement and in terms of accuracy of spectral reconstruction are mostly obtained in average using the sets of Munsell's hues as training sets. These results are even better than those obtained using the textile samples themselves as training set (e.g. the R, GY, PB and RP hues in terms of accuracy of colour measurement (Table 12.3 and Figure 12.2 (a)), and the R and B hues in terms of accuracy of spectral reconstruction (Table 12.4 and Figure 12.2 (b))). On the other hand, better results are obtained in average using the CCDC chart as training set than using the sets of Munsell's hues for the BG, PB, and P hues in terms of accuracy of colour measurement (Table 12.3 and Figure 12.2 (a)) and for the PB and P hues in terms of accuracy of spectral reconstruction (Table 12.4 and Figure 12.2 (b))), and using all Munsell's colour patches instead of the sets of Munsell's hues in average for the BG hue in terms of accuracy of colour measurement (Table 12.3 and Figure 12.2 (a)), and for the BG, P, and RP hues in terms of accuracy of spectral reconstruction (Table 12.4 and Figure 12.2 (b))). These results are consequence of several factors. Firstly, the fact that, apart from the set of textile samples, the training sets used consisted of standardized colour samples, which are quite different from the textile samples measured, whereas the training set should be of the same kind of the samples to be measured. Secondly, the limitations of the classification in hues of the test samples and the use of training sets homogeneous in hue to train the imaging system hue by hue, already detected in sub-section 9.2.4: the classification method is not fine enough and does not work for some samples (samples on border zones of Munsell hues and/or out of Munsell a*b* domain), and the limited gamut defined by all training sets homogeneous in hue used that cannot cover at all the whole CIELAB space of the textile samples used as test set. Finally, the reflectance spectra of colour samples, different from the textile samples, used as training sets, i.e. the CCDC's colour samples and the Munsell's colour patches, were measured using a tele-spectracolorimeter PhotoResearch PR650, whereas the reflectance spectra of the textile samples were measured using a MACBETH ColorEye 7000 Spectrophotometer, which is a contact spectrophotometer. Using different measuring instruments and different measuring geometry could lead to some differences between the reflectance spectra of the textile samples and the rest of colour samples considered (CCDC's and Munsell's) and, consequently, to some systematic errors in the subsequent colour measurement and spectral reconstruction performed that would affect results obtained lowering the system's accuracy.

Table 12.3 *Mean, minimum, maximum and standard deviation of the ΔE^*_{ab} values of the sets of textile samples (TS) classified in Munsell's hues, using the TS themselves, the CCDC chart, the sets of Munsell's hues, and all Munsell's colour patches as training sets.*

Training Set	TS	CCDC	Munsell R	All Munsell
meanΔE^*_{ab}	6.780	8.265	3.963	8.149
minΔE^*_{ab}	0.663	5.203	1.602	2.212
maxΔE^*_{ab}	11.072	11.503	7.462	14.150
std. dev. ΔE^*_{ab}	3.958	2.462	2.389	4.393

TS	CCDC	Munsell YR	All Munsell	*Training Set*
2.197	2.689	2.328	6.666	**meanΔE^*_{ab}**
0.261	1.206	1.617	3.044	**minΔE^*_{ab}**
4.248	4.339	3.083	10.258	**maxΔE^*_{ab}**
2.207	1.684	0.684	3.989	**std. dev. ΔE^*_{ab}**

Training Set	TS	CCDC	Munsell Y	All Munsell
meanΔE^*_{ab}	6.012	11.988	3.867	7.470
minΔE^*_{ab}	0.774	8.823	1.931	2.161
maxΔE^*_{ab}	12.536	15.385	6.290	11.976
std. dev. ΔE^*_{ab}	5.902	3.482	1.819	5.092

TS	CCDC	Munsell GY	All Munsell	*Training Set*
3.971	8.816	9.435	6.262	**meanΔE^*_{ab}**
3.945	8.612	9.213	6.099	**minΔE^*_{ab}**
3.997	9.021	9.657	6.425	**maxΔE^*_{ab}**
0.037	0.289	0.314	0.231	**std. dev. ΔE^*_{ab}**

Training Set	TS	CCDC	Munsell B	All Munsell
meanΔE^*_{ab}	2.961	8.178	6.191	10.818
minΔE^*_{ab}	2.304	7.443	5.901	10.170
maxΔE^*_{ab}	3.619	8.912	6.481	11.466
std. dev. ΔE^*_{ab}	0.930	1.039	0.410	0.916

TS	CCDC	Munsell PB	All Munsell	*Training Set*
2.665	2.171	2.601	3.246	**meanΔE^*_{ab}**
2.396	1.826	2.475	2.925	**minΔE^*_{ab}**
2.935	2.515	2.727	3.566	**maxΔE^*_{ab}**
0.382	0.487	0.178	0.454	**std. dev. ΔE^*_{ab}**

Training Set	TS	CCDC	Munsell P	All Munsell
meanΔE^*_{ab}	2.448	4.924	4.942	5.170
minΔE^*_{ab}	0.514	0.741	1.500	0.978
maxΔE^*_{ab}	7.634	14.780	11.511	10.840
std. dev. ΔE^*_{ab}	1.702	4.009	3.478	3.064

TS	CCDC	Munsell RP	All Munsell	*Training Set*
5.445	6.514	4.542	5.742	**meanΔE^*_{ab}**
0.095	4.317	3.845	3.088	**minΔE^*_{ab}**
9.443	8.052	5.874	11.709	**maxΔE^*_{ab}**
3.425	1.372	0.689	3.248	**std. dev. ΔE^*_{ab}**

Table 12.4. *Mean, minimum, maximum and standard deviation of the RMSE values of the sets of textile samples (TS) classified in Munsell's hues, using the TS themselves, the CCDC chart, the sets of Munsell's hues, and all Munsell's colour patches as training sets.*

Training Set	TS	CCDC	Munsell R	All Munsell
meanRMSE	2.831E-02	4.656E-02	2.326E-02	2.803E-02
minRMSE	7.381E-03	3.253E-02	1.012E-02	1.298E-02
maxRMSE	3.993E-02	7.582E-02	4.577E-02	4.319E-02
std. dev. RMSE	1.221E-02	1.754E-02	1.215E-02	1.155E-02

TS	CCDC	Munsell YR	All Munsell	*Training Set*
1.373E-02	5.424E-02	4.123E-02	4.418E-02	**meanRMSE**
4.998E-03	3.033E-02	3.663E-02	3.085E-02	**minRMSE**
2.077E-02	7.504E-02	5.325E-02	5.696E-02	**maxRMSE**
7.302E-03	2.133E-02	8.034E-03	1.422E-02	**std. dev. RMSE**

Training Set	TS	CCDC	Munsell Y	All Munsell
meanRMSE	2.049E-02	6.085E-02	3.572E-02	4.016E-02
minRMSE	1.309E-02	3.954E-02	1.990E-02	2.814E-02
maxRMSE	3.059E-02	8.245E-02	4.445E-02	5.768E-02
std. dev. RMSE	8.289E-03	2.002E-02	1.153E-02	1.247E-02

TS	CCDC	Munsell GY	All Munsell	*Training Set*
1.471E-02	4.528E-02	4.344E-02	3.271E-02	**meanRMSE**
1.415E-02	4.367E-02	4.279E-02	3.203E-02	**minRMSE**
1.527E-02	4.689E-02	4.409E-02	3.339E-02	**maxRMSE**
7.936E-04	2.276E-03	9.202E-04	9.610E-04	**std. dev. RMSE**

Training Set	TS	CCDC	Munsell B	All Munsell
meanRMSE	1.577E-02	3.883E-02	1.162E-02	3.420E-02
minRMSE	1.317E-02	3.701E-02	1.042E-02	3.279E-02
maxRMSE	1.837E-02	4.064E-02	1.281E-02	3.562E-02
std. dev. RMSE	3.673E-03	2.562E-03	1.686E-03	2.005E-03

TS	CCDC	Munsell PB	All Munsell	*Training Set*
1.258E-02	3.436E-02	3.584E-02	3.901E-02	**meanRMSE**
1.054E-02	3.261E-02	3.393E-02	3.671E-02	**minRMSE**
1.463E-02	3.612E-02	3.774E-02	4.131E-02	**maxRMSE**
2.896E-03	2.486E-03	2.695E-03	3.251E-03	**std. dev. RMSE**

Training Set	TS	CCDC	Munsell P	All Munsell
meanRMSE	1.564E-02	3.836E-02	4.051E-02	3.886E-02
minRMSE	5.936E-03	1.310E-02	2.332E-02	2.217E-02
maxRMSE	3.526E-02	5.940E-02	6.451E-02	8.198E-02
std. dev. RMSE	6.646E-03	1.408E-02	1.067E-02	1.398E-02

TS	CCDC	Munsell RP	All Munsell	*Training Set*
2.300E-02	4.103E-02	2.487E-02	1.969E-02	**meanRMSE**
3.125E-03	2.699E-02	1.034E-02	9.175E-03	**minRMSE**
3.162E-02	6.476E-02	5.187E-02	3.667E-02	**maxRMSE**
1.235E-02	1.563E-02	1.628E-02	1.079E-02	**std. dev. RMSE**

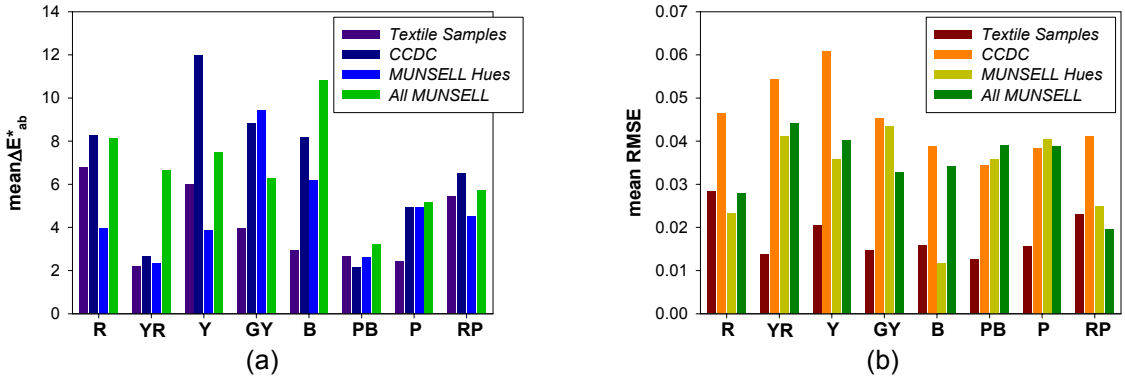

Figure 12.2 *Bar plots of the mean (a) ΔE^*_{ab} values and (b) RMSE values for the sets of Textile Samples classified in Munsell's hues, using the textile samples themselves, the CCDC chart, the sets of Munsell's hues, and all Munsell's colour patches as training sets.*

12.2 Accuracy of system's performance in detecting both the colour differences and the spectral differences between pairs of textile samples

The second study carried out in this section is focused on determining if the multispectral imaging system developed is able to reproduce both the colour and the spectral differences existing between the samples of each pair of textile samples used, according to what they were made to, and to establish the accuracy achieved on this reproduction.

Once the reflectance spectrum of each textile sample is reconstructed using the textile samples themselves, the CCDC chart, the sets of Munsell's hues, and all Munsell's colour patches as training sets, the CIELAB colour difference and the RMSE are computed between the reconstruction of the textile samples of each pair. Both the real values, calculated directly from the measured reflectance spectra, and the reconstructed values, calculated from the reconstructed reflectance spectra obtained using the different training sets mentioned above, of the CIELAB colour difference and the RMSE are presented together with the percentage of variation in Tables 12.5 and 12.7, respectively, for each pair of textile samples. The percentage of variation of the reconstructed CIELAB colour difference and RMSE values with regard to the real values is calculated as the percentage of the real value that the absolute difference between the real and the reconstructed value is.

As can be observed, however smaller the real CIELAB colour difference values and the RMSE values are, an approximate reproduction of these values is achieved by the multispectral imaging system, although a quite low accuracy is obtained for most of the pairs of textile samples (% of variation in Tables 12.5 and 12.7). This is an outstanding result since it proves that the multispectral imaging system developed is able to detect slight differences both in colour and in reflectance spectra between real samples, making it useful for applications that require discrimination. On the other hand, the low accuracy obtained is a direct consequence of the factors that affect the results obtained. The first step to improve these results should be finding a complete training set made up of sets of textile samples homogeneous in hue, or whatever the samples to be measured are, that allows a correct classification of the test samples in hues, and covers the whole space defined by the samples to be measured either in the CIELAB space or in the reflectance spectra space.

Table 12.5 *CIELAB colour difference values (ΔE^*_{ab}) and percentage of variation(*) between the AB pairs of textile samples (TS) measured (Real ΔE^*_{ab}) and reconstructed using the TS, the CCDC chart, the sets of Munsell's hues, and all Munsell's colour patches as training sets.*

		ΔE^*_{ab} between AB pairs reconstructed				% of variation vs the real ΔE^*_{ab}			
AB pairs of TS	Real ΔE^*_{ab}	TS	CCDC	MUNSELL's Hues	ALL MUNSELL	TS	CCDC	MUNSELL's Hues	ALL MUNSELL
25A25B	1.221	2.061	2.259	3.274	2.153	68.84	85.08	168.24	76.38
18A18B	0.750	1.047	0.915	1.388	1.238	39.56	21.98	84.98	65.01
19A19B	3.339	2.710	2.693	2.320	2.417	18.84	19.36	30.53	27.63
45A45B	0.764	0.622	0.666	0.682	0.643	18.63	12.89	10.82	15.82
2A2B	2.692	1.559	1.369	0.671	0.907	42.10	49.17	75.07	66.31
43A43B	0.797	0.591	0.531	0.251	0.397	25.91	33.35	68.49	50.21
7A7B	3.400	2.487	2.351	2.523	2.309	26.83	30.83	25.79	32.09
24A24B	0.784	1.181	1.106	0.967	1.106	50.60	41.03	23.36	41.11
39A39B	0.354	0.366	0.432	0.449	0.457	3.34	21.78	26.70	28.93
12A12B	0.343	0.364	0.305	0.314	0.287	6.18	11.00	8.52	16.19
23A23B	1.135	0.952	0.960	0.942	1.022	16.11	15.49	16.99	10.01
29A29B	2.088	3.792	2.762	2.156	2.147	81.58	32.27	3.23	2.81
10A10B	0.957	0.755	0.687	0.459	0.564	21.11	28.16	52.03	41.07
36A36B	0.826	0.592	0.596	0.621	0.584	28.37	27.89	24.79	29.33
30A30B	1.857	1.108	1.190	1.189	1.346	40.32	35.92	35.96	27.52
6A6B	0.860	0.789	0.904	0.934	0.821	8.16	5.18	8.70	4.45
27A27B	3.018	2.660	2.072	1.479	1.311	11.85	31.35	51.00	56.56
42A42B	2.382	1.887	1.796	1.671	1.953	20.80	24.60	29.87	18.01
37A37B	0.951	0.796	0.791	0.786	0.687	16.26	16.84	17.34	27.74
40A40B	1.324	0.894	1.165	2.381	1.261	32.49	12.03	79.85	4.77
41A41B	2.921	1.977	2.911	3.835	4.129	32.30	0.32	31.31	41.38
1A1B	3.394	3.175	2.570	2.638	2.364	6.45	24.28	22.28	30.34
16A16B	1.846	2.256	3.614	2.472	4.121	22.21	95.74	33.90	123.25
31A31B	5.901	6.188	6.182	7.200	6.216	4.86	4.76	22.00	5.33
32A32B	8.548	6.755	6.646	6.667	6.375	20.99	22.25	22.01	25.43
5A5B	0.259	0.827	0.678	0.488	0.496	219.67	161.93	88.73	91.88
47A47B	1.473	1.421	1.596	1.478	1.819	3.47	8.39	0.34	23.54
38A38B	0.788	0.831	0.624	0.548	0.468	5.46	20.84	30.44	40.63

Table 12.6 *Mean, minimum, maximum and standard deviation of the CIELAB colour difference values (ΔE^*_{ab}) and the percentage of variation(*) between the AB pairs of textile samples (TS) measured (Real ΔE^*_{ab}) and reconstructed using the TS, the CCDC chart, the sets of Munsell's hues, and all Munsell's colour patches as training sets.*

		ΔE*ab between AB pairs reconstructed				***% of variation vs the real ΔE*ab***			
	Real ΔE*ab	**TS**	**CCDC**	**MUNSELL's Hues**	**ALL MUNSELL**	**TS**	**CCDC**	**MUNSELL's Hues**	**ALL MUNSELL**
meanΔE*ab	1.963	1.809	1.799	1.814	1.771	31.90	31.95	39.05	36.56
minΔE*ab	0.259	0.364	0.305	0.251	0.287	3.34	0.32	0.34	2.81
maxΔE*ab	8.548	6.755	6.646	7.200	6.375	219.67	161.93	168.24	123.25
std. dev. ΔE*ab	1.818	1.594	1.578	1.732	1.627	41.44	33.12	35.36	28.07

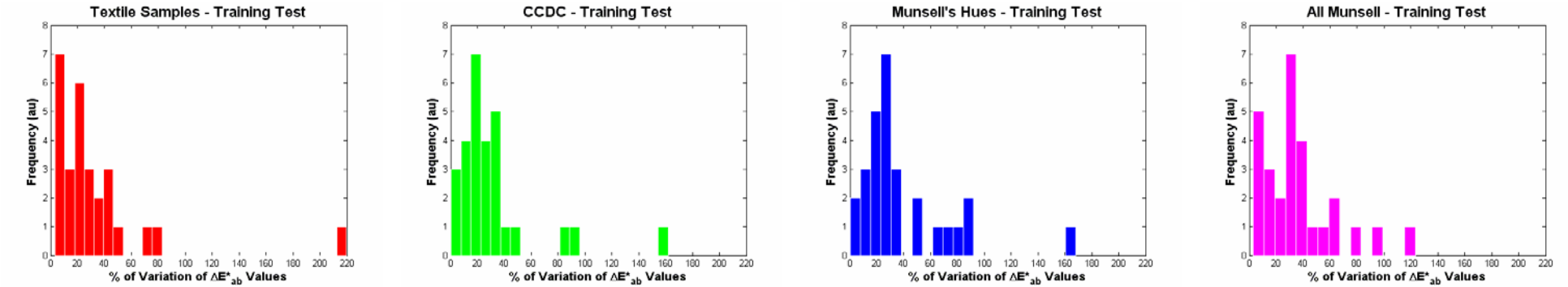

Figure 12.3 *Histograms of the percentage of variation of the ΔE^*_{ab} values between the AB pairs of textile samples (TS) measured (Real ΔE^*_{ab}) and reconstructed using (a) the TS, (b) the CCDC chart, (c) the sets of Munsell's hues, and (d) all Munsell's colour patches as training sets.*

(*) Percentage of Variation of the ΔE^*_{ab} values between the reconstructed AB pairs ($Rec\Delta E^*_{ab}$) and the real ΔE^*_{ab} between the AB pairs measured by a spectrophotometer ($Real\Delta E^*_{ab}$):

$$\%Variation\Delta E^*_{ab} = 100 \cdot \frac{\left| Real\Delta E^*_{ab} - Rec\Delta E^*_{ab} \right|}{Real\Delta E^*_{ab}}$$

Table 12.7 *RMSE values (ΔE^*_{ab}) and percentage of variation(*) between the AB pairs of textile samples (TS) measured (Real RMSE) and reconstructed using the TS, the CCDC chart, the sets of Munsell's hues, and all Munsell's colour patches as training set.*

		RMSE between AB pairs reconstructed				*% of variation vs the Real RMSE*			
AB pairs of TS	**Real RMSE**	**TS**	**CCDC**	**MUNSELL Hues**	**ALL MUNSELL**	**TS**	**CCDC**	**MUNSELL Hues**	**ALL MUNSELL**
25A25B	2.429E-02	2.216E-02	2.856E-02	9.322E-03	2.153E-02	8.78	17.59	61.63	11.39
18A18B	3.971E-03	4.443E-03	4.797E-03	6.405E-03	5.174E-03	11.90	20.80	61.29	30.28
19A19B	1.710E-02	1.868E-02	1.985E-02	1.273E-02	1.609E-02	9.20	16.07	25.58	5.90
45A45B	1.807E-03	2.012E-03	2.209E-03	1.861E-03	2.088E-03	11.33	22.23	2.98	15.50
2A2B	1.548E-02	1.180E-02	1.073E-02	2.847E-03	7.172E-03	23.80	30.70	81.61	53.68
43A43B	2.208E-03	3.800E-03	4.357E-03	2.849E-03	3.140E-03	72.07	97.31	28.99	42.17
7A7B	1.744E-02	1.178E-02	1.384E-02	1.361E-02	1.362E-02	32.44	20.65	21.95	21.88
24A24B	1.660E-03	3.643E-03	4.661E-03	3.844E-03	3.938E-03	119.53	180.83	131.61	137.32
39A39B	9.407E-04	1.757E-03	2.125E-03	2.012E-03	2.066E-03	86.74	125.91	113.93	119.60
12A12B	1.169E-03	1.553E-03	1.293E-03	1.053E-03	1.009E-03	32.82	10.58	9.93	13.74
23A23B	4.795E-03	3.880E-03	3.895E-03	3.383E-03	3.292E-03	19.08	18.78	29.46	31.36
29A29B	3.270E-02	3.271E-02	4.036E-02	3.173E-02	3.374E-02	0.01	23.41	2.96	3.16
10A10B	3.335E-03	3.747E-03	3.150E-03	1.029E-03	1.811E-03	12.36	5.54	69.15	45.71
36A36B	7.179E-03	5.326E-03	5.813E-03	5.621E-03	4.946E-03	25.81	19.02	21.69	31.09
30A30B	1.106E-02	3.278E-03	4.491E-03	4.527E-03	4.488E-03	70.35	59.38	59.05	59.40
6A6B	5.694E-03	6.665E-03	6.779E-03	5.785E-03	6.259E-03	17.06	19.05	1.60	9.92
27A27B	1.001E-02	8.579E-03	8.816E-03	1.183E-02	7.375E-03	14.33	11.96	18.18	26.35
42A42B	1.381E-02	1.582E-02	1.341E-02	1.461E-02	1.110E-02	14.55	2.91	5.82	19.62
37A37B	4.252E-03	3.672E-03	4.408E-03	4.089E-03	3.893E-03	13.62	3.68	3.83	8.44
40A40B	1.450E-02	1.005E-02	9.122E-03	8.376E-03	7.927E-03	30.69	37.08	42.22	45.32
41A41B	2.340E-02	1.400E-02	1.343E-02	9.954E-03	1.381E-02	40.14	42.60	57.45	40.99
1A1B	2.953E-02	2.715E-02	2.431E-02	2.179E-02	2.012E-02	8.06	17.69	26.22	31.87
16A16B	2.305E-02	2.568E-02	4.461E-02	4.115E-02	5.091E-02	11.39	93.49	78.48	120.82
31A31B	9.041E-02	9.940E-02	1.021E-01	1.120E-01	9.362E-02	9.93	12.91	23.83	3.54
32A32B	1.164E-01	9.241E-02	9.378E-02	8.527E-02	8.109E-02	20.65	19.46	26.77	30.36
5A5B	4.235E-03	9.899E-03	9.384E-03	6.468E-03	6.000E-03	133.74	121.59	52.73	41.67
47A47B	4.034E-03	3.779E-03	4.454E-03	4.674E-03	3.609E-03	6.33	10.41	15.86	10.54
38A38B	4.459E-03	5.055E-03	4.232E-03	3.806E-03	3.320E-03	13.37	5.09	14.65	25.54

Table 12.8 *Mean, minimum, maximum and standard deviation of the RMSE values and the percentage of variation(*) between the AB pairs of textile samples (TS) measured (Real ΔE^*_{ab}) and reconstructed using the TS, the CCDC chart, the sets of Munsell's hues, and all Munsell's colour patches as training sets.*

	RMSE between AB pairs reconstructed					*% of variation vs the Real RMSE*			
	Real RMSE	**TS**	**CCDC**	**MUNSELL's Hues**	**ALL MUNSELL**	**TS**	**CCDC**	**MUNSELL's Hues**	**ALL MUNSELL**
meanRMSE	1.746E-02	1.617E-02	1.746E-02	1.545E-02	1.547E-02	31.07	38.10	38.91	37.04
minRMSE	9.407E-04	1.553E-03	1.293E-03	1.029E-03	1.009E-03	0.01	2.91	1.60	3.16
maxRMSE	1.164E-01	9.940E-02	1.021E-01	1.120E-01	9.362E-02	133.74	180.83	131.61	137.32
std. dev. RMSE	2.617E-02	2.406E-02	2.529E-02	2.548E-02	2.309E-02	34.16	44.48	33.70	34.96

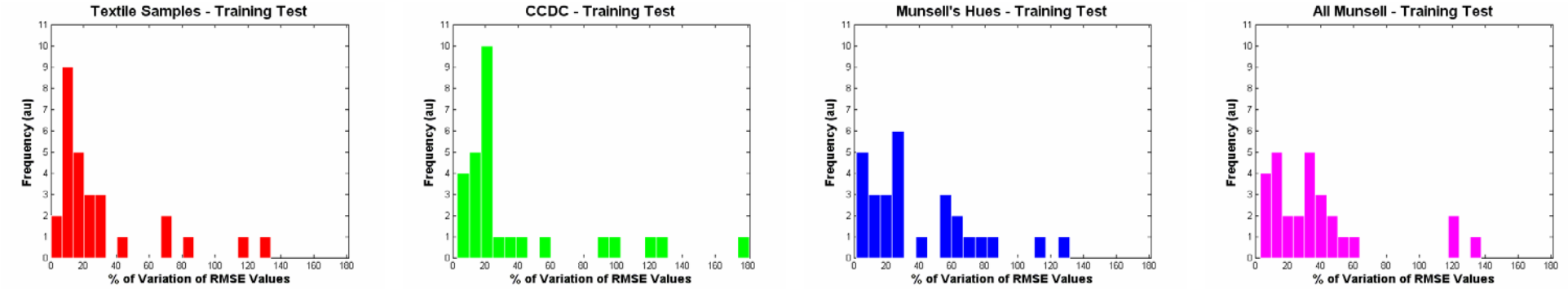

Figure 12.4 *Histograms of the percentage of variation of the RMSE values between the AB pairs of textile samples (TS) measured (Real RMSE) and reconstructed using (a) the TS, (b) the CCDC chart, (c) the sets of Munsell's hues, and (d) all Munsell's colour patches as training sets.*

(*) Percentage of Variation of the RMSE values between the reconstructed AB pairs (*RecRMSE*) and the real RMSE between the AB pairs measured by a spectrophotometer (*RealRMSE*):

$$\%VariationRMSE = 100 \cdot \frac{|RealRMSE - RecRMSE|}{RealRMSE}$$

Finally, in order to have an average picture of results obtained, the mean, minimum, maximum and standard deviation of both the real and reconstructed CIELAB colour difference and RMSE values between pairs of textile samples for all training sets used, and the respective percentages of variation, are presented in Tables 12.6 and 12.8 and in Figures 12.3 and 12.4.

Comparing the mean, minimum, maximum and standard deviation values (Table 12.6) and the histograms (Figure 12.3) of the percentages of variation of the CIELAB colour differences, it can be easily observed that the best reproduction of the CIELAB colour difference values between pairs of textile samples is achieved in average using the CCDC chart (lowest mean and standard deviation), followed by using the textile samples themselves, all Munsell's colour patches and, finally, the sets of Munsell's hues as training sets.

On the other hand, regarding the percentage of variation of the RMSE (Table 12.8 and Figure 12.4), the best reproduction of the RMSE values between pairs of textile samples is achieved in average using the textile samples (lowest mean and standard deviation), followed by using all Munsell's colour patches, the sets of Munsell's hues and, finally, the CCDC chart as training sets.

Summing up, firstly, the multispectral imaging system developed is proved to be able to detect slight differences both in colour and in reflectance spectra between real samples, making it useful for applications that require discrimination. Secondly, the accuracy of system's performance in detecting both the colour differences and the spectral differences between pairs of textile samples obtained is quite low and different in terms of the CIELAB colour difference and the RMSE values depending on the training set used. This is probably a direct consequence of the factors that affect results obtained such as the fact that, apart from the set of textile samples, the training sets used are not of the same kind of the samples to be measured, the limitations of the classification in hues of the test samples, the use of training sets homogeneous in hue to train the imaging system hue by hue, and differences between the textile samples and the rest of colour samples considered (CCDC's and Munsell's) in the measuring instruments and the measuring geometry used to determine the reflectance spectra of samples.

In order to improve these results the first stage would be, as it was mentioned before, finding a complete training set of textile samples made up of sets homogeneous in hue, or whatever the samples to be measured are, that allows a correct classification of the test samples in hues, and covers the whole space defined by the samples to be measured either in the CIELAB space or in the reflectance spectra space. This all is left for future work.